An exploration of experimental and numerical approaches to design of a ducted helical air turbine

by

Philip Vipond

A thesis submitted in partial fulfillment of the

requirements for the degree of Master of

Applied Science (MASc) in Engineering

Science

The Faculty of Graduate Studies

Laurentian University

Sudbury, Ontario, Canada

THESIS DEFENCE COMMITTEE/COMITÉ DE SOUTENANCE DE THÈSE
Laurentian Université/Université Laurentienne
Office of Graduate Studies/Bureau des études supérieures

Title of Thesis
Titre de la thèse   Experimental and numerical comparative study of a ducted helical air turbine

Name of Candidate
Nom du candidat   Vipond, Philip C.

Degree
Diplôme   Master of Science

Department/Program		Date of Defence
Département/Programme	Applied Science - Engineering Science	Date de la soutenance January 06, 2023

APPROVED/APPROUVÉ

Thesis Examiners/Examinateurs de thèse:

Dr. Dean Millar
(Supervisor/Directeur(trice) de thèse)

Dr. Derek Grandsen
(Committee member/Membre du comité)

Dr. David Cerantola
(Committee member/Membre du comité)

Approved for the Office of Graduate Studies
Approuvé pour le Bureau des études supérieures
Tammy Eger, PhD
Vice-President Research (Office of Graduate Studies)
Dr. Abdessalem Bourreouk   Vice-rectrice à la recherche (Bureau des études supérieures)
(External Examiner/Examinateur externe)   Laurentian University / Université Laurentienne

ACCESSIBILITY CLAUSE AND PERMISSION TO USE

Abstract

The proposed device is a ducted air turbine with a 2-bladed helical rotor. To attempt to characterize the performance of the device, as well as establish a methodology for further experimentation, a campaign of testing was undertaken. The campaign described in the work culminates in a comparative study between a simulated experiment (undertaken using Computational Fluid Dynamics) and a physical experiment (undertaken with a dynamometer, and a duct system connected to a flow meter and centrifugal air pump). The simulated experiment has been transformed using the similarity laws, and the resulting data has been used to predict the performance of the physical experiment by interpolating to the setpoints observed in the physical experiment. These setpoints are defined (in both the simulated and physical experiments) by experimental input variables: bulk flow velocity of the fluid, and rotational velocity of the rotor. Each successful experiment produces experimental output variables: braking torque applied to the rotor, and pressure drop across the duct section which encloses the rotor.

A direct comparison of simulated and physical performance data through the use of nondimensional coefficients demonstrates good agreement between the two experiments, though some discrepancy in torque has been identified. The degree of agreement suggests that this implementation of CFD and the similarity laws would be a good basis for future analysis of turbine performance.

Keywords: Ducted turbine, Helical turbine, Air turbine, Computational Fluid Dynamics, Comparative study, Similarity Laws, Nondimensional Coefficients

Acknowledgements

I would like to thank Dean Millar, and committee members David Cerantola and Derek Gransden, for their support and guidance throughout my research.

I would like to thank Greg Lakanen and Alex Hutchison for their advice and assistance with manufacturing and testing methodologies.

I would like to thank Simscale moderator Sebastian Block for his knowledge offered through the Simscale Help Chat.

I would like to thank my parents for their support throughout my academic career.

This would not have been possible without the contributions of all those who supported me.

Declaration

All work set out in this thesis has been undertaken by the candidate.

Table of contents

List of tables

List of figures

Nomenclature

γ_{air} - isentropic coefficient of air

ε - absolute surface roughness

ε_{rel} - relative surface roughness

μ - dynamic viscosity

μ_k - kinetic friction coefficient

υ - dynamic viscosity

ρ - density

Ω - specific dissipation rate

C - coefficient of discharge

C_D - drag coefficient

C_P - heat capacity at a constant pressure

E - Young's modulus

e - coefficient of expansion

f_D - Darcy friction factor

g - gravitational constant

K - turbulent kinetic energy

k - spring constant (also, general unknown coefficient)

R_{air} - specific gas constant of air

Re - Reynolds number

Re_F - Fan Reynolds number

α - angular acceleration (in rad/s^2)

β - flow angle

Γ - power coefficient

η - efficiency

θ_d - deflection angle, measured from a vertical axis

τ - shear stress

φ - flow coefficient

ψ - pressure coefficient

ω - rotational speed (in rad/s)

A - area of a surface or cross-section

a - displacement to a point

b - displacement to a point

D - diameter

d - radial deflection of a beam or rotating eccentric body

E - energy

F - force

f - frictional energy loss (in J/kg)

H - total enthalpy

h - vertical height

$\dot{I}$ - angular momentum

I - moment of inertia

J - moment of inertia of rotation

L - length

M - moment

m - mass

N - rotational speed (in rpm)

P - pressure (gauge or absolute)

Q - flowrate

q - heat energy loss (in J/kg)

r - radius
T - torque
$T(°C)$ - temperature
t - thickness
U - internal energy
u - instantaneous fluid velocity (of a velocity profile)
V - volume
v - flow velocity
$\dot{W}$ - power; rate of energy transfer over time
w - work energy (in J/kg)
x - displacement along a specified x-axis
y - radial displacement (between two viscous surfaces)
z - displacement along a vertical axis

Subscripts and superscripts
0 - at a position where displacement = 0, or at a time designated as 0 seconds
α - corresponding to the simulation, or simulated geometry
β - corresponding to the physical experiment, or physical geometry
τ - pertaining to shear stress
A - air power
b - pertaining to the rotor blade
d - friction drum
e - of an eccentric load
f - friction force (which applies torque via the rotating tension drum)
fx - friction force (in the axial direction of the rotating friction drum)
G - experimentally observed gauge pressure
i - general notation for iterative nomenclature (positions 1, 2, ..., configurations α, β, ..., etc.)
j - the direction of a linear vector
M - mechanical power
m - pertaining to the bearing mounts used in the physical experiment
N - normal force
n - normal to the tangent of rotation of the turbine blade
o - pertaining to the orifice meter used in the physical experiment
p - pertaining to the duct/pipe section of the duct system
S - pertaining to a spring (especially of the two spring balances used in the physical experiment)
s - pertaining to the rotor shaft
T - experimental observation, torque analog
t - tangential to the rotation of the turbine blade
w - sail force, caused by airflow exiting a duct
x_1 - corresponding to position x_1
atm - pertaining to ambient atmospheric conditions
avg - an average of observed data
$bearings$ - pertaining to the ball bearings attached to the rotor shaft
$corr$ - correction/reduction factor (especially a pressure reduction)
dyn - dynamic pressure
err - relative error
$exit$ - pertaining to the outlet of the physical test rig
exp - expected value, modeled from the simulation to predict physical observations
in - pertaining to the inlet of the simulated geometry
$loss$ - loss of energy, work, or pressure

max - pertaining to a local maximum

out - pertaining to the outlet of the simulated geometry

$phys$ - pertaining to the physical experiment

rel - pertaining to a relative frame of reference

sim - pertaining to the simulated experiment

str - pertaining to the tension strap connected to the friction drum in the physical experiment

$*$ - experimental setpoint

1 Introduction

This Master's thesis concerns the design and validation of a prototype turbine device. This introductory chapter outlines the functionality and purpose of the device, as well as the structure and purpose of the thesis itself.

1.1 Design intent and thesis scope

The prototype device has a helical turbine rotor, which has airflow forced onto it. The ultimate intent of the device is for it to be installed on vehicles in motion to harness captured airflow as the bulk of the air passes over and around the body.
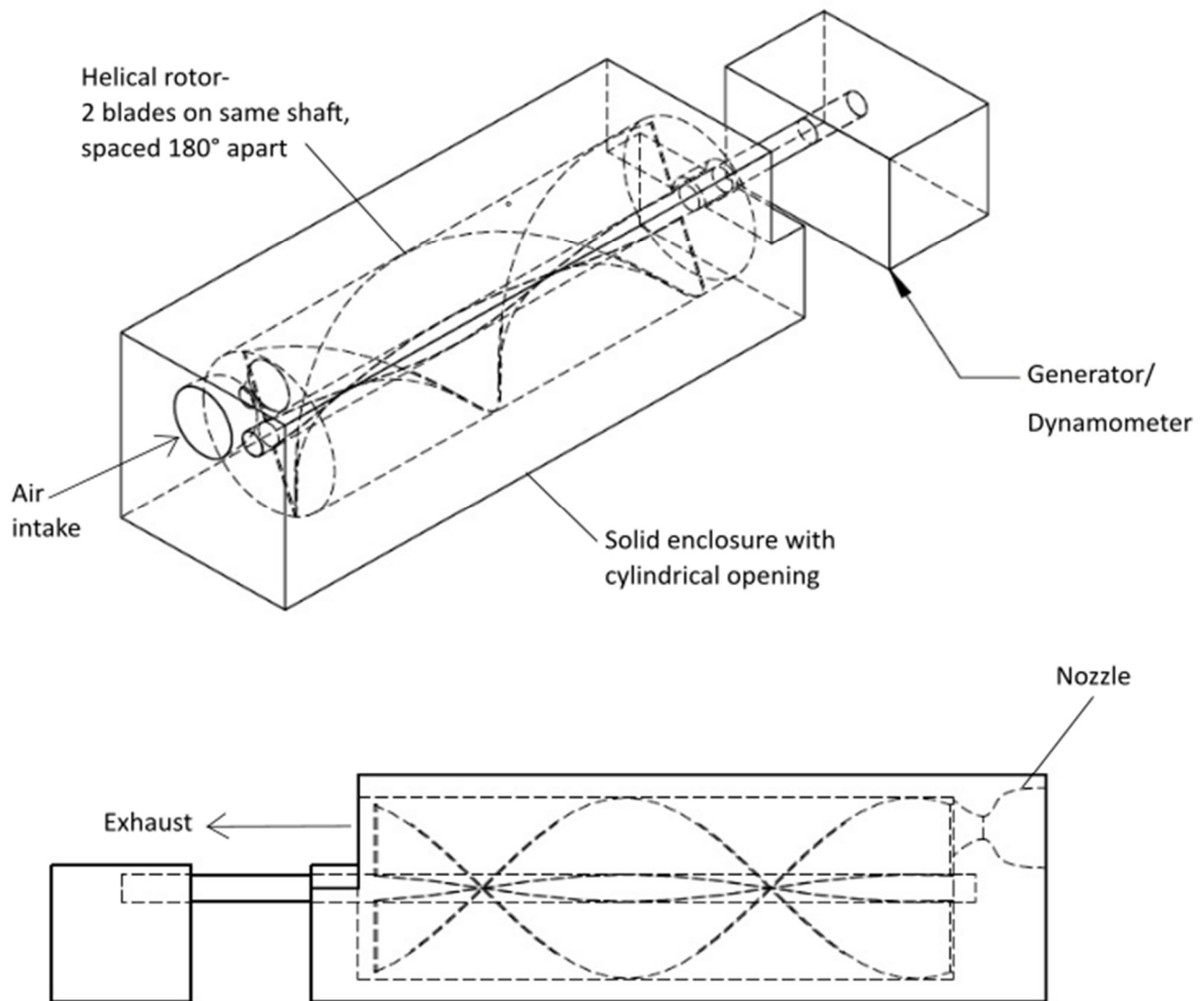
Figure 1.1: Sample schematics used in patent application for prototype device; design includes partial admission of flow, with arbitrary nozzle profile at intake

This study focuses on the rotor being mounted in a duct. Multiple variations of the device may incorporate partial or full admission of flow, and any combination of nozzle, diffuser or neither. Figure 1.1 is an early concept, which included a nozzle of arbitrary geometry and partial admission.

The design intent is for the turbine-generator to act as an auxiliary device which will exploit pressure differentials known to occur around a vehicle when it is in motion. For example, in Figure 1.2, a high-pressure region under an automotive vehicle and a low-pressure region at the rear of the vehicle would create a differential that could be exploited, given proper placement of the turbine device. Another such pressure differential exists between the top and bottom of an airplane wing.
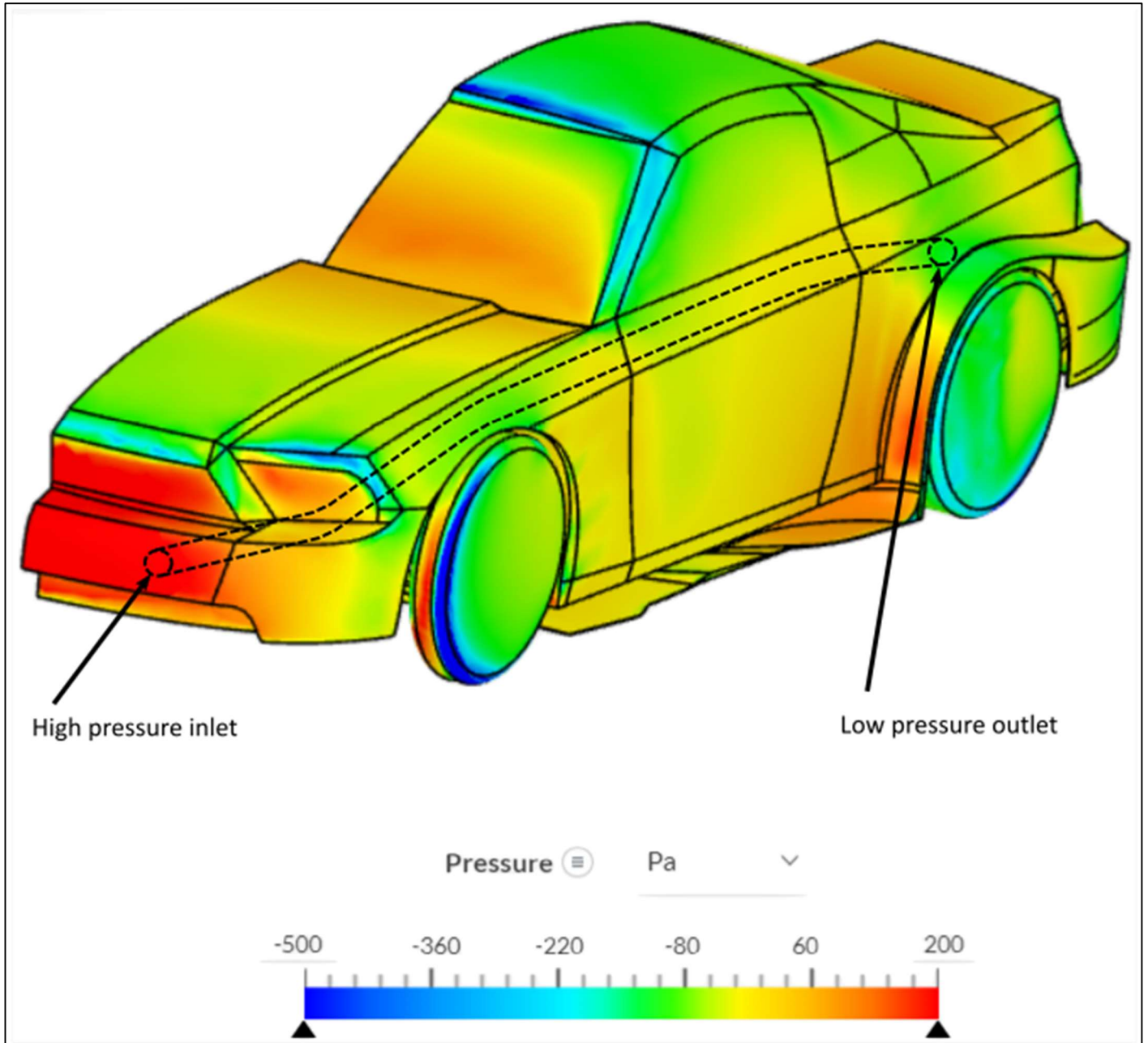
Figure 1.2: Depiction of hypothetical positioning of prototype device, based on pressure distribution on an automobile (Simscale, 2022a)

Note that these positions may not be ideal in a practical setting, as the study of aerodynamics has resulted in highly refined designs of vehicle bodies (Barnard, 2001). For that reason, this thesis focuses on the turbine rotor performance without necessarily considering a specific vehicle, or location of installation thereupon. As an auxiliary unit, it is conceived that the turbine would generate electricity and consume this immediately by powering on-board systems, including a charge controller and battery.

This overall concept is protected by a patent applied for by the candidate (Vipond, 2019).
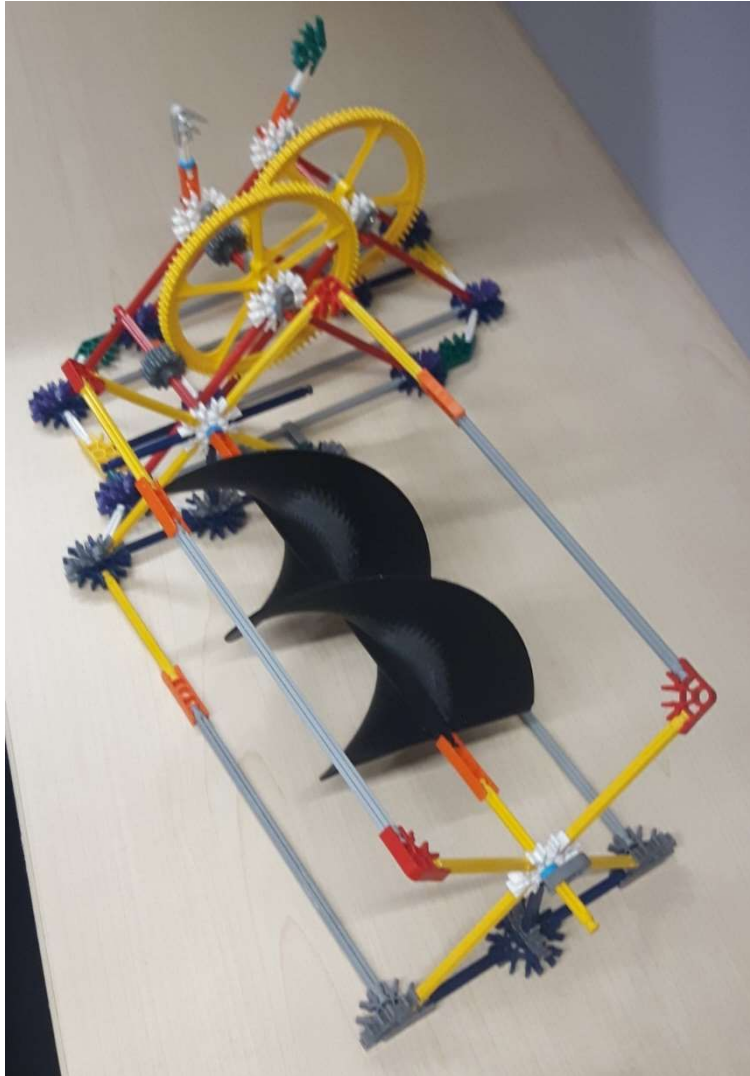
Figure 1.3: Preliminary prototype test; K'Nex test setup with single blade, 3D printed rotor

In advance of patent application submission, preliminary experimental investigations were undertaken using K'Nex building components to form the rotor and mounting assembly. Airflow was provided simply by a handheld blower. These preliminary tests were rudimentary and purely qualitative; the goal was to compare the performance of the proposed helical blade to a conventional fan blade, so multiple configurations of the helical rotor were created and tested, with the same applying to a 4-bladed Horizontal Axis Wind Turbine (HAWT) rotor. In these experiments, assuming a consistent output from the handheld blower, the rotational speed of each blade configuration was

measured and compared. No resistance torque was applied to control the rotational speed of the rotors and so represented a no-load condition for each case.

The fact that the helical blades rotated at similar speeds to the conventionally bladed rotor was encouraging. While not a conclusive determination, this result was deemed was sufficient to justify further testing and the helical rotor design became the basis for further tests with 3D printed blades and the same test setup (see Figure 1.3). After another round of comparative testing the rotor was enclosed in a stiff paper cylinder to contain the airflow as it passed along the blade. A simple nozzle shape was also affixed to the inlet of the test rig to increase the admission velocity (Figure 1.4).
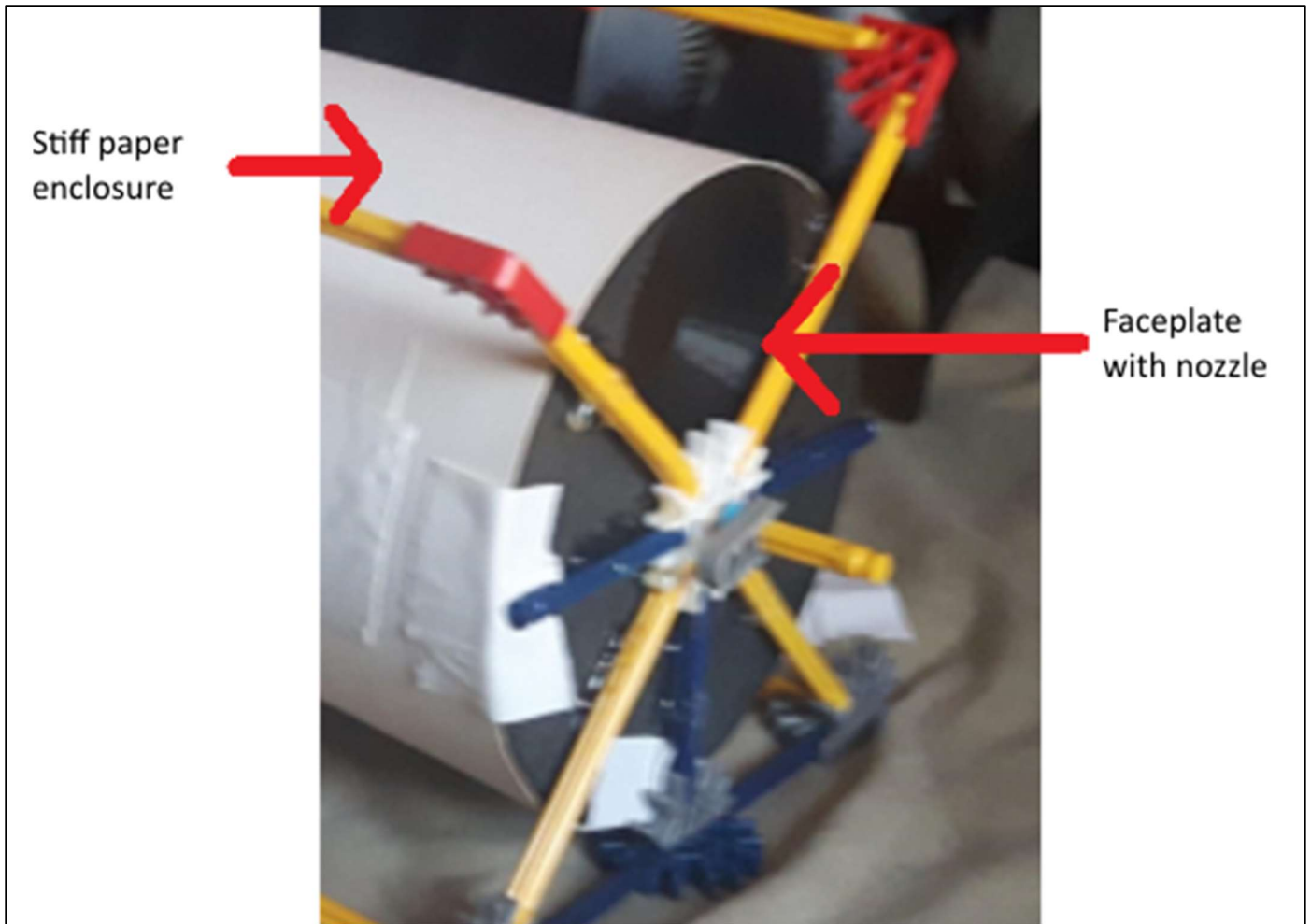
Figure 1.4: Preliminary prototype test; simple 3D printed nozzle attachment for partial admission of flow

Tests of multiple helical rotors, as well as 3D printed instances of a 4-blade HAWT rotor, had each produced significant rotor speeds under the no-load condition, but there was no conclusive result establishing which rotor had better performance. It became apparent that a much more refined and rigorous, scientific testing approach was required, which motivated the investigations set out in this thesis. Although Computer Aided Drafting (CAD) technologies provide rapid and accurate prototyping capabilities, it was also realized that investigating the helical air rotor using Computational Fluid Dynamics (CFD) would be advantageous in helping to identify the ultimate

performance to be expected of a rotor of that form. The use of CFD could assist in hypothesis formulation in design and performance assessment according to the scientific method. As a result, CFD investigations were also included in the scope of the master thesis investigations. Instead of comparisons between different rotor types, comparisons would be made between experimental performance tests on helical turbines and those of CFD simulations adopting similar geometry and operating conditions. Experimental investigations of bladed rotors were not deemed necessary as these are well characterized by others in the literature (e.g., Burton et al., 2001).

It should be noted that practical implementation of the device will require significant further testing and optimization. The obvious drawback associated with its intended use is that the rotor-turbine itself adds resistance to the vehicle body in motion, diminishing the overall efficiency of its propulsion. However, this is no different than the use of an alternator being driven from the drive shaft of an internal combustion engine. It is the utility of the form of energy required for the vehicle systems which dictates. Nevertheless, to minimize the resistance associated with gaining such utility, the rotor must be designed and positioned in such a manner as to maximize power takeoff, that is: it should efficiently convert available air power into work.

While it seems obvious that a turbine cannot operate at 100% efficiency and therefore could never provide more power than it loses in added resistance, it is also true that there are inevitable losses associated with vehicle form itself (Barnard, 2001). Vehicles will always have certain areas of their form that must increase resistance by necessity of their function. The device under investigation aims to opportunistically exploit such losses and convert them to useful work. Some minimum usefulness could be found simply in powering emergency systems in case of power failure.

As a pedagogical exercise, the scope of the master thesis work was also deemed valuable to support the ongoing development of the patent-protected concept following thesis completion. In this sense, the process of testing and designing such a device is valuable in its own right. By simply creating a test piece and validating (or invalidating) it, a great deal of knowledge can be gained pertaining to CFD and experimental investigation, for advanced design purposes.

1.2   Key research questions

1.2.1   What is the expected performance of a helical air turbine?

The ability to accurately predict the performance of the turbine device is crucial to the development process. The quantities of relevance to performance assessment are the pressure drop across the rotor, the air flowrate (or velocity) through it and the torque developed while the rotor is under load at specific operating speeds. Ideally, the optimum operating conditions for the device at a given scale, or vehicle speed and duty would be determined.

1.2.2   What design methodology should be adopted for helical air turbines?

Many different configurations of the device have been investigated in a rudimentary fashion already. A thorough exploration of the rotor performance should seek to determine which combinations of nozzle, duct and diffuser

around the rotor will produce the optimum performance for prescribed applications. Other variables that may be optimized include, but are not limited to, relative dimensions of the duct, pitch of the blade, and number of blades. Development could be accelerated through the adoption of CFD simulations in advance of further fabrication and testing of prototype devices, but only if the CFD method produces results comparable with physical prototype testing. The thesis will enable assessment of whether the CFD approach is valid in this respect.

1.3 Aims

1.3.1 Explore the use of CFD for performance assessment

This exploration will seek to analyze the performance of the turbine device using CFD software. The aim of this exercise is to determine whether the software can reliably deliver performance data that are relevant to a characterization of the turbine's performance. There are many levels of sophistication and complexity that may be considered in CFD simulations: adoption of appropriate equation of state for the fluid, selection of other fluid properties including turbulence model, use of a rotating frame of reference, and discretization of problem geometry are just four important aspects of use of CFD that the thesis work aims to clarify to render the technique fit-for-purpose as a turbine rotor design tool.

1.3.2 Explore experimental approaches to performance assessment

This exploration will seek to analyze the performance of the turbine device through physical testing. The aim of this exercise is to determine whether practical experimentation in a laboratory setting can reliably deliver results that are relevant to a characterization of the turbine's performance.

1.3.3 Compare and appraise CFD and experimental approaches

This exploration will culminate in an appraisal of both methods of assessing the turbine's performance. In the context of this thesis, the aim is to determine the validity of the simulated results, and potentially to diagnose any flaws in the experimental design of either methodology. In so doing, a basis for further exploration of the turbine and its performance can be established.

1.4 Structure of thesis

The document is divided into 7 main chapters, as follows:

Chapter 1 introduces the design concept, then elaborates upon the motivations and objectives of the thesis.

Chapter 2 presents a review of relevant concepts pertaining to fluid dynamics and turbines.

Chapter 3 describes the methodology used in the CFD portion of experimentation. It expands on the topic of CFD and establishes terminology that is specific to the software that was used during experimentation. It also includes justifications for decisions made pertaining to the design of simulated experiments. The raw performance data generated by the CFD simulation software are presented. The auxiliary procedures used to reduce the raw data to performance variables that can be compared with the experimental results are also presented.

Chapter 4 factually records the test setup for the physical portion of the experiment. It also includes justifications for design decisions made pertaining to experimental design.

Chapter 5 describes the final methodology used in the physical portion of experimentation and presents the raw data recorded from physical experiments, parsed for relevance.

Chapter 6 compares the data obtained in chapters 3 and 5, and discusses the results of the comparative study. Possible sources of error are identified and discussed, and recommendations are made to improve upon the method in further work as appropriate.

Chapter 7 summarizes the outcomes of the work and proposes further work that might be undertaken to build upon it.

2 Background

This chapter provides supporting information which is relevant to the validation of the device. It also explores the existing state of the art, as it pertains to the prototype device. There are many well-established practices and principles that can be examined and applied to the validation of the prototype device. This section provides a brief explanation of each of the principles used in its examination.

2.1 Introduction to turbine design

There is clearly much more to turbine design than set out in this short contribution. Rather than try to present a completely comprehensive discourse on the topic, herein a focus has been retained on presenting the necessary material so that an understanding of mechanisms of power takeoff can be conveyed, as pertains to the specific turbine that is the subject of this thesis. The way that torque is developed by a fluid on a turbine rotor can be described via Euler's turbomachine equation, and two relevant examples have been provided covering the principal classes of turbine type: centrifugal radial flow turbines and axial flow turbines. The way torque can develop on rotors has also been discussed in the context of aerodynamics of HAWT blades and rotors. In these cases, zones of negative and positive pressure arise on either side of the blading. Integration of these pressure forces leads to lift and drag forces developing. These forces, when resolved to the direction of rotation of the turbine rotor also permit estimates of rotor torque and thrust to be established. Such aerodynamic effects arise whenever a fluid of any type is admitted to rotor blading in turbines of all types. Important distinguishing conditions that lead to the selection of varying turbine types to deploy in specific situations include whether the flow is confined, whether the flow is compressible or incompressible.

2.1.1 Euler's turbine equation

The key to understanding how any turbine works is to in turn understand how torque is developed by the rotor through the action of fluid impinging upon it. The angular momentum equation as set out by Cengel and Cimbala (2013) describes net torque, T, arising from a rigidly rotating body with moment of inertia, I, experiencing angular acceleration, α, and angular velocity, ω, as follows:

$$T = I\alpha = I\frac{d\omega}{dt} = \frac{d(I\omega)}{dt} = \frac{d\dot{I}}{dt} \tag{2.1}$$

The net torque can be seen to equate to the time rate of change of angular momentum, $\dot{I} = I\omega$, and is analogous to the linear momentum equation. For a fluid control volume, and steady flow conditions, this can be shown to be:

$$T = \sum_{out}(\bar{r} \times \dot{m}\bar{v}) - \sum_{in}(\bar{r} \times \dot{m}\bar{v}) \tag{2.2}$$

which says the net torque acting on the control volume during steady flow is equal to the difference between the outgoing and incoming angular momentum flow rates. Radius of outlet or inlet, $\bar{r}$, is shown as a vector in (2.2) meaning that the cross product with momentum vector $\dot{m}\bar{v}$ results in a product normal to $\bar{r}$. Analysis with (2.2)

applied to rotating machines recognizes that components of $\bar{v}$, or pressure forces acting on inlets or outlets, that act through the axis of rotation do not contribute to driving torque. Consequently, the critical components of fluid velocity are those that act in tangential directions at control surfaces 1 and 2 of the control volume:

$$T = \dot{m}(r_2 v_{2,t} - r_1 v_{1,t})$$ (2.3)

and this is known as the Euler turbomachine formula. It applies to pumps where work is input, as well as turbines where work is abstracted from the flowing fluid. Importantly, for a pump, control surface 1 is an inlet and control surface 2 is an outlet. For turbines, it is conventional to define control surface 2 as an inlet and control surface 1 as an outlet. Equation (2.2) is applied in absolute terms.
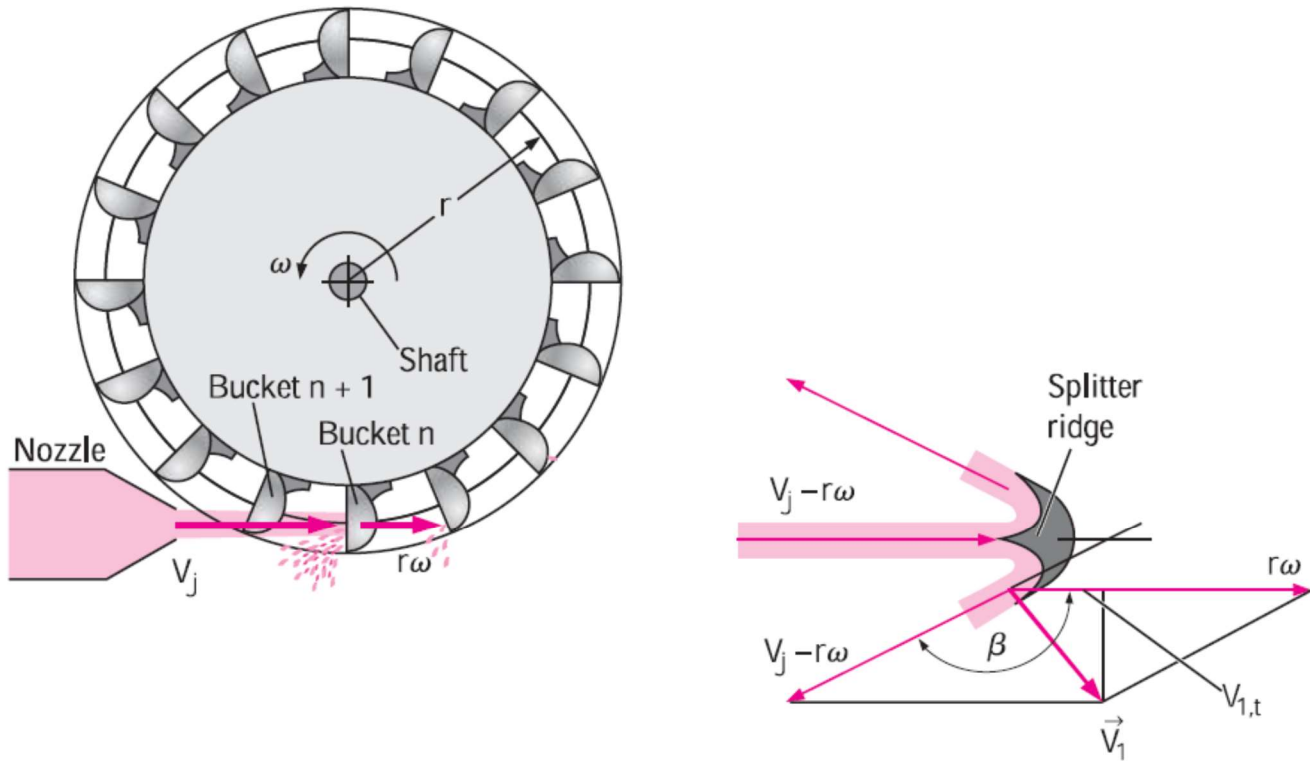
Figure 2.1: LHS- Pelton wheel turbine schematic, RHS- Velocity diagram at input (2) and outlet (1) of bucket n (Cengel & Cimbala, 2013)

The absolute tangential velocity of fluid at inlet, 2, is $V_{2,t} = V_j$ and the absolute tangential velocity of fluid at outlet, 1 is $v_{1,t} = r\omega + (v_j - r\omega)\cos\beta$ with $r_2 = r_1 = r$ produces:

$$\dot{W} = T\omega = \dot{m}r\omega(v_j - [r\omega + (v_j - r\omega)\cos\beta])$$ (2.4)

Equation (2.4) predicts maximum power at $\beta = 180°$ which is not practical as the deflected jet will splash back on the n-1 bucket. 160° to 165° produces maximum power.

According to Gulliver and Arndt (1990) some general features of turbine control behaviour can be described with the aid of the basic equation for a rotating system:

$$J\frac{d\omega}{dt} = T_t - T_{loss}$$ (2.5)

9

where J is the moment of inertia of rotating components, ω is the angular velocity, and T_{loss} is a resisting torque principally due to the load on the turbine rotor. If $T_t = T_{loss}$ then the rotational motion is steady with zero angular acceleration. For either $T_t > T_{loss}$ or $T_t < T_{loss}$, the motion is unsteady as the angular acceleration is non-zero and, usually, a governor is applied so that the turbine output matches the load from a generator connected to the turbine rotor, at a given design operating speed. If such a rotating system suffers an abrupt loss of load, then the turbine rotor will start to accelerate up to a so-called runaway speed.

2.1.2 Application to an axial flow turbine

For an axial flow turbine, such as a propellor turbine, a horizontal axis wind turbine, or the turbine that is the subject of this thesis, there is no component of absolute tangential velocity of the fluid at inlet, 2. Within a stream of oncoming fluid with velocity v_2, the rotor rotates with constant angular velocity, ω, so that the blade at a specific radius, r, has an angle of attack that is optimal in that it maximizes lift force and minimizes drag force.

At the outlet of the control volume, the direction of the velocity of the fluid relative to the blade is frequently taken to be parallel with the blade trailing edge (Cengel & Cimbala, 2013, Burton et al., 2001, Boyle, 2012). For incompressible, or nearly incompressible flow, the magnitude of the velocity of the fluid relative to the blade is determined by the continuity requirement that the magnitude of the normal component of the absolute velocity of the fluid at outlet, $v_{1,n}$, should equal the normal component of the absolute velocity at inlet, $v_{2,n}$. Thereafter the Euler turbomachine equation can be applied to identify the torque developed by the fluid on the turbine rotor. For a control volume that is an annular cylinder with thickness $2\delta r$ with the mid plane annular midsurface at radius r, application of the Euler turbomachine equation produces:

$$T = -\sum_{r=hub}^{r=tip} \rho v_2 \pi r v_{1,t}(r + \delta r)(r - \delta r)$$

(2.6)

where the summation is along the span of the blade from hub to tip.
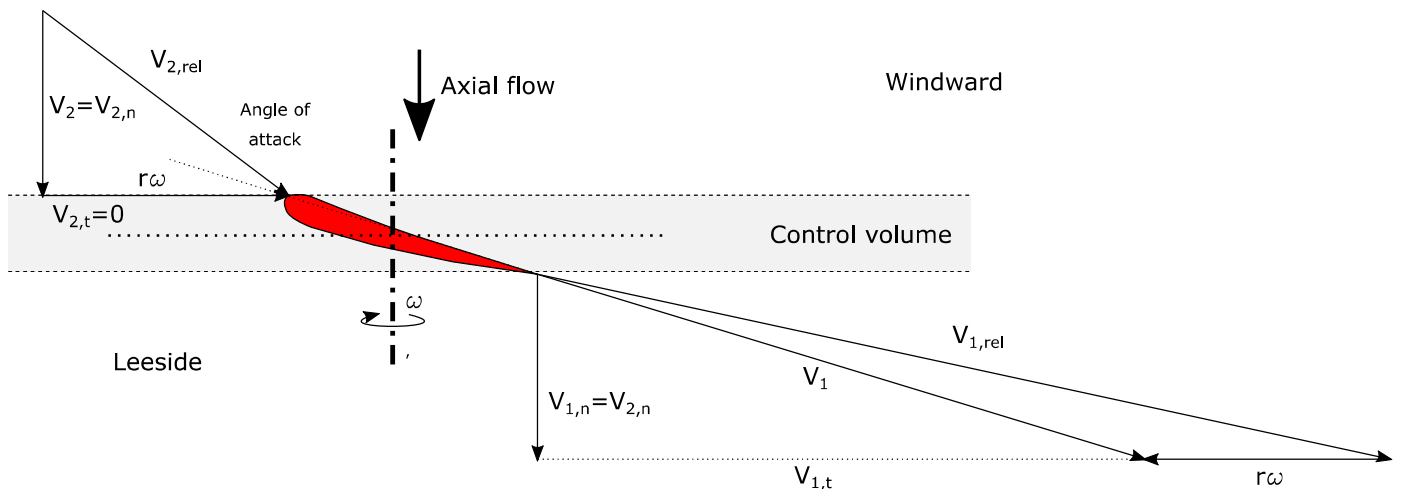
Figure 2.2: Velocity triangles at inlet (2) and outlet (1) of an annular control volume (thickness $\mathbf{2\delta r}$) around a horizontal axis wind turbine blade element

10

2.1.3 Horizontal Axis Wind Turbine

In a reaction turbine, or impulse-reaction turbine, the stator blading has the effect of redirecting, depressurising, and accelerating the fluid, effectively from rest in a reservoir of pressurised fluid. Some turbines are designed to harness work from fluids that are not initially confined in a reservoir, but flow in a free stream at ambient pressure. The fluids in these free streams nevertheless possess harness-able energy, through their movement (kinetic energy). In such cases, those turbines may have no stator blading at all, and the design of the rotor blades must allow for unaccelerated, or un-redirected, flow through the rotor. Such 'free stream' turbines include all types of wind turbine and tidal current turbines.

If individual blades in the rotor cascade have very large spacing, the nozzling effect of the blade passages becomes negligible, the blades act independently and the pressure variations around the blade form alone develop forces that work on the rotor.
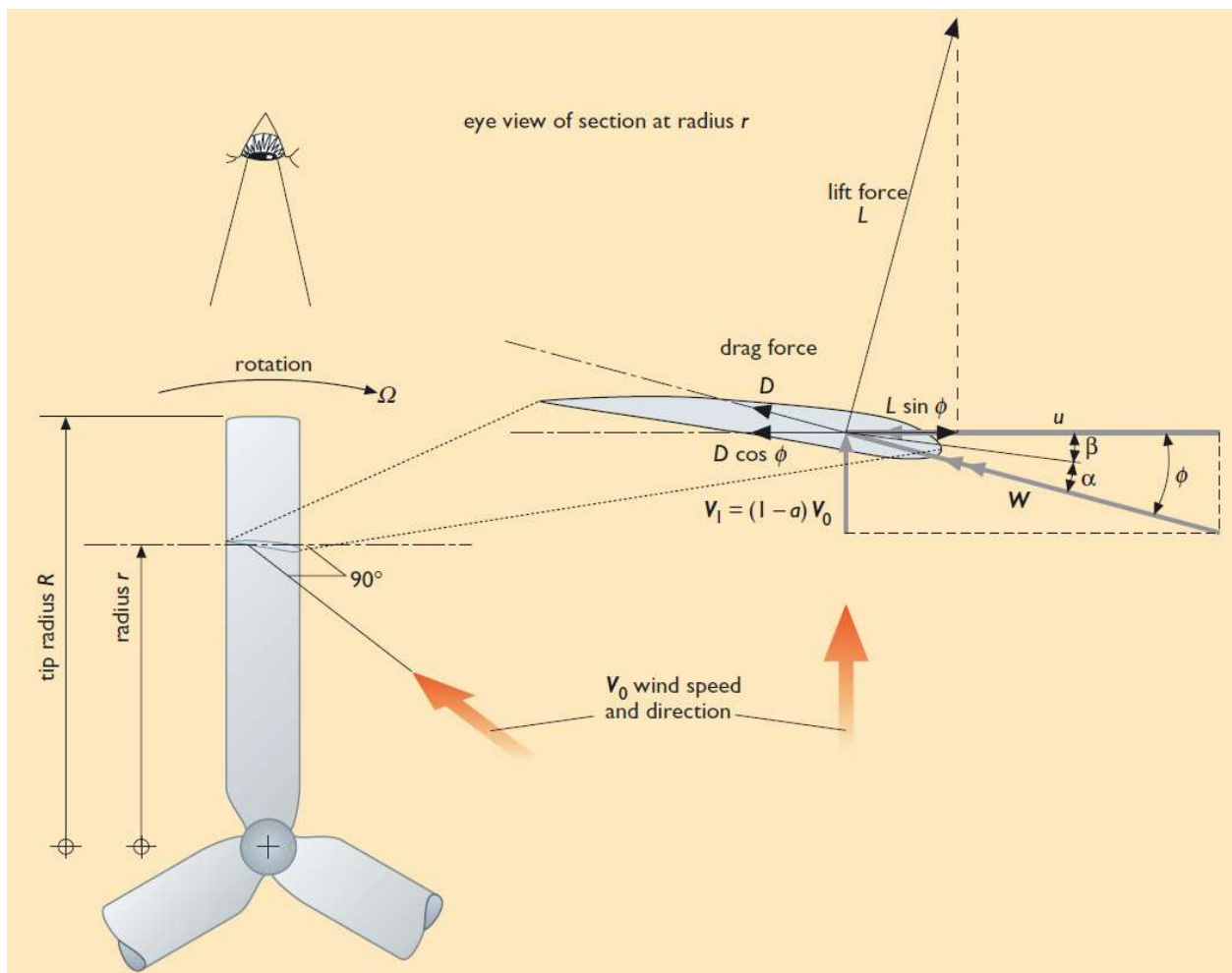
Figure 2.3 Velocity diagram, and context, for horizonal axis wind turbine blading (Boyle, 2012)

The wind direction (the axial direction) is from the bottom of the page upward. Free field (undisturbed) wind speed is v_0. At the radius, r, of the blade profile from the rotating axis, the blade profile has absolute velocity u, constrained to be in the plane about the rotating axis. At the blade profile, in comparison to the undisturbed wind velocity, the

11

absolute axial velocity of the wind is reduced by an approach factor (1-a). The velocity of the wind relative to the blade is W, which is also referred to as the 'relative wind'. One way of interpreting relative wind is that it is the magnitude and direction of wind 'felt by' the blade. Note that the relative wind significantly depends on the rotor peripheral speed at the blade section.
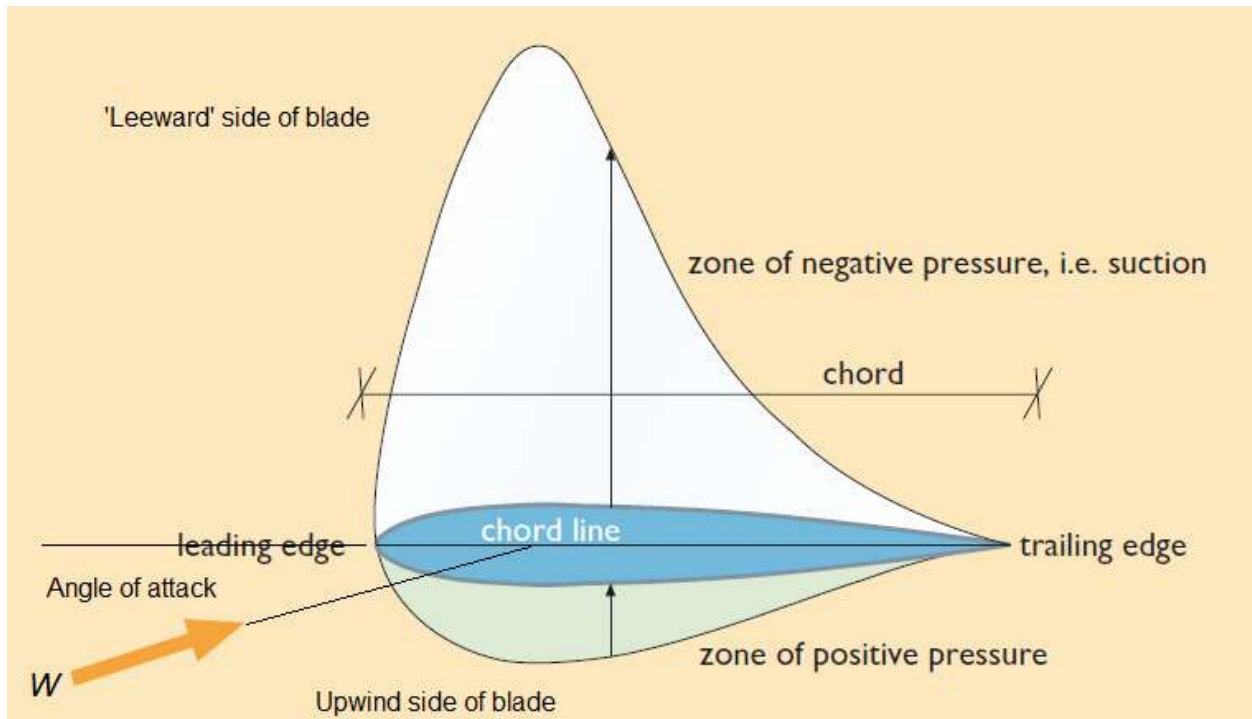
Figure 2.4: Pressure distribution around an aerofoil with a fluid steam impinging upon it with relative wind W forming a small angle of attack with the blade chord (Boyle, 2012); pressure on the blade surface everywhere acts normally to that surface; the extent of the positive and negative pressure zones on the diagram illustrates the magnitude of the pressure acting

As the fluid flows over the blade profile, it must split somewhere around the leading edge of the profile. If the angle of attack is zero, the air will split approximately evenly between the leeward and upwind sides of the blade profile; forces acting on the blade are minimised. If the angle of attack is small, the airflow splits on the upwind side of the blade, close to the leading edge, and the air on the leeward side of the blade must accelerate to rejoin the body of the air flow at the trailing edge to maintain the fluid continuum. The higher fluid velocities along the leeward parts of the blade profile arise with a fall of pressure relative to ambient due to the Bernoulli effect. At the same time, a zone of higher pressure arises on the upwind side of the blade profile due to relatively lower fluid velocities on these parts of the blade periphery.

By integrating the resulting pressure distributions applying over the complete blade profile, accounting for the fact that the pressure acts normal to the blade profile surface everywhere, a resultant force acting on the blade profile can be computed. By convention, and in 2 dimensions, this force is decomposed into 2 force components, one of which reports the magnitude of the force acting in the direction of the relative wind, and a second which reports the magnitude of the force acting at right angles to the relative wind direction. These two components are referred to as the drag force (D, in Figure 2.4) and the lift force (L, in Figure 2.4), respectively.

12

The motion of the rotor is constrained to rotate about the axis of rotation only. Thus, to establish the force developed in the direction of rotor motion, the rotor drag force and the rotor lift force can be resolved independently to an orientation in the direction of motion of the rotor and perpendicular to the direction of rotor motion (the axial direction). The integral of all drag and lift force components from all blade profiles on all rotor blades in the axial direction results in the total axial force acting on the rotor. There is no motion of the rotor in axial direction hence no work is done by the axial force. The total axial force is an important quantity in determining the ratings of bearings and mountings of the rotor. The product of the sum of components of the lift force and the drag force of a blade profile at radius r acting in the tangential direction, and the radius r of the blade profile results in a torque contribution to driving the rotor. Integration of torque contributions due to all blade profiles along the complete radius of the blade, and over all blades of the rotor, produces the overall driving torque of the rotor.

As the relative wind experienced by the blade, depends strongly on the blade peripheral speed, the angle of attack of the relative wind on blade profiles of a blade with uniform cross section will vary with r, for constant rotor angular velocity and steady axial speed of the wind impinging on the rotor. For blade profiles of a given form, there exists an optimum angle of attack that results in the maximisation of the lift force, *L*, and minimisation of the drag force, *D*, and hence maximisation of the driving torque contribution produced by the profile. Such considerations motivate the 'twisting' of the blade profile along the blade length so that the angle of attack of the relative wind on all blade profiles of a turbine blade has the same optimal value along the blade.

2.1.4 Confined flow on an axial turbine and purpose of stator blading

A turbine rotor of the same general form as that of a wind turbine (i.e., axial flow, three bladed, blades of aerodynamic form) can be imagined to be housed within a duct or casing such that the fluid motion impinging on the rotor is confined. For incompressible fluids, such an arrangement can be readily conceived to be a Kaplan or propellor turbine as used in some hydropower installations. With a confined fluid flow of either compressible or incompressible fluid impinging upon such a rotor, the notion that the fluid can be admitted to the duct in a pressurised form can be readily accepted. Such a flow would contain a greater amount of energy per unit mass, than that arising in the kinetic energy of a free stream of fluid alone, of the same diameter. This being the case, the notion that a stator could be 'reintroduced' ahead of the rotor can also be readily accepted. As far as the rotor is concerned, in essence, the mechanism of interaction of the fluid with the rotor blading remains as before. The design intent of introducing such a stator is then to accelerate and direct the fluid flow onto the rotor. Coupled with reconsideration of design rotational speed, the effect will be to increase the relative wind (or 'relative water') over the blade profile, to deepen zones of low pressure on the leeward side of blade profiles and to elevate high pressure zones on their windward sides. In turn, this may produce greater lift for the optimum tip speed ratio and greater torque may thus be realised by a rotor of the same diameter and same number of blades as considered previously for a free stream. Alternatively, one may think of the benefit in a more economically minded fashion as the same amount of torque could be realised in a rotor of smaller diameter.

When rotor blade spacing is reduced so that individual blades may be deemed to interact with one another, nozzle shaped blade passages will accelerate flow around the blades further, further deepening low pressure zones on blade leesides and further elevating high pressure zones on 'upwind' blade sides. Lift and drag forces, and torque will also be developed, their magnitudes and directions continuing to depend on rotor angular velocity, blade geometry and the relative 'wind' impinging on the blades. As can be seen in Figure 2.5, the same principles of power take off can be seen to apply, even when the bulk flow of the fluid through the turbine is no longer axial.
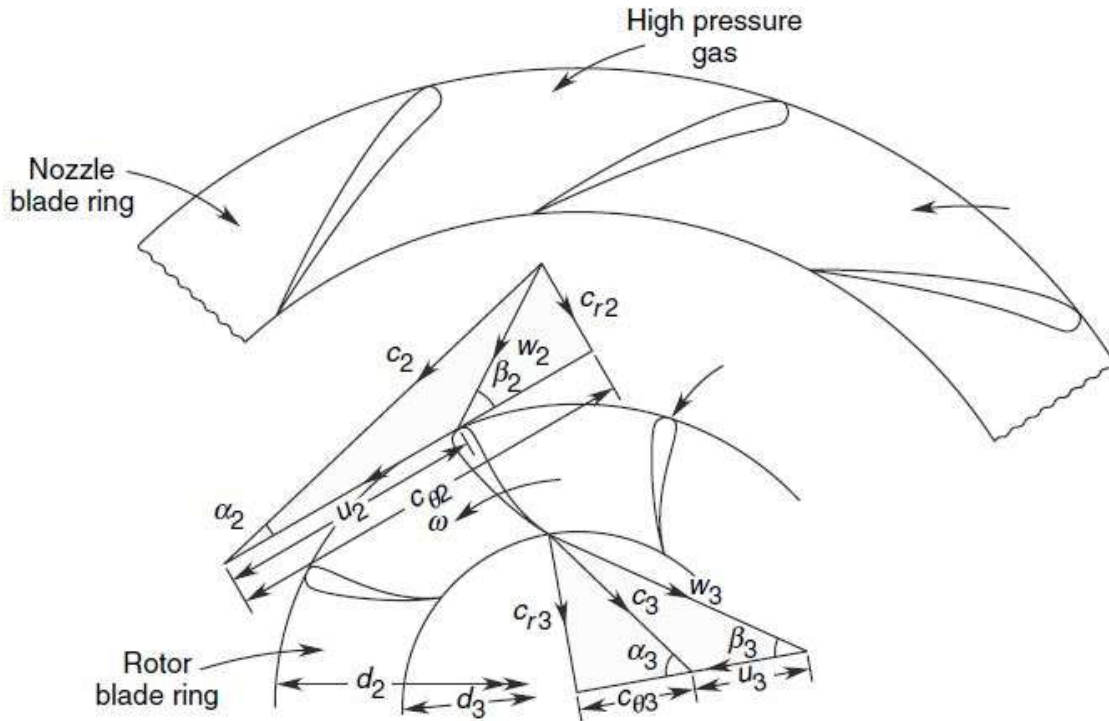
Figure 2.5: Velocity diagrams at inlet and outlet for a radial flow turbine, also illustrating absolute and relative paths of fluid passing through the rotor (Yahya, 2000); the pivoted guide vanes effectively comprise a stator cascade with adjustable blading

-- u_i is the peripheral velocity, c_i is the absolute fluid velocity, w_i is the velocity of the fluid relative to the blade

2.2   Mechanism of power takeoff in helical air rotor

The following figure (Figure 2.6) depicts simulation data that was obtained through CFD experimentation. A full description of CFD procedures applied to the modelling of the turbine will be presented subsequently, but, here, results of CFD modelling on the helical rotor are presented simply to convey to the reader the mechanism through which the helical rotor develops power. The colour gradient represents the local static pressure, while the vector arrows represent the local velocity. For these depictions, the flow of air would be coming out of the page.
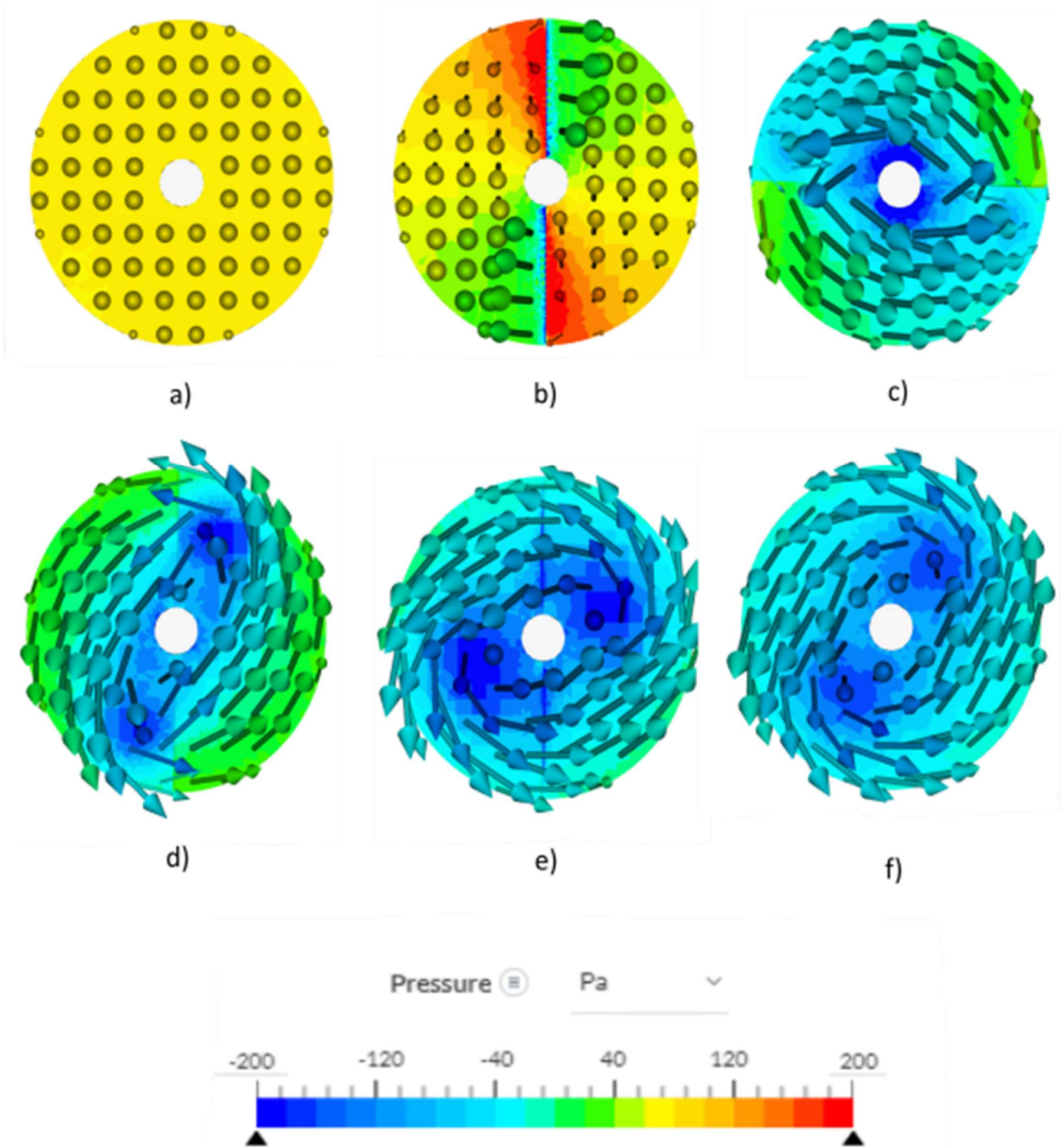
Figure 2.6: Gradient pressure cross-sections with velocity vector arrows, from CFD simulation with a flow of 15 m/s (out of the page) and a rotor

speed of 100 rad/s (CW)

a) just upstream of rotor, b) leading edge of rotor, c) quarter section of rotor,

d) midsection of rotor, e) trailing edge of rotor, f) just downstream of rotor

In Figure 2.6 b), note the high-pressure region at the flow-facing "top" surface of each blade and the low-pressure region on the "bottom" side. This demonstrates that the rotor develops lift as the air flows across it.

As the swirling flow becomes uniform, this pressure distribution becomes less pronounced. After a quarter length down the rotor (the section labeled c) in Figure 2.6), the pressure distribution has become nearly uniform, with nonuniform regions existing near the blade edges. In contrast, the trailing edge of the rotor (labeled e) in Figure 2.6) displays uniform flow despite the presence of the rotor. In terms of the pressure distribution, sections c) and d) demonstrate a continuum between the leading edge and trailing edge of the rotor blades. In these sections, there is a visible discontinuity in the pressure gradient caused by the blades, whereas the pressure distribution in section e) seems to be nearly uninterrupted by the presence of the rotor blades.
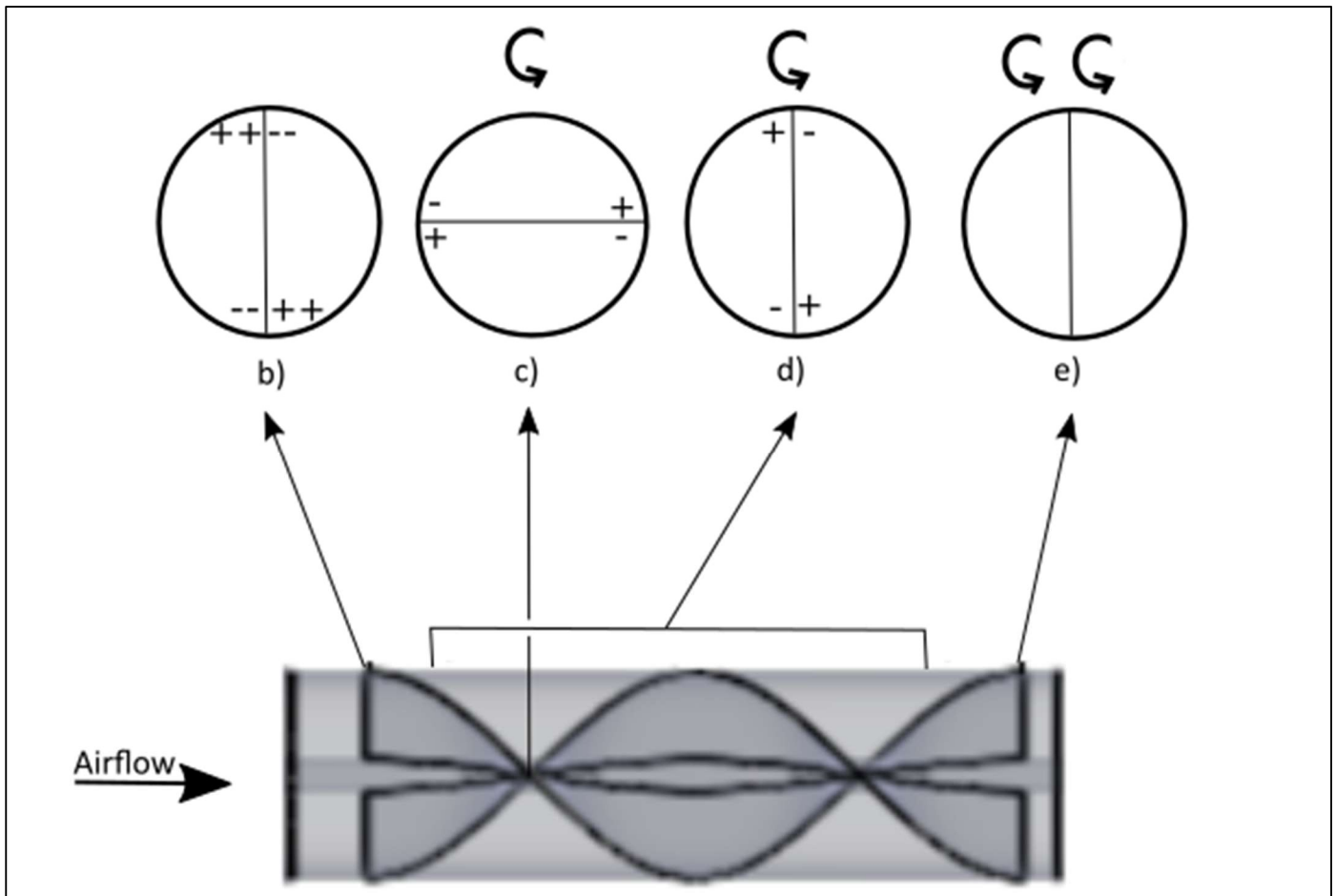
Figure 2.7: Representation of power takeoff in ducted helical air turbine, given flow from left to right (simplified from Figure 2.6)

Based on observations of Figure 2.6, Figure 2.7 depicts a simplified, provisional, representation of the mechanism of power takeoff. The high-pressure and low-pressure regions are shown as +'s and −'s, and the degree of swirl imparted by the rotor on the flow is depicted by the circular arrows above each cross-section. As in Figure 2.6, the cross-sections are consistent with a flow coming out of the page.

The ducted helical turbine behaves like a lift turbine at the leading edge, driven by a pressure differential between the blade surfaces. This effect is greatest at the leading edge (section b)). Note that sections c) and d) are nearly

16

identical. Figure 2.7 depicts section d) as the representative behaviour along the majority of the rotor's length. The effect of this aerodynamic force is diminished as the swirling flow normalizes, until the trailing edge of the rotor blades. Here, the uniform, swirling flow leaving the rotor causes a reactive force that contributes to rotation, as visualized in Figure 2.2 and explained in section 2.1.2.

2.2.1   Similarities and differences to Archimedean screw turbines

The Archimedean Screw is a water turbine, which incorporates a helical rotor and an enclosure that forces fluid over the rotor's surface (see Figure 2.8). While bearing many aesthetic similarities to the proposed device, the operation of the Archimedean Screw turbine is fundamentally different from that considered in this thesis and so it is simply mentioned here to make this distinction. The Archimedean Screw turbine is a stationary turbine which exploits the potential energy drop in falling water (YoosefDoost & Lubitz, 2020). As water flows from the higher intake end to the lower outlet, it drives the rotor. This mechanism of power takeoff may be seen as analogous to the aerodynamic force applied to the helical air turbine. The sum of gravitational forces applied to the top of the rotor is greater than that which is applied to the underside, and the angle of the shaft is such that the component of these forces (which is tangent to the axis of rotation) will dive rotation. In other words, the rotation is driven by a difference in the sum of forces on either side of the rotor blades but is caused by a difference in potential energy rather than a change in the direction of flow.
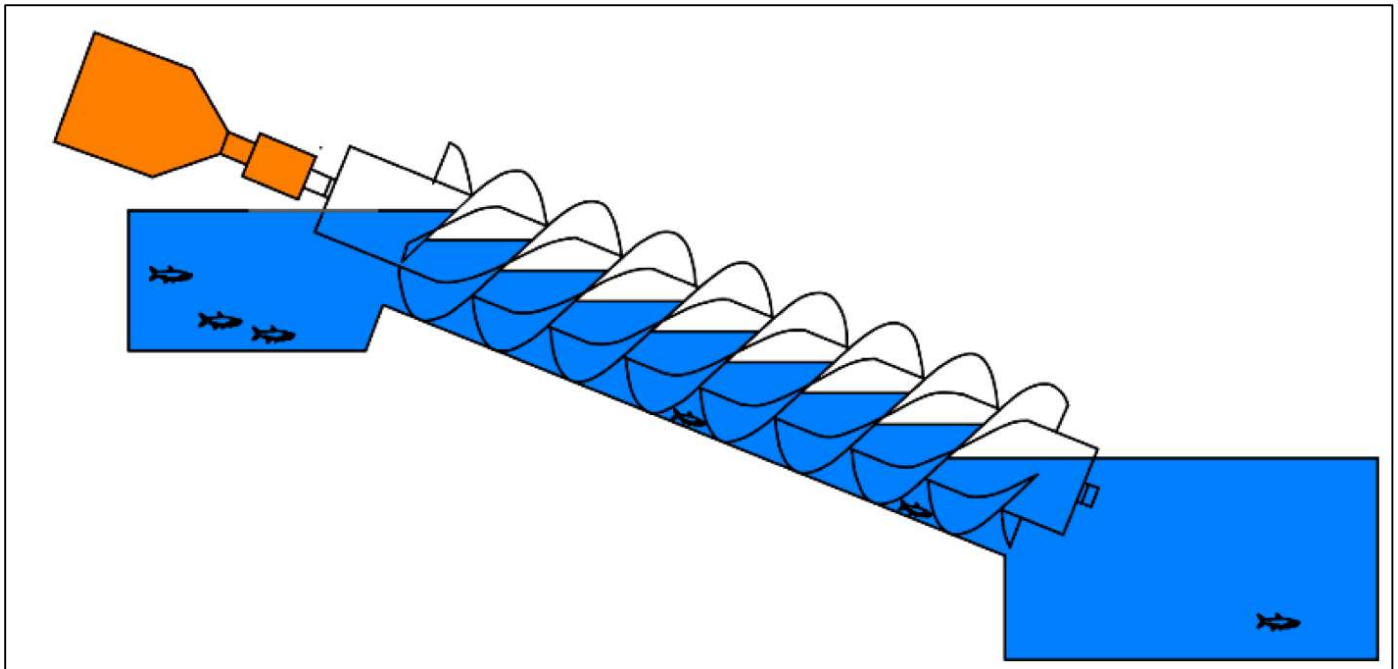
Figure 2.8: Archimedean screw turbine (YoosefDoost & Lubitz, 2020)

The other key difference is the working fluid. Water and air both flow through the device, but the denser fluid only fills the bottom half of the channel (YoosefDoost & Lubitz, 2020). For this reason, Archimedean Screw turbines need not be fully enclosed and therefore, they do not function in the same manner as a typical enclosed (ducted) turbine.

2.2.2 Contemporary studies on helical turbines

Citation	Methodology	Summary	Relevance to, and differences from this work
Akwa et al. (2012)	Comparison of CFD and physical experiments	A compilation of analyses from CFD and physical experiments on Savonius rotors, comparing the performance of various designs	-Comparison of helical rotor to conventional design -Performance/optimization analysis of a helical rotor -Comparison of different numbers of blades -Savonius is VAWT helical rotor (not enclosed)
Damak et al. (2013)	Physical experiment	A helical Savonius rotor is tested under flows of varying Reynolds numbers	-Comparison of helical rotor to conventional design -Savonius is VAWT helical rotor (not enclosed)
Damak et al. (2018)	Physical experiment	The performance of a helical Savonius rotor is analyzed to determine optimal operating conditions	-Performance/optimization analysis of a helical rotor -Savonius is VAWT helical rotor (not enclosed)
Le et al. (2014)	CFD experiment	The performance of a helical Darrieus rotor is compared to a straight-bladed Darrieus rotor	-Comparison of helical rotor to conventional design -Darrieus is vertical axis helical hydro-turbine rotor (not enclosed)
Li et al. (2021)	CFD experiment	The performance of a novel helical rotor for a Roots blower is compared to the conventional three-lobe design	-Comparison of different numbers of blades/lobes -CFD analysis of a novel helical rotor -Two helical rotors are used as a (vertical axis) pump, not a turbine
Rahman et al. (2016)	Comparison of CFD and physical experiments	Helical Savonius rotors with varying numbers of blades are analyzed via CFD and physical experimentation	-Comparative study using CFD and physical experiments -Comparison of different numbers of blades -Performance analysis of a helical wind turbine -Savonius is VAWT helical rotor (not enclosed)
Zhang et al. (2013)	CFD experiment	Helical bladed rotors in an enclosed tube are simulated to assess thermo-hydraulic characteristics	-CFD simulation of an enclosed, horizontal axis helical rotor -Analysis is focused on heat transfer as opposed to power generation through applied torque

2.3   Air flow systems comprising an enclosed duct

As the turbine under consideration within this thesis is envisaged to be mounted within a duct somewhere on a moving vehicle, this section reviews key aspects of subsonic duct airflows. This material provides foundation for interpretation of some of the experimentally measured quantities obtained when testing the prototype.

The energy of a fluid flowing through a pipe (or duct) will rise and fall in predictable ways which correspond to the geometry and roughness of the pipe, among other features. In AMCA (2012), this behaviour is depicted as a graph of local pressure (static, dynamic, and total) and is mapped to the features of a duct system (as seen in Figure 2.9). For example, the resistance element causes a decrease in pressure, while the fan causes a sharp increase.
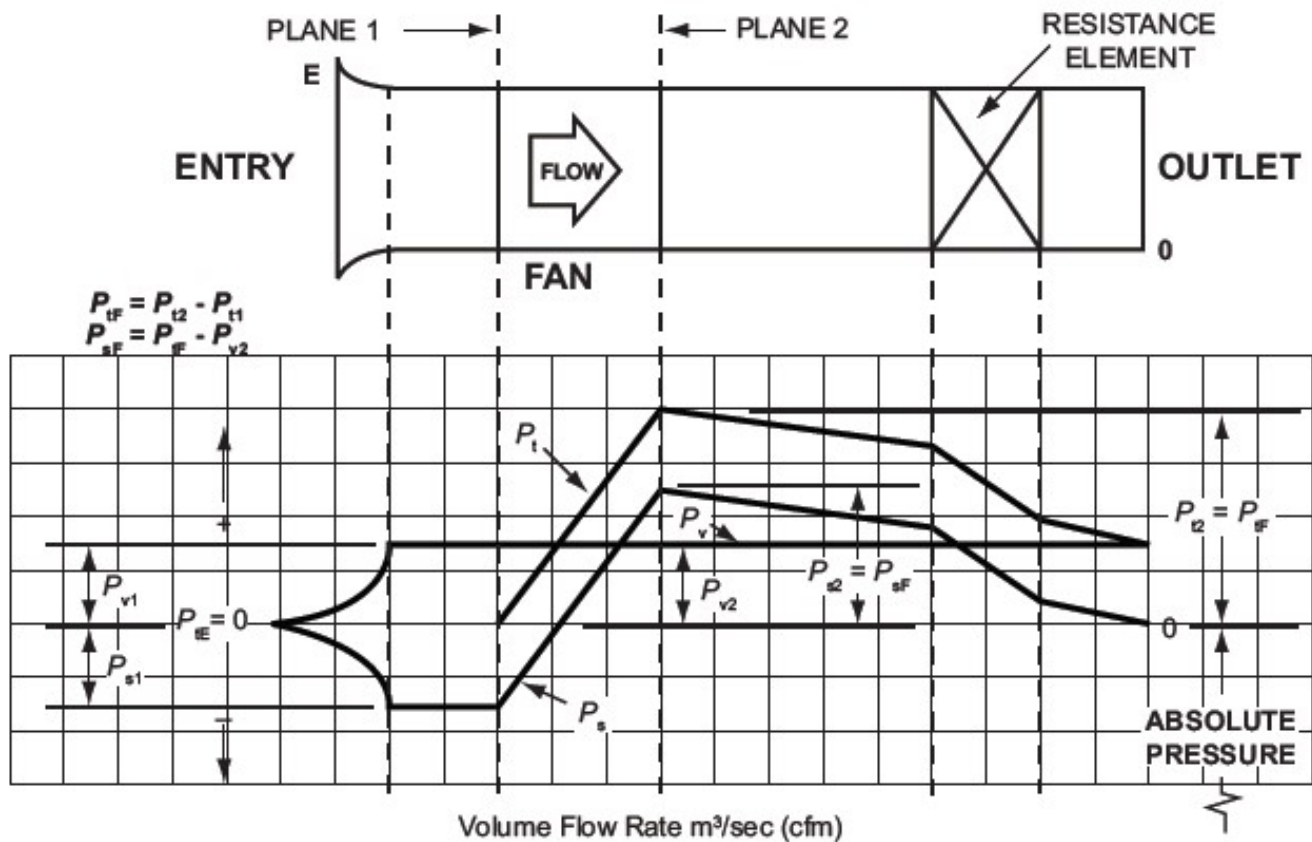
Figure 2.9: Diagram of dynamic, total, and static pressure behaviours in a duct system; fan with inlet resistance element, from AMCA (2012)

The duct system depicted in Figure 2.9 contains a fan. If the duct contained a turbine rather than a fan, the pressure curve would fall in the direction of flow rather than rise.

Each element in a duct system can be associated with such a change (rise or fall) in pressure. This pressure change is a function of the square of the bulk flow velocity (Idel'chik, 1984). Based on mass continuity, it can be assumed that a ducted system must have a constant flowrate throughout the system (barring any splitting or joining of branches in the system). As a result, the bulk flow velocity may be greatly affected by changes in the size or shape of the duct. In Figure 2.9, this is made evident by the change in slope between the larger diameter inlet section and the main duct (when looking at the static or total pressure curves).

Note that, while maintaining a constant cross-sectional area, the duct causes a constant rate of pressure decrease throughout the system (AMCA, 2012), such that the slope of the static pressure curve is parallel along any section where no other behaviour is present. This constant frictional resistance also implies that the duct must be made of the same material throughout the system. This is because the rate of pressure decrease is not only based on qualities of the flow such as turbulence, but also based on the surface roughness of the pipe in question.

The degree of turbulence can be quantified by the Reynolds number, a ratio which represents the interaction between inertial and viscous forces (Reynolds, 1883). While there are some specialized forms of the Reynolds number, the conventional form (which is appropriate for flow in a circular pipe, as is the case here) is calculated using the following equation,

$$\text{Re} = \frac{\rho v D}{\mu} \tag{2.7}$$

where Re is the Reynolds number, ρ is the density of the fluid medium (given in kg/m^3 in SI units), v is the bulk flow velocity (given in m/s in SI units), D is the linear dimension of the flow channel (in this case, the diameter of a pipe, given in m in SI units), and μ is the dynamic viscosity of the fluid (given in Pa*s in SI units, such that Re is dimensionless).

A flow that is significantly more influenced by inertial forces than by viscous forces is considered fully turbulent (about $\text{Re} > 3000$, according to Figure 2.10). A flow that is significantly more influenced by viscous forces than by inertial forces is considered laminar (about $\text{Re} < 2000$, according to Figure 2.10). Each type of flow is associated with a different resistance behaviour. This resistance is quantified by a friction factor, f_D, which is determined by the average roughness of the pipe's surface (known as the absolute surface roughness, ε), relative to the pipe's diameter, D.

Moody Diagram
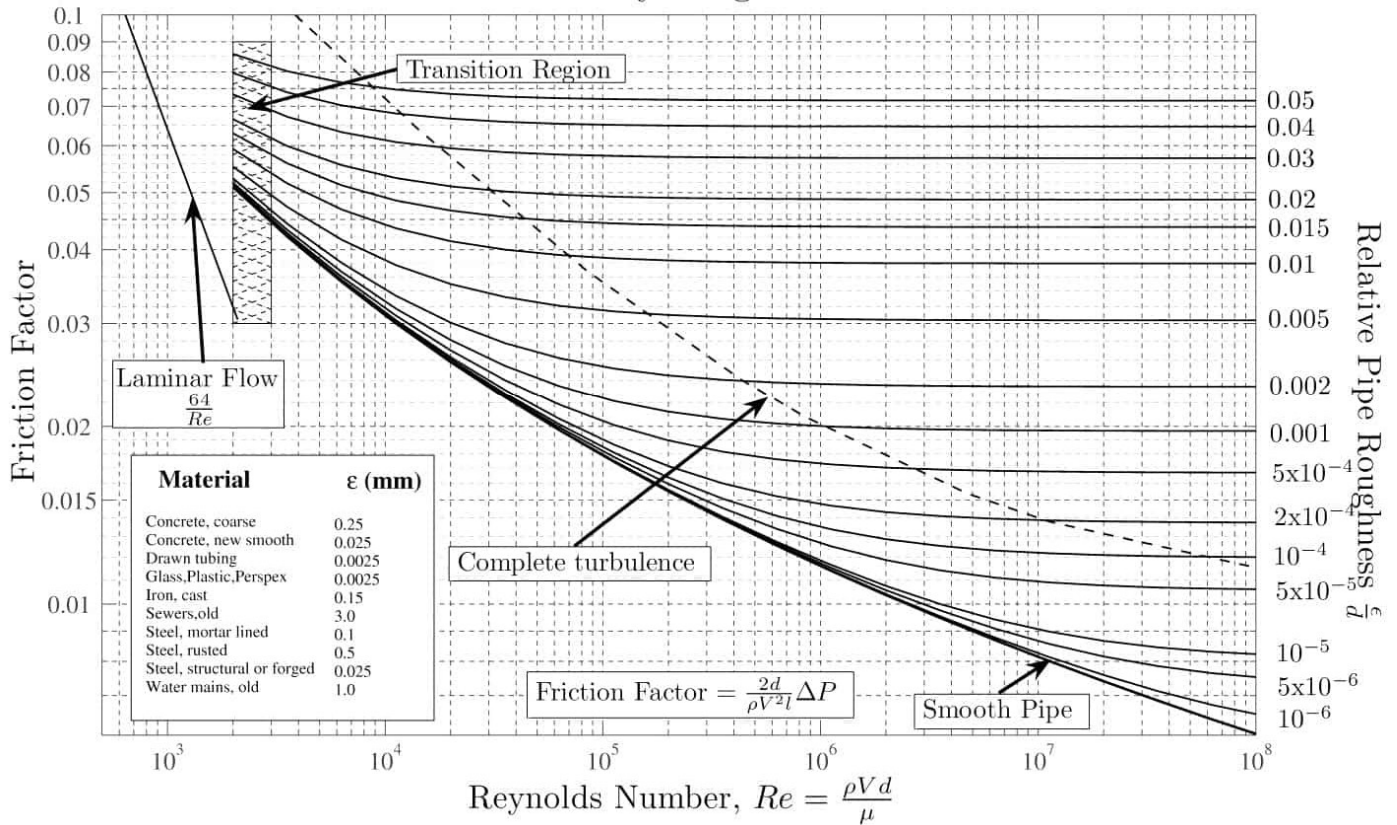
Figure 2.10: Moody chart for circular and rectangular sections (Nuclear Power, 2021)

For a uniform pipe surface with a constant f_D, the frictional resistance associated with the pipe is constant. Further, each element comprising the system can be associated with such a frictional loss; these are conventionally referred to as major losses (Idel'chik, 1984). For instance, in the turbulent regime, a surface with negligible roughness will be modeled as a "smooth pipe" (lowest curve in Figure 2.10), using the following equation:

$$f_D = \frac{0.316}{\text{Re}^{1/4}} \tag{2.8}$$

$$\Delta P_{loss,p} = f_D \frac{\rho v^2 L_p}{2D} \tag{2.9}$$

Where $\Delta P_{loss,p}$ is the pressure loss associated with a length of "smooth pipe", and L_p is the length of the duct or pipe in question.

Other elements of a duct system which may produce a change in pressure are changes in the form, size, or orientation of the duct. Idel'chik (1984) refers to such pressure behaviour as minor losses. An example of minor loss related to a change in size is the pressure change associated with a nozzle or diffuser. An example of a minor loss in a more complex duct system would be a junction which splits or joins the flow.

Since each element can be associated with a specific pressure behaviour, it follows that removing a component from the system will produce a graph which is parallel, but with different pressure, based on the pressure change associated with the removed component.

21

The pressure change associated with a given component remains consistent, irrespective of behaviour elsewhere in the system (McPherson, 1993). For this reason, local pressure measurements at two points can be used to record the pressure behaviour associated with a section of the system between those two points. This makes it possible to isolate the pressure behaviour associated with a specific component, simply by taking the difference between the system's pressure behaviour with and without that component. However, this is only possible when components in the system are spaced such that the pressure behaviour associated with the element does not overlap the pressure behaviour associated with another element. Such interference might make it impossible to isolate one behaviour from another.

2.3.1   Diffusers and system exit losses

Enclosed turbines prevent loss of flow in the radial direction and thus control the working fluid in comparison to free stream turbines. This advantage can be further improved upon using combinations of nozzles and diffusers. Directing flow onto the rotor with a nozzle increases flow velocity at the cost of increased pressure resistance (Eastop & McConkey, 1993). Adding a diffuser decreases the overall kinetic energy loss as airflow exits a system. This provides a greater system pressure drop to be utilized across the turbine rotor.

2.3.2   Rotor speed control and rotor start-up

The electricity generated by turbines must be of constant frequency since most common appliances rely on a set frequency to function (Burton et al., 2001). As the frequency is a function of the rotational speed of the rotor, the rotor speed must be strictly controlled. This is the reason that the convention for depicting the performance of turbines is based on a set rotational speed (such as in Figure 2.11). Changes in fluid density, size as well as rotational speed will result in changes in the performance of the fan or turbomachine, and so these are all reported in performance specifications. The actual rotational speed of a turbine rotor that is directly coupled to a generator depends on the number of pole pairs in the generator and the required grid frequency. Some modern turbines break this relationship in order to maintain optimal tip speed ratio and in such cases power electronics are used to rectify variable frequency AC to DC which is in turn inverted to AC at the required frequency (e.g. most Enercon HAWTs[1]).

Along with speed control, stand-alone (not connected to the utility grid) turbines must also have a means of dumping excess power, so that they do not overload.

---

[1] Example specifications may be viewed at: https://www.enercon.de/en/products/

SIZE 30 FAN AT N RPM

P_t

P_s

η_t

η_s

H

OPERATION AT
STANDARD DENSITY

PRESSURE, P

POWER, H

EFFICIENCY, η PERCENT

100
90
80
70
60
50
40
30
20
10
0

AIRFLOW, Q
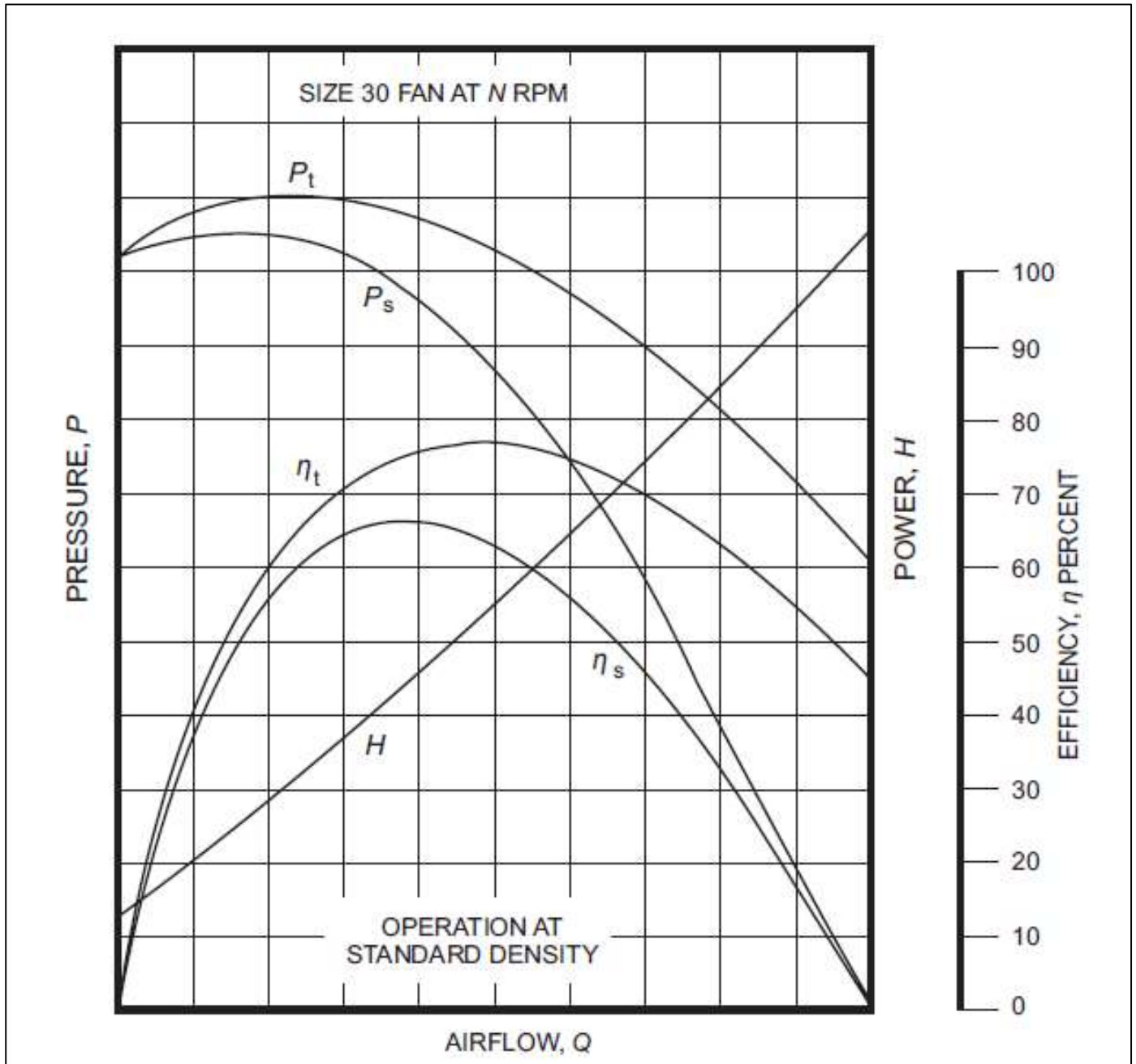
Figure 2.11: Sample fan curves, as seen in AMCA (2007)

Additionally, it is important to realize that the velocity diagrams for turbine rotors (such as that shown in Figure 2.2) apply only when the rotor itself is rotating (at design speed). This can be quite easy to miss in the study of static diagrams in textbooks. Only at those conditions does the impingement of the fluid on the rotor blading produce work that, in-turn, keeps the rotor moving under load. If the rotor is in a starting condition where rotation is 0, then the angle of attack of the fluid to the blade can be very different than that in the design operating condition. The magnitude and direction of resulting forces on the rotor may be such that sufficient rotor torque for sustained operation is not developed. For this reason, frequently in the design of turbines, auxiliary starter motors may have to operate to bring the rotor up towards design operating speed, so that the rotor motion under load is sustained. The

blading on some turbine rotors can be designed so that the fluid impinging on the rotor at start-up will cause the rotor to rotate under a no-load condition. Then the need for such an auxiliary motor may be avoided; the load can be gradually applied to the rotor once it has approached operating speed. Other 'starting condition' measures may apply too, such as varying the velocity of the fluid impinging on the rotor (its magnitude and direction) or altering the pitch of the rotor blades.

2.4   Determination of rotor performance via similarity laws

As will be seen in chapter 3, the similarity laws are drawn upon to transform performance variables determined from CFD simulations to conditions identical to those of the physical experiments.

The similarity laws (known as the fan laws when applied to fan systems) are a set of equations which represent the relationship between fans or other turbomachinery that have similar geometry (in the mathematical sense), as they operate at different sizes, fluid velocities, rotational speeds, or in different fluid media (as discussed, for example, in Streeter et al., 1997). In practice, they may be used to predict the performance of a fan or turbine rotor. Providing the condition of geometric similarity holds, a known performance, which is observed under certain operating conditions, may be transformed to obtain an expected performance under a different set of operating conditions. In this work, their main application is in calculation of the transformed pressure and torque developed which is illustrated with a small sample of data below, in Table 2.1.

From the simulated CFD data, power and efficiency can be approximated using the following equations:

$$\dot{W}_M = T\omega \tag{2.10}$$

$$\dot{W}_A = \Delta PQ \tag{2.11}$$

$$\eta = \frac{\dot{W}_M}{\dot{W}_A} = \frac{T\omega}{\Delta PQ} \tag{2.12}$$

where $\dot{W}_M$ represents mechanical power, $\dot{W}_A$ represents air power, η approximates efficiency, T is taken from the moment applied to the rotor about the axis of rotation, ω is the rotational speed in rad/s, ΔP is the difference between the intake pressure and the pressure immediately before the diffuser, and Q is the intake velocity times the annular area of the duct.

Note, in equation (2.12), that the denominator defines air power as $\dot{W}_A = \Delta PQ$. It is important to understand that this formulation is specific to the experimentation in this work, as it relies on an assumption of incompressibility. This assumption is based on the range of flow velocities selected for the CFD and physical experiments, which reflect typical city driving speeds in an automobile.

Using the sample CFD data (LHS of Table 2.1) with equations (2.10) to (2.12), the CFD simulation data can be reduced to the following results:

Table 2.1: Sample CFD data and results, including calculated power and efficiency, organized by constant N (no similarity laws applied)

v_α	ω_α	D_α	P_1	P_2	T_α	Q_α	ΔP_α	$\dot{W}_{A,\alpha}$	$\dot{W}_{M,\alpha}$	η_{sim}
m/s	rad/s	m	Pa	Pa	N-m	m³/s	Pa	W	W	%
15	100	0.0401	86.5	-102	0.003516	0.0185	188	3.49	0.352	10.1
10	100	0.0401	36.3	-45.5	0.001486	0.0123	81.8	1.01	0.149	14.7
5	100	0.0401	7.51	-10.1	0.000288	0.00617	17.6	0.109	0.0288	26.5

The first similarity law is as follows:

$$Q_\beta = Q_\alpha \left(\frac{\omega_\beta}{\omega_\alpha}\right)\left(\frac{D_\beta}{D_\alpha}\right)^3 \tag{2.13}$$

where Q_i is the flowrate of the ith configuration of the rotor, ω_i is the rotational speed of the ith configuration of the rotor, and D_i is the diameter of the cross-sectional flow area of the ith configuration of the rotor. Note that, in this context, configuration α corresponds with the dimensions of the simulation and configuration β corresponds with the dimensions of the physical experiment.

The second similarity law is as follows:

$$\Delta P_\beta = \Delta P_\alpha \left(\frac{n_\beta}{n_\alpha}\right)^2 \left(\frac{D_\beta}{D_\alpha}\right)^2 \left(\frac{\rho_\beta}{\rho_\alpha}\right) \tag{2.14}$$

where ΔP_i is the pressure developed by the ith configuration of the rotor, and ρ_i is the density of the fluid in the ith configuration of the rotor.

Finally, power can be calculated with the third similarity law:

$$\dot{W}_{A,\beta} = \dot{W}_{A,\alpha} \left(\frac{n_\beta}{n_\alpha}\right)^3 \left(\frac{D_\beta}{D_\alpha}\right)^5 \left(\frac{\rho_\beta}{\rho_\alpha}\right) \tag{2.15}$$

where $\dot{W}_{A,i}$ is the air power of the fluid in the duct, in the ith configuration of the rotor.

When using the similarity laws, efficiency remains constant between configurations. Therefore, equation (2.12) can be used to find $\dot{W}_{M,\beta}$, the mechanical power generated by the rotor in a configuration which corresponds with the physical experimental dimensions. In this context, η_{sim} represents the efficiency of the simulated turbine.

Finally, note that an expected torque, T_{exp}, can be calculated by dividing the mechanical power by the rotational velocity. The above procedure can be used to tabulate expected data (Table 2.2) for the physical experiment.

For a given rotational setpoint, N^*, the sample CFD data is transformed and reduced to produce the following results:

Table 2.2: Simulated CFD results, after similarity transformations to physical experimental setpoint conditions

N^*	v_α	D_β	ω_β	Q_β	v_β	ΔP_β	$\dot{W}_{A,\beta}$	η_{sim}	$\dot{W}_{M,\beta}$	T_{exp}
rpm	m/s	m	rad/s	m³/s	m/s	Pa	W	%	W	N-m
100	15	0.15242	10.5	0.107	5.84	29.9	3.18	10.1	0.320	0.0306
100	10	0.15242	10.5	0.0710	3.89	13.0	0.920	14.7	0.135	0.0129
100	5	0.15242	10.5	0.0355	1.95	2.79	0.099	26.5	0.0262	0.00250

2.5 Necessary conditions for valid application of similarity laws

It has been noted in Sutton (1967), that the similarity laws are not universal, and that pumps or turbines with different design philosophies, or specific speeds will not always maintain a consistent efficiency through different points of a similarity laws transformation. Importantly, a connection was drawn between this behaviour and a variation in the Reynolds number (as measured with respect to rotation). Phelan et al. (1979) observes that this so-called "size effect" is diminished at greater Reynolds numbers and proposes a minimum Reynolds threshold be employed which would effectively negate the effects of Reynolds number on performance.

This phenomenon is often ignored when applying the similarity laws, because most pumps and turbomachinery operate above Phelan's Reynolds threshold (or its contemporaries). However, in certain flow regimes, it is necessary to consider this phenomenon to ensure that it will not greatly affect the application of a similarity laws transformation.

By current standards (e.g. AMCA, 2007), the similarity laws are most reliable when used at a sufficiently high Reynolds number. This Reynolds threshold is measured as a Fan Reynolds number, Re_F, which is a specialized form of Reynolds number that uses the tip speed (rather than bulk flow velocity).

$$\mathrm{Re}_F = \frac{\omega D_b^2 \rho}{2\mu} \tag{2.16}$$

Here, ω is the rotational velocity in rad/s, D_b is the diameter of the rotor (in m), ρ is the fluid density, and μ is the fluid's dynamic viscosity.

While $\mathrm{Re}_F < 3000000$, the transformation will have some uncertainty related to viscous effects. This is a greater concern if the full-size dimensions have a Fan Reynolds number that is greater than the threshold (AMCA, 2007). For instance, if one model is below the threshold, and the other model is above, there may be an increase in efficiency in the high-Reynolds model as compared to the low-Reynolds number, and this is a consequence of transitioning from one flow regime to another in the transformation.

This is the size effect referred to in Phelan et al. (1979). It occurs when the inertial effects overcome the viscous effects at the larger size and not at the smaller size, even with equivalent values of the conventional (bulk flow) Reynolds number. When this happens, the power losses of the larger fan will decrease relative to the smaller fan.

Note that the diameter and rotational velocity in Table 2.1 would result in a Fan Reynolds number of 5220, well below the threshold. This suggests that there may be some discrepancy in results that are transformed with the similarity laws under these conditions.

This criterion is not always considered by all workers and frequently turbomachine performance curves are transformed without reference to it. The impact on accuracy of this action in some reported results is not conclusively researched, however the issue has been investigated by Pelz and Hess (2010) and other researchers.

Figure 2.12 depicts efficiencies of the same fan at different Reynolds numbers. The curves are projected fan performance based on a method proposed in Pelz and Hess (2010), and a conventional scaling equation which they attribute to J. Ackeret. Note that the discrepancy is said to be greatest when approaching the peak efficiency of the turbomachine (at higher Reynold's numbers). It is clear from Figure 2.12 that transforming performance data across the Reynold's threshold can lead to erroneous representation of the actual performance under the transformed conditions.
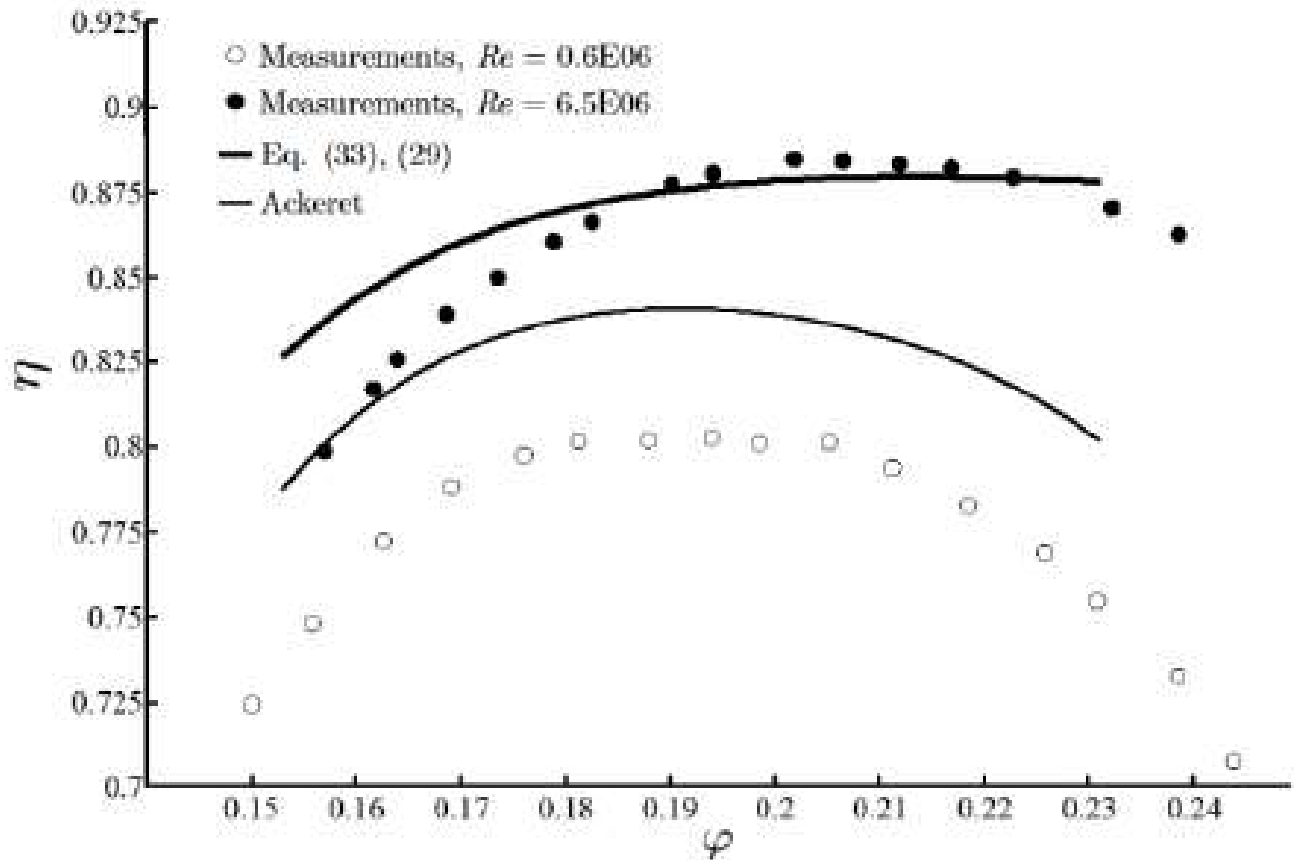
Figure 2.12: Graphical representation of data (Pelz & Hess, 2010); a demonstrated discrepancy in efficiency between observed and predicted results, when operating at different Reynolds numbers

2.6 Nondimensionalized coefficients

Fan curves, or more generally, performance curves (such as Figure 2.11) comprise a characterization of pressure, mechanical power, and efficiency. These characteristic behaviours are plotted as a function of airflow. However, swirling flow introduces greater complexity to the analysis of air flow systems and their performance. Systems will perform differently at different rotational velocities. While the similarity laws may be used to transform performance data from one operating point to another, nondimensionalized coefficients may be used to compare these data directly.

27

To nondimensionalize the airflow in the system, a flow coefficient, φ, is used. The formulation used in Phelan et al. (1979) may be simplified into the following equation:

$$\varphi = \frac{v}{\omega r} \tag{2.17}$$

To nondimensionalize the pressure drop over the rotor, a pressure coefficient, ψ, is used. The formulation used in Phelan et al. (1979) may be simplified into the following equation:

$$\psi = \frac{2\Delta P}{\rho \omega^2 r^2} \tag{2.18}$$

To nondimensionalize the mechanical power generated from the rotor, a power coefficient, Γ, is used. The formulation used in Phelan et al. (1979) may be simplified into the following equation:

$$\Gamma = \frac{2\dot{W}_M}{Q\rho \omega^2 r^2} \tag{2.19}$$

Finally, note that efficiency, η, is already dimensionless and can be plotted against the flow coefficient directly.

2.7   Measuring flowrate with an orifice meter

An orifice meter is a simple measurement device which can be used to determine flowrate. The method for accomplishing this involves computing the energy at the orifice of the device and converting that into a flowrate at the outlet. The equations used in these calculations (as they are explained in Streeter et al., 1997) are outlined below. From the equations of conservation of energy and conservation of mass, the following formulae have been derived,

$$\frac{1}{2}(v_1^2 - v_2^2) = \frac{1}{\rho}(P_2 - P_1) \tag{2.20}$$

$$v_i = \frac{4Q}{\pi D_i^2} \tag{2.21}$$

where v_i is the fluid velocity at point i, ρ is the fluid density, P_i is the pressure at point i, Q is the flowrate, and D_i is the pipe diameter at point i.

By combining equations (2.20) and (2.21), and isolating Q, the following equation can be derived,

$$Q = \sqrt{\frac{1}{1 - \left(\frac{D_2}{D_1}\right)^4}} \frac{\pi D_2^2}{4} \sqrt{\frac{2(P_2 - P_1)}{\rho}}$$

However, since this formula only accounts for ideal, frictionless flow, a coefficient of discharge, C, and a coefficient of expansion, e, are incorporated, resulting in the final equation of,

$$Q = Ce\sqrt{\frac{1}{1 - \left(\frac{D_2}{D_1}\right)^4}} \frac{\pi D_2^2}{4} \sqrt{\frac{2(P_2 - P_1)}{\rho}} \tag{2.22}$$

where the coefficient of expansion is computed as

$$e = 1 - \left(0.41 + 0.35\left(\frac{D_2}{D_1}\right)^4\right)\frac{P_2 - P_1}{\gamma_{air} P_1} \tag{2.23}$$

using an isentropic coefficient, γ_{air}, of 1.4, and the coefficient of discharge is formulated as

$$C = 0.5961 + 0.0261\left(\frac{D_2}{D_1}\right)^2 - 0.216\left(\frac{D_2}{D_1}\right)^8 + 0.000521\left(\frac{D_2}{D_1}\right)\frac{10^{6\,0.7}}{Re}$$

$$+ \left(0.0188 + 0.0063\left(\frac{D_2}{D_1}\right)\frac{19000^{0.8}}{Re}\right)\left(\frac{10^6}{Re}\right)^{0.3}\left(\frac{D_2}{D_1}\right)^{3.5} \tag{2.24}$$

$$+ 0.043\left(1 - 0.11\left(\left(\frac{D_2}{D_1}\right)\frac{1900}{Re}\right)^{0.8}\right)\frac{\left(\frac{D_2}{D_1}\right)^4}{1 - \left(\frac{D_2}{D_1}\right)^4}$$

3 CFD modeling of rotor performance

In this chapter, the methodology is outlined which was used for computational analysis of the device. An overview of the simulation software and its practical usage is also included, along with a discussion of some investigative notes regarding its capabilities.

3.1 Practical considerations of the use of a CFD code

This section will review some key concepts of the formulation and use of CFD code for the reader. A CFD tool will be used to assess the performance of the turbine design. CFD results will be directly compared to experimental results from a fabricated turbine in order to assess the effectiveness of CFD in design of turbines.

3.1.1 Features of Simscale software

Simscale is an online CFD software service, which offers a free trial license to students, and limited free public licenses. The CFD's user interface is browser based and has cross-compatibility with most widely used CAD software. CAD files can be uploaded to the user's project workbench and converted into a matrix of finite elements called a mesh. The service can run mechanical and fluid simulations with the generated mesh and has its own online CAD software.

Once the mesh has been generated, the online service computes the simulation remotely, using Simscale's own cloud computing resources. Simulations are budgeted based on core hours. The term "core hours" refers to the cloud computing cores that are connected to the processing server. Using more cores simultaneously will result in fewer hours of use, and fewer cores will result in more hours. This means that, at peak usage, a simulation may take longer, though it will cost the same number of core hours.

There are multiple types of Simscale licensing subscriptions, including the professional license and the student license, mentioned earlier. A professional license will have priority on core usage, meaning simulations can be completed relatively quickly with this license. The student license has the same capabilities, but it will not receive core priority, and it is limited to 1000 free core hours. For context, the geometry used in this experimentation contains geometric complexities such as the diffuser and the helical rotor. This level of complexity can be meshed at a cost of roughly 2 core hours, and an incompressible simulation can be completed on such a mesh using around 50 core hours.

The Simscale software is based on an open-source toolbox of CFD solvers, called OpenFOAM (OpenFOAM, 2021). OpenFOAM includes a series of solvers for turbulence, wall behaviour for surfaces, and thermodynamics, among others (Simscale, 2021f). These numerical solvers use an iterative algorithm that aggregates the numerical models to solve the Navier-Stokes equations (for example, as shown in Cengel & Cimbala, 2013), then discretizes the mathematical model to account for non-linear variables (smoothing) (Simscale, 2021f). Simscale has made some proprietary changes to the source code, but the original OpenFOAM toolbox is fully available on their website (Greenshields, 2019).

3.1.2 Navier Stokes in CFD

In CFD, the Navier Stokes model refers to a mathematical model based on three governing equations. These Navier Stokes equations (NS equations) reflect conservation of mass, momentum, and energy (Stokes, 1850). Conservation of mass is represented by the continuity equation (for example, as shown in Cengel & Cimbala, 2013), which effectively states that the mass flowrate through a region or body must be continuous. Modeling this can be complicated by changes in density and fluid behaviour.

Conservation of momentum is represented by Newton's second law of motion (for example, as shown in Cengel & Cimbala, 2013). It effectively states that momentum at a given instant is consistent with the starting momentum, plus or minus any forces applied within the system. Incorporating this equation allows the model to account for fluid behaviour.

Conservation of energy is represented by the first law of thermodynamics (for example, as shown in Rogers & Mayhew, 2007). It effectively states that the total of work and heat energy in the system must remain constant from one instant to another. Modeling this equation is greatly simplified in an incompressible medium (Cebeci et al., 2005), allowing the change in heat energy to be isolated and controlled. Incorporating this equation allows the model to account for changes in density (Cebeci et al., 2005).

Compressibility and the Reynolds number will both be used to determine the behaviour of fluid in the model. In the NS equations, the Reynolds number is related to viscous effects and turbulence (Reynolds, 1883). Based on the fluid medium selected for the model, limiting flow speed might allow for the system to be modeled as an incompressible fluid (Rogers & Mayhew, 2007). This will also limit the Reynolds number. A sufficiently low Reynolds number will reduce or eliminate the effects of turbulence in the system (Reynolds, 1883). In more specific terms, a Reynolds number of less than 4000 in a circular pipe section is considered a transition regime, between fully turbulent and fully laminar. Given the same section, a Reynolds number of less than 2300 would be considered fully laminar.

A common type of turbulence model (the one used in Simscale) is RANS, or Reynolds-averaged Navier Stokes (Cebeci et al., 2005). This models the flow by averaging the fluctuations caused by turbulence. The general form of the Reynolds-averaged Navier Stokes equations, as specified by SimScale (2023), are as follows:

Continuity equation:

$$\frac{\partial \bar{u}}{\partial x} + \frac{\partial \bar{v}}{\partial y} + \frac{\partial \bar{w}}{\partial z} = 0 \tag{3.1}$$

Navier Stokes for x-direction:

$$\rho \left(\frac{\partial \bar{u}}{\partial t} + \bar{u} \frac{\partial \bar{u}}{\partial x} + \bar{v} \frac{\partial \bar{u}}{\partial y} + \bar{w} \frac{\partial \bar{u}}{\partial z} \right) = \rho g_x - \frac{\partial \bar{p}}{\partial x} + \mu \left(\frac{\partial^2 u}{\partial x^2} + \frac{\partial^2 u}{\partial y^2} + \frac{\partial^2 u}{\partial z^2} \right) \tag{3.2}$$

RANS turbulence models such as K-omega, K-epsilon, and K-omega-SST use coefficients to approximate different behaviours (Cebeci et al., 2005). In the K-omega model, the K coefficient represents turbulent energy, while the omega coefficient represents a dissipation factor. In the K-epsilon model, the epsilon coefficient also represents the dissipation rate (Menter, 1992), but it uses a different formulation. The K-omega model is specialized for turbulent flow near walls and boundary layers (Wilcox, 1998), while the K-epsilon model is specialized for free-shear flows (Bardina et al., 1997).

According to the Simscale documentation, K-omega-SST is the industry standard. The K-omega-SST model incorporates both the K-omega model and the K-epsilon model (Menter, 1992). SST stands for Shear Stress Transport. This denotes that shear turbulence in transport regions is handled by the free-shear model, K-epsilon. By switching between turbulence models as needed, the K-omega-SST model can account for the disadvantages of one model with the advantages of the other. Namely, K-omega has higher fidelity while requiring more core hours, and K-epsilon has lower fidelity while requiring fewer core hours.

One drawback of the RANS turbulence model is that its accuracy is diminished when modeling swirling flows. This is due to the effects of vorticity in the flow which often results in eddies. In a RANS model, such effects would be simplified as a result of averaging the Reynolds number across the flow. Greater accuracy can be achieved using Large Eddy Simulation (LES) or Direct Numerical Simulation (DNS), as discussed in Geurts (2022). DNS solves the NS equations for every node in the mesh, which requires significantly more memory and processing power, but guarantees the utmost accuracy. LES will simplify that process with low-pass filtering- meaning that, below a certain length scale, the behaviour may be approximated.

The tradeoff between accuracy and memory/processing requirements is a common consideration in CFD, and the individual application may determine the type of turbulence model which is required. In David et al. (2015), this issue is addressed by comparing the results of a Simscale simulation with a physical experiment, under varying intensity of swirling flow. The analysis determines that there is very good agreement between the two experiments, under a greater degree of swirl than will be seen in the experiments which follow. For this reason, the level of accuracy provided by the RANS turbulence model has been deemed sufficient for the purpose of this work.

Atmospheric turbulence is non-isotropic, but experimentally generated turbulence (wind tunnel experiments, simulations, etc.) are generally isotropic, and this is what is expected of both CFD simulations and verifying experiments.

3.1.3 Boundary conditions

The NS equations can be solved based on the model's boundary conditions. Boundary conditions are known conditions within a domain which are necessary to solve a system of differential equations which represents that domain (Cheng & Cheng, 2005). Types of boundary conditions which are used in CFD models include:

Dirichlet - classical boundary conditions; for example, a known velocity or pressure value.

Neumann - for more complex modeling; incorporates a derivative term. Can be seen as an extension of Dirichlet. For example, where Dirichlet might have a velocity condition, Neumann might have an acceleration condition.

Robin - used to describe the behaviour of pressure waves as they interact with walls.

Dirichlet and Neumann boundary conditions are relevant to this paper. Robin boundary conditions are not.

In CFD, typical Dirichlet boundary conditions may include pressure, or fluid velocity, at an intake or outlet orifice, or a no-slip surface (Cheng & Cheng, 2005). These boundary conditions would be used to determine inertial forces. The typical use of Neumann boundary conditions is to describe behaviour relating to wall friction (Cheng & Cheng, 2005). All these boundary conditions will relate to the turbulence in the model. As alluded to in 3.1.2, turbulent flow is modeled based on the Reynolds number. For this reason, it is important to understand how the selection of these boundary conditions will affect the simulated fluid flow.

3.1.4   Creating a mesh

A mesh is a matrix of finite elements (Thompson et al., 1998). Each element is connected to adjacent elements along faces, edges, and nodes. To solve a boundary problem using a mesh, each element is treated as its own boundary problem (Thompson et al., 1998), which can be solved to find the boundary conditions for the next element. By discretizing the whole of the system into elements, the flow can be modeled by progressing iteratively through the elements, face to face or node to node. Where one calculation of a complex system might not be practical with the NS equations, relatively straightforward calculations of thousands of simple systems would be trivial when processed algorithmically. It is therefore necessary to ensure that an appropriate mesh is generated.

Elements that are not sufficiently small will not be able to account for more complex behaviour (Thompson et al., 1998). Wherever local geometry in the flow region might cause abrupt changes in flow direction, the element must be small enough to discretize the flow (Thompson et al., 1998). Swirling flows, and interactions with internal geometry represent a potential obstacle in this finite element analysis.

This discretization of the element size can be depicted numerically, by calculating a y^+ value. The y^+ value is a ratio of inertial and viscous effects, like the Reynolds number (Murad, 2020). Unlike the Reynolds number, y^+ is calculated for a point, rather than the entire channel. Distance to a given surface and local velocity vectors are used instead of overall system values. The instantaneous, local calculation of this value is what determines which turbulence model is used at any point in a mesh, when using the K-omega-SST model (described in section 3.1.2). According to the Simscale documentation, a y^+ value of less than 30 will trigger the K-omega turbulence model (Murad, 2020). This higher fidelity turbulence model is preferred if the accuracy of the results is being prioritized over processing requirements. Furthermore, a y^+ value between 5 and 30 corresponds to a transition regime, where laminar is less than 5 and fully turbulent is greater than 30. It is especially important to ensure that wall boundaries are modeled as laminar, as well as any other regions where the behaviour must be modeled as a gradient. The most

conservative recommendations, for simulations which require a very high degree of accuracy, will state that all boundaries should have a y^+ value no greater than 1 (Ariff et al., 2009).

Additionally, different element geometries will be better suited to different types of flows (Thompson et al., 1998). For instance, if a mesh generated with tetrahedrons results in faces that are parallel to the flow direction, it will produce a different result than if the faces are orthogonal to the flow. As a result, it may be necessary to use a different geometry or to change the method of discretization.

The most basic setting that can be used to change the method of discretization is the degree of coarseness of the elements. In Openfoam (Greenshields, 2019), a mesh can be generated using either automatic or manual settings. Manual settings require the user to specify a minimum and maximum edge length which will be applied to all mesh elements (Simscale, 2021a). Automatic meshing uses a coarseness number, which determines the characteristic element size (Simscale, 2021a). Rather than using equally small elements throughout the mesh, the automatic mesh generator will scale elements based on the local geometry of the domain. More complex regions will generate smaller mesh elements as needed. In practice, this helps to limit the memory usage of the meshing process, since less complex regions can be discretized with fewer (larger) elements.

3.1.5   Initial conditions

Like boundary conditions, initial conditions are a set of assumed parameters used in the model (Simscale, 2021b). These parameters include global field variables such as pressure, velocity, and turbulence. Local values are calculated throughout the mesh and delivered as an output. These local values can also be pre-set by specifying a subdomain in the geometry. Certain parameters (namely, velocity) can be initialized in such a subdomain (Simscale, 2021b). Other parameters which are relevant to this paper are gauge pressure, and the two coefficients of the selected turbulence model- turbulent kinetic energy and specific dissipation rate (see section 3.1.2). These three parameters can only be initialized as global variables.

The NS equations are initialized with the selected parameters and solved. This will produce some of these same field variables as local outputs, where mesh elements are treated as subdomains of the geometry. By entering these output values back into the model, it is possible to iteratively correct the output. In this way, the output values will converge upon a more precise solution to the NS equations. Between each iteration of the numerical function, the difference between the output values is referred to as a residual value. The concepts of convergence and residual values are an important aspect of the numerical solvers, which will be discussed in greater detail in the following section.

This numerical method of error correction must also assume the model is stable. Simulation stability refers to the tendency of the numerical solver to converge on a solution. If the simulation diverges, or if it neither converges nor diverges, it is said to be unstable. Note that, in this context, convergence time might not always refer to a stable simulation. For an unstable model, convergence time describes the number of iterations before the model begins to reach a pseudo-steady, oscillating state. Alternatively, if the model diverges, convergence time would be infinite. For

the sake of clarity, this concept will be referred to instead as settling time, since regardless of convergence or divergence of the model, it will eventually settle into a predictable, repetitive state.

Aside from error correction, this method of inputting output values as initial conditions in the NS equations also allows a simulation to be reinitialized after having been completed. This can be useful if the simulation has not converged to an acceptable margin of error.

3.1.6   Numerical settings

Once an appropriate mesh has been generated, the CFD software will use its solving algorithms (solvers) to iterate through the elements and model the system. As mentioned in 3.1.3, there are different mathematical solutions to boundary problems that are specialized to a given application. However, in addition to choosing an appropriate solver, it is necessary to select appropriate settings to ensure that the numerical solution converges for the model. Note that the iterations through each of the mesh elements are themselves iterated in a numerical model (Greenshields, 2019). Since the mesh is solved by discretizing the flow into manageable elements, it can only approximate the solution. For this reason, the model is corrected by feeding those approximate values back into the system and solving again until the solution converges to an acceptably small residual value (Greenshields, 2019), as set by the user. Without properly selected settings, this numerical model might not converge at all.

Numerical settings include relaxation factors, non-orthogonal correctors, and residual tolerances (Simscale, 2022b). In Simscale, these settings can be edited by the user. Therefore, it is important to understand how each will affect the numerical solvers.

Practical consequences of these settings, such as the degree of memory usage, can be generally understood as a matter of computational intensity. A computational process is considered more intensive if it requires more iterations of a calculation. This might be a result of the complexity of the model, of the number of elements in the mesh, or of concurrent corrective processes which aid the stability of the simulation. In Simscale, computational intensity is analogous to core hours.

The relaxation factors limit the maximum amount by which a new value may change from the value that has been entered into the numerical function (Simscale, 2021c). Lowering relaxation factors will cause the function to be more stable at the cost of a greater settling time. There are two relaxation methods, manual and automatic. Automatic relaxation will allow the relaxation factor to change during the simulation, to accommodate the function as it converges. Manual Relaxation will remain at the selected relaxation factor (Simscale, 2021c).

The next setting is the number of non-orthogonal correctors (Simscale, 2022b). This dictates the number of times the pressure equation is resolved in an iteration of a simulation. Multiple corrections will help the stability of a complex model by smoothing out any inconsistencies created by flaws in the mesh.

The residual tolerance setting is measured as an absolute tolerance. This represents a measure of the residual value between iterations. Specifically, the chosen value represents the value that will trigger the numerical solver to stop (Simscale, 2022b). Using low residual tolerances in a complex simulation can result in a crashed simulation. In an

unstable or sluggish simulation, the numerical model might never approach the tolerance (illustrated in Figure 3.1) within the time of the simulation. These residual values will be graphically represented as a convergence plot as part of the data output. A smooth convergence plot represents a stable simulation (illustrated in Figure 3.2).
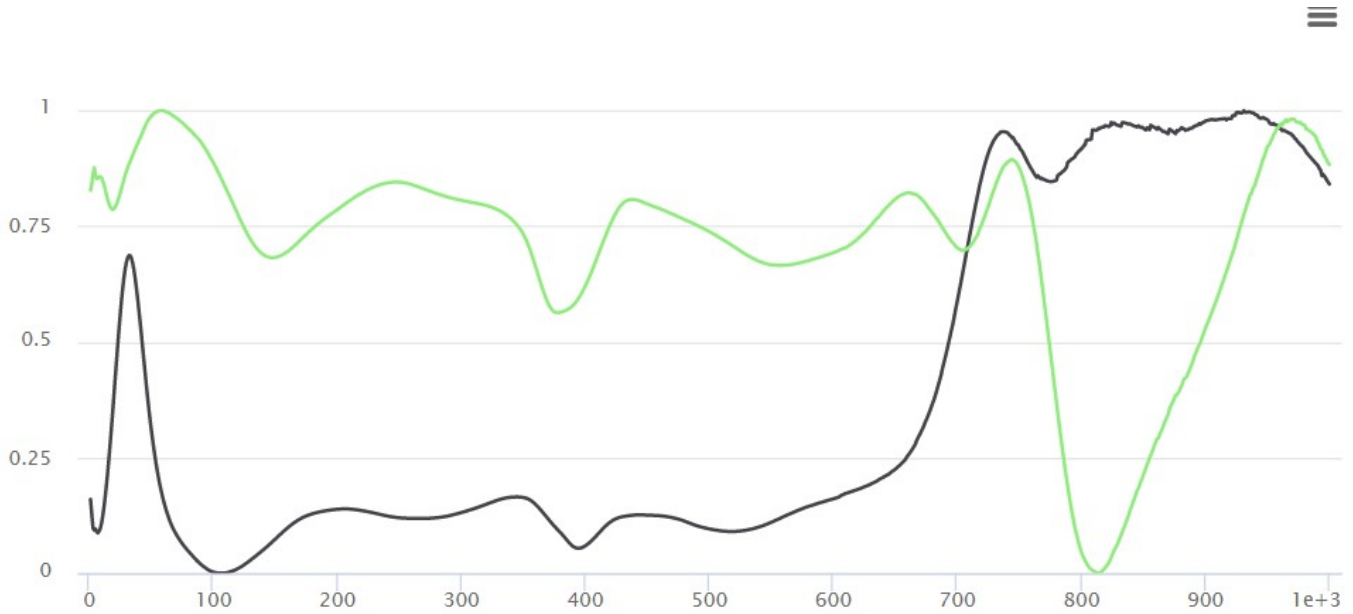
Figure 3.1: Two arbitrary sample plots showing non-convergence
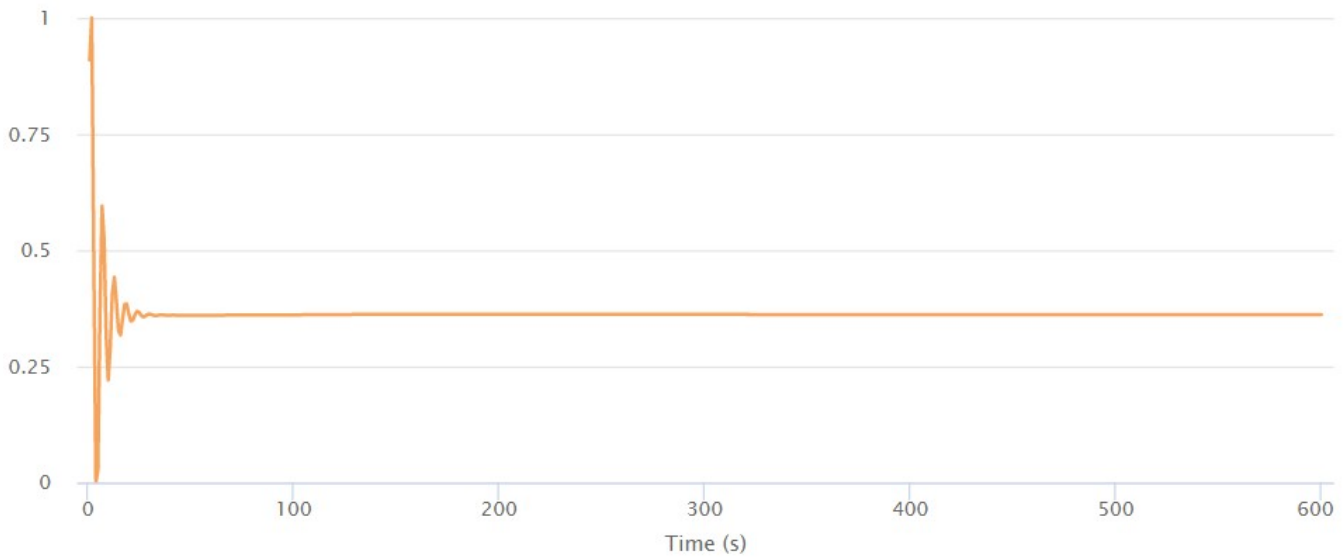
Figure 3.2: Arbitrary sample plot showing convergence

Note that Figure 3.1 and Figure 3.2 are plots of convergence. Convergence is plotted as a unitless value between 1 and 0. This represents a fraction of the highest value in the convergence function, and is useful for scaling different, incompatible dimensions to compare their convergence behaviour. Figure 3.1 depicts the plots of two vectors of outlet velocity in the model, while Figure 3.2 depicts the plot of inlet pressure.

3.2 Simulation campaign

This section contains specific details regarding settings and conditions used in simulations. It also contains a tabulation of all the raw data obtained from the CFD simulations.

3.2.1 Description of model geometry

A CAD model was imported to Simscale to create each mesh that was used in simulations. Figure 3.3 (below) depicts a configuration of the model with a diffuser that has a half angle of 15 degrees. The coordinate system established at the bottom left of the figure is consistent with all geometries used in simulations.
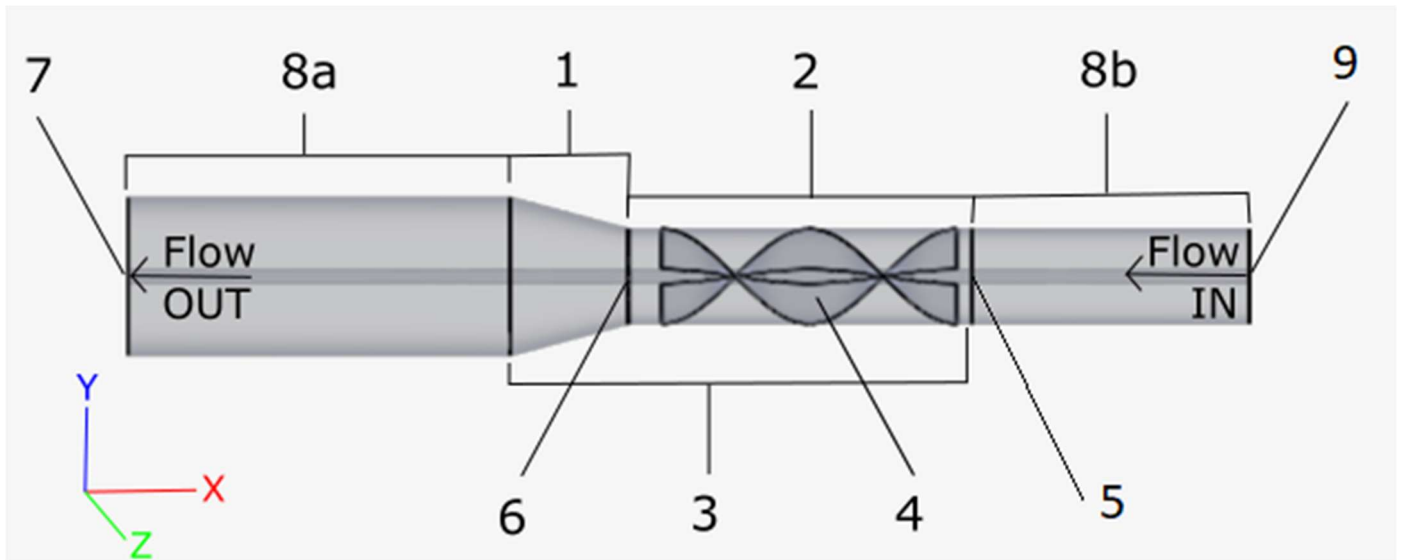
Figure 3.3: CFD model, with coordinate system and labels for terminology

Some important features of the geometry include:

1. diffuser,
2. enclosed blade section, or duct,
3. duct system,
4. rotor (with two helical blades),
5. system intake (position of first virtual instrument for pressure, P_1),
6. diffuser mouth (position of second virtual instrument for pressure, P_2),
7. geometry outlet (atmospheric pressure boundary),
8. inlet/outlet extrusions,
9. and geometry inlet (fluid velocity boundary).

The diffuser mouth (labelled as 6) is an important area, as it is used to measure outlet pressure in the simulation. It should be noted that the physical test will be completed without a diffuser. As such, the pressure must be taken in such a way that the influence of the diffuser is eliminated from the reading.

Abrupt changes in geometry create a resistance which can significantly alter the flow of a fluid (see section 3.1). In the model, using immediate inlet and outlet of fluid would create resistances that would not reflect the physical

system. Therefore, it is necessary to extrude the inlet and outlet (8a and 8b). This is common practice and is meant to allow the simulated fluid to normalize its flow before it interacts with the rotor, and to stabilize after leaving the diffuser outlet (Simscale Help Chat, S. Block, personal correspondence, 2021).

3.2.2   Root parameters

Every simulation undertaken in this study was defined by the following constants/constraints:

- the fluid was set as Air;
  - Newtonian viscosity model;
  - kinematic viscosity of v=1.259e-5 m^2/s;
  - density of ρ=1.196 kg/m^3;
- Standard Atmospheric Temperature and Pressure (SATP);
  - Ambient temperature of $T(°C)_{atm}$=19.85 °C;
  - Atmospheric pressure of P_{atm}=1.013e5 Pa;
- global field variables for Initial conditions;
  - Gauge pressure of $P_{G,0}$=0 Pa;
  - fluid velocity of v_0=0 m/s;
  - Turbulent kinetic energy of K=3.75e-3 m^2/s^2;
  - Specific dissipation rate of Ω=3.375 s^{-1};
- pressure was defined by a constant outlet pressure at geometry outlet (7 in Figure 3.3);
  - $P_{out} = P_{atm}$;
- flow was defined by a constant inlet velocity, v_{in}, at geometry inlet (9 in Figure 3.3);
- geometry of the flow region was defined by a duct system, which comprised a duct portion and a diffuser portion;
- geometry of the rotor was a pair of helical blades, running a full 360⁰ around the shaft at a 45⁰ incline (as measured at the outermost blade edge);
- default wall boundaries were used, meaning they were modeled as perfectly smooth surfaces (ie. 0 roughness);
  - the blade and shaft surfaces were defined by a No Slip wall boundary condition;
  - the outer wall of the flow region (inner wall of the duct system) was defined by a Rotating wall boundary condition;
    - rotational speed was defined by an MRF rotating zone;
    - rotational speed was consistent with a blade turning Clockwise;
- Final mesh settings;
  - Standard algorithm with automatic sizing;

- o Fineness of 5;

- o Physics-based meshing;

- o Hex element core;

- o Boundary layer gradation on no-slip boundary generated with specific growth rate of 1.2;

- o Local element size of 0.0001m on blade edge;

- o Local element size of 0.001m on blade surface;

- Solver for pressure field was GAMG;

  - o Geometric agglomerated Algebraic Multigrid;

  - o advanced solver for positive definite, diagonally dominant matrix;

  - o Gauss-Seidel smoother;

- Solver used for velocity, turbulence, and dissipation fields was Smooth solver;

  - o basic iterative solver for symmetric and asymmetric matrices;

  - o Gauss-Seidel smoother;

- stabilized by 2 non-orthogonal correctors;

- virtual pressure instruments located at duct intake and diffuser mouth; and

- Force/Moment output measured on the top and bottom surfaces of both helical blades.

3.2.3   Airflow system geometries explored
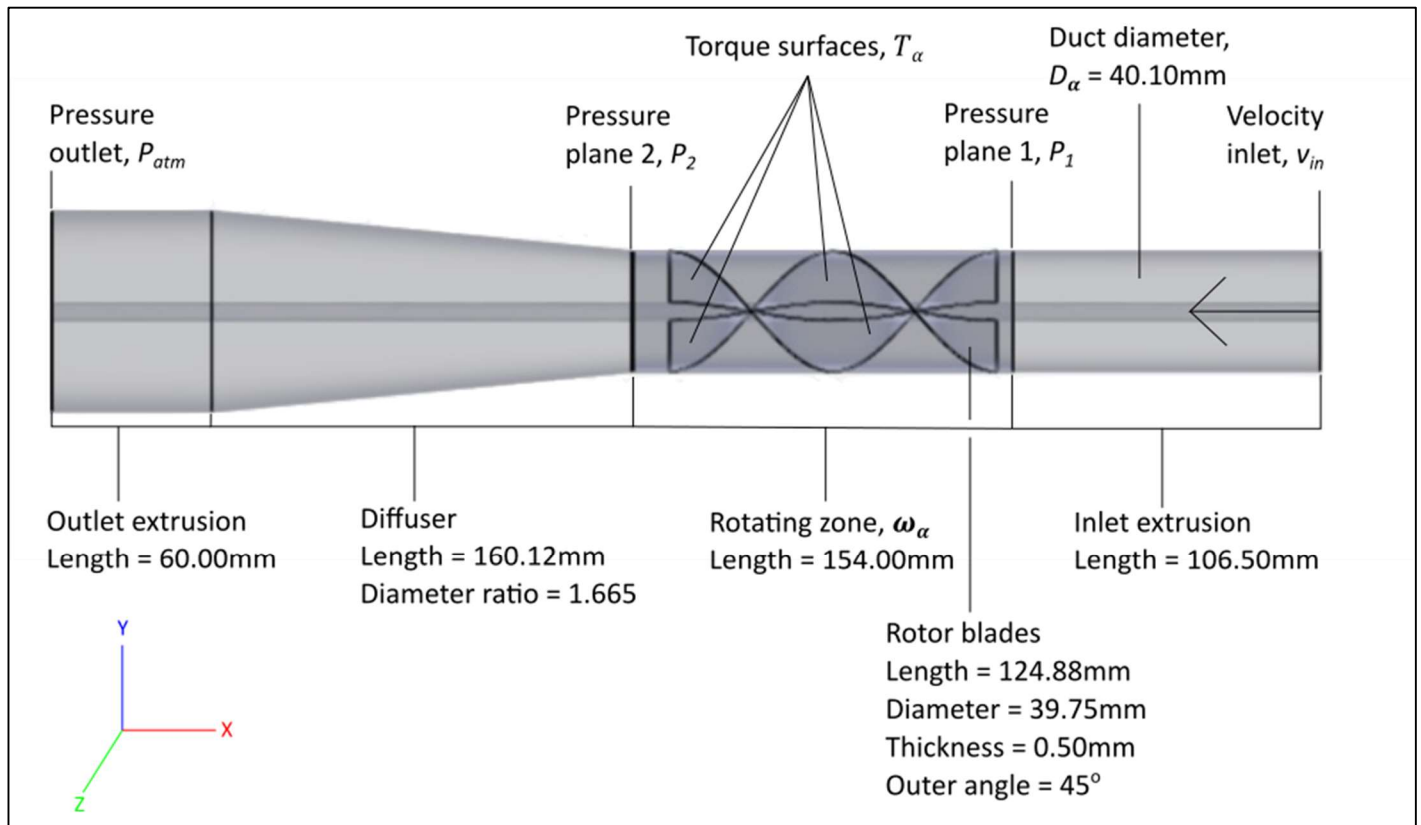
Figure 3.4: Dimensioned diagram of simulated geometry 2,depicting standard boundary conditions and virtual instruments

The simulated geometry was altered several times throughout the course of the CFD experiments. For quick reference, Figure 3.4 depicts a dimensioned diagram of geometry 2, which was the basis of the experimental data used in the final analysis. What follows is a detailed description of each geometry, so that they may be differentiated.Geometry 1: the basic geometry; 45-degree angle at the outermost edge of the blade, which has a thickness of 0.5mm, and a length of 124.88mm (approximate, driven by the angle and radius); the enclosed blade section is 136mm long and 40.10mm in diameter; the blade diameter is 39.75mm, meaning it has a clearance of 0.175mm from the wall; the leading edge of the blade has an 11.5mm offset from the mouth of the duct; the diffuser has a 3-degree half-angle, a 1.25 diameter ratio, and a length of 95.41mm; the duct is extruded by 122.5mm at inlet and by 60.5mm at outlet; the shaft, which extends throughout, has a diameter of 6mm. See Figure 3.5.
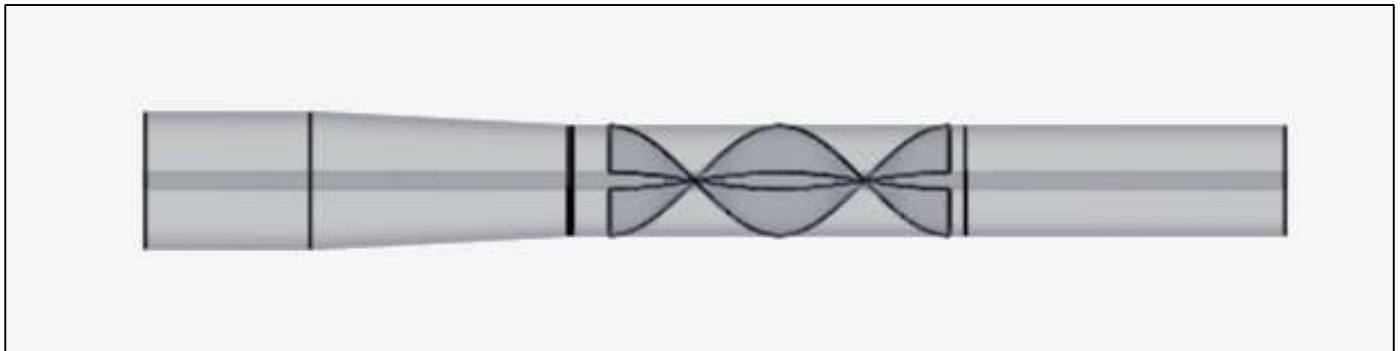
Figure 3.5: Geometry 1 (troubleshooting model); 3-degree half-angle diffuser

Geometry 2: the updated geometry; the enclosed blade section is identical to that of geometry 1, including the extrusions at inlet and outlet; the diffuser has a 4.56-degree half-angle, a 1.665 diameter ratio, and a length of 160.12mm. See Figure 3.6.

Figure 3.6: Geometry 2 (final test model); 4.56-degree half-angle diffuser

Geometry 3: this geometry varies the diffuser angle for the purpose of loss analysis; the enclosed blade section is identical to that of geometry 1, including the extrusion at inlet; this case represents a long duct with no diffuser; the outlet is extruded by 120.5mm. See Figure 3.7.
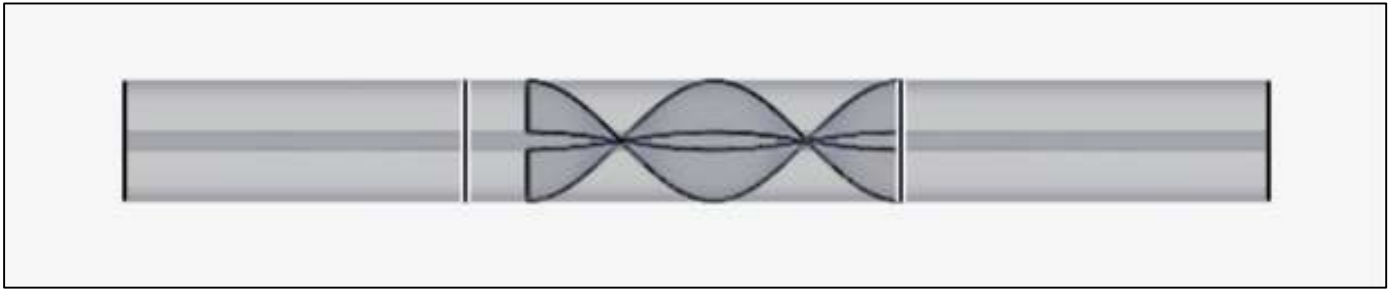
Figure 3.7: Geometry 3 (diffuser test model); straight pipe, 0-degree diffuser

Geometry 4: this geometry varies the diffuser angle for the purpose of loss analysis; the enclosed blade section is identical to that of geometry 1, including the extrusion at inlet; the diffuser has a 15-degree half-angle, a 1.665 diameter ratio, and a length of 49.76mm; the diffuser is extruded by 160.5mm at outlet. See Figure 3.8.
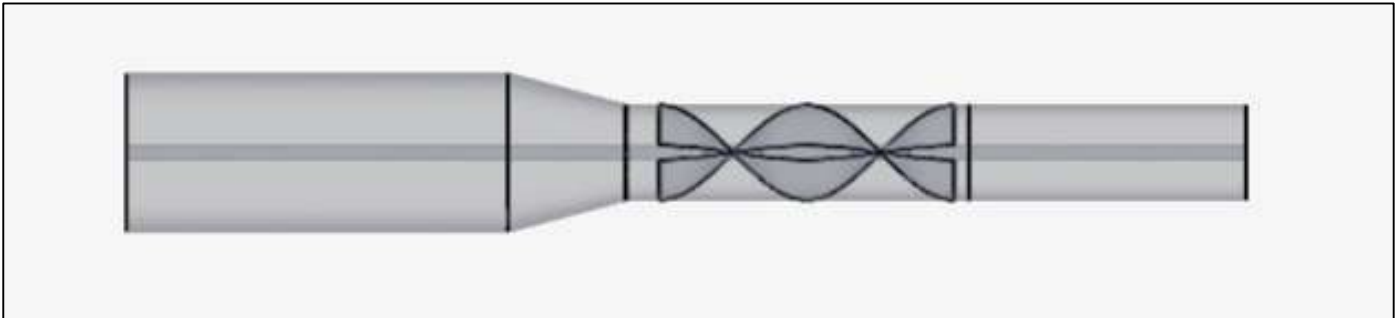
Figure 3.8: Geometry 4 (diffuser test model); 15-degree half-angle diffuser

Geometry 5: this geometry varies the diffuser angle for the purpose of loss analysis; the enclosed blade section is identical to that of geometry 1, including the extrusion at inlet; the diffuser has a 45-degree half-angle, a 1.665 diameter ratio, and a length of 13.33mm; the diffuser is extruded by 195.5mm at outlet. See Figure 3.9.
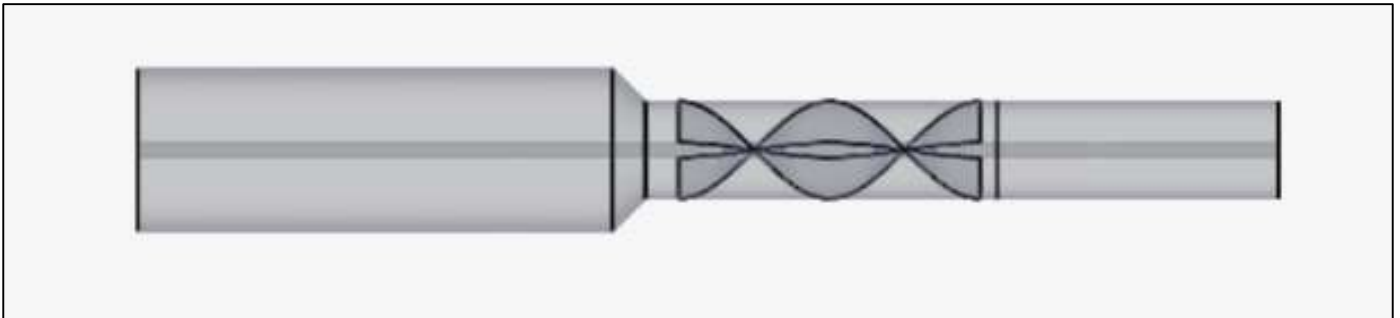
Figure 3.9: Geometry 5 (diffuser test model); 45-degree half-angle diffuser

3.2.4 Interpretation of simulation output data
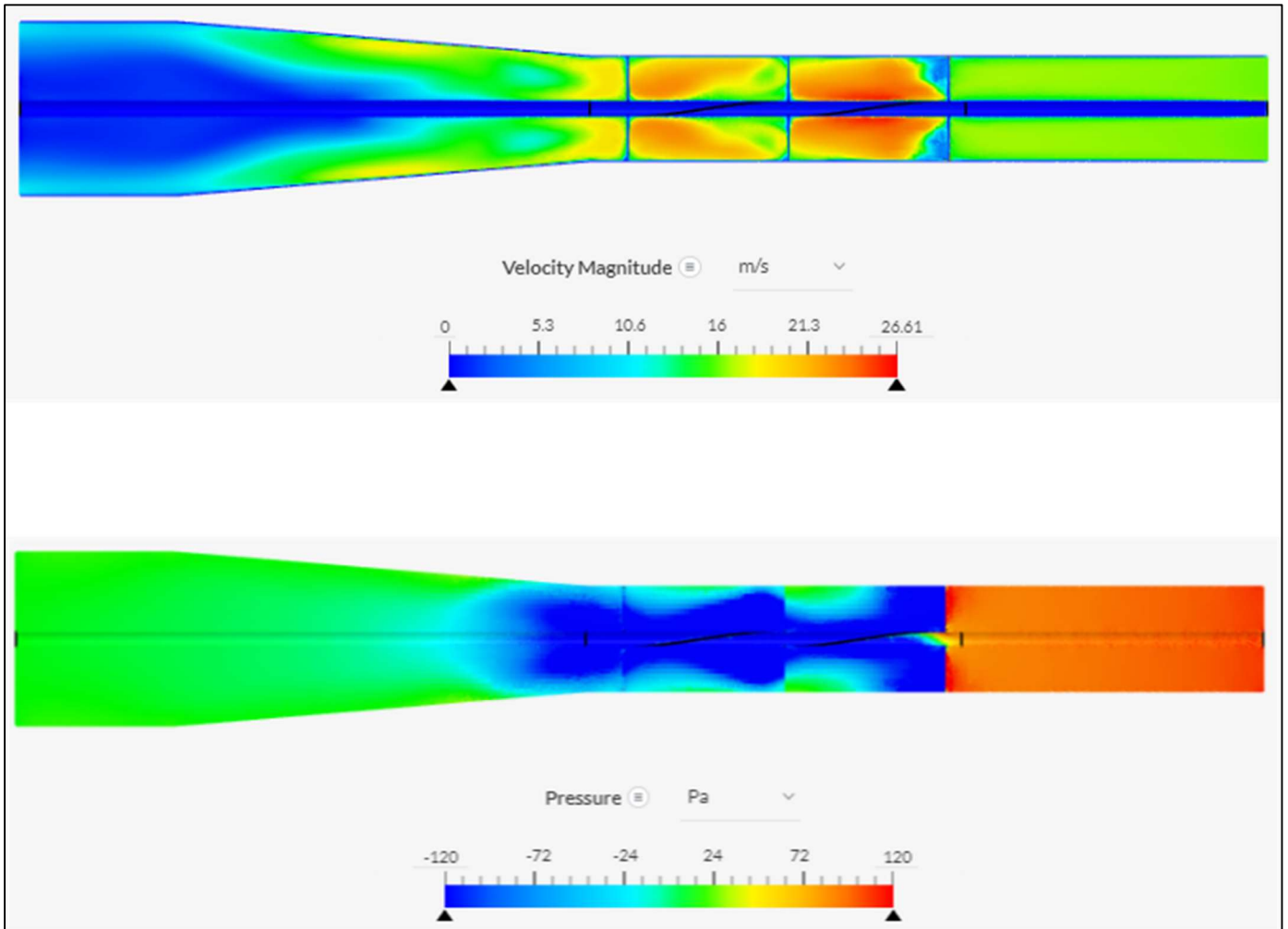
Figure 3.10: Sample gradient plots of velocity magnitude and local static pressure; Geometry 2, 15 m/s inlet velocity, 100 rad/s rotational velocity

Figure 3.10 depicts two gradient plots of simulated CFD data. The colour gradient is defined by the scale below each image and is based on mesh data that has been generated by the CFD simulation.

The upper plot in Figure 3.10 depicts the velocity magnitude throughout the system, as calculated at the nodes of each element. Note that the inlet velocity is 15 m/s (left) in this simulation, depicted in light green at the rightmost edge of the plot. The magnitude of the flow velocity increases as a swirling motion is imparted by the rotor. This is visible in the red region which follows the leading edge of the helical rotor. After the midpoint of the rotor, the flow becomes more uniform and a vortex forms around the shaft, shown in light green. At the trailing edge of the rotor, the bulk of the flow is forced to the outer walls of the geometry by the momentum of the swirling motion. This is visible in yellow at the mouth of the diffuser. As the diameter of the flow region increases along the length of the diffuser, the magnitude of the velocity decreases, but remains at the outer wall due to the swirling motion. In light blue, the bulk of the flow at the geometry outlet is roughly 7 m/s, decreasing to 0 m/s as it approaches the shaft in the radial direction.

The lower plot in Figure 3.10 depicts the local static pressure throughout the system, as calculated at the nodes of each element. Note that the outlet pressure is 0 Pa in this simulation, depicted in green at the leftmost edge of the plot. The virtual pressure instruments are located first in the pale orange region on the right side of the leading edge of the rotor, then in the blue region at the diffuser mouth, to the left of the trailing edge of the rotor. These virtual instruments are calculated as the average of pressures over the cross-section of the duct at that point, using 2-dimensional cell data rather than node data.

The pressure differential between the blade surfaces (left and right, here) that was described in section 2.2 can be observed at the leading edge of the rotor. Note the small red region to the right of the leading edge and the dark blue region to the left. At the midpoint of the rotor, this behaviour has diminished, as the low-pressure region moves toward the rotor shaft. Finally, the diffuser gradually normalizes the pressure distribution as the local pressure returns to the atmospheric pressure datum at the geometry outlet.

3.2.5 Hierarchical atlas of simulations

Due to the degree of variation in the simulation settings, the hierarchical atlas has been deliberately placed in advance of the justifications for any design decisions which have been supported by simulation data. The hierarchical atlas will establish a system of reference codes which will be used to classify and refer to simulated test cases in the text.

Listed below are the eight main variables which dictated the type and quality of the simulations. For the sake of brevity, the individual simulations are outlined in Table 3.1, which specifies the permutations of these variables.

- Geometry: the geometry of the CAD file uploaded and used in the simulation. See section 3.2.3.
- Absolute/Relative analysis: absolute motion or relative frame of reference. See section 3.3.8 for justification of final design selection.
- Incompressible/Compressible flow: compressibility behaviour of the fluid medium. See section 3.3.7 for justification of final design selection.
- Intake velocity: constant intake velocity specified for the simulation. For the sake of mathematical simplicity, values are only multiples of 5. The selected range is based on driving speeds that are consistent with city driving (18 km/h, 36 km/h, and 54 km/h).
- Rotational velocity: constant rotation of the blade/reference frame, as specified in the simulation. Recall from section 2.3.2 that rotational velocity is treated as an independent variable to reflect the nature of power generation. The frequency of rotation must be controlled to produce a consistent frequency as a power supply.
- Number of iterations: iterations of the numerical model before the simulation completes. See section 3.3.1 for justification of final design selection.
- Relaxation type: manual or automatic. See section 3.1.6.

- Relaxation factors: input values in Numerical Settings, displayed in the form (Pressure field, Velocity equation, Turbulent kinetic energy equation, Specific dissipation ratio). Note that these fields are displayed in a different order when selecting Relaxation settings for a compressible simulation, but the order is preserved for all cases in Table 3.1, which follows.

Sim	Geom	Abs/Rel	Inc/ Comp	v_{in} (m/s)	ω_α (rad/s)	Iter.	Rel. Type	Relax. Factor
1RC-1	1	R	C	10	7.54	200	Auto	0.3, 0.675, 0.7, 0.7
1RC-2	1	R	C	10	250	600	Auto	0.3, 0.675, 0.7, 0.7
1RI-1	1	R	I	10	7.54	200	Auto	0.3, 0.675, 0.3, 0.3
1RI-2	1	R	I	10	39.8	200	Auto	0.3, 0.675, 0.3, 0.3
1RI-3	1	R	I	10	250	200	Auto	0.3, 0.675, 0.3, 0.3
1RI-4	1	R	I	10	17.5	200	Auto	0.3, 0.675, 0.3, 0.3
1RI-5	1	R	I	25	625	200	Auto	0.3, 0.675, 0.3, 0.3
1RI-6	1	R	I	17.5	437.5	200	Auto	0.3, 0.675, 0.3, 0.3
1RI-7	1	R	I	15	375	200	Auto	0.3, 0.675, 0.3, 0.3
1RI-8	1	R	I	20	500	200	Auto	0.3, 0.675, 0.3, 0.3
1RI-9	1	R	I	19	475	200	Auto	0.3, 0.675, 0.3, 0.3
1RI-10	1	R	I	21	525	200	Auto	0.3, 0.675, 0.3, 0.3
1RI-11	1	R	I	10	250	1000	Auto	0.3, 0.675, 0.3, 0.3
1RI-12	1	R	I	10	250	2000	Auto	0.3, 0.675, 0.3, 0.3
1RI-13	1	R	I	10	200	600	Auto	0.3, 0.675, 0.3, 0.3
1RI-14	1	R	I	10	100	600	Auto	0.3, 0.675, 0.3, 0.3
1RI-15	1	R	I	10	125	600	Auto	0.3, 0.675, 0.3, 0.3
1AI-1	1	A	I	10	137.5	1500	Man	0.3, 0.7, 0.7, 0.7
2AI-1	2	A	I	10	125	600	Man	0.3, 0.7, 0.7, 0.7
2AI-2	2	A	I	10	137.5	600	Man	0.3, 0.7, 0.7, 0.7
2AI-3	2	A	I	10	112.5	600	Man	0.3, 0.7, 0.7, 0.7
2AI-4	2	A	I	10	100	600	Man	0.3, 0.7, 0.7, 0.7
2AI-5	2	A	I	10	50	600	Man	0.3, 0.7, 0.7, 0.7
2AI-6	2	A	I	10	40	600	Man	0.3, 0.7, 0.7, 0.7
2AI-7	2	A	I	10	25	600	Man	0.3, 0.7, 0.7, 0.7
2AI-8	2	A	I	10	7.54	600	Man	0.3, 0.7, 0.7, 0.7
2AI-9	2	A	I	15	100	600	Man	0.3, 0.7, 0.7, 0.7
2AI-10	2	A	I	5	100	600	Man	0.3, 0.7, 0.7, 0.7
3AI-1	3	A	I	10	100	600	Man	0.3, 0.7, 0.7, 0.7
3AI-2	3	A	I	5	100	600	Man	0.3, 0.7, 0.7, 0.7
4AI-1	4	A	I	5	100	600	Man	0.3, 0.7, 0.7, 0.7
5AI-1	5	A	I	5	100	600	Man	0.3, 0.7, 0.7, 0.7
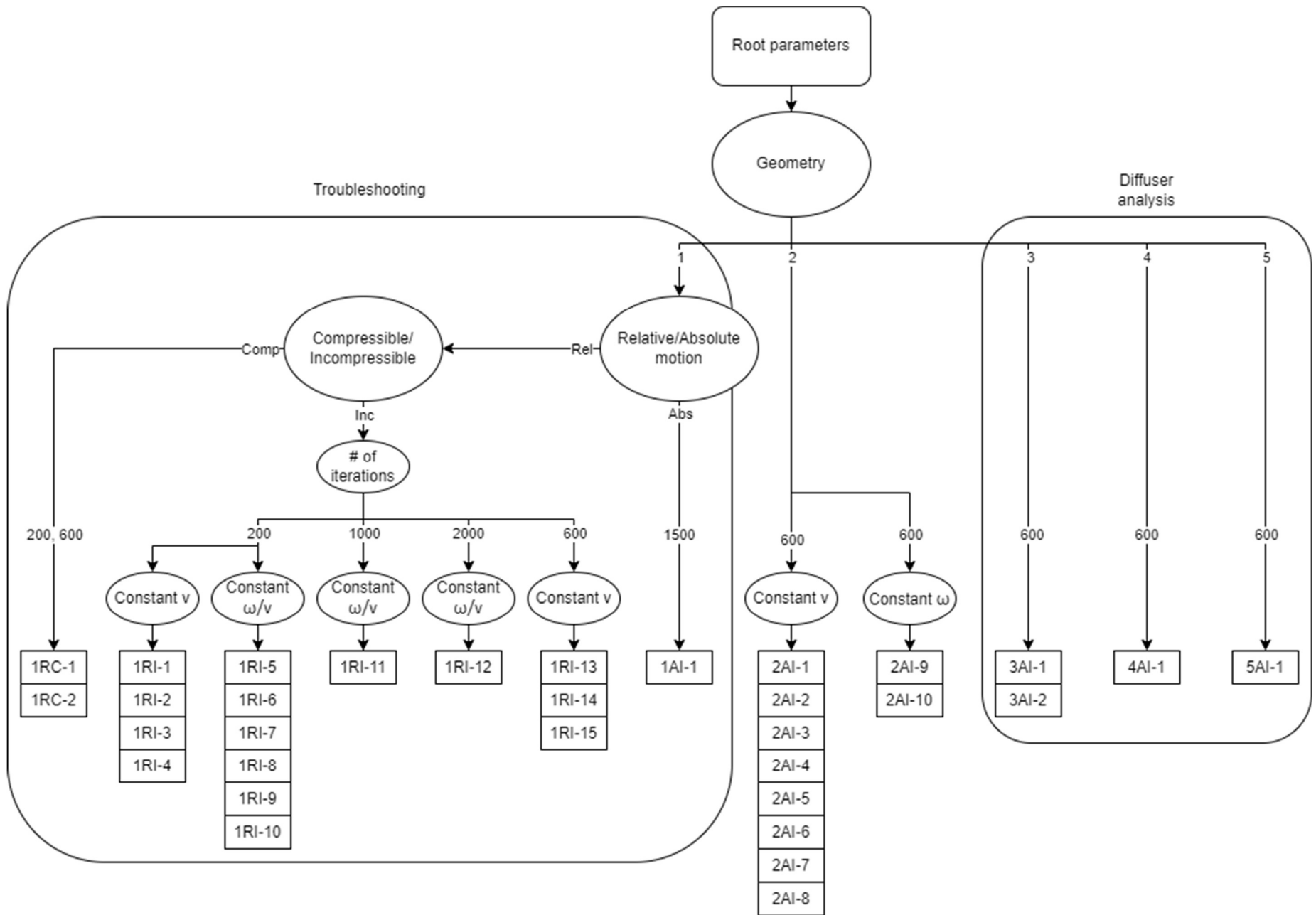
Figure 3.11: Hierarchical atlas of simulations (visual depiction)

3.2.6   Classification of data into subsets

Data set 1XX-T: Troubleshooting. This data represents a trial-and-error phase, used to verify the selected settings used in the final simulations.

Data set 2AI-N: Constant rotational velocity, variable intake flow. This subset contains a set of simulations (using final settings) which varies only based on intake velocity. Geometry and rotational speed are consistent.

Table 3.2: Data set 2AI-N (constant rotational velocity, N)

Sim	v_{in}	ω_α	P_1	P_2	ΔP_α	T_α
#	m/s	rad/s	Pa	Pa	Pa	Nm
2AI-4	10	100	36.29	-45.46	81.75	0.001486
2AI-9	15	100	86.49	-102.0	188.49	0.003516
2AI-10	5	100	7.513	-10.09	17.60	0.000299

Data set 2AI-v: Constant intake flow, variable rotational speed. This subset contains a set of simulations (using final settings) which varies only based on rotational speed. Geometry and intake velocity are consistent.

Table 3.3: Data set 2AI-v (constant intake flow, v)

Sim	v_{in}	ω_α	P_1	P_2	ΔP_α	T_α
#	m/s	rad/s	Pa	Pa	Pa	Nm
2AI-1	10	125	29.53	-45.44	74.97	0.001346
2AI-2	10	137.5	32.25	-45.51	77.76	0.001400
2AI-3	10	112.5	34.22	-45.44	79.66	0.001441
2AI-4	10	100	36.29	-45.46	81.75	0.001486
2AI-5	10	50	45.18	-44.97	90.15	0.001656
2AI-6	10	40	47.14	-44.82	91.96	0.001690
2AI-7	10	25	50.32	-44.23	94.55	0.001736
2AI-8	10	7.54	53.58	-43.62	97.20	0.001791

Data set #AI-D: Analysis of diffuser loss. This data represents an analysis of the effects of the diffuser angle on the power loss of the system. Only the geometry changes, while intake velocity and rotational speed are consistent.

Table 3.4: Data set #AI-D (variable diffuser angle)

Sim	v_{in}	ω_α	P_1	P_2	ΔP_α	T_α
#	m/s	rad/s	Pa	Pa	Pa	Nm
2AI-4	10	100	36.29	-45.46	81.75	0.001527
2AI-10	5	100	7.513	-10.09	17.60	0.000299
3AI-1	10	100	86.69	8.634	78.06	0.001466
3AI-2	5	100	19.24	2.115	17.13	0.000271
4AI-1	5	100	9.456	-8.437	17.89	0.000295
5AI-1	5	100	9.015	-8.456	17.47	0.000289

3.2.7 Tables of raw data from Simscale

Table 3.5: Factual statement of all simulated data

Sim	v_{in}	ω_α	P_1	P_2	ΔP_α	T_α
#	m/s	rad/s	Pa	Pa	Pa	Nm
1RC-1	10	7.54	104.5‡	0*	104.5	0.001934
1RC-2	10	250	175.6‡	0*	175.6	0.003313
1RI-1	10	7.54	56.9	-35.8	92.7	0.001772
1RI-2	10	39.8	59.0	-33.8	92.8	0.001882
1RI-3	10	250	128.9	-24.8	153.7	0.003004
1RI-4	10	18.02	56.9	-35.1	92.0	0.001795
1RI-5	25	625	684.2	-147.1	831.3	0.017352
1RI-6	17.5	437.5	349.6	-74.3	423.9	0.008751
1RI-7	15	375	264.0	-55.1	319.1	0.006519
1RI-8	20	500	449.6	-96.1	545.7	0.011309
1RI-9	19	475	548.7	53.7	495.0	0.010250
1RI-10	21	525	493.2	-105.5	598.7	0.012424
1RI-11	10	250	126.3	-12.0	138.3	0.002829
1RI-12	10	250	120.7	-31.6	152.3	0.002680
1RI-13	10	200	159.2	-26.0	185.2	0.003180
1RI-14	10	100	134.8	-23.7	158.5	0.002793
1RI-15	10	125	139.6	-24.1	163.7	0.002872
1AI-1	10	137.5	42.1	-32.2	74.3	0.001333
2AI-1	10	125	29.53	-45.44	74.97	0.001346
2AI-2	10	137.5	32.25	-45.51	77.76	0.001400
2AI-3	10	112.5	34.22	-45.44	79.66	0.001441
2AI-4	10	100	36.29	-45.46	81.75	0.001486
2AI-5	10	50	45.18	-44.97	90.15	0.001656
2AI-6	10	40	47.14	-44.82	91.96	0.001690
2AI-7	10	25	50.32	-44.23	94.55	0.001736
2AI-8	10	7.54	53.58	-43.62	97.20	0.001791
2AI-9	15	100	86.49	-102.0	188.49	0.003516
2AI-10	5	100	7.513	-10.09	17.60	0.000299
3AI-1	10	100	86.69	8.634	78.06	0.001466
3AI-2	5	100	19.24	2.115	17.13	0.000271
4AI-1	5	100	9.456	-8.437	17.89	0.000295
5AI-1	5	100	9.015	-8.456	17.47	0.000289

*-   Rounded value (see section 3.3.2)

‡- P_{in} used instead of P_1 (see section 3.3.2)

3.3   Verification of selected CFD settings

This section presents an investigation of CFD settings available in Simscale. The settings outlined in the previous section were selected both by consulting the website's documentation, and by running test simulations to troubleshoot the necessary conditions for the model. The computational limitations of the software were also considered when selecting settings.

3.3.1   Finding timestep for steady state of numerical calculation results

The steady-state and transient models use the same interface in Simscale. This results in a quirk in the wording where the length of a simulation is counted in seconds, regardless of the type of simulation that is run. However, by changing the timestep and duration, the user can specify total number of iterations.

NOTE: Iterations will always be duration divided by timestep. In a steady-state simulation, 1000s duration and 1s timestep is the same as 200s duration and 0.2s timestep.

Based on the numerical settings used for the solver (see section 3.1.6), the simulation will require a minimum number of iterations as a settling time for the numerical function. To determine the necessary settling time, the user can start a simulation which has previously completed, allowing them to extend the range of data generated by the simulation. As discussed in section 3.1.5, this will use the field variables output by the simulation as the initial conditions in the next iteration of the solver. By extending the simulation well beyond the necessary range for convergence and analyzing the output, a minimum number of iterations can be determined which should provide data to within a consistent margin of error. Figure 3.12 shows such a simulation. On the graphical output in Simscale, the fluctuations seen here are invisible to the naked eye. However, by plotting the data and zooming in the axes, what appears to be a flat, straight line now shows slight fluctuations which represent the margin of error for the virtual instrument. It is plain to see in the image that the margin of error decreases over time. Therefore, the error for a reading taken at 1500 iterations is less than or equal to the error for a reading taken at 600 iterations.

Using 600 iterations as a benchmark, the margin of error can be determined by finding the next highest point and the next lowest point in the fluctuations. Since all subsequent readings are within 1e-5 of the reading, that is assumed as the margin of error. Therefore, torque readings taken from Simscale's graphical output at 600 iterations can be safely recorded with 3 significant digits.

Applying the same methodology to the pressure data from the same simulation (data plotted in Figure 3.13), an acceptable margin of error is determined to be 1 Pa.
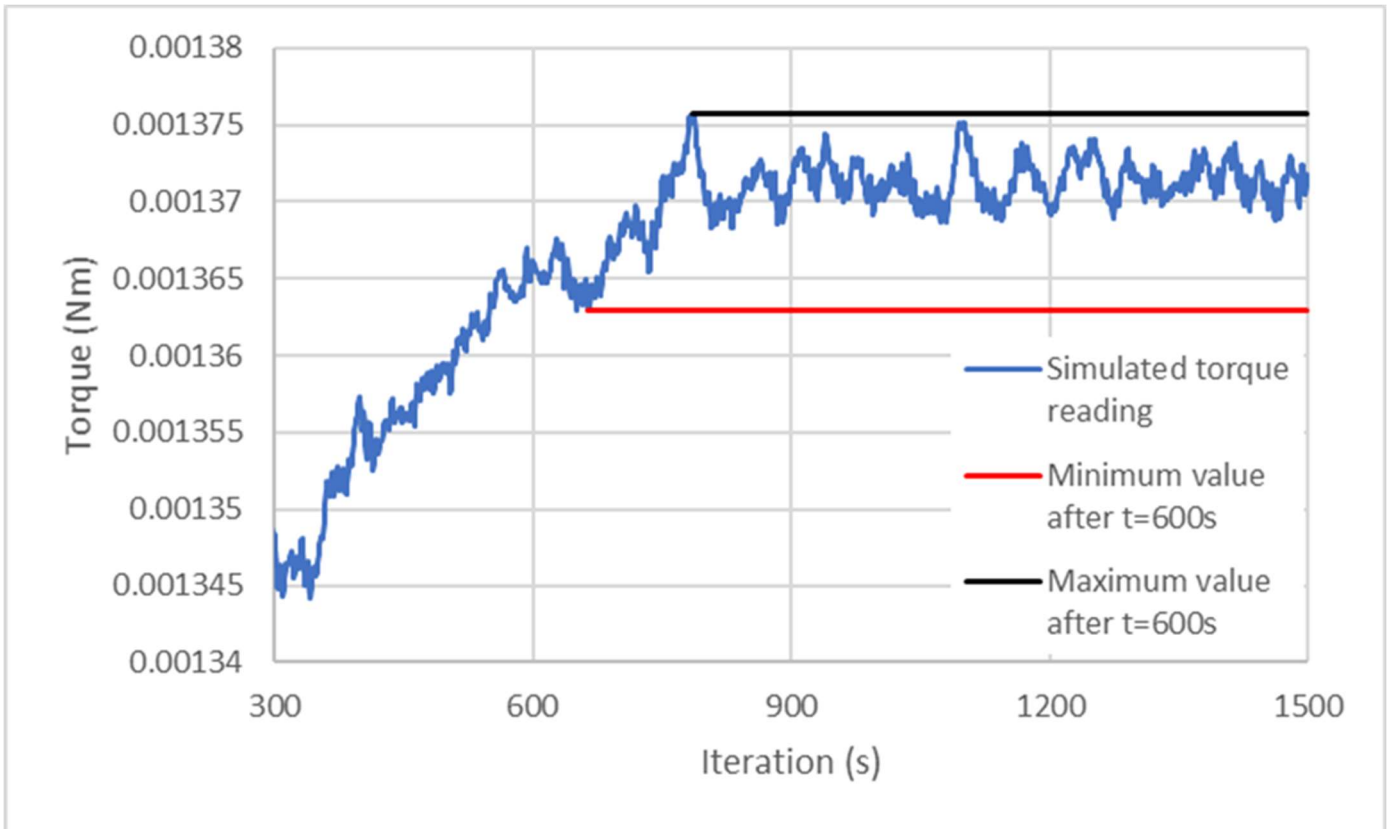
Figure 3.12: Illustration of approximate margin of error after 600 second timestep (from simulated CFD torque data)
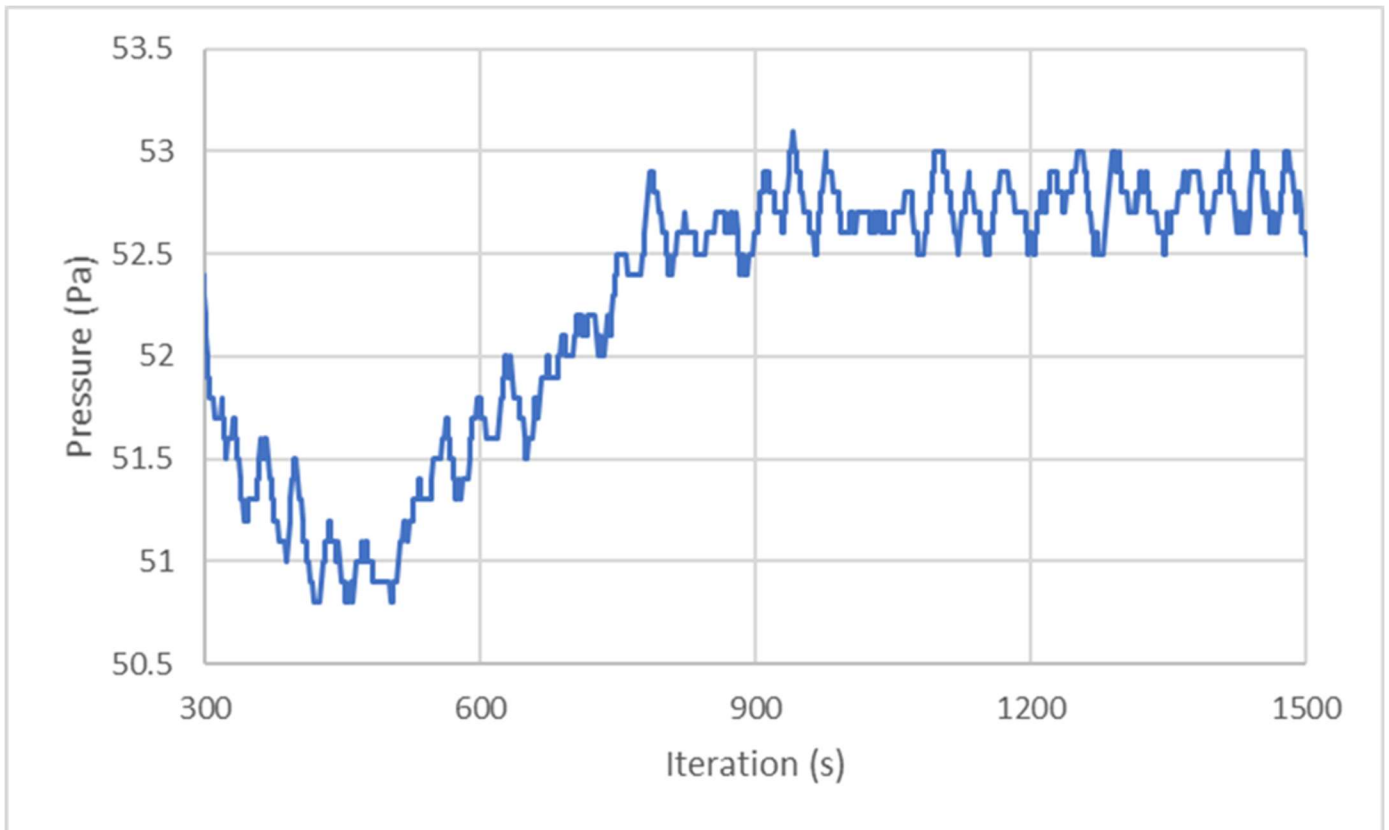
Figure 3.13: Settling behaviour for pressure data

3.3.2   Definition of virtual instrumentation

As discussed in section 3.1, Simscale generates data by iteratively solving a meshed geometry using the NS equations. Certain parameters are input by the user and the software will display outputs of selected fields. In terms of analysis, these inputs and outputs represent independent and dependent variables, respectively.

Equation (2.12) establishes the four parameters that will be required to complete the analysis of the data. They are T, torque, ω, rotational velocity, ΔP, the pressure drop across the enclosed blade section, and Q, the flowrate of the simulated fluid. Note that Q is proportional to v, fluid velocity, and can be calculated from such if the cross-sectional area is known at the point where the velocity is taken.

Each CFD simulation is initiated with specified values for ω and v. Thus, the parameters ω and Q are independent variables. Note that P_{atm} is also a required input. Designating a surface to be at atmospheric pressure dictates the absolute pressure throughout the rest of the system. This allows for the calibration of local fluid effects such as density, which would be especially important in a compressible fluid simulation. These three input boundary conditions are depicted in Figure 3.14.
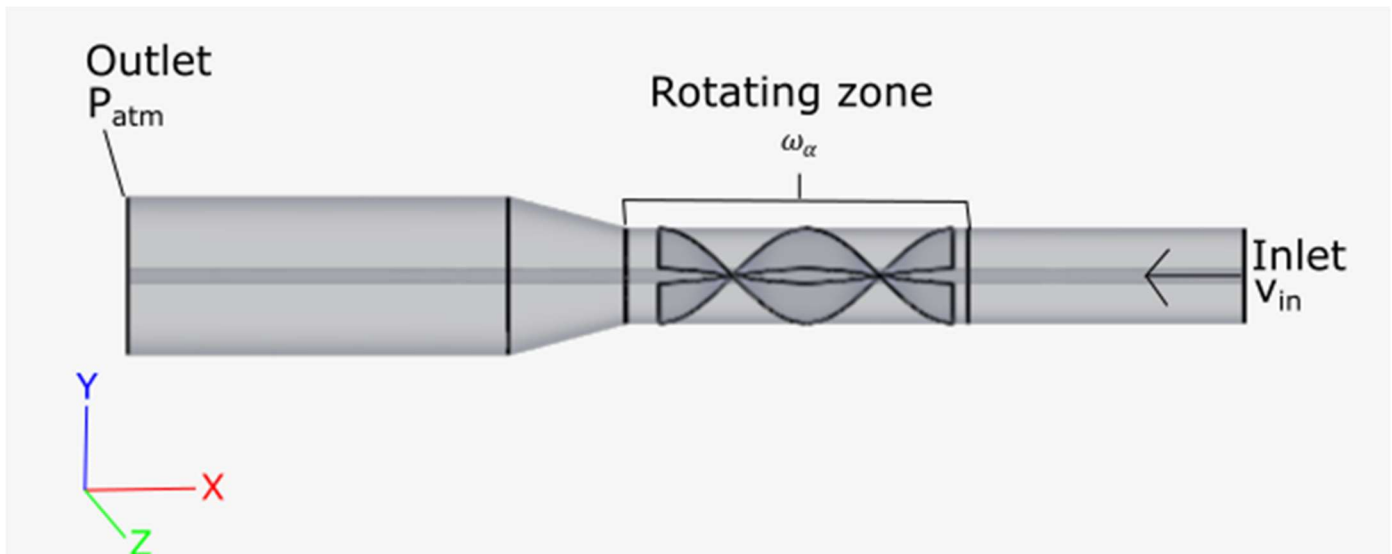
Figure 3.14: Diagram of boundary condition inputs in Simscale software; geometry 4 used for illustration

To establish a consistent methodology for collecting data from the Simscale program, it is necessary to explain the operation of the software's virtual instrumentation. In Simscale, numerical functions are output graphically as a function of time (see section 3.3.1 for more detail on iterations and timestep). To collect data from this graphical representation, the user may hover their mouse cursor over any point on the function (as shown in Figure 3.15). By selecting an appropriate duration for their simulations (see section 3.3.1), the user can simply read the last point on the graph for a consistent reading. Using this method, torque and pressure readings are taken directly from the simulation.
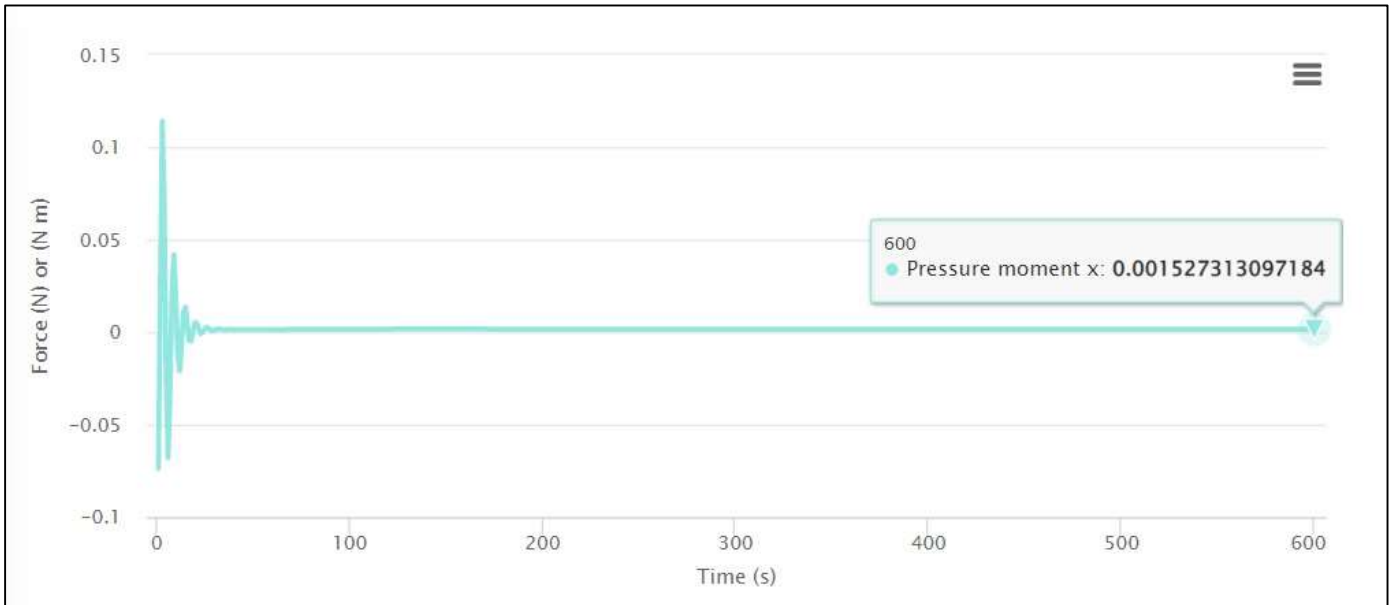
Figure 3.15: Simscale user interface for data output; demonstration of digital resolution for torque readout

To produce these outputs, Simscale requires the user to select surfaces within the model to designate areas in the mesh where data should be collected (see Figure 3.16). When a set of surfaces is designated for the blade, a torque output can also be generated by selecting this set for a Forces and Moments output (so named in Simscale). For these simulations, the top and bottom surfaces of the helical blade (meaning the surface facing the inlet and the surface facing the outlet, respectively) were designated as the blade surface. Figure 3.15 depicts the moment of torque about the blade's shaft that is created by pressure forces. Note that the shaft has been designated as the x-axis in the simulation, as specified by Figure 3.14.

Moments about each axis are calculated for viscous and porous effects as well. Since there is no porous moment about the shaft, an applied resistance torque would be a function of the sum of the shear (viscous) resistance and the pressure forces on the blade. The torque, T, generated by the blade is therefore taken as the sum of the pressure moment and the viscous moment about the shaft.

Pressure at inlet, P_{in}, will be included in the output if the user creates an Area Average output (so named in Simscale) and selects the inlet face. However, this pressure is based on the system's reference pressure, P_{atm}. This means that it represents a total pressure drop across the entire duct system, and not just across the enclosed blade section. Since the reference pressure is designated at the geometry outlet (as outlined in section 3.2.2), additional analysis must be done to find the pressure drop over the blade section specifically.
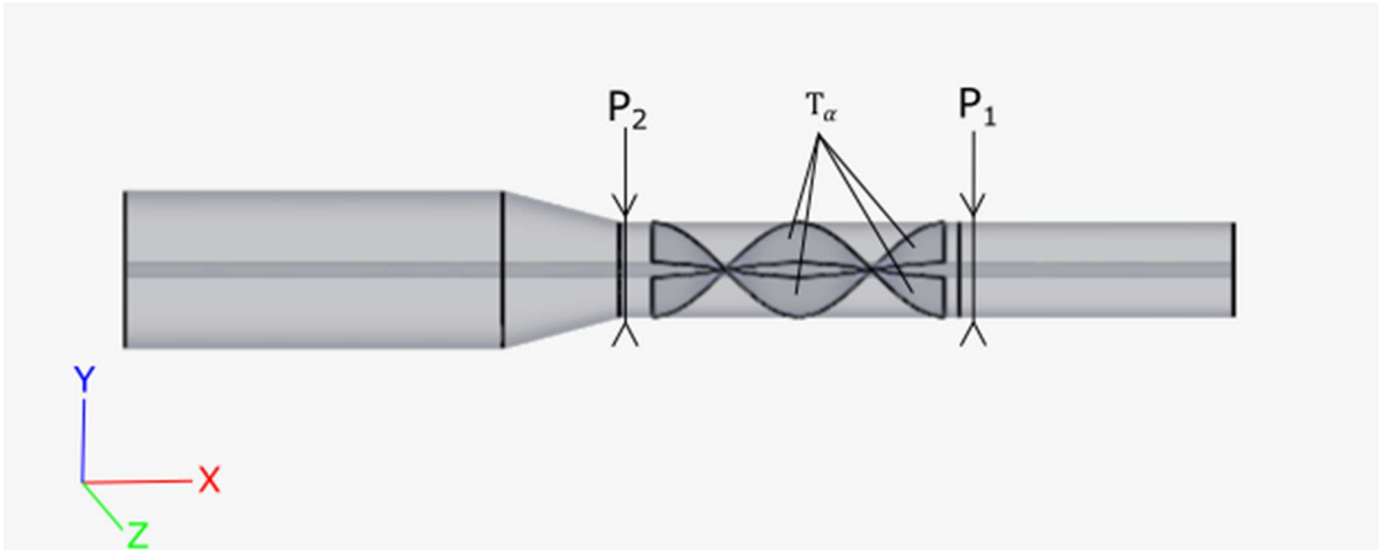
Figure 3.16: Diagram depicting the positions of surfaces designated as virtual instruments for pressure and torque; geometry 4 used for illustration

Simscale allows for a Bulk Calculation of data (so named in Simscale) across a specified plane in the model. By default, this function will be applied to the final state of the simulation. This means that the diffuser pressure can be taken from the simulation using the same timestep convention as the torque readings.

By specifying the x-coordinates of two cross-sectional planes on either side of the enclosed blade section (see Figure 3.16), virtual instruments can be established for a Bulk Calculation of the pressure data. P_1 is designated at $x = 0.195m$, representing the inlet of the duct. P_2 is designated at $x = 0.041m$, representing the mouth of the diffuser. Note that these points maintain the same x-position, regardless of any changes in diffuser geometry. This means that a consistent area can be used to collect data, regardless of the geometry selected for the simulation.

Finally, the difference between the two pressures will produce the relevant data for ΔP, the pressure drop across the enclosed blade section only.

Note that in compressible simulations, all pressures are displayed as absolute pressures. For this reason, the Bulk Calculation display (which only provides 4 significant digits) will not provide sufficient resolution to show a relative pressure between $25\ Pa$ and $-75\ Pa$. Additionally, this meant that the inlet pressure for compressible simulations was taken at the geometry inlet instead of at P_1, for greater precision.

3.3.3   Verification of selected mesh settings

As outlined in section 3.2.2, the final mesh settings were as follows:

- o   Fineness of 5
- o   Physics-based meshing
- o   Hex element core
- o   Boundary layer gradation on no-slip boundary generated with specific growth rate of 1.2
- o   Local element size of 0.0001m on blade edge
- o   Local element size of 0.001m on blade surface

The fineness setting used in the meshing algorithm will be discussed in greater detail in the following section.

Physics based meshing with hex element core is the standard setting for a Simscale mesh. Hex element core is recommended for CFD, as opposed to FEA (Simscale, 2021e). Physics based meshing specifies that the mesh should give priority to physics-based details (such as boundary conditions) when scaling element size.

Boundary layers have a graded mesh (Simscale, 2021e). In other words, elements are smaller the closer they get to a boundary layer. The degree of gradation is set using a scalar growth rate, which corresponds to the size ratio between subsequent elements. The no slip surface in the final mesh (including the blade shown in Figure 3.18) uses a specific growth rate of 1.2. This is slightly lower than the default global gradation rate of 1.22 (Simscale, 2021e); this is to conserve core hours. A smaller gradation rate means fewer element layers between the hex dominant flow region and the boundary.
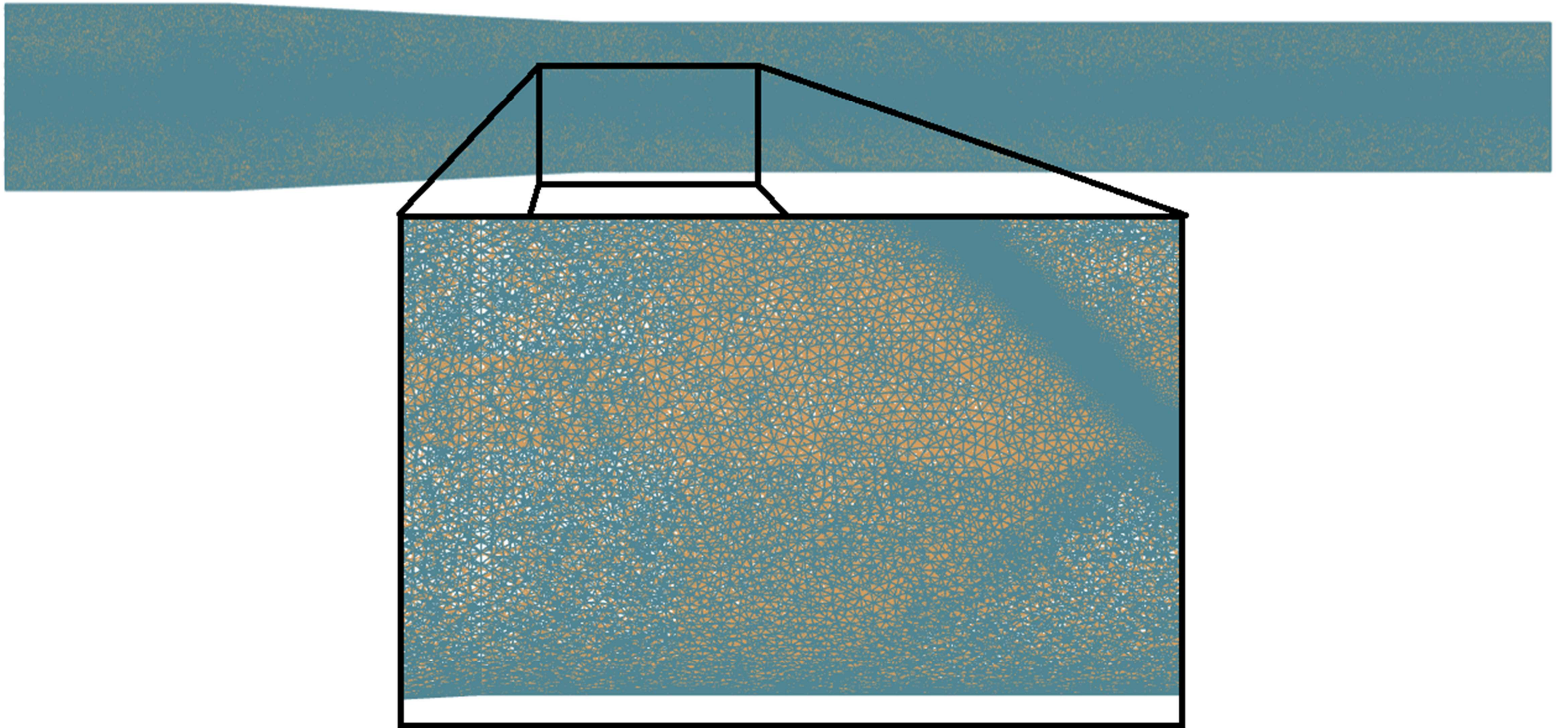
Figure 3.17: Mesh of geometry 1, with zoomed-in portion
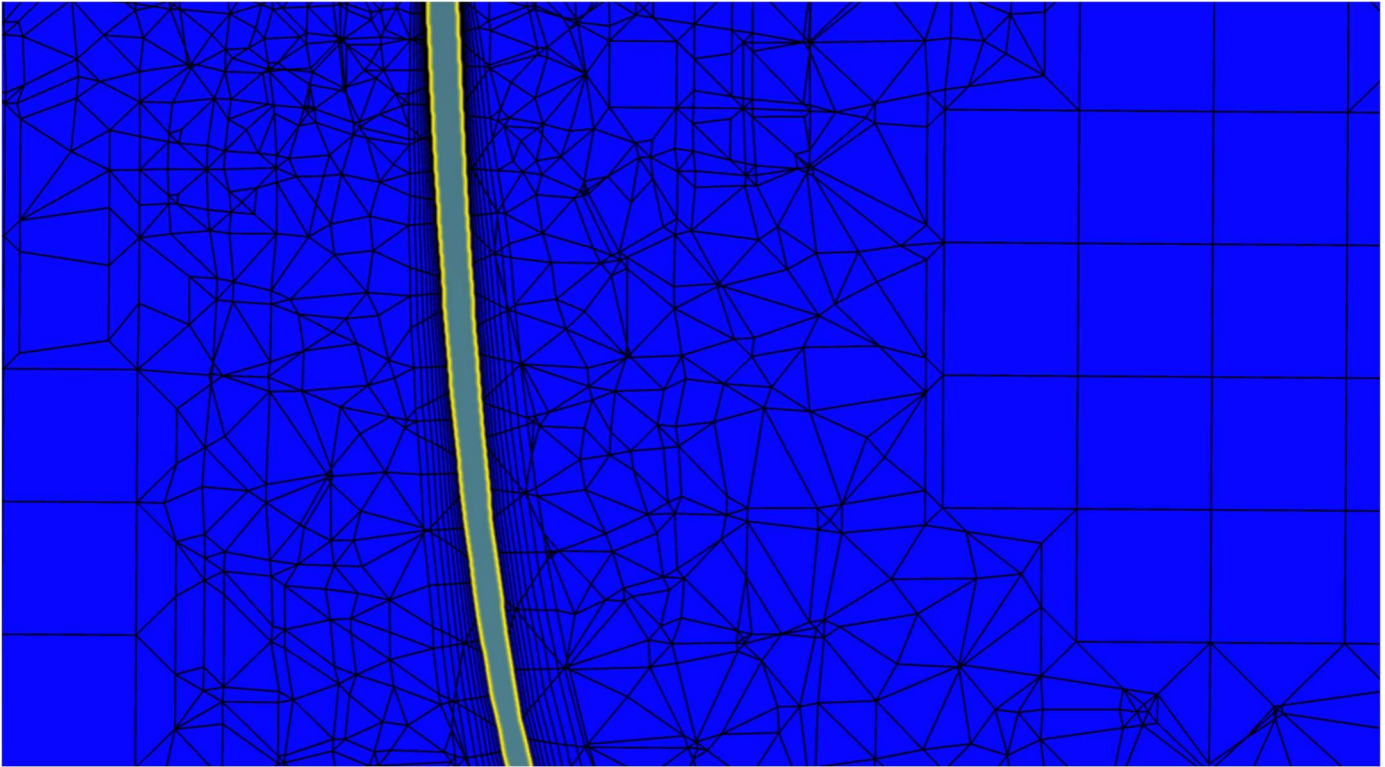
Figure 3.18: Cross-section of geometry 1 mesh, taken as normal to the tangent of the blade edge (zoom of a single blade)

The local element size at the blade edge surface is set to be half the distance between the blade edge and the nearest wall. In , the difference between the meshing along the blade edge is visibly denser than the rest of the mesh. This is to ensure that there is more than one element between the two surfaces. Without this degree of discretization, any effects related to air flowing past the blade would not be reflected in the simulation.

The local element size at the rest of the blade surface is set to ten times the size at the blade edge. While the blade surface is the main area of interaction with the fluid flow, and therefore requires the most analysis, there is no driving dimension to govern the specific size used. For this reason, an arbitrarily small value was chosen.
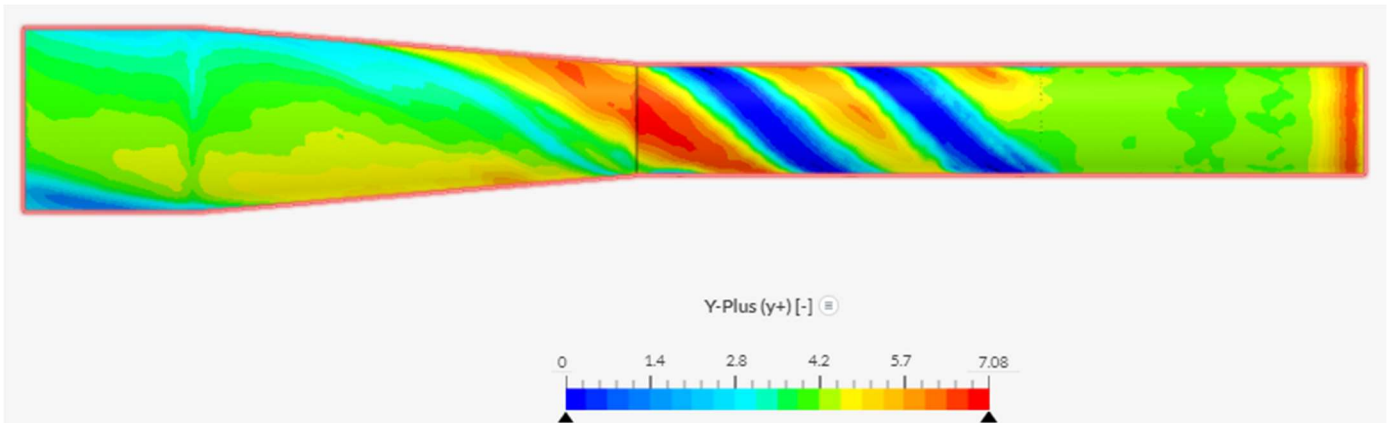
Figure 3.19: Y-plus gradient for 15 m/s flowrate (100 rad/s rotation on geometry 2)

56

The y^+ values throughout the geometry were consistently low, staying below a value of 7.1. While it is preferred that all areas of the boundary should have a y^+ value of less than 5, according to Ariff et al. (2009), it is generally acceptable to have a y^+ value of approximately 5 so long as the regions of greatest concern are sufficiently low. As mentioned in section3.1.4,a y^+ of less than 1 is the most conservative requirement for very detailed simulations. In Figure 3.19, the regions where the blade edges are closest to the wall boundary are all consistently less than 1. This is appropriate since this is the region which would require the greatest detail and is therefore the region of greatest concern.

However, y^+ is not the only measure of reliability in the simulation. Note that an abrupt change in the gradation of the mesh can cause problems with the discretization of the solution (such as from the inflated boundary layer at the blade surface to the larger mesh of the hex dominant flow region, see Figure 3.18). It is unknown whether the observed change is sufficiently abrupt to cause such a problem. However, this remains as a potential source of error in the simulation setup.

3.3.4 Exploration of mesh dependency

As noted in Section 3.3.3, computationally intensive settings could cause the simulation to time out or even crash. For this reason, the more complex geometry necessitated a coarse mesh. However, using a mesh that was too coarse might compromise the validity of the simulation. To assess the validity of the results, a suite of simulations was carried out with increasingly coarse meshes.

Table 3.6: Analysis of mesh dependency; comparison of output variables based on selected fineness of mesh

Mesh	Fineness	Cells	P_1	P_1	ΔP_α	T_α
Test A	0	5516589	43.23	-52.71	95.94	0.001538
Test B	2.5	5437163	35.37	-56.36	91.73	0.001529
Final	5	5828179	47.86	-45.46	93.32	0.001527

Note that the coarsest mesh (of fineness 0) has more elements than the next finer mesh. By examining the types of elements in the mesh (see Table 3.7), the reason becomes apparent. Recall from section 3.2.2 that the mesh algorithm generates a hex dominant core. As the elements become increasingly fine, the number of hexahedral elements increases exponentially, even as the number of tetrahedral and prism elements stays relatively constant. This is because the automatic meshing algorithm generates mesh around boundary layers and internal geometry in a consistent manner, then populates the empty flow region (first with hexahedral elements, then with other geometries). Thus, if the element size becomes too coarse, the boundary layer elements will take up more space in the mesh, forcing the algorithm to fill in the gaps in the hex dominant flow area with more tetrahedra and prisms.

Table 3.7: Breakdown of mesh into all constituent elements, based on selected fineness of mesh

Mesh	Fineness	Cells	Nodes	Tetrahedra	Hexahedra	Prisms	Pyramids
Test A	0	5516589	1908506	2877608	7622	2591851	39508
Test B	2.5	5437163	1906707	2759677	11744	2622627	43115

Final	5	5828179	2070190	2952358	73864	2725415	76542
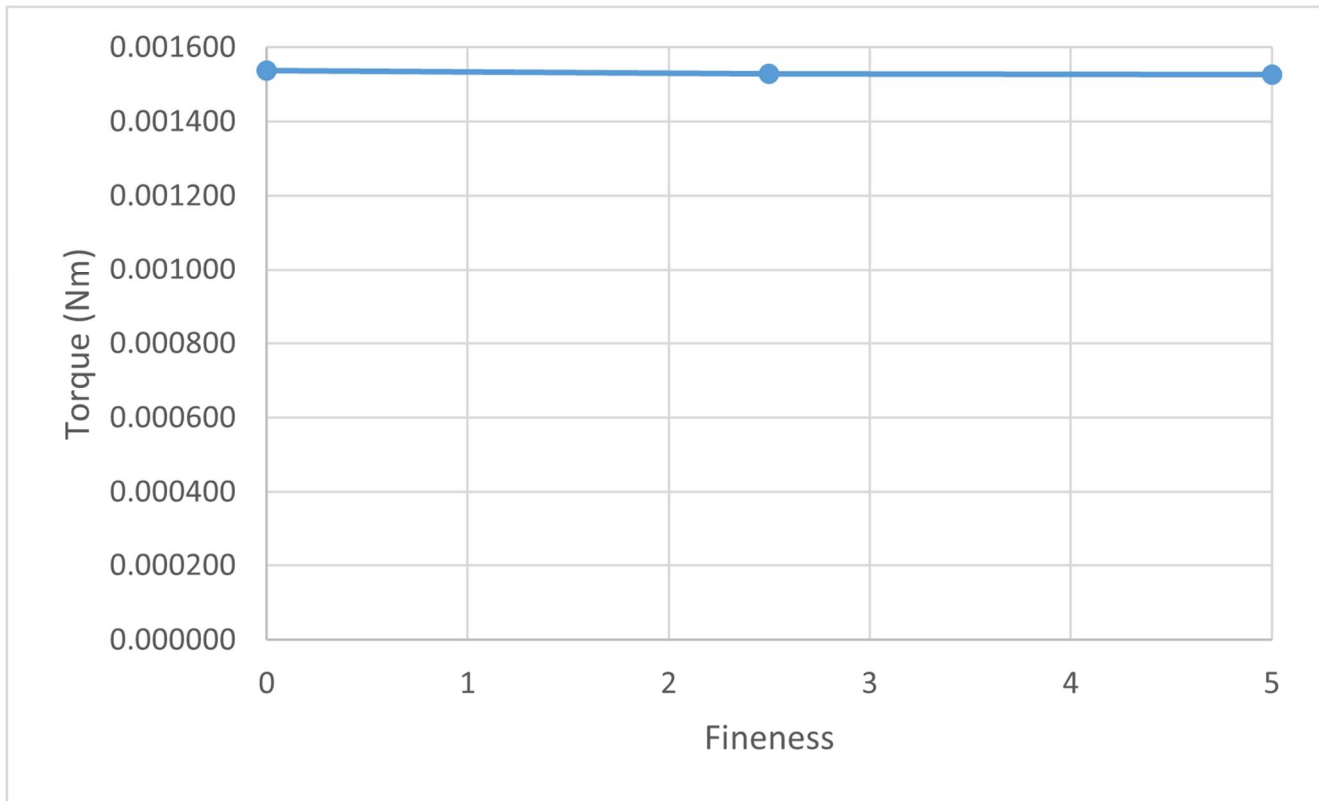
Figure 3.20: Plot of mesh dependency - Torque vs. fineness
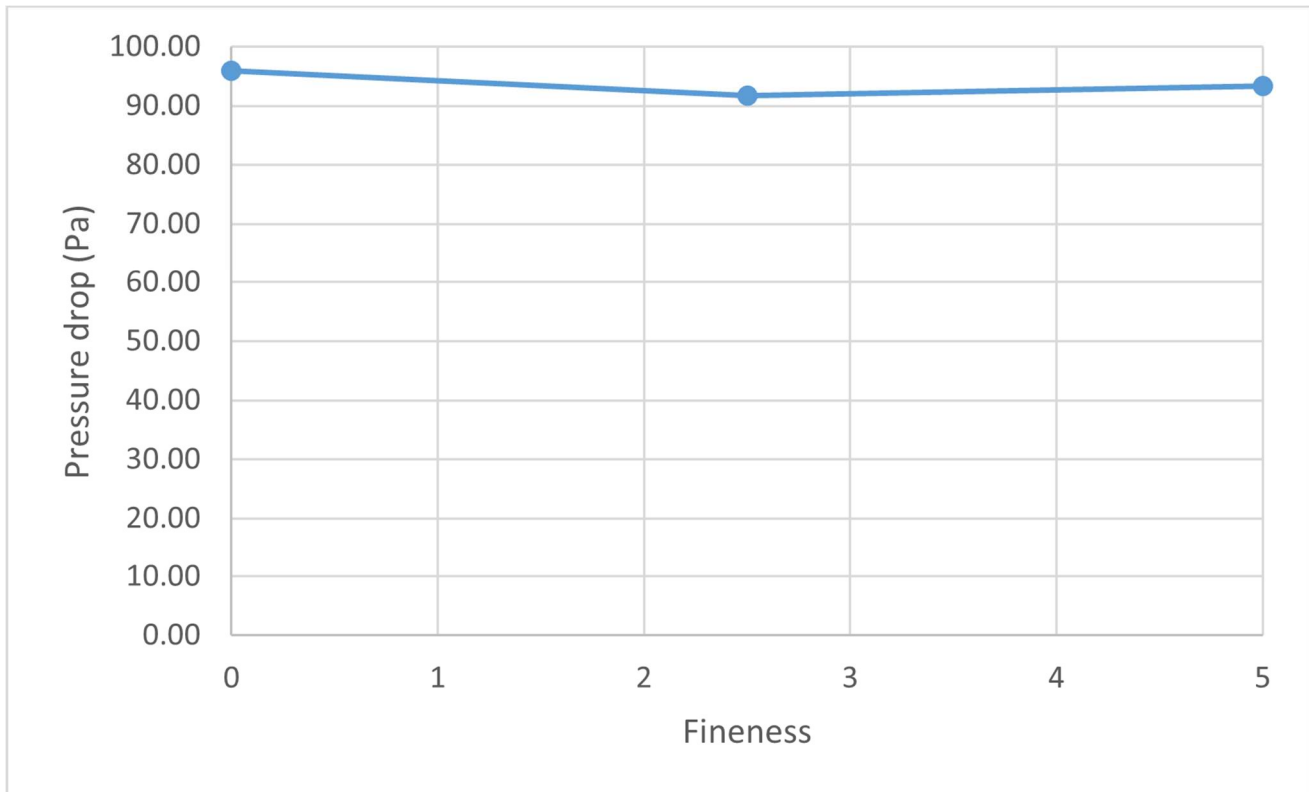
Figure 3.21: Plot of mesh dependency - Pressure drop vs. fineness
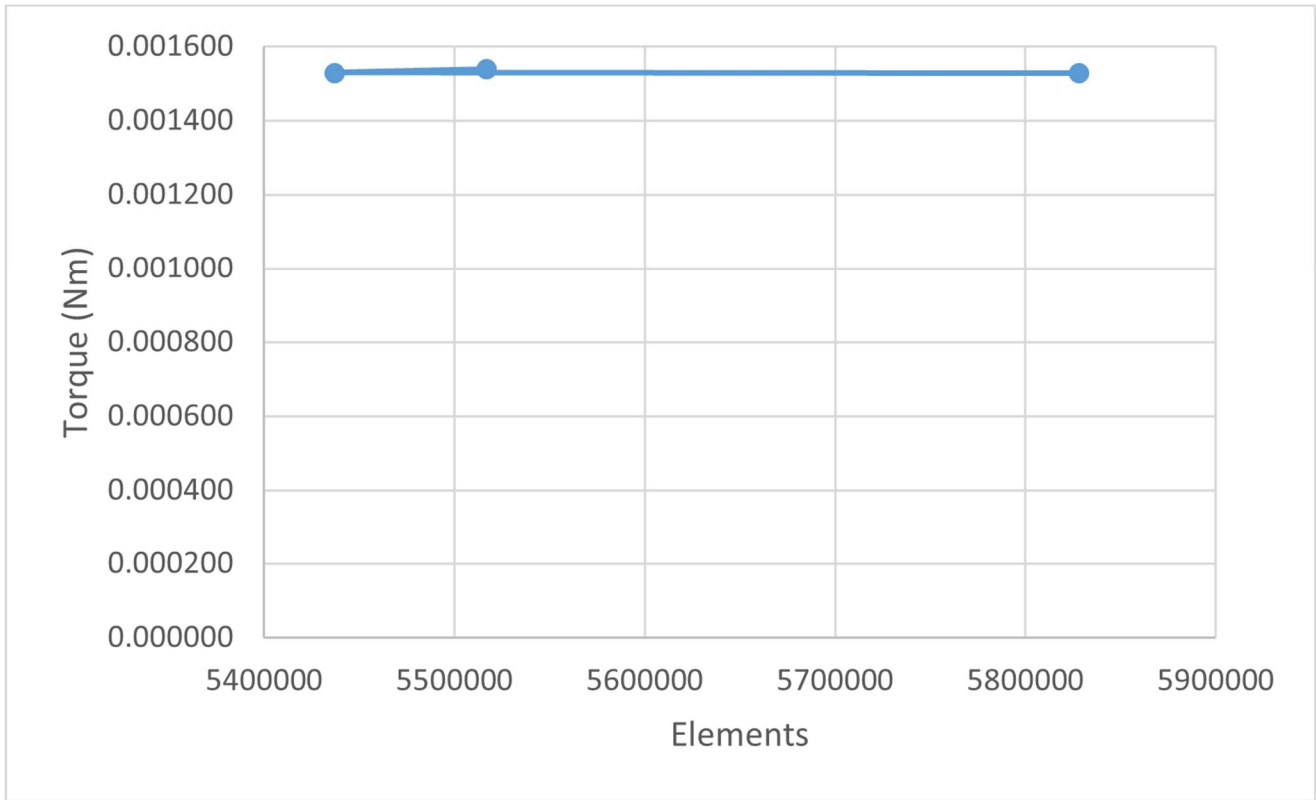
Figure 3.22: Plot of mesh dependency - Torque vs. total elements
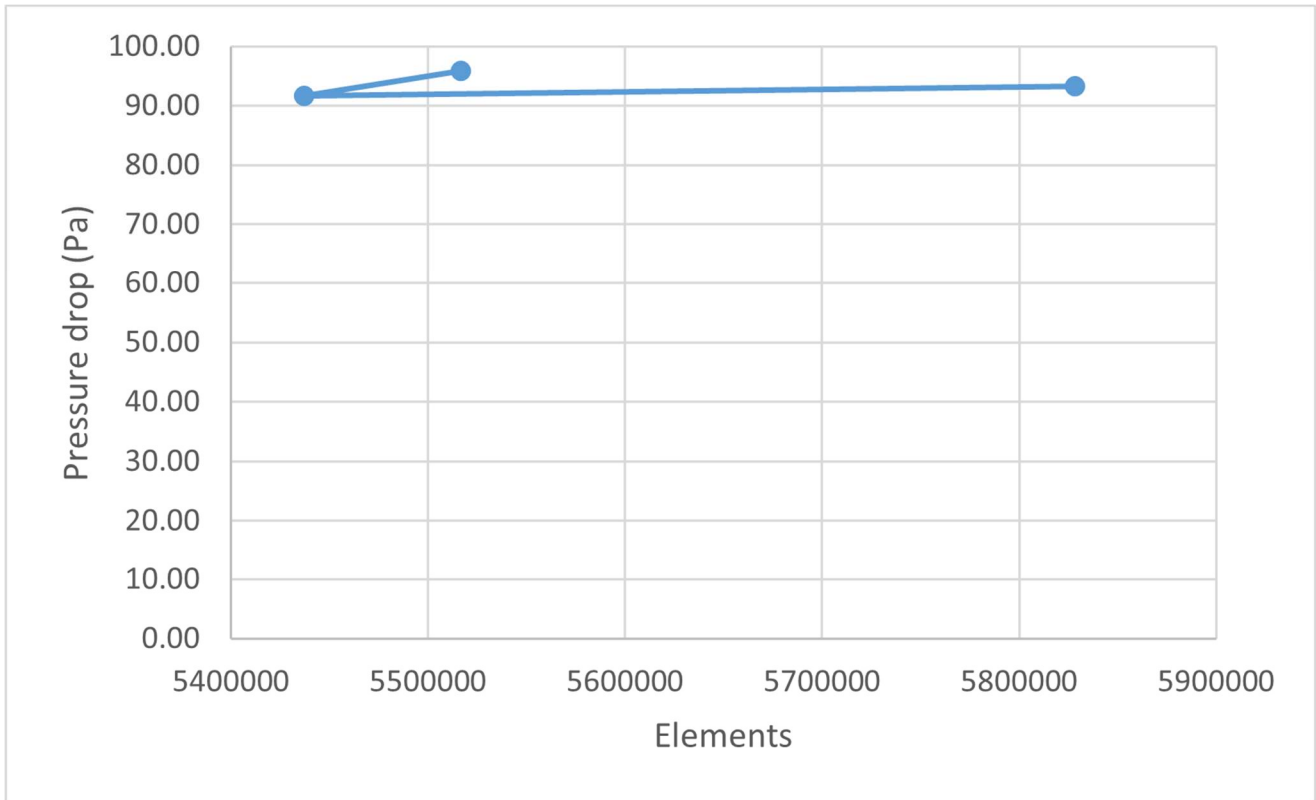
Figure 3.23: Plot of mesh dependency - Pressure drop vs. total elements

The collected data suggested that Torque readings were stable and approaching convergence. The pressure difference data seem to be unstable on initial inspection. However, the difference between the pressure readings

59

represents a small variance when expressed as a percentage of the total value. It was therefore deemed to be within an acceptable margin of error.
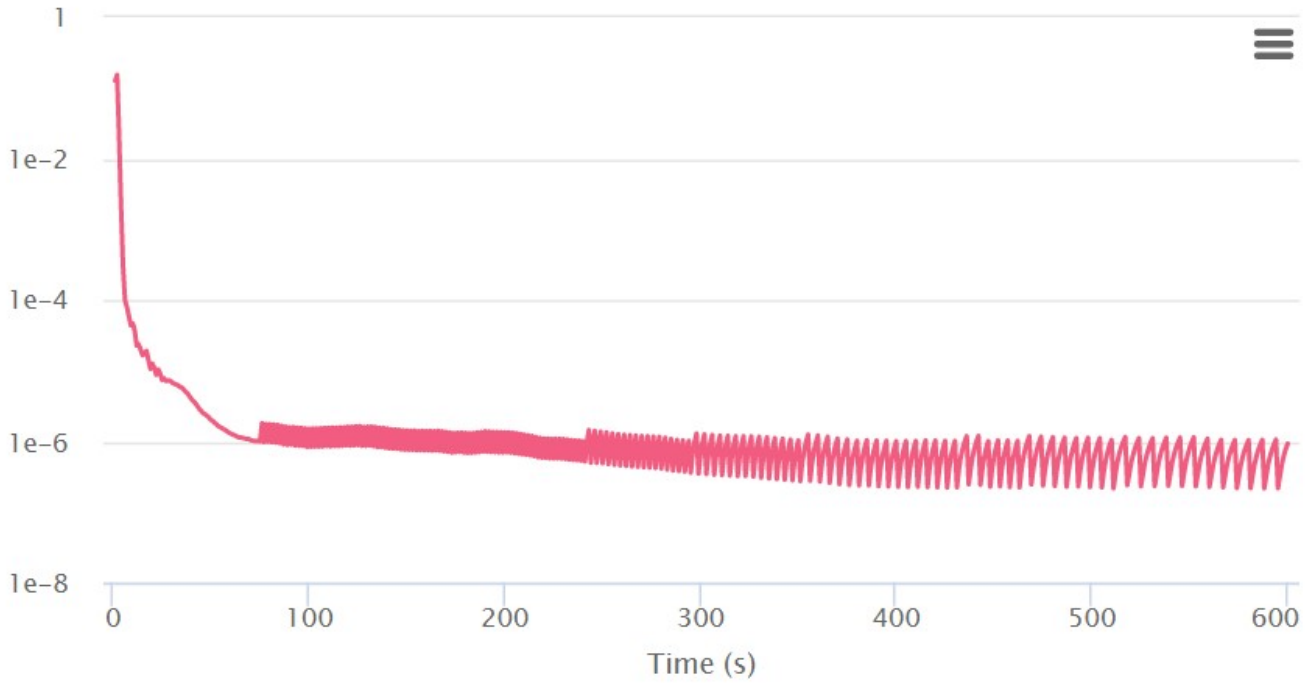
Figure 3.24: Plot of residual for specific dissipation rate (with fineness of 0)
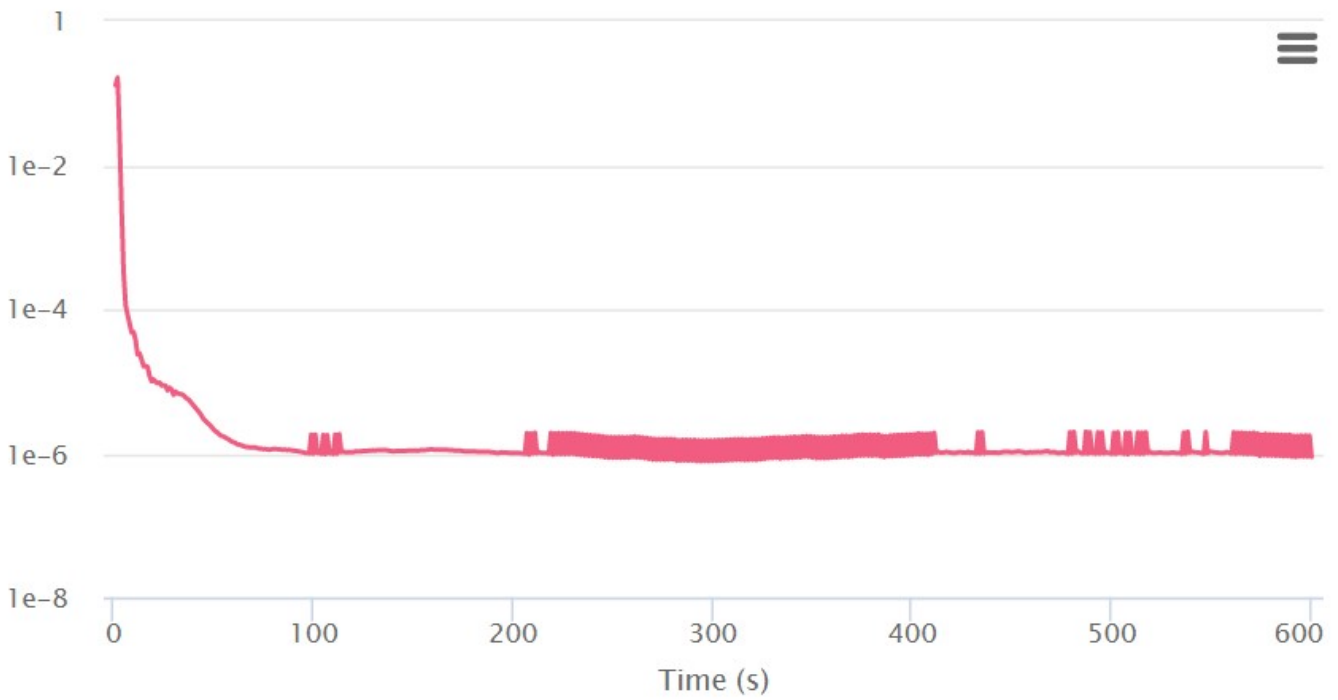
Figure 3.25: Plot of residual for specific dissipation rate (with fineness of 5)

Section 3.1.6 introduces the concept of residual values and convergence plots. The relevant residuals are for pressure, turbulent energy, and dissipation rate. Referring to Figure 3.24 and Figure 3.25, the behaviour of the residuals for specific dissipation rate suggests that a finer mesh might yield more stable results. At a fineness setting of 5, the residual is visibly more stable than at fineness 0. Where the residual plot for the coarser mesh fluctuates up and down as it approaches convergence, the relatively fine mesh has periods with almost no change in the residual value. It is therefore reasonable to assume that a sufficiently fine mesh would produce a simulation where the dissipation rate would converge and stay consistent as all other field variables converge. However, since Simscale limits the user to a set number of core hours, it is necessary to consider the computational intensity of the simulation.

Of all the residual plots, the omega residual is the only value to fluctuate in this way, yet it is potentially beneficial to increase fineness until all residuals converge, to maximize stability. Therefore, weighing this hypothetical benefit against the added computational intensity of using a finer mesh, it was determined that the consistency of the two main output parameters (torque and pressure) was sufficient to justify using less than the maximum fineness of 10.

3.3.5   Verifying position of virtual instruments

Recall, from section 2.3, that the pressure change associated with a component in a duct system is consistent for a given flowrate, irrespective of other pressure behaviour elsewhere in the system. Knowing this, a properly set-up CFD simulation should give the same pressure drop over an identical section, regardless of any changes made to the rest of the simulated geometry. Therefore, by varying the diffuser angle and analyzing the pressure behaviour in the simulated system, the established virtual pressure instruments could be used to confirm the proper setup of the CFD simulation. A consistent pressure drop across the section designated by the virtual instruments would verify their placement in the simulation and ensure a consistent methodology in data collection. Conversely, an inconsistent pressure drop across the same component in different geometries could reveal any previously unknown flaws in the CFD settings. Obviously, the above holds true only when Q and ω remain the same in the component.

Section 2.3 notes that overlapping of the pressure behaviours associated with particular elements may create interference in the local pressure readings, so the possibility for a consistent measurement would depend on proper placement of the virtual instruments. All pressure behaviour caused by components within the section should be within the bounds of the virtual instruments, and all pressure behaviour caused by components outside of the section should be outside of the bounds of the virtual instruments. To place the virtual instruments in accordance with these conditions, cross-sectional images were generated of the system's pressure and velocity gradients (see Figure 3.26).
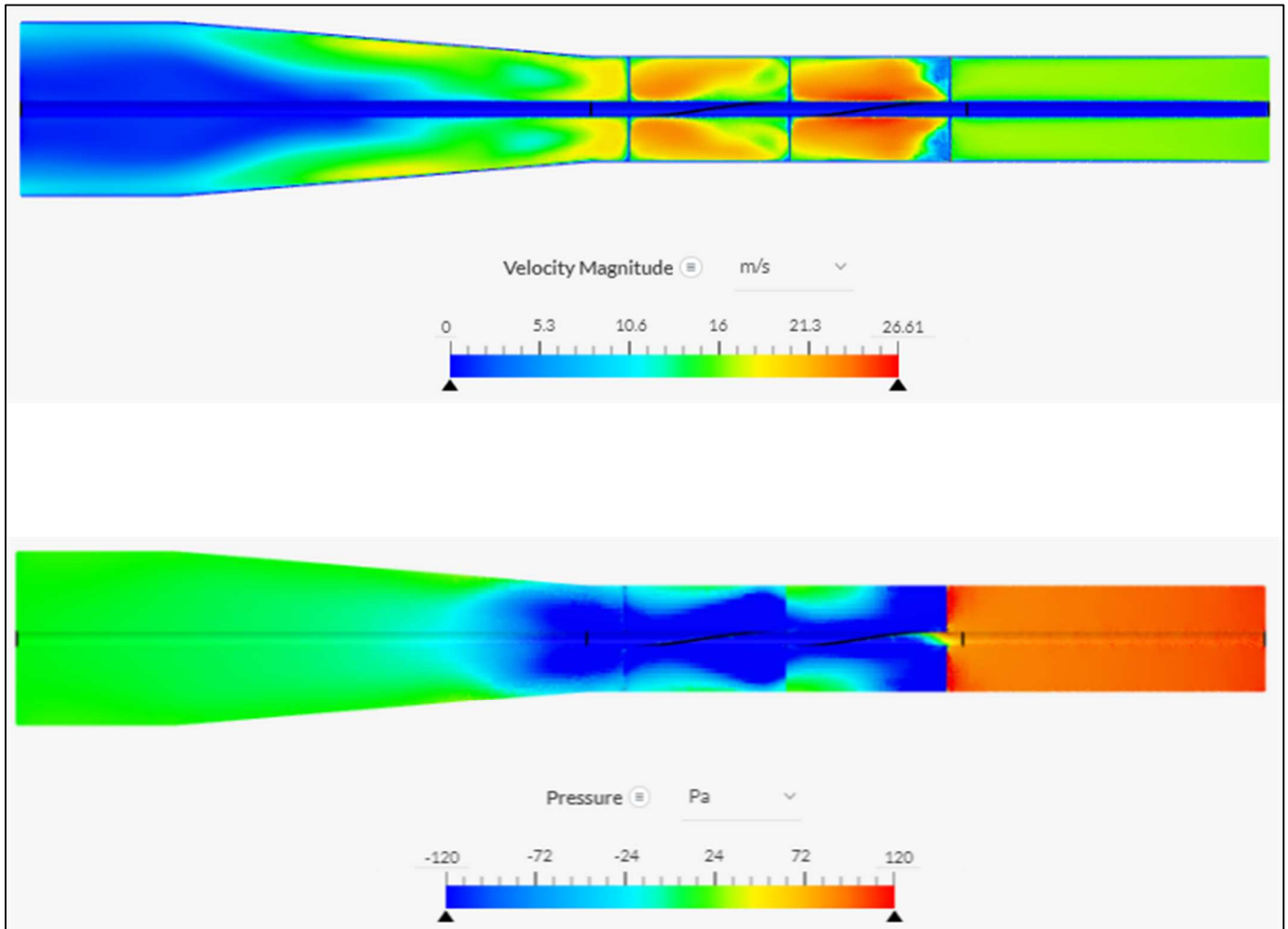
Figure 3.26: Pressure and velocity gradients (geometry 2, with 15 m/s flow at intake and 100 rad/s rotation)

Based on the pressure gradient of the maximum flowrate, the first virtual instrument is offset to avoid any anomalous local pressure effects. For instance, note the increased pressure at the leading edge of the rotor. The first virtual pressure instrument (P_1) is offset from the leading edge of the rotor by 30mm (in the simulation, x=0.195m). For a consistent position, with minimal interference from the system, the second virtual pressure instrument is placed at the mouth of the diffuser (in the simulation, x=0.041m). These offsets are constant between all geometries and the same positions are used in geometry 3 (where no diffuser is included).

To analyze the diffuser behaviour, additional virtual instruments were created at the geometry inlet and outlet, as a redundancy to confirm the outlet pressures reported by the Area Average outputs, P_{in} and P_{out}. A final virtual instrument was placed at the outlet of the diffuser. See Figure 3.27 and Table 3.8.
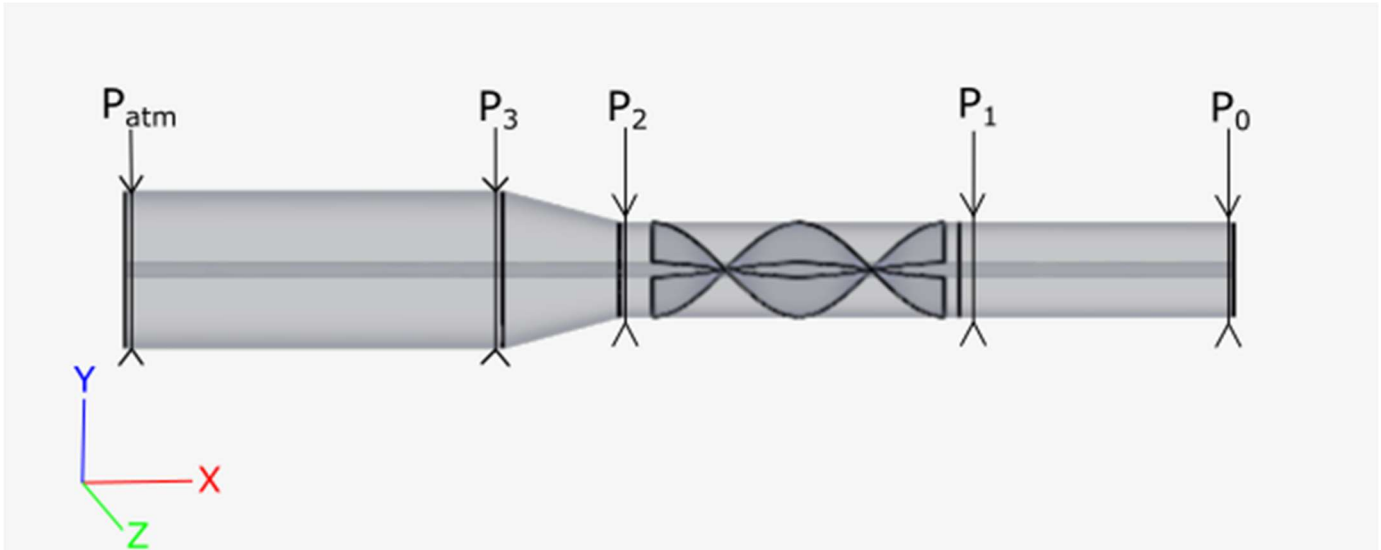
Figure 3.27: Positions of additional virtual instruments (placed for diffuser pressure analysis); geometry 4 used for illustration

Table 3.8: x-positions of virtual instruments, for each diffuser geometry

Half angle of diffuser	x_0	x_1	x_2	x_3	x_{atm}
degrees	m	m	m	m	m
0	0.3	0.195	0.041	-0.0734	-0.0734
4.7	0.3	0.195	0.041	-0.121	-0.1796
15	0.3	0.195	0.041	-0.009	-0.1698
45	0.3	0.195	0.041	0.025	-0.1686

Having placed the virtual instruments, the following set of pressure data was observed:

Table 3.9: Area average pressure from virtual instruments, for each diffuser geometry

Half angle of diffuser	v_{in}	P_0	P_1	P_2	P_3	P_{atm}
degrees	m/s	Pa	Pa	Pa	Pa	Pa
0	10	96.16	86.69	8.634	0.267	0.267
4.7	10	47.47	36.29	-45.46	-1.422	0.0024
0	5	22.42	19.24	2.115	0.03	0.03
4.7	5	11.38	7.513	-10.09	-0.8076	-0.0029
15	5	13.37	9.456	-8.437	-3.557	0.009
45	5	12.93	9.015	-8.456	-6.145	0.017
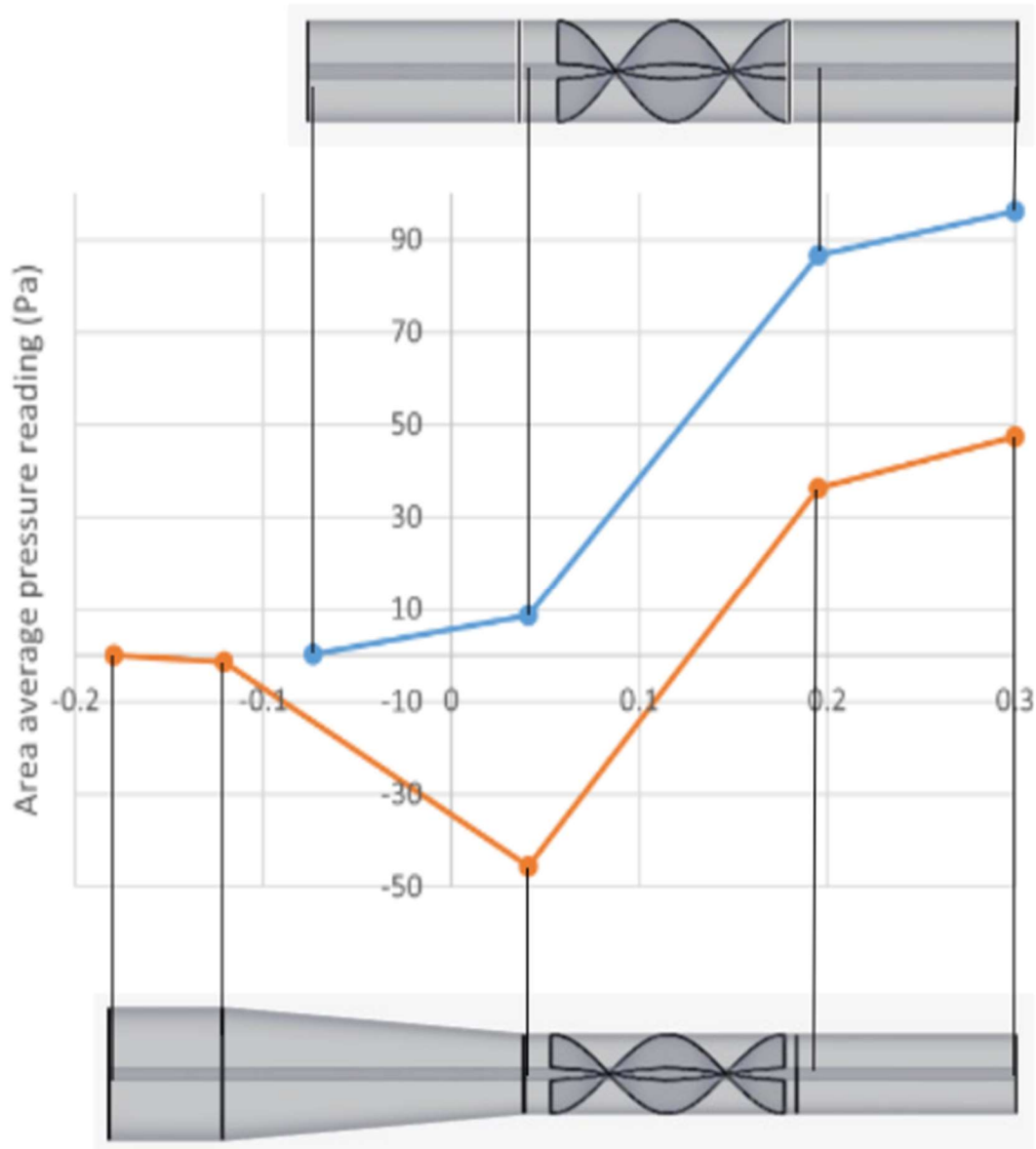
Figure 3.28: Diagrams of pressure behaviour (static pressure) in simulated duct geometries, from simulated data for geometries 2 and 3

The pressure behaviour seemed consistent in all cases except for the geometry with no diffuser. Referring to the cross-sectional pressure gradient diagram for that geometry (Figure 3.29), it was observed that an increased pressure region exists at the trailing edge of the rotor. In all simulations, some flow separation can be observed in the same section of the geometry (a selection of gradient plots is collected in Appendix A). Such behaviour can be attributed to the swirling flow coming from the trailing edge of the rotor. However, when a diffuser is not present, the separation impedes the flow, causing behaviour that mimics a nozzle. This pseudo-nozzle effect explains the deviation in pressure behaviour that was observed in this geometry.

After identifying the source of the deviation, the selected virtual instruments could be confirmed to produce a consistent measurement for a geometry which included a diffuser.
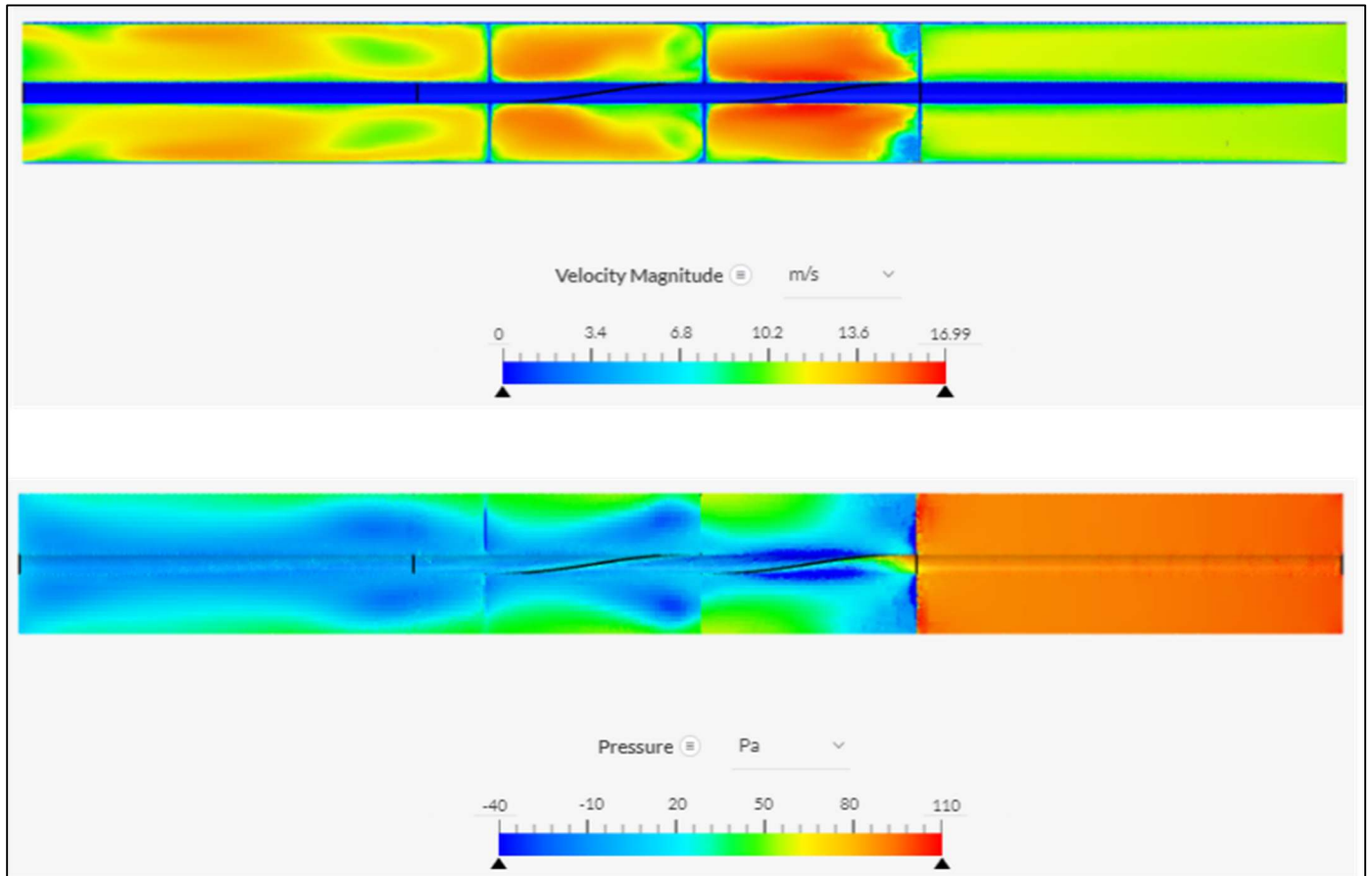
Figure 3.29:Pressure and velocity gradients (geometry 3, with 10 m/s flow at intake and 100 rad/s rotation)
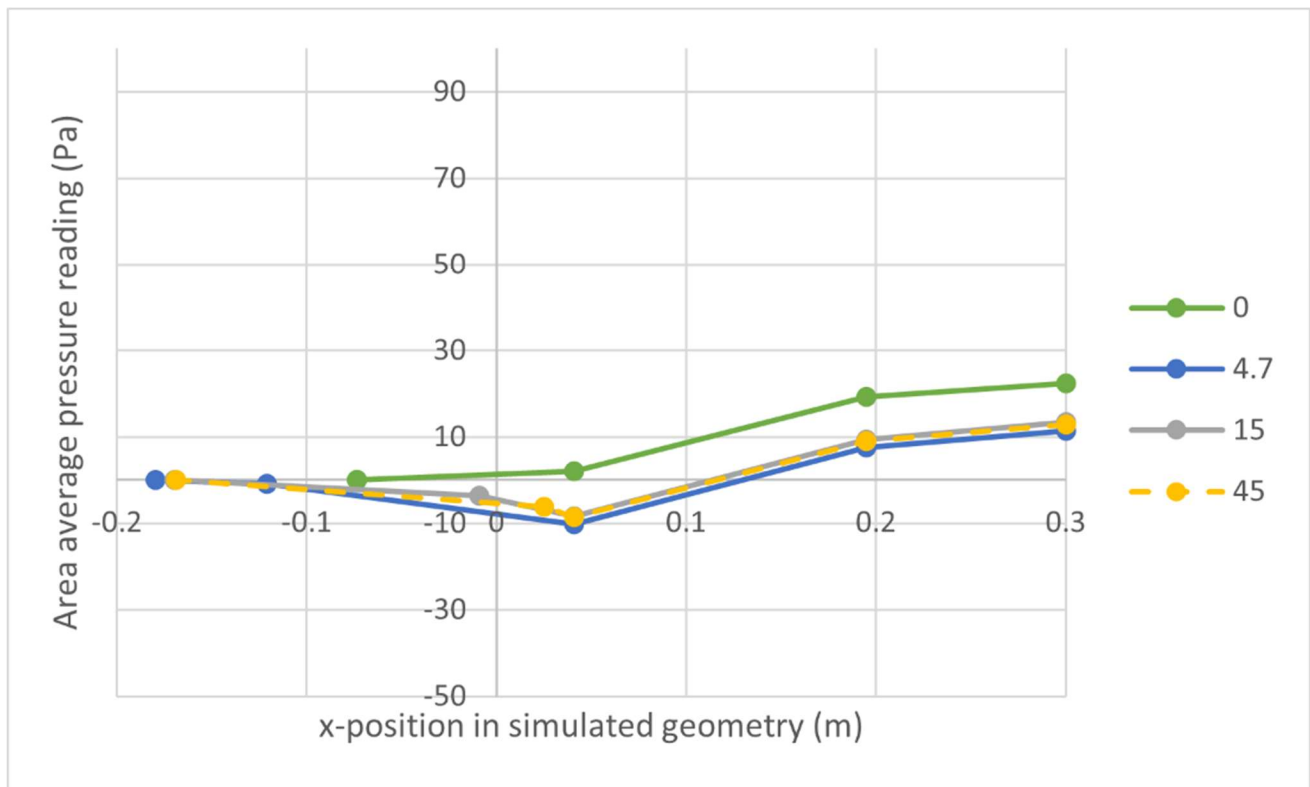
Figure 3.30: Simulated pressure behaviour; agreement between different geometries at 5 m/s

65

3.3.6 Verifying torque surface selection

As mentioned in section 3.3.1, the CFD torque output accounts for a pressure moment and a viscous moment applied to the selected surfaces. The virtual torque instruments were created using the inlet-facing and outlet-facing surfaces of the helical blade. To confirm that these surfaces would be an adequate representation of torque, the shear resistance was calculated for all other surfaces on the rotor, namely the blade edge and shaft surface.

Assuming linearity, the following equation may be used (as implemented in Engineer's Edge, 2020):

$$\tau = \mu \frac{u}{y} \tag{3.3}$$

where τ is the shear stress on a surface, μ is the dynamic viscosity of the working fluid, and u is the component of the fluid's velocity which is perpendicular to rotation, as measured at the rotating surface. Finally, y is the perpendicular distance from the pipe surface, denoted by subscript p, to the rotating surface. The two rotating surfaces in question are the exposed surface of the shaft, denoted by subscript s, and the outermost edge of the blade, denoted by subscript b. Using this convention, u and y can be defined as:

$$u_s = \frac{D_s \omega}{2}; u_b = \frac{D_b \omega}{2}$$

$$y_s = \frac{D_p - D_s}{2}; y_b = \frac{D_p - D_b}{2}$$

The stress can be described as a shear force, F, applied along the entire rotating surface. This force can then be converted into a resistance torque, T, using the following equations:

$$F_\tau = \tau A \tag{3.4}$$

$$T_\tau = r F_\tau \tag{3.5}$$

where A is the rotating area of the surface, and r is the perpendicular distance from the axis of rotation to the rotating surface. Given the length of the shaft, l, in the rotating zone, and the thickness of the blade, t, A and r can be defined as:

$$A_s = l(\pi D_s); A_b = t(2\pi D_b)$$

$$r_s = \frac{D_s}{2}; r_b = \frac{D_b}{2}$$

By combining equations (3.3), (3.4), and (3.5), then substituting the values as they are defined for either surface, the following equations can be derived:

$$T_{\tau,s} = \frac{\mu l \omega \pi D_s^3}{2(D_p - D_s)} \tag{3.6}$$

$$T_{\tau,b} = \frac{\mu t \omega \pi D_b^3}{D_p - D_b} \tag{3.7}$$

Table 3.10: Table of given values for calculation of viscous resistance

μ	L	t	D_s	D_b	D_p
N-s/m^2	m	m	m	m	m
0.0000181	0.144	0.0005	0.006	0.03975	0.0401

Given the values in Table 3.10, viscous resistances are calculated for each surface, over a range of rotational speeds.

Table 3.11: Calculated viscous resistance, for all simulated rotational velocities

ω	$T_{\tau,s}$	$T_{\tau,b}$	ΣT_τ
rad/s	Nm	Nm	Nm
137.5	3.57E-09	7.02E-07	7.05E-07
125	3.24E-09	6.38E-07	6.41E-07
112.5	2.92E-09	5.74E-07	5.77E-07
100	2.59E-09	5.10E-07	5.13E-07
50	1.30E-09	2.55E-07	2.56E-07
40	1.04E-09	2.04E-07	2.05E-07
25	6.48E-10	1.28E-07	1.28E-07
7.54	1.96E-10	3.85E-08	3.87E-08

Comparing this torque with the values obtained from the simulation, it was determined that the shear resistance torque was negligible. For this reason, the selected surfaces for the virtual instrument should give an adequate representation of torque.

Table 3.12: Comparison of simulated and shear-corrected torque

ω	ΣT_τ	T	$T - \Sigma T_\tau$
rad/s	Nm	Nm	Nm
137.5	7.05E-07	0.001346	0.001345
125	6.41E-07	0.001400	0.001399
112.5	5.77E-07	0.001441	0.001441
100	5.13E-07	0.001486	0.001486
50	2.56E-07	0.001656	0.001656
40	2.05E-07	0.001690	0.001690
25	1.28E-07	0.001736	0.001736
7.54	3.87E-08	0.001791	0.001791

3.3.7 Verifying incompressible fluid simulation

These computations were intended to model the most basic application of the prototype turbine device; the settings are based upon city driving speeds for a car. It was assumed that these significantly subsonic input speeds would yield adequate results with an incompressible CFD analysis of the fluid flow. To verify this assumption, supplemental simulations (see Table 3.13) were attempted using a compressible fluid medium. The settings used in the simulation

were identical to those used in an existing incompressible simulation, save for those changed by the fluid properties. Wherever possible, default values were kept, to preserve uniformity between the simulations.

Table 3.13: Comparison of compressible simulations with incompressible equivalents

Sim	v_{in}	ω_α	P_1	P_2	ΔP_α	T_α
#	m/s	rad/s	Pa	Pa	Pa	Nm
1RC-1	10	7.54	104.5*	0.0*	104.5	0.001934
1RC-2	10	250	175.6*	0.0*	175.6	0.003313
1RI-1	10	7.54	56.9	-35.8	92.7	0.001772
1RI-3	10	250	128.9	-24.8	153.7	0.003004

*-   See section 3.3.2

Recall from section 3.3.2 that pressure readings in a compressible simulation are displayed as absolute pressures. Since Bulk Calculation virtual instruments are only visible to 4 significant digits, this greatly increases the uncertainty of differential pressure data which are below 1000Pa. It is possible to overcome this limitation by using the geometry inlet and outlet faces to acquire pressure data from Area Average outputs. However, this would necessitate additional reductions to be applied to the data and would eliminate the benefit of the inlet and outlet extrusions in the CFD model.

For a preliminary inquiry into the efficiency of the device, the results were deemed to be adequate. Upon completing the preliminary tests and becoming more experienced with the software, future simulations could be attempted using compressible flow to provide further analysis of the device's behaviour at high speeds.

3.3.8 Consideration of moving reference frame

The initial troubleshooting setup of the CFD simulation (simulation set 1XX-T, as explained in section 3.2.6) was based on relative motion. The available turbine tutorials and documentation available on Simscale's website (Simscale, 2022c) were based on either water turbines or unenclosed wind turbine blades. Neither provided a methodology which could be used directly in the intended application. After some trial and error, a workaround was devised to allow the simulation to run. Rather than rotating the blade and holding the walls at 0 rpm as in the final simulations, the entire flow area was rotated around the stationary blade. Using the same rotational speed as in the later tests, the Rotating Wall at the outside surface of the pipe was set to match the rotation of the MRF zone.

While this served as a good starting point to determine proper simulation settings, the simulations were unstable, and it was unclear whether this method could provide adequate results. Upon further research (Simscale Help Chat, S. Block, personal correspondence, 2021), an "absolute motion" setup was devised. This setup rotated the blade and flow area, while keeping the pipe and diffuser stationary and fell more in line with the conventional turbine methodology as seen in (Simscale, 2022c).

As has been stated previously, the Navier Stokes equations are solved along the mesh, element by element. Thus, the transition between rotating zones in the relative frame of reference would be handled in the same manner as it would be in a model which represents "absolute motion". The major difference between these two models is the

nature of the inlet flow. Note that the extrusions at inlet are included in order to normalize the flow before it

impinges on the rotor (i.e., interacts with the rotating zone).
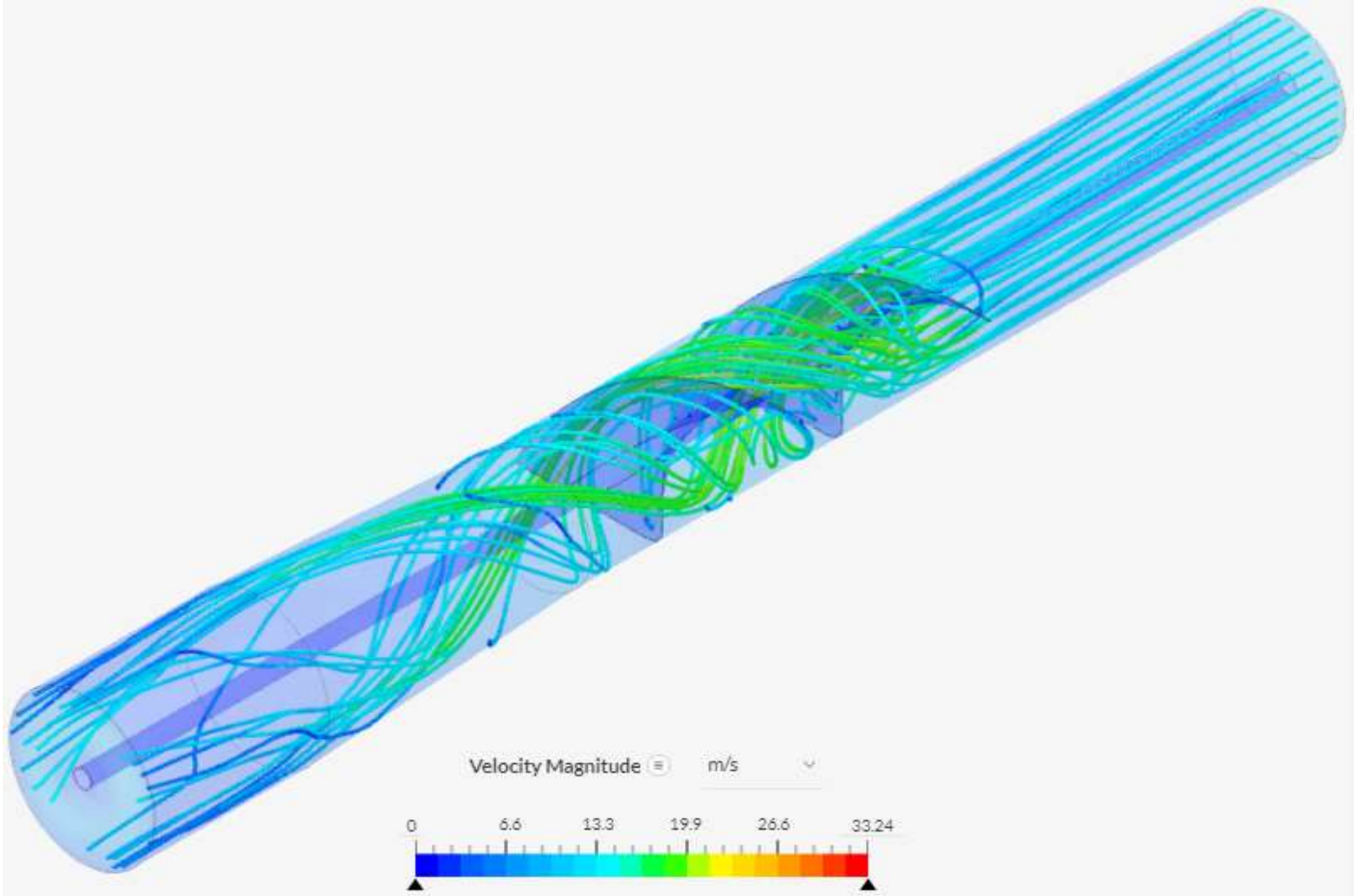
Figure 3.31: Particle trace generated using "relative motion" model (10m/s and 100 rad/s)
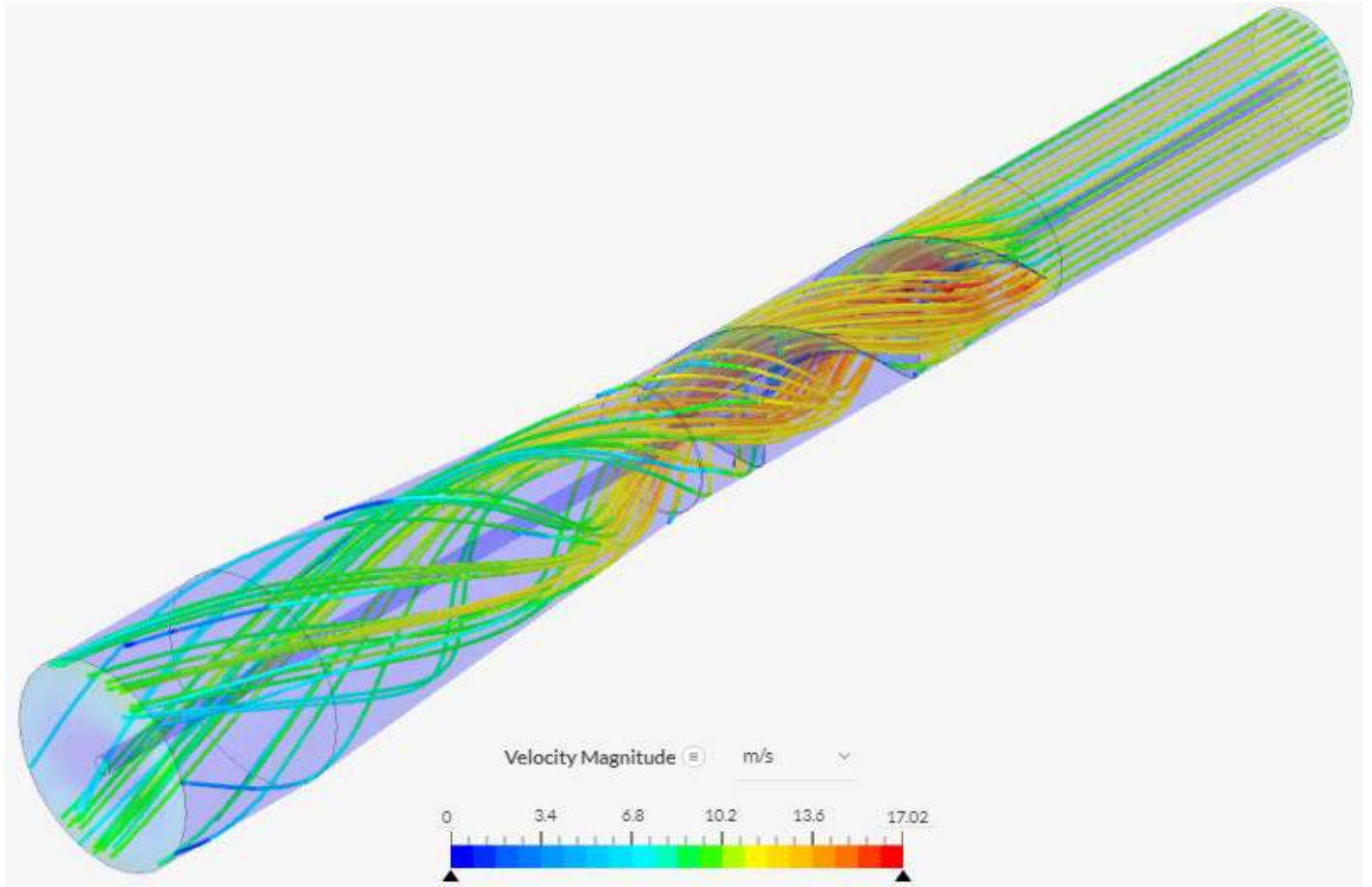
Figure 3.32: Particle trace generated using "absolute motion" model (10 m/s and 100 rad/s)

To check the validity of the initial setup, identical inputs and settings were used in the new simulation. Upon comparing the results of these two models, it seems that the relative frame of reference produces less consistent (or less stable) results. In Figure 3.31, note the maximum magnitude of velocity, which is nearly double the maximum value observed in Figure 3.32. This demonstrates that the swirling flow entering the blade section (in the "relative" model) has considerably more kinetic energy than the straight flow (in the "absolute" model). The data obtained from this brief exploration serve to highlight the efficacy of the "absolute motion" convention, including the use of extrusions at inlet and outlet. As a result, the relative motion methodology was not pursued. Consequently all related simulation results were discarded.

Table 3.14: Comparison of relative motion model to absolute motion model in a similar range

Sim	v_{in}	ω_α	P_1	P_2	ΔP_α	T_α
#	m/s	rad/s	Pa	Pa	Pa	Nm
1RI-13	10	200	159.2	-26.0	185.2	0.003180
1RI-14	10	100	134.8	-23.7	158.5	0.002793
1RI-15	10	125	139.6	-24.1	163.7	0.002872
1AI-1	10	137.5	42.1	-32.2	74.3	0.001333

70

3.3.9 Consideration of transition to fully dynamic model

The CFD portion of the experiment was conducted using a steady state model. However, Simscale also provides an option for a transient simulation (Simscale, 2021d). This model is based on a different type of rotating zone (AMI). Some consideration was made toward using this model; ultimately, it was decided that this would unnecessarily complicate the simulations. Like the compressible fluid model, this function uses greater processing power and would introduce more variables to this preliminary exploration of the device. For the same reasons, it was deemed unnecessary for this level of experimentation.

There is some hypothetical benefit to using a transient model. Since the intended use of the device is to be mounted on a moving vehicle, it might be fruitful to analyze the behaviour of the device from a resting position. This might allow for the diagnosis of any complications that might arise during the acceleration and deceleration process. However, power generation should be optimized for a consistent traveling speed. This means that the simulation need only be a representation of the device once it has reached a steady state. This was the justification for using the steady state model.

While the steady state model should be sufficient for the purpose of this exploration, this once again presents an area for future research if the device can be validated with these simple, early tests.

3.4 Discussion on relevance of data

All data pertaining to Geometry 1 were deemed inapplicable to the final analysis. While the differences in geometry could be accounted for (see section 2.4), the relative motion model did not agree with the conventional method. Additionally, simulation 1AI-1 was usable as a verification of the methodology outlined in section 2.4, but it was superfluous to the analytical data and has thus been disregarded.

3.5 Determination of experimental setpoints for subsequent physical experiment

Recall that the simulated data is intended to be compared to a physical experiment operating under similar conditions. This will be accomplished using various data reductions, including the similarity laws described in section 2.4. This transformation will be based on the known diameters of the physical experiment's duct and of the simulated duct. The ratio of these diameters will be used to transform data into expected data at desired experimental setpoints.

Recall from section 3.2.5 that simulated intake velocities were selected based on city driving speeds, and exclusively as multiples of 5 for mathematical simplicity. A similar philosophy has been used to select velocity setpoints for the physical experiment.

Also recall from section 2.3.2 that power generation with a turbine is trivial when operating with a constant rotational velocity. Thus, rotational velocity may be treated as an independent variable; this represents a base case for implementation of the device, where no rectifier is used to maintain optimal tip speed during operation.

The physical experiment would have a D_β of 0.15242 m and would be tested at a range of setpoints combining flow velocity and rotational speed. The flow velocity setpoints were 5, 10, 15, and 20 m/s. The rotational setpoints were 100, 150, 200, 250, 500, 750, and 1000 RPM. Every combination thereof would represent a unique experimental setpoint, which could be represented using the following setpoint codes:

Table 3.15: Designation codes for intended physical experimental setpoints

Rotational speed (rpm)	Airflow velocity (m/s)			
	5	10	15	20
100	A5	A10	A15	A20
150	B5	B10	B15	B20
200	C5	C10	C15	C20
250	D5	D10	D15	D20
500	E5	E10	E15	E20
750	F5	F10	F15	F20
1000	G5	G10	G15	G20

3.6   Simulated data reduction and interpolation

As seen in section 2.4, the similarity laws can be used to transform (SL transform) the simulated data to match the dimensions of the physical test rig. Table 3.16 combines data sets 2AI-N and 2AI-v, and includes the results obtained from equations (2.10) to (2.12).

Table 3.16: Table of results from CFD simulations; duct diameter = 40.10mm

Sim #	v_α m/s	Q_α m^3/s	ω_α rad/s	P_1 Pa	P_2 Pa	ΔP_α Pa	T_α N-m	$\dot{W}_{A,\alpha}$ W	$\dot{W}_{M,\alpha}$ W	η_{sim} %
2AI-9	15	0.0185	100	86.49	-102.0	188.49	0.003516	3.491	0.3516	10.07
2AI-4	10	0.0123	100	36.29	-45.46	81.75	0.001486	1.009	0.1486	14.72
2AI-10	5	0.0062	100	7.513	-10.09	17.60	0.000288	0.109	0.0288	26.47
2AI-2	10	0.0123	137.5	29.53	-45.44	74.97	0.001346	0.926	0.1850	19.99
2AI-1	10	0.0123	125	32.25	-45.51	77.76	0.001400	0.960	0.1750	18.23
2AI-3	10	0.0123	112.5	34.22	-45.44	79.66	0.001441	0.984	0.1622	16.49
2AI-5	10	0.0123	50	45.18	-44.97	90.15	0.001656	1.113	0.0828	7.44
2AI-6	10	0.0123	40	47.14	-44.82	91.96	0.001690	1.135	0.0676	5.95
2AI-7	10	0.0123	25	50.32	-44.23	94.55	0.001736	1.167	0.0434	3.72
2AI-8	10	0.0123	7.54	53.58	-43.62	97.20	0.001791	1.200	0.0135	1.13
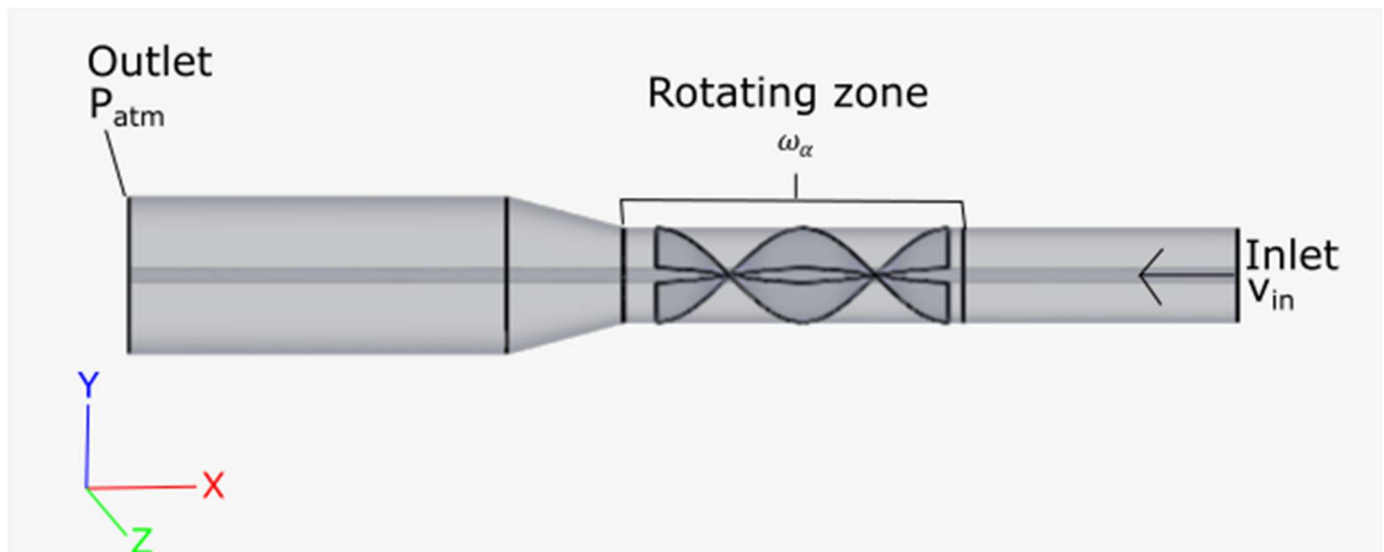
Figure 3.33: Diagram of simulated geometry 4, with boundary conditions

Referring to Figure 3.33, note that the rotor shaft stretches through the entire length of the geometry. This means that the flowrate must be corrected for an annular diameter. This can be calculated by subtracting the area of the shaft from the areas before and after the diffuser.

By using this area ratio, or a ratio of the equivalent diameters, the flow at input (described as a velocity) can be used to predict the flow at output. This knowledge can be used to confirm the flowrate calculated in the simulation.
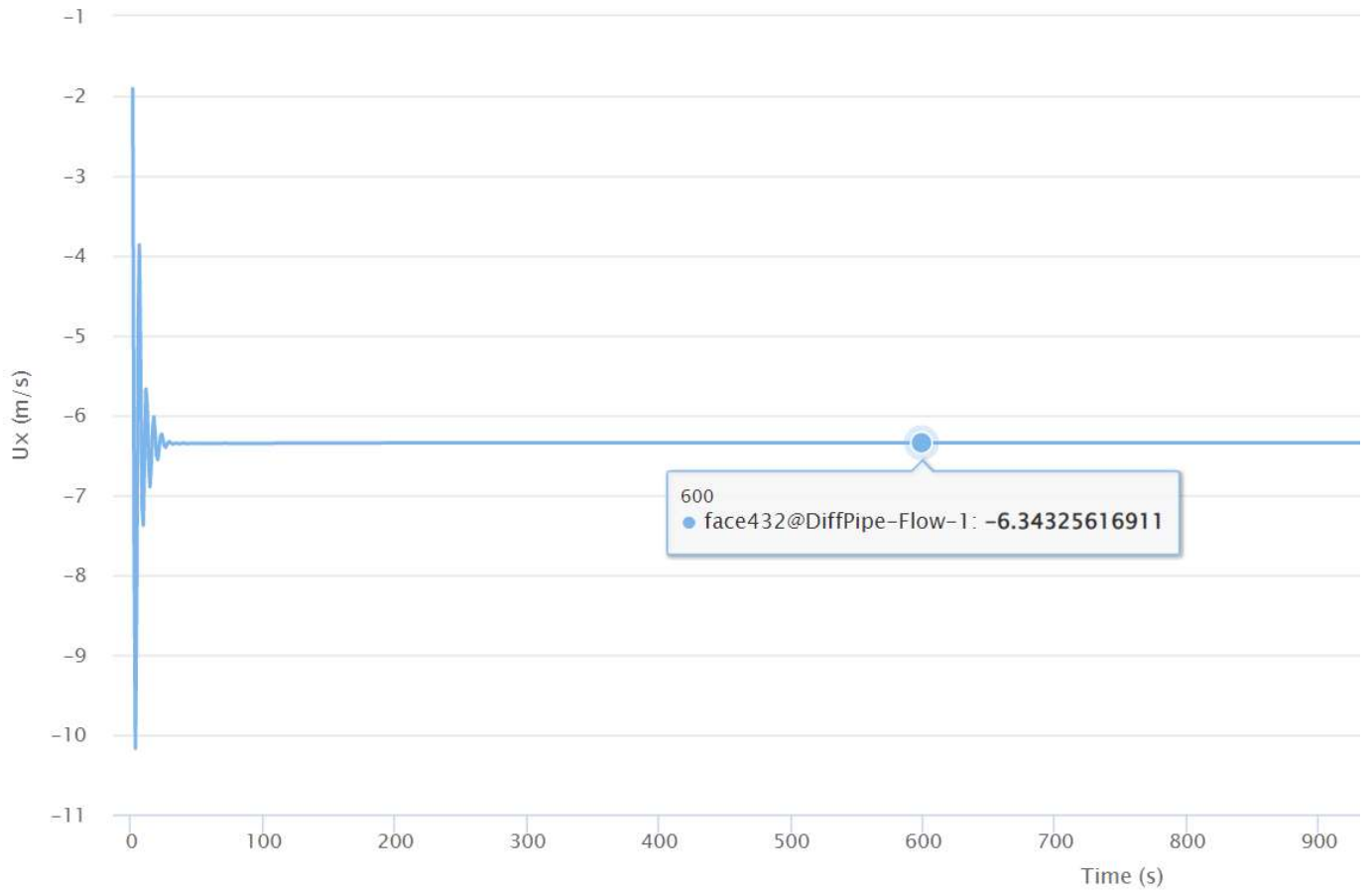
Figure 3.34: Axial velocity at geometry output, from simulation 1AI-1 (cropped for legibility)

To ensure that any observed error was not influenced by the convergence of the simulation, the timestep test model was used (named simulation 1AI-1 in section 3.2.5). Consulting the axial component of velocity at the output of the diffuser (see Figure 3.34 for cropped plot, full plot in Appendix A), a consistent output velocity was taken as the true simulated value, v_{true}.

$$A' = A - A_s \tag{3.8}$$

$$D' = \sqrt{D^2 - D_s^2} \tag{3.9}$$

$$v_{out} = v_{in} \left(\frac{D_{in}}{D_{out}}\right)^2 \tag{3.10}$$

where A' is the annular area of a cross-section A, and D' is the equivalent annular diameter. A_s and D_s are the cross-sectional area and diameter of the shaft, respectively.

Equation (3.10) describes the flow continuity based on the diameter ratio. Recall that v_{in} is the flow velocity designated in the simulation; it corresponds to the diffuser inlet diameter, D_{in}. An outlet velocity, v_{out}, can be calculated for the diffuser outlet diameter, D_{out}. Likewise, using the annular diameter ratio would produce an annular exit velocity, v_{out}'.

Table 3.17: Diameters of geometry 1 (including annular diameters)

D_{in}	D_{out}	$\dfrac{D_{out}}{D_{in}}$	D_s	D_{in}'	D_{out}'	$\dfrac{D_{out}'}{D_{in}'}$
m	m	--	m	m	m	--
0.0401	0.050125	1.25	0.006	0.039649	0.049765	1.255142

Table 3.18: Comparison of output velocities, with and without annular correction

v_{in}	v_{true}	v_{out}	v_{err}	v_{out}'	v_{err}'
m/s	m/s	m/s	%	m/s	%
10	6.343	6.4	0.90%	6.347668	0.07%

As seen in Table 3.18, correcting for annular area has accurately predicted exit velocity to within 0.07%, as compared to a 0.90% error without the annular correction. For this reason, all flowrates used in Table 3.16 have been calculated with an annular diameter, D_{in}'. Note however, that the full diameter, D_{in}, is used in equations (2.13) to (2.15), since this represents the direct equivalent to the dimensions of the physical experiment.

The Similarity Laws may be used to transform data to predict performance under different operating conditions, such as different sizes, flowrates, and rotational speeds. By repeating the SL transformation procedure (as outlined in section 2.4) for each setpoint of rotational speed in Table 3.15, performance could be projected for the physical experiment. it should be noted however, that these data points would not correspond precisely with flow velocity setpoints. With a simple SL transformation, only approximate matches would be available to assess the accuracy of the physical experiment. The data sets which most closely match the flow velocity setpoints for the physical experiment are highlighted below in green.

Table 3.19: Transformed CFD results, 100 rpm setpoint

N^*	v_β	ω_β	Q_β	ΔP_β	$\dot{W}_{A,\beta}$	$\dot{W}_{M,\beta}$	T_{exp}	Physical equivalent
rpm	m/s	rad/s	m³/s	Pa	W	W	Nm	Setpoint code
100	5.84	10.5	0.107	29.9	3.18	0.320	0.0306	A5
100	3.89	10.5	0.0710	13.0	0.920	0.135	0.0129	--
100	1.95	10.5	0.0355	2.79	0.0990	0.0262	0.00250	--
100	2.83	10.5	0.0516	6.28	0.324	0.0649	0.00619	--
100	3.11	10.5	0.0568	7.88	0.448	0.0816	0.00780	--
100	3.46	10.5	0.0631	9.97	0.629	0.104	0.00991	--
100	7.78	10.5	0.142	57.1	8.11	0.604	0.0576	--
100	9.73	10.5	0.178	91.1	16.2	0.963	0.0919	A10
100	15.6	10.5	0.284	240	68.1	2.53	0.242	A15
100	51.6	10.5	0.942	2709	2551	28.7	2.74	--

Table 3.20: Transformed CFD results, 150 rpm setpoint

N^*	v_β	ω_β	Q_β	ΔP_β	$\dot{W}_{A,\beta}$	$\dot{W}_{M,\beta}$	T_{exp}	Physical equivalent
rpm	m/s	rad/s	m³/s	Pa	W	W	Nm	Setpoint code
150	8.76	15.7	0.160	67.2	10.7	1.08	0.0688	--
150	5.84	15.7	0.107	29.1	3.10	0.457	0.0291	--
150	2.92	15.7	0.0533	6.28	0.334	0.0884	0.00563	--
150	4.25	15.7	0.0775	14.1	1.09	0.219	0.0139	--
150	4.67	15.7	0.0852	17.7	1.51	0.276	0.0175	--
150	5.19	15.7	0.0947	22.4	2.12	0.350	0.0223	B5
150	11.7	15.7	0.213	129	27.4	2.04	0.130	--
150	14.6	15.7	0.266	205	54.6	3.25	0.207	B15
150	23.3	15.7	0.426	539	230	8.54	0.544	--
150	77.4	15.7	1.41	6095	8609	96.9	6.17	--

Table 3.21: Transformed CFD results, 200 rpm setpoint

N^*	v_β	ω_β	Q_β	ΔP_β	$\dot{W}_{A,\beta}$	$\dot{W}_{M,\beta}$	T_{exp}	Physical equivalent
rpm	m/s	rad/s	m³/s	Pa	W	W	Nm	Setpoint code
200	11.7	20.9	0.213	119	25.4	2.56	0.122	--
200	7.78	20.9	0.142	51.8	7.36	1.08	0.0517	--
200	3.89	20.9	0.0710	11.2	0.792	0.210	0.0100	--
200	5.66	20.9	0.103	25.1	2.60	0.519	0.0248	C5
200	6.23	20.9	0.114	31.5	3.58	0.653	0.0312	--
200	6.92	20.9	0.126	39.9	5.03	0.830	0.0396	--
200	15.6	20.9	0.284	229	64.9	4.83	0.231	C15
200	19.5	20.9	0.355	364	129	7.70	0.368	C20
200	31.1	20.9	0.568	959	545	20.2	0.966	--
200	103	20.9	1.88	10835	20406	230	11.0	--

Table 3.22: Transformed CFD results, 250 rpm setpoint

N^*	v_β	ω_β	Q_β	ΔP_β	$\dot{W}_{A,\beta}$	$\dot{W}_{M,\beta}$	T_{exp}	Physical equivalent
rpm	m/s	rad/s	m³/s	Pa	W	W	Nm	Setpoint code
250	14.6	26.2	0.266	187	49.7	5.01	0.191	D15
250	9.73	26.2	0.178	81.0	14.4	2.12	0.0808	D10
250	4.86	26.2	0.0888	17.4	1.55	0.409	0.0156	--
250	7.08	26.2	0.129	39.3	5.07	1.01	0.0387	--
250	7.78	26.2	0.142	49.3	7.00	1.28	0.0487	--
250	8.65	26.2	0.158	62.3	9.83	1.62	0.0619	--
250	19.5	26.2	0.355	357	127	9.43	0.360	D20
250	24.3	26.2	0.444	569	253	15.0	0.574	--
250	38.9	26.2	0.710	1498	1064	39.5	1.51	--
250	129	26.2	2.35	16930	39856	448	17.1	--

Table 3.23: Transformed CFD results, 500 rpm setpoint

N^*	v_β	ω_β	Q_β	ΔP_β	$\dot{W}_{A,\beta}$	$\dot{W}_{M,\beta}$	T_{exp}	Physical equivalent
rpm	m/s	rad/s	m³/s	Pa	W	W	Nm	Setpoint code
500	29.2	52.4	0.533	747	398	40.0	0.765	--
500	19.5	52.4	0.355	324	115	16.9	0.323	E20
500	9.73	52.4	0.178	69.7	12.4	3.28	0.0626	E10
500	14.2	52.4	0.258	157	40.6	8.11	0.155	--
500	15.6	52.4	0.284	197	56.0	10.2	0.195	E15
500	17.3	52.4	0.316	249	78.7	13.0	0.248	--
500	38.9	52.4	0.710	1428	1014	75.4	1.44	--
500	48.6	52.4	0.888	2277	2020	120	2.30	--
500	77.8	52.4	1.42	5992	8509	316	6.04	--
500	258	52.4	4.71	67720	318846	3588	68.5	--

Table 3.24: Transformed CFD results, 750 rpm setpoint

N^*	v_β	ω_β	Q_β	ΔP_β	$\dot{W}_{A,\beta}$	$\dot{W}_{M,\beta}$	T_{exp}	Physical equivalent
rpm	m/s	rad/s	m³/s	Pa	W	W	Nm	Setpoint code
750	43.8	78.5	0.799	1680	1342	135	1.72	--
750	29.2	78.5	0.533	729	388	57.1	0.727	--
750	14.6	78.5	0.266	157	41.8	11.1	0.141	F15
750	21.2	78.5	0.387	353	137	27.4	0.348	--
750	23.3	78.5	0.426	444	189	34.4	0.439	--
750	25.9	78.5	0.473	561	266	43.8	0.557	--
750	58.4	78.5	1.07	3214	3423	255	3.24	--
750	73.0	78.5	1.33	5122	6819	406	5.17	--
750	117	78.5	2.13	13482	28717	1067	13.6	--
750	387	78.5	7.06	152370	1076106	12109	154	--

N^*	v_β	ω_β	Q_β	ΔP_β	$\dot{W}_{A,\beta}$	$\dot{W}_{M,\beta}$	T_{exp}	Physical equivalent
rpm	m/s	rad/s	m³/s	Pa	W	W	Nm	Setpoint code
1000	58.4	105	1.07	2986	3181	320	3.06	--
1000	38.9	105	0.710	1295	920	135	1.29	--
1000	19.5	105	0.355	279	99.0	26.2	0.250	G20
1000	28.3	105	0.516	628	324	64.9	0.619	--
1000	31.1	105	0.568	788	448	81.6	0.780	--
1000	34.6	105	0.631	997	629	104	0.991	--
1000	77.8	105	1.42	5713	8113	604	5.76	--
1000	97.3	105	1.78	9106	16164	963	9.19	--
1000	156	105	2.84	23968	68071	2530	24.2	--
1000	516	105	9.42	270879	2550769	28703	274	--

Some of the desired setpoints for the physical experiment (recall Table 3.15) could not be matched directly to the reduced CFD results. It is also worth noting that the imprecision in the matching of velocity setpoints would correspond with some inaccuracy in the corresponding transformed pressure, since the resistance pressure would be a function of the flowrate. This would result in some known variance between the simulated and physical observations.

Therefore, the reduced results for each rotational setpoint were used to create curves of best fit. This would allow the interpolation of values for pressure and torque at each rotational setpoint. Since there should logically be no pressure change in the system and no torque generated when there is no flow, the origin was included as a valid point on each curve. Both behaviours are modeled as second order curves of best fit, based on an R^2 value of 1.0000. The curves of best fit for the 100 RPM setpoint are shown in Figure 3.35 and Figure 3.36.

Note that this correlation coefficient reflects a great degree of consistency across individual CFD simulations. However, due to the imprecise nature of physical experimentation with a real turbine, the physical data setpoints that would be observed in the experiment could not be expected to perfectly match the intended setpoints listed in Table 3.15. Once again, it must be stressed that this imprecision in matching would result in some known variance between the simulated and physical observations.

After the physical experiment has been completed, this imprecision may be fully eliminated as a source of error. This can be accomplished by using the exact values of the observed data setpoints when calculating expected pressure and torque values from the interpolation curves. For fluid velocity, the torque and pressure interpolations may be generated using the observed value of fluid velocity. For rotational velocity, a similar variance will be observed due to the variance in observed data. To address this issue, a final SL transformation may be performed to reach the observed value of rotational velocity.
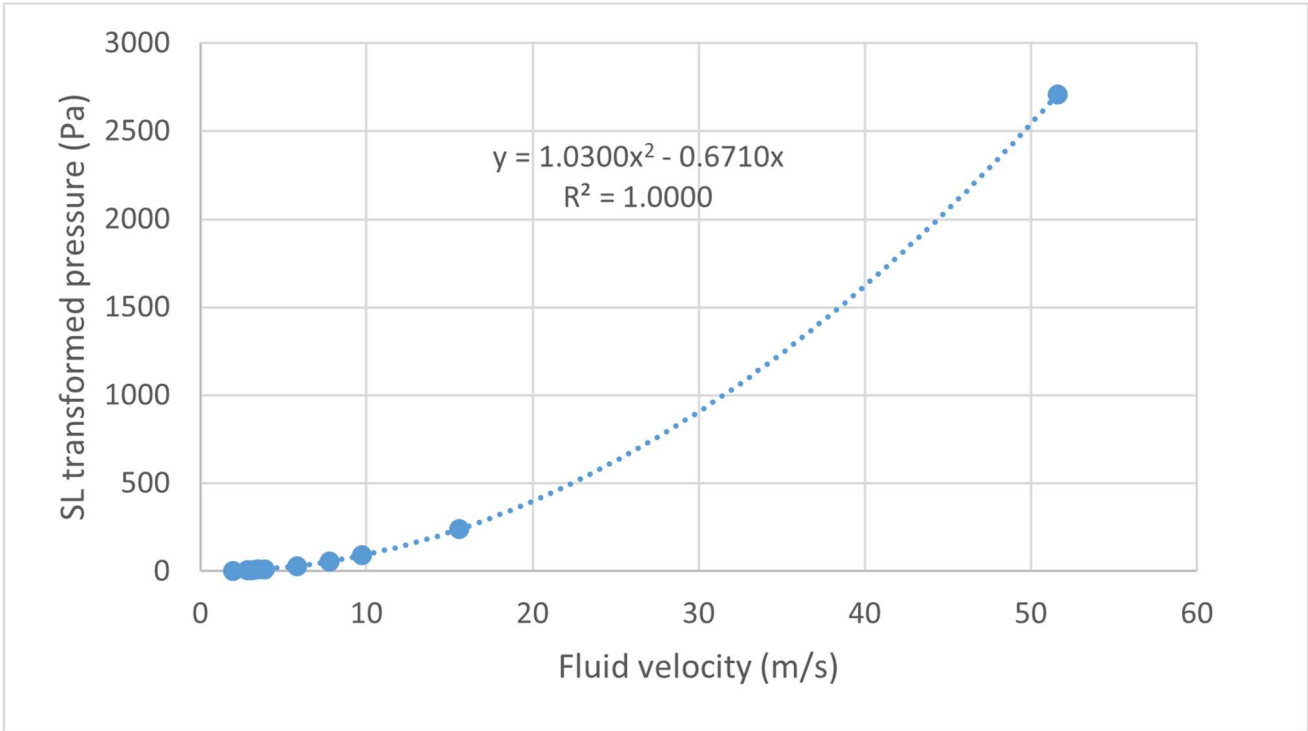
Figure 3.35: Projected pressure behaviour at 100 rpm setpoint; obtained from similarity law transformed data
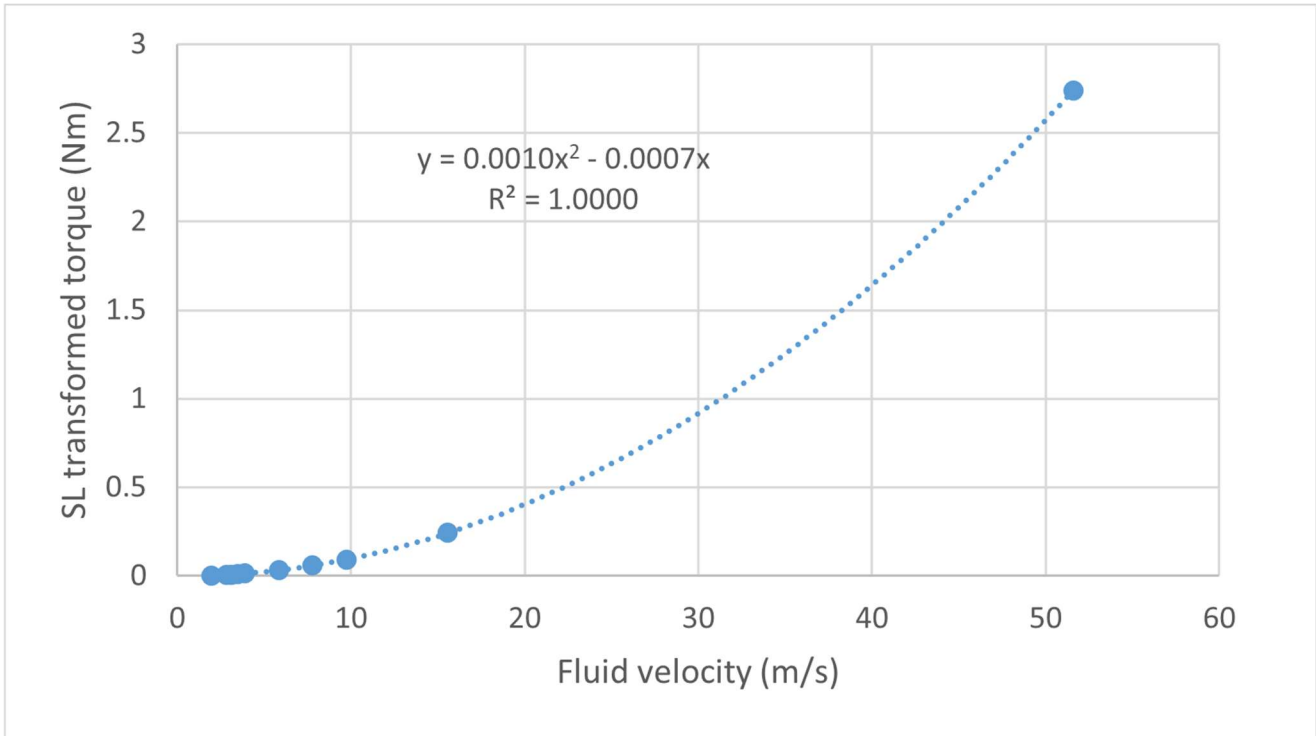
Figure 3.36: Projected torque behaviour at 100 rpm setpoint; obtained from similarity law transformed data

3.7 Summary of CFD findings

Figure 3.35 and Figure 3.36 demonstrate consistent, high quality simulation results. This may serve as a final verification of the settings explored in section 0. Briefly, the selected timestep, meshing, and virtual instruments were all deemed appropriate for this application. Additionally, the compressible fluid analysis and dynamic model had too much computational cost to warrant adoption but were deemed unnecessary for this application. Judging by the correlation coefficients of the SL transformed trends, these determinations were sound.

These trends will be used as interpolation functions to compute dependent variable values at the same independent variable setpoints as for the physical experiments which follow.

Finally, the SL transformed data may be used to characterize the performance of the turbine design, in the form of a set of performance curves. Note that the following performance curves have been transformed to a constant rotational setpoint, while maintaining the dimensions of the simulated geometry. Aside from the SL transformation (section 2.4), no other reductions (from section 3.6) have been applied to the data.
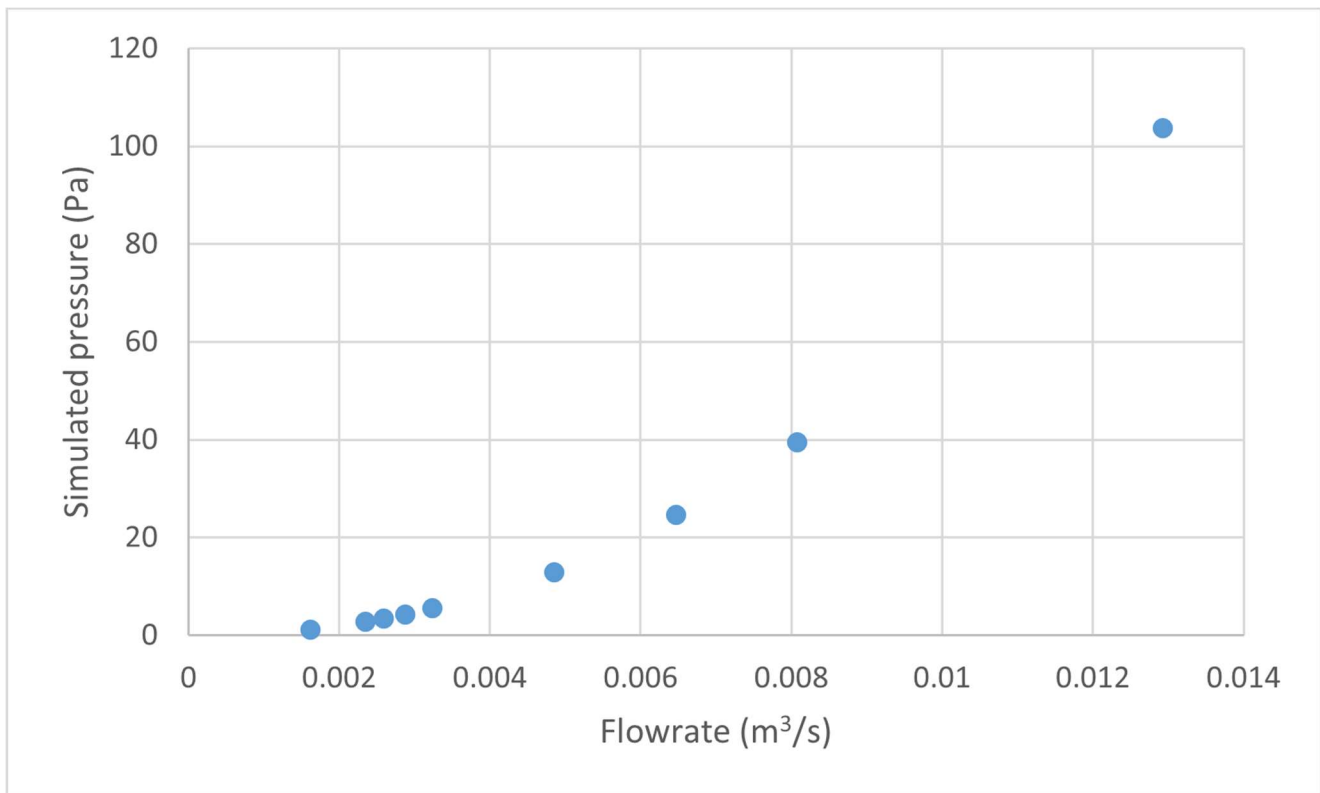
Figure 3.37: Performance curve (pressure vs flowrate), simulated 0.0401m diameter, transformed to 250 rpm setpoint
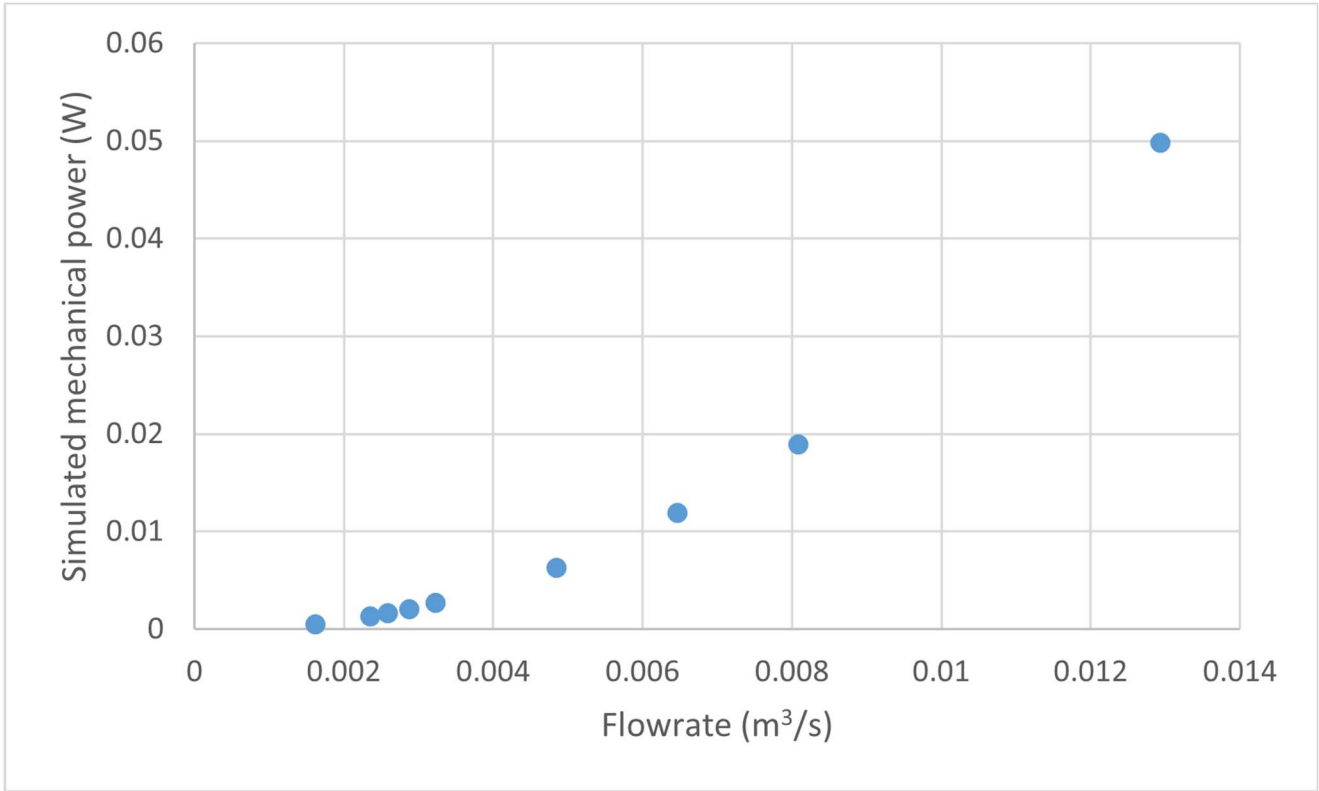
Figure 3.38: Performance curve (mechanical power vs flowrate), simulated 0.0401m diameter, transformed to 250 rpm setpoint
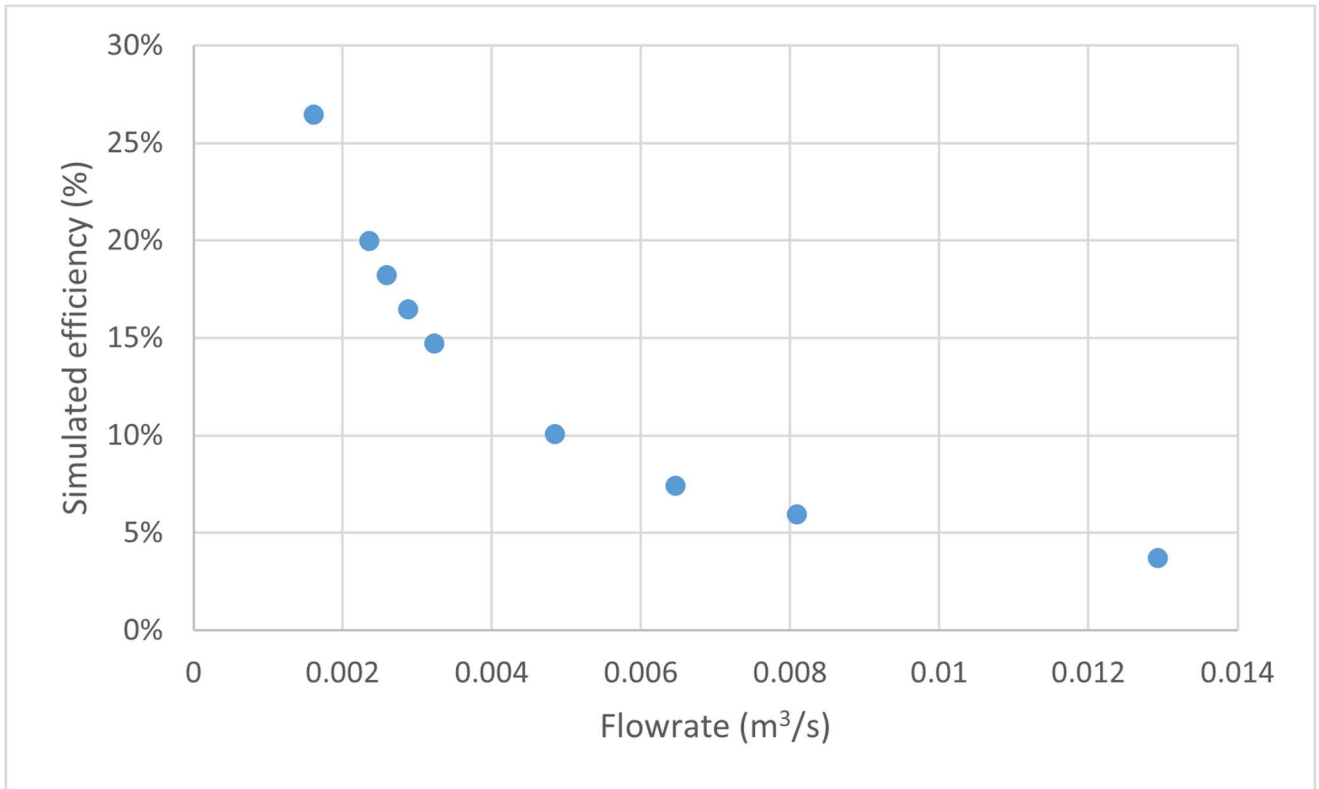
Figure 3.39: Performance curve (efficiency vs flowrate), simulated 0.0401m diameter, transformed to 250 rpm setpoint

4   Design, specifications, and assembly of test apparatus

This section outlines the design and commissioning of the physical test setup. Specifications of selected components are tabulated herein, as well as the limiting factors which justify their use.

4.1   Objectives of testing

4.1.1   Variables to be determined experimentally

To create a digital twin for the simulated data, equivalent values must be obtained from the physical experiment. As in the simulations, the independent variables will be rotational speed, N, and intake airflow, Q. These must be measurable and adjustable by the technician. Additionally, total pressure drop, ΔP, and generated torque, T, must be measurable outputs.

This data will allow for the creation of performance curves based on the operating efficiencies at arbitrary setpoints.

4.1.2   Torque measurement
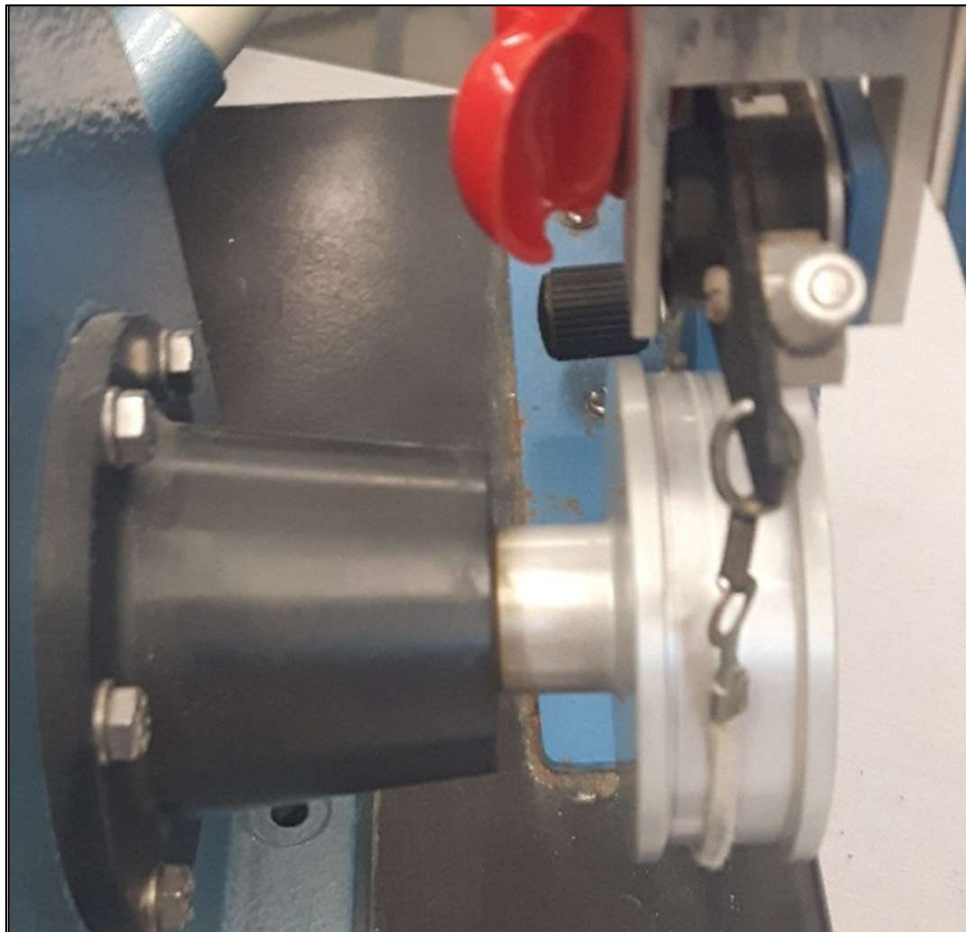
Figure 4.1: Operational Pelton Wheel experimental apparatus with dynamometer attachment

A rudimentary dynamometer was devised for testing. This simple device was based on similar implementations commonly employed in Pelton Wheel experiments (as shown in Figure 4.1). The device consisted of a drum affixed to

the shaft, a strap tightened against the drum, and an adjustable tension arm connected to both ends of the strap (as shown in Figure 4.2). Torque was applied to the shaft via the friction of the strap against the drum.

Figure 4.2: Dynamometer drum with cloth strap

Figure 4.3: Dynamometer scales, attached to tension arm

To control and measure this force, a set of spring balance scales were attached to each end of the strap. The strap could be tensioned by the tension arm (as shown in Figure 4.3). This tension, along with the weight of the strap, constituted the normal force applied between the strap and the drum (F_N, as shown in Figure 4.4). Once the turbine system reached equilibrium, the friction force (F_f) could be calculated as the difference between the two spring forces (F_{S1} and F_{S2}) measured by the scales (as in Engineer's Edge, 2022). These forces were recorded during testing and could be converted into Torque by multiplying the radius of the drum.
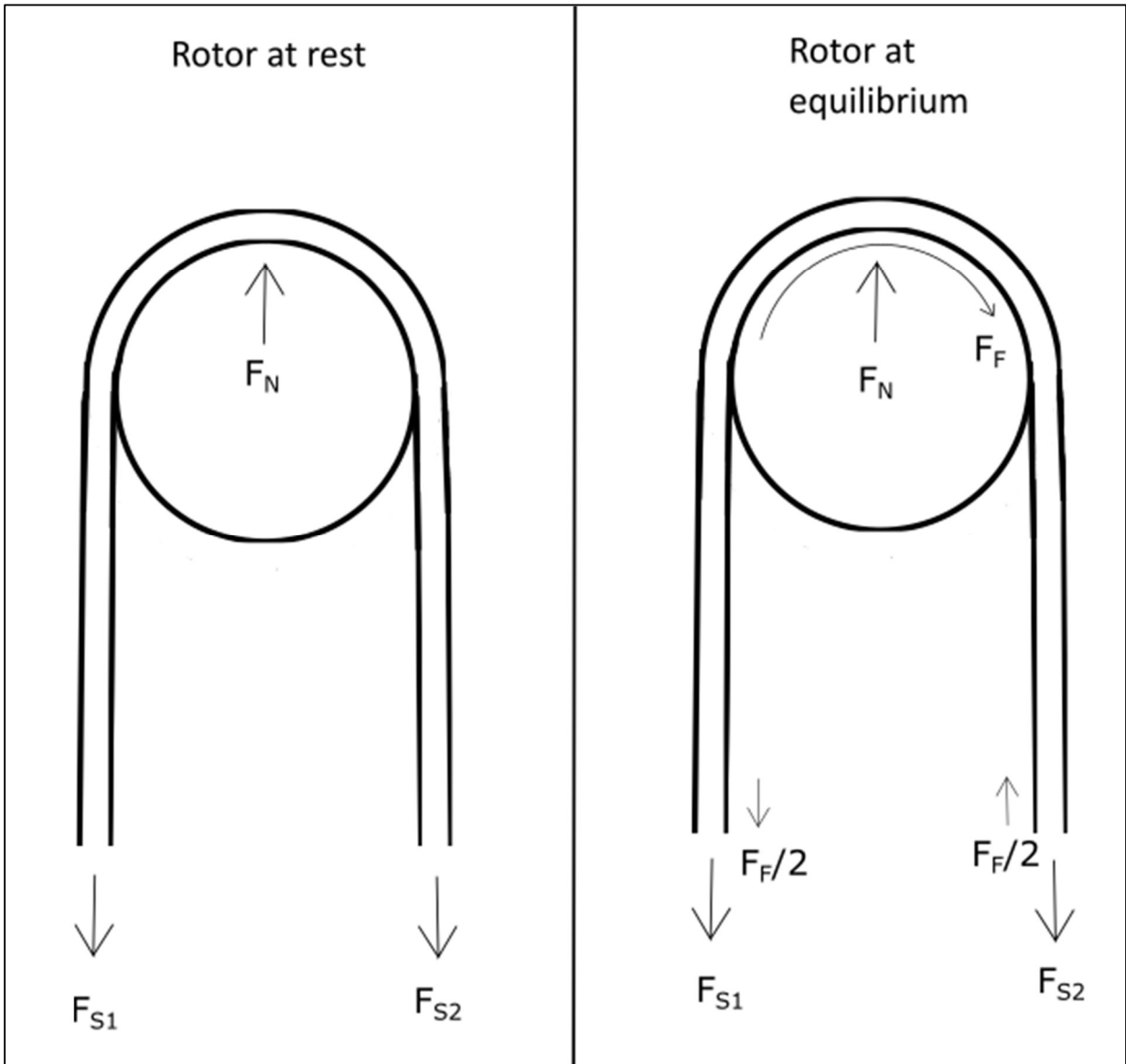
Figure 4.4: Force diagram; measurement of force on friction drum as difference of spring forces

4.2 Factual description of final test setup

4.2.1 Process flow diagram

To visually depict the interactions of all relevant instrumentation in the experimental setup, a process flow diagram has been prepared (see Figure 4.5, legend follows in Table 4.1).
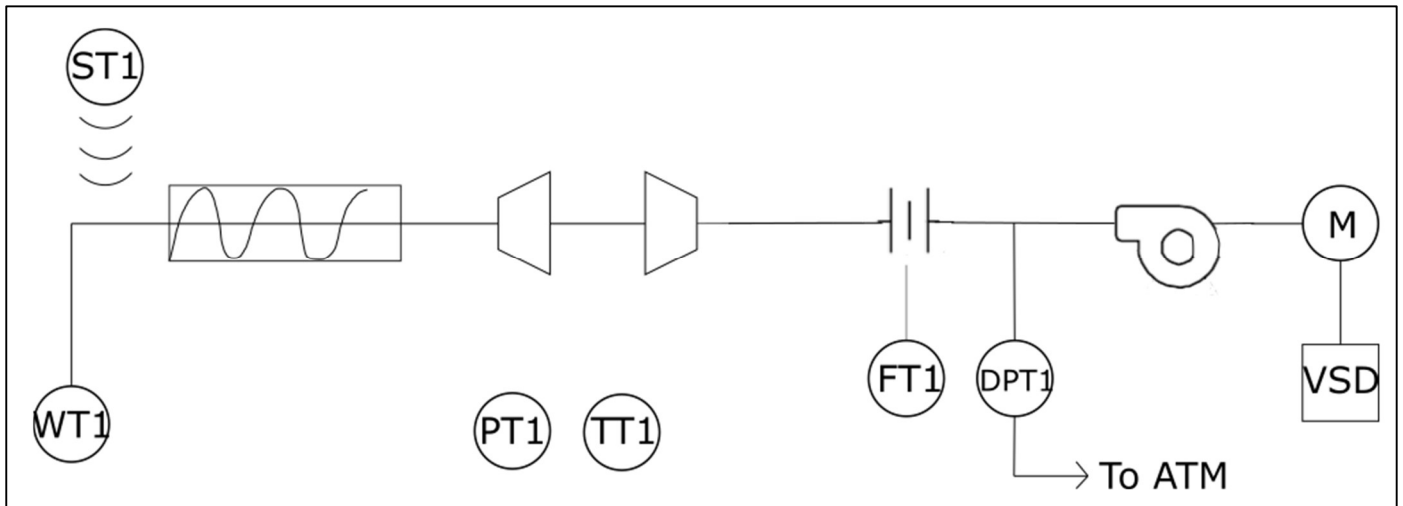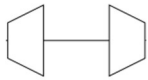
Figure 4.5: Process flow diagram for experimental setup

Table 4.1: Legend (for Figure 4.5: Process flow diagram for experimental setup)

Symbol	Function	Instrument(s)
VSD	Voltage source	-
M	Motor	Shunt motor
(centrifugal fan symbol)	Centrifugal fan	-
DPT1	Differential pressure	Digital manometer
(orifice meter symbol)	Orifice meter	-
FT1	Flowrate	Orifice meter, Digital manometer
(flow conditioning symbol)	Flow conditioning	-
(ducted turbine symbol)	Ducted turbine	-
TT1	Temperature	Digital hygrometer
PT1	Pressure	Pressure standard
ST1	Rotational velocity	Digital tachometer
WT1	Force	2x Digital scale

4.2.2   Anemometer calibration rig with orifice meter and flow conditioner
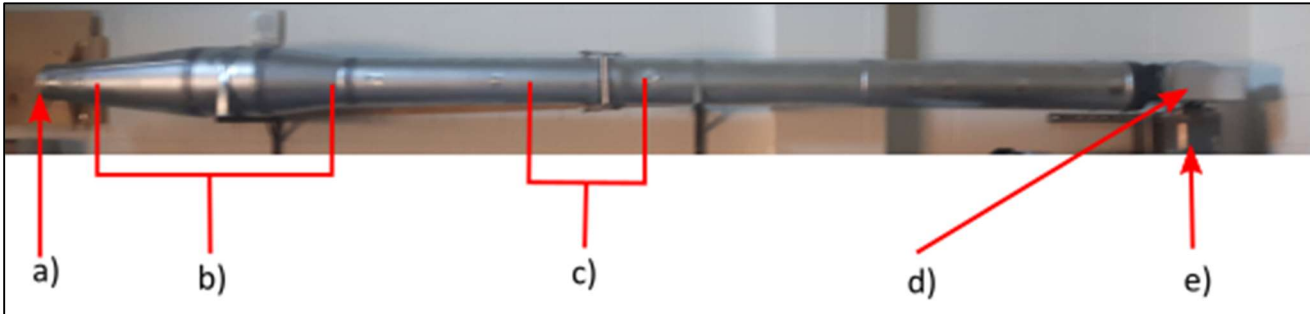
Figure 4.6: Labeled diagram of anemometer calibration rig

a) airflow outlet, b) flow conditioning section, c) built-in orifice meter with replaceable orifice plates (of variable diameter),

d) centrifugal air pump, e) shunt motor

The air supplied to the turbine prototype under test was provided by a duct system that is specially designed to calibrate anemometers (Figure 4.6). Two important features of the duct system are the flow conditioning section and the orifice meter.

The flow conditioning section includes a diffuser and a nozzle. The straight section in the middle contains a specialized honeycomb structure (see Figure 4.7) that eliminates vorticity in the flow. By eliminating the vorticity of the flow, then collecting the flow with the nozzle section, the resulting flow at the outlet is uniform and steady. As a source of conditioned airflow, this calibration rig was ideal for physical experimentation.

The built-in orifice meter was used to measure flowrate through the pipe. During the experimental procedure, ambient Temperature and Pressure were taken before each set of tests. For each test, orifice pressure and total pressure drop were recorded. These pressures varied somewhat, so an average was estimated within a range of variance. That error was also recorded.

The mensuration principles and procedures to produce flow rate observations from differential pressure observations across the orifice are well established and are presented in section 2.7. In between each set of tests, the pressure sensor was also checked for zero drift. While the blower was off, the orifice pressure was expected to read 0.0 Pa. Whenever it was observed to be consistently above or below that value, the technician would reset the zero using the orifice pressure as a baseline. Removable orifice plates (of variable orifice diameter) allowed for appropriate resistance at different flowrates, as needed, to maintain accuracy over a wide range of flow rates.
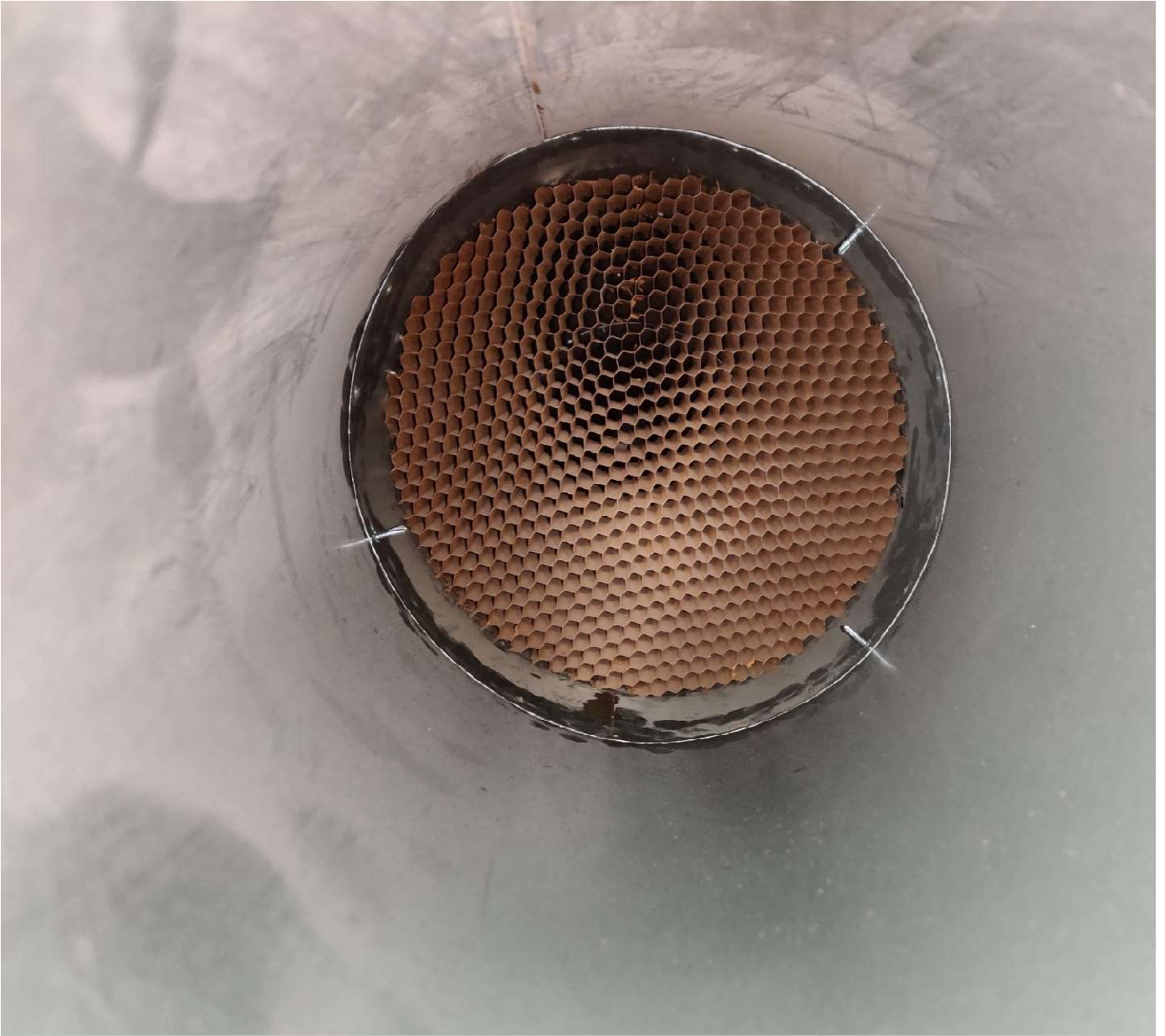
Figure 4.7: Photograph of flow conditioning honeycomb structure (courtesy of Stephen Young)

4.2.3 Instrument specifications

Table 4.2: Table of specifications for instrument used in experimental data collection

Instrument	Model	Range	Precision	Accuracy
Shunt motor	-	210V DC, 3000 RPM	-	-
Digital manometer	TSI 5825	±3725 Pa	0.1 Pa	±1% read, ±1Pa
Orifice meter	-	-	-	-
Digital hygrometer	Dwyer Series 485	-40 ^{o}C - 80 ^{o}C	0.1 ^{o}C	±0.3^{o}C at 25°C
Pressure standard	Paroscientific Digiquartz 745-23A	0-23 psia	0.01 Pa	±0.008% FS
Digital tachometer	Reed AT-6	2-99999 RPM	0.1-1 RPM	±0.05% read
Digital scale	South Bend Digital Hanging Fishing Scale	0-50kg	0.02kg	±0.01kg
Hotwire anemometer	TSI9535	0-30 m/s	0.001 m/s	±3% read, ±0.015 m/s

4.2.4 Drawings of components and assemblies

This section collects the diagrams for any manufactured pieces for which the naming or geometry may not be evident. Any dimensions that cannot be determined from the diagram were chosen arbitrarily and are not relevant to the function of the test rig.
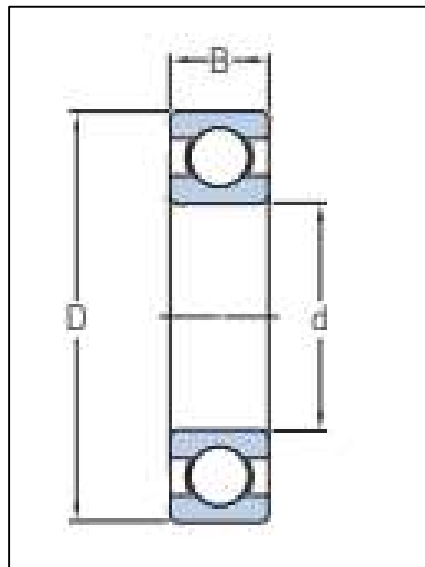
Figure 4.8: Dimensions of SKF 6201 bearing, as published by SKF Group, 2018
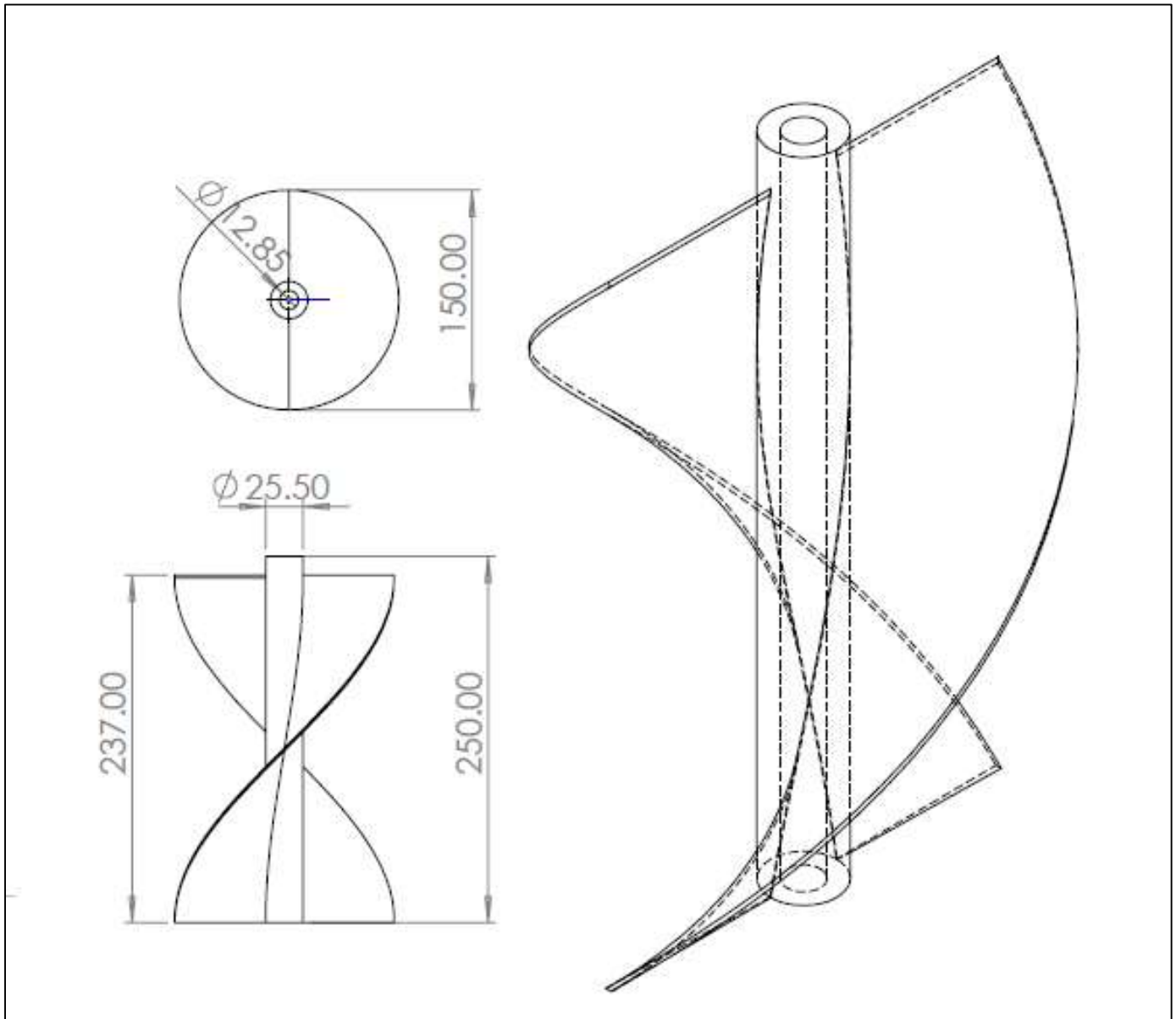
Figure 4.9: Half of the 2 blades turbine rotor, 3D printed twice for assembly
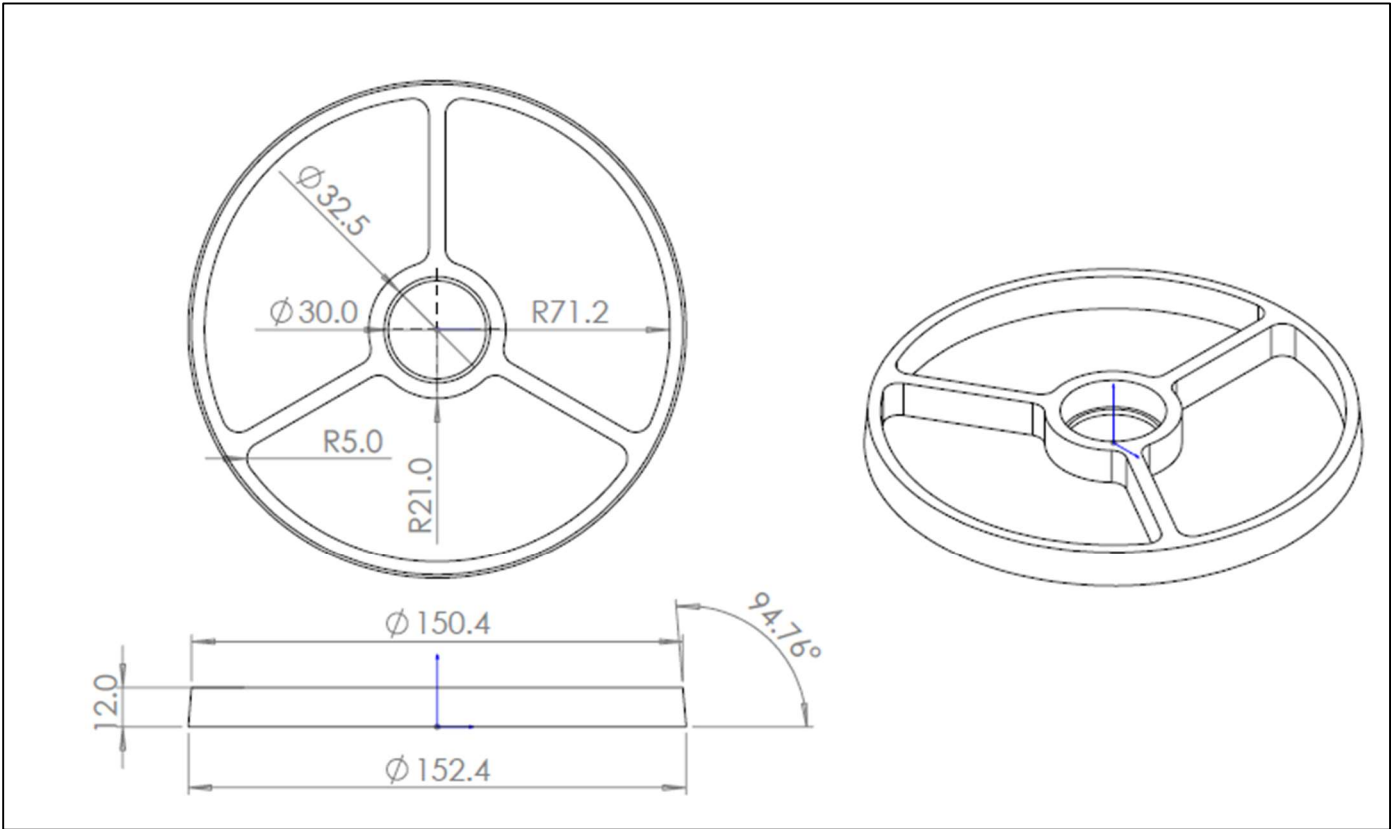
Figure 4.10: Bearing mount design, dimensioned in millimetres
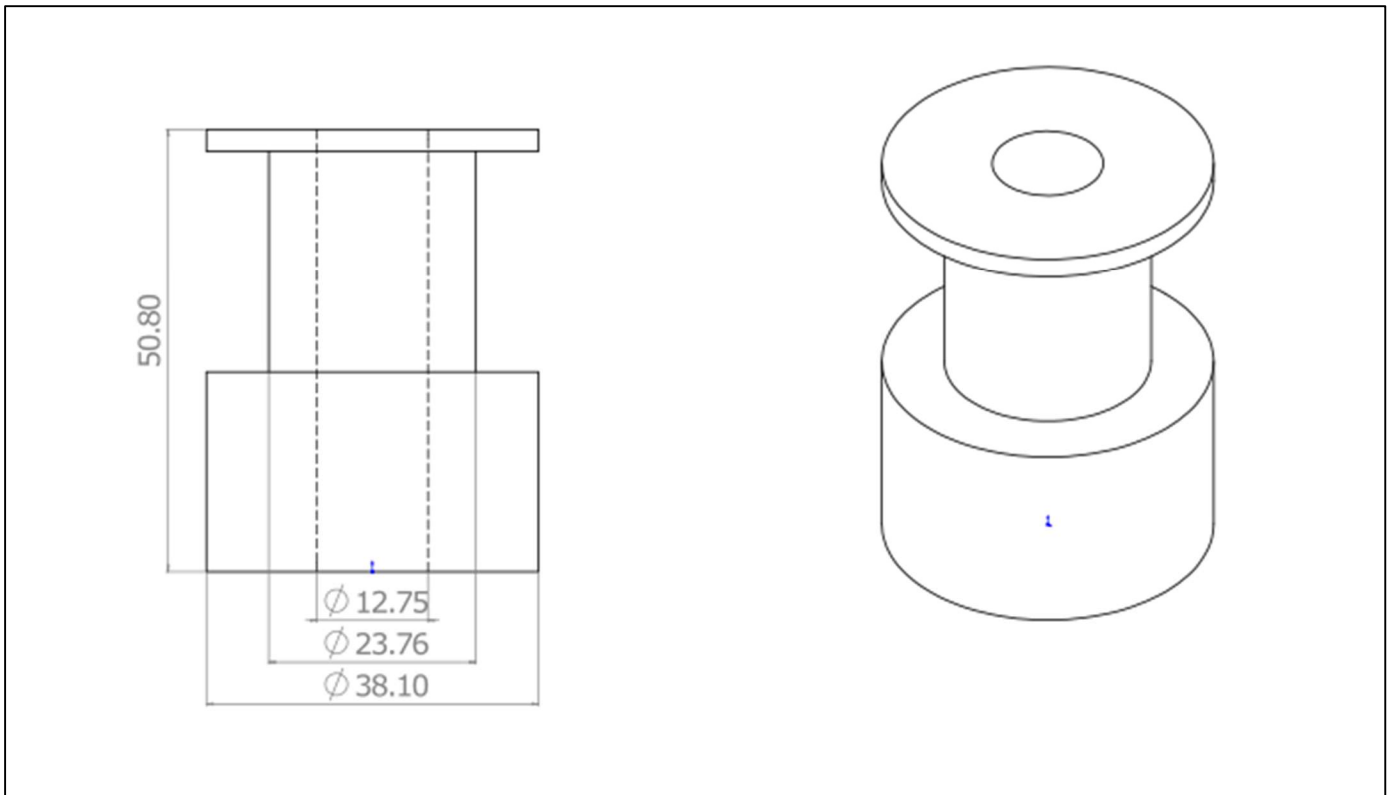
Figure 4.11: Friction drum design, dimensioned in millimetres

4.2.5   Turbine apparatus
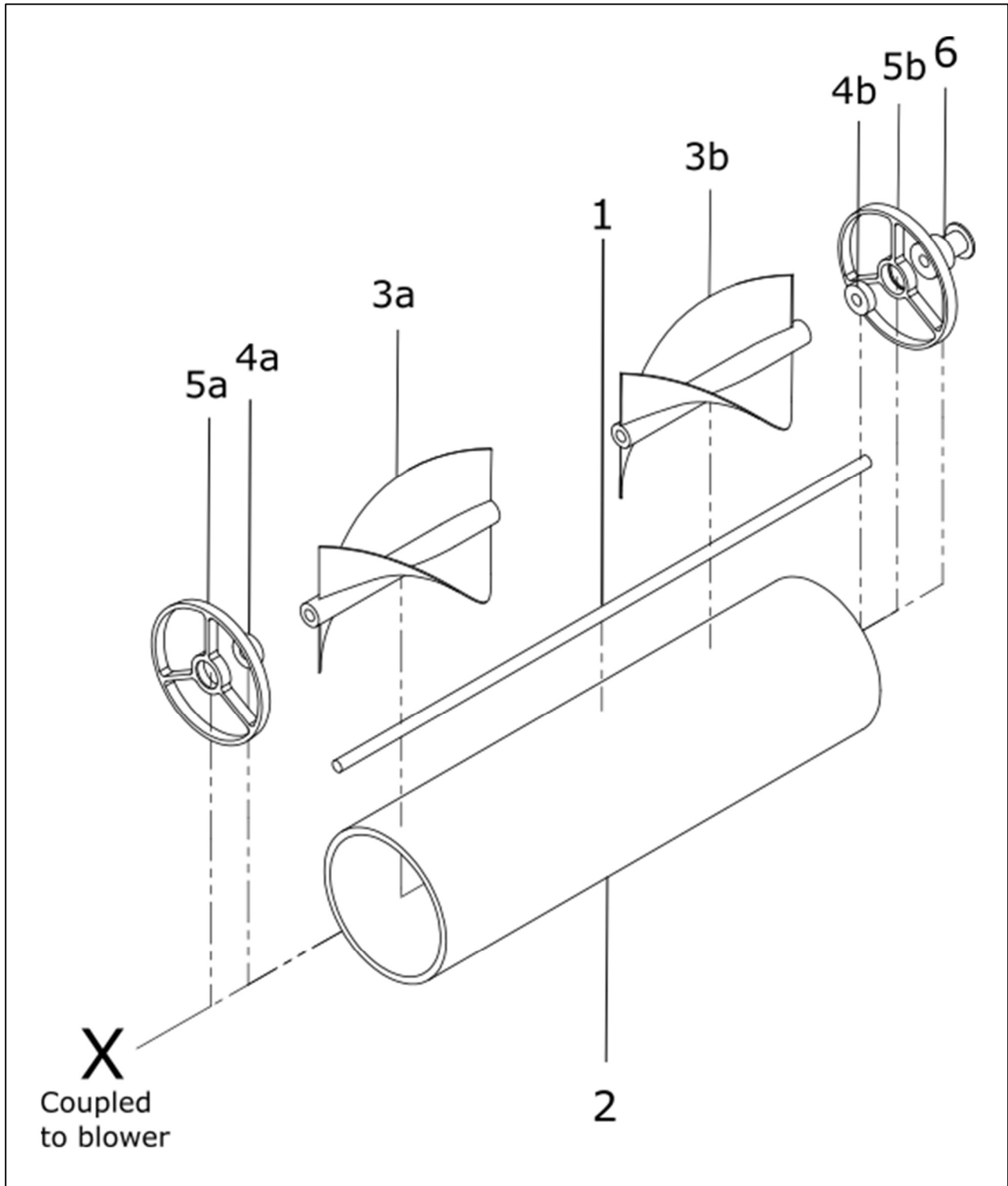
Figure 4.12: Labeled assembly diagram of experimental setup (exploded view)

Figure 4.12 depicts the assembly of the ducted turbine apparatus for the physical experimental setup. The parts are labeled as follows:

1. Shaft
   - ½" diameter 1081 low-carbon steel bar stock; 73.2 cm length
2. Pipe (Duct)
   - 6" schedule-40 PVC pipe; 60 cm length, 0.0015mm absolute roughness (rated)
3. Rotor, or blade
   - 3D-printed PLA plastic; dimensions outlined in Figure 4.9
4. Bearing
   - Two SKF 6201 Explorer bearings; as labelled in Figure 4.8, d= 0.472", D= 1.260", B=0.394"; rated for up to 32000 rpm
5. Bearing mount
   - Two pieces 3D-printed in PLA plastic; dimensioned in Figure 4.10
6. Friction drum
   - HDPE plastic, turned on a lathe; dimensioned in Figure 4.11
X   Pipe coupling (not pictured)
   - Fernco rubber pipe coupling; 6" ID, with stainless steel band clamps on either end

For the sake of brevity, "blower" refers to the anemometer calibration rig described in section 4.2.2, and includes a variable speed centrifugal fan, ducting, a flow conditioner, and an orifice meter

4.2.6   Dynamometer tension arm arrangement
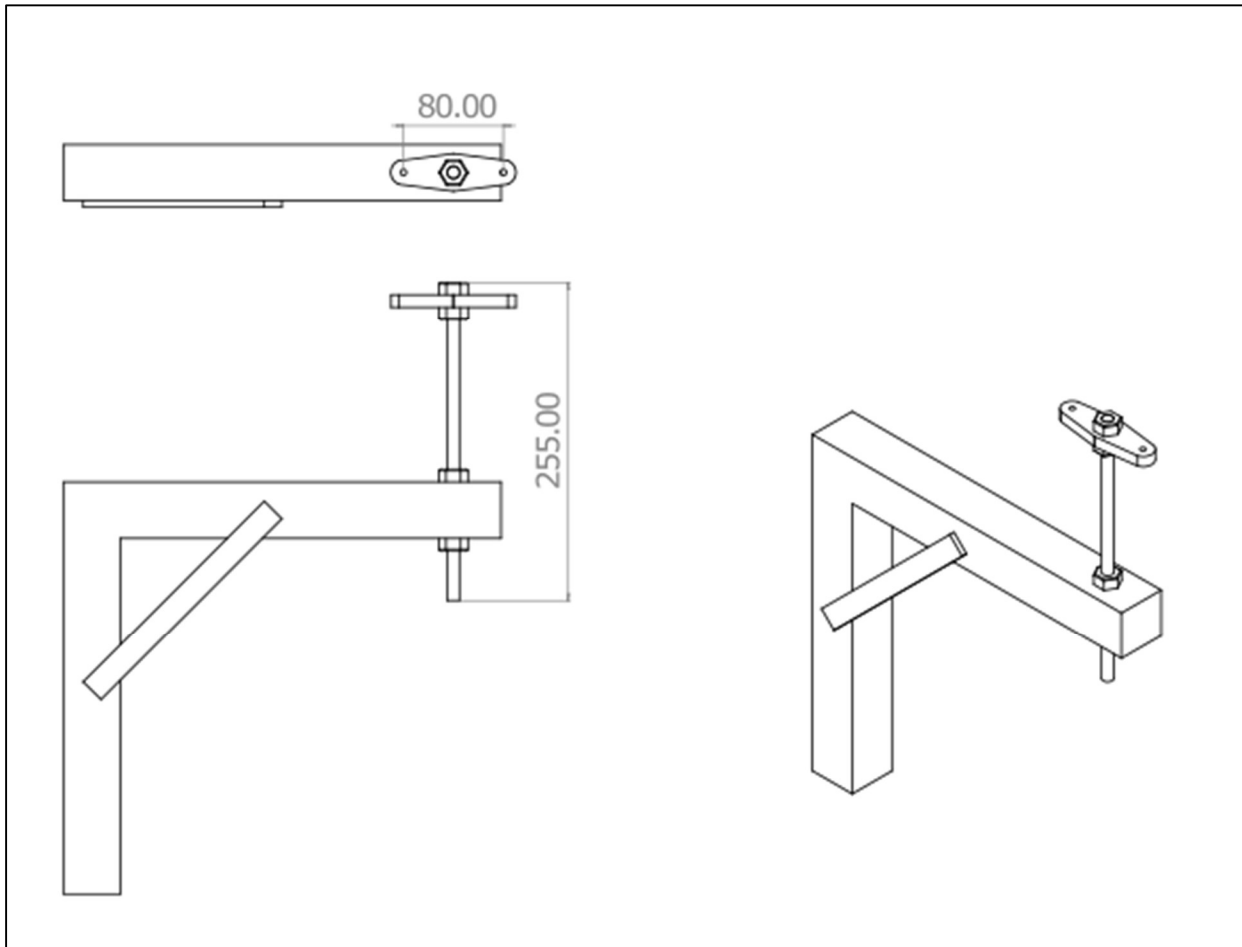
Figure 4.13: Tension arm design, dimensioned on millimetres

Figure 4.13 depicts the assembly of the dynamometer tension arm used in the physical experimental setup. The specifications for the manufactured parts are as follows:

Tension arm

- o   Steel L-shaped arm, mounted to wall; threaded rod through horizontal bar, nuts on either side can be tightened/loosened to adjust height; scales hook into rectangular plate secured at top of threaded rod; see Figure 4.13, as compared to Figure 4.3

Scales (not pictured)

- o   Two digital scales, tied together at the handles by a long cloth; see Table 4.2 for specifications

Tension strap (not pictured)

- o   Cotton cloth strip; approximately 8' in length, tied to scales where the strip will be taut at the required height (see section 4.2.7), excess length hangs; approximately ½" in width, when folded in half to ensure a uniform friction surface

4.2.7 Alignment of the turbine rotor and the dynamometer tension arm
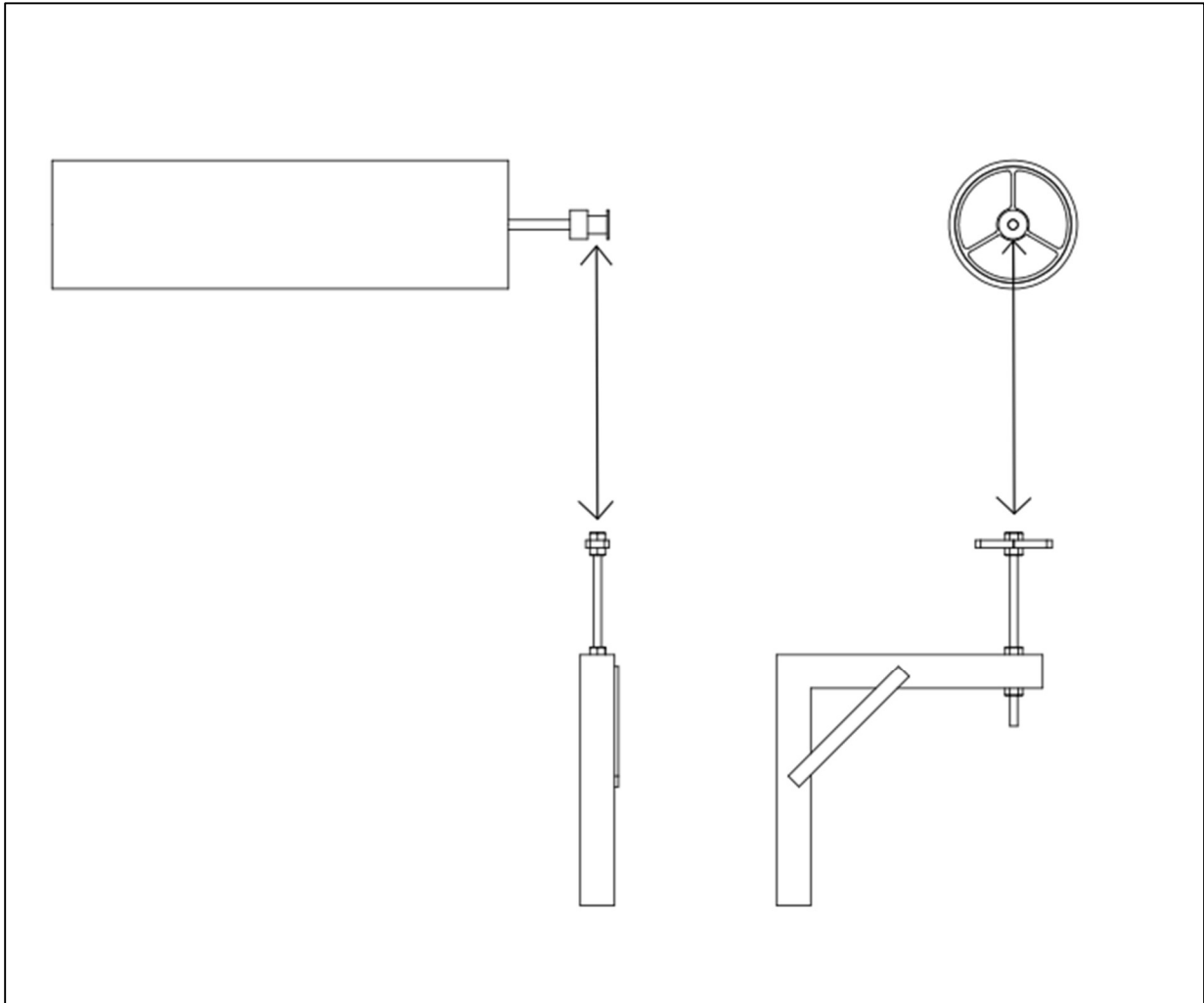
Figure 4.14: Depiction of assembly alignment

The pipe was affixed to the blower using a rubber pipe coupling. As shown in Figure 4.14, the threaded rod should be aligned vertically with the center of the friction drum. Due to flexible brackets holding blower outlet, the tolerance for the alignment of the tension arm is within 2" of the friction drum.

As mentioned in section 4.2.6, the cloth strap should be attached to the scales when taut. This position should represent a minimum vertical displacement from the friction drum. Leaving room to loosen the threaded rod and remove the strap, this minimum displacement is chosen based on the angle of the cloth strap (from vertical).

In Figure 4.14, note that the friction drum was grooved, to ensure that the strap would not be pushed out of place by the airflow. While the friction drum was vertically aligned with the tension arm, sharing a centerline with the rectangular plate (that served to anchor the cloth strap and digital scales), the inner groove diameter of the drum was not vertically aligned with the edges of the rectangular plate. As such, the two halves of the strap would form equal and opposite angles with respect to a vertical axis, which could be calculated trigonometrically. Knowing the thickness of the drum and the distance between the two hooks attached to the tension arm's rectangular plate, the

angle was calculated to be less than 2⁰ for a vertical displacement of 3'. Thus, 3' was chosen as a standard starting displacement for experiments.

4.3   Deflection analysis to validate 3D blade dimensions versus pipe diameter

A rotating shaft with a loaded end presented a danger of deflection. Should the blade have touched the inner wall of the duct, added friction would have been caused as the two surfaces scraped together. To prevent this, some clearance was provided between the turbine blade and the inner wall of the duct. The current blade design was dimensioned in Metric units. Since the PVC pipe (which was to be used as the duct for the turbine) was expected to be 6", the blade was scaled to 15cm and the difference between the two diameters would be the proposed clearance. (In other words, the maximum allowable clearance was 0.12cm.)

Deflection was estimated by treating the shaft as a stationary beam (as shown in Figure 4.15) and applying the eccentric load as a force on the beam. This allowed for the use of the standard bending equations (as demonstrated by StructX, 2014).
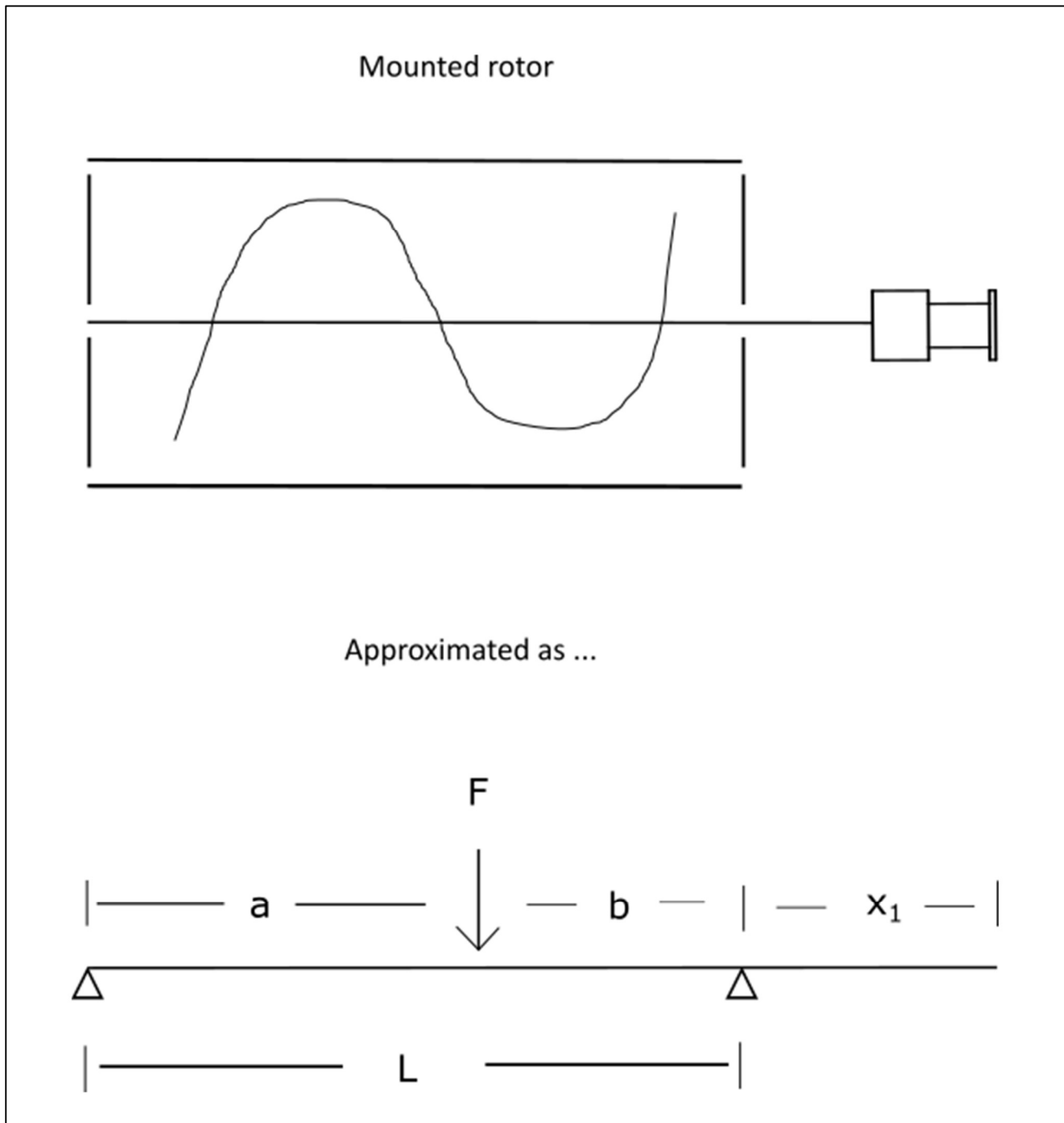
Figure 4.15: Mounted rotor, approximated as overhanging beam

The friction force between the strap and drum required a normal force to be applied to the hanging end of the beam. This was applied as a static force using the following equation:

$$d_{max} = Fx_1{}^2 \frac{L + x_1}{3EI} \tag{4.1}$$

where d_{max} was the maximum deflection in the beam, F was the applied force, x_1 was the hanging length, L was the length of beam between supports, E was the Young's modulus of the beam, and I was the moment of inertia of the beam.

The deflection at the hanging end was also calculated using the following equation:

$$d_{x_1} = 0.06415 F x_1 \frac{L^2}{EI}$$

(4.2)

where d_{x_1} was the deflection at point x_1.

To determine the maximum required normal force, the modified simulation data was used. The projected Torque was converted into a force using the proposed drum diameter. Then that friction force was converted into a normal force using an accepted coefficient of kinetic friction (for plastic on rubber) of 0.2 (provided by The Engineering ToolBox, 2001).

To determine an equivalent force for the eccentric load, the following equation was used:

$$F_e = m_e r_e \omega^2$$

(4.3)

where F_e represented the approximate eccentric load, m_e was the eccentric mass on the rotating body, r_e was the radial position of the eccentric load when represented as a point, and ω was the rotational velocity of the body.
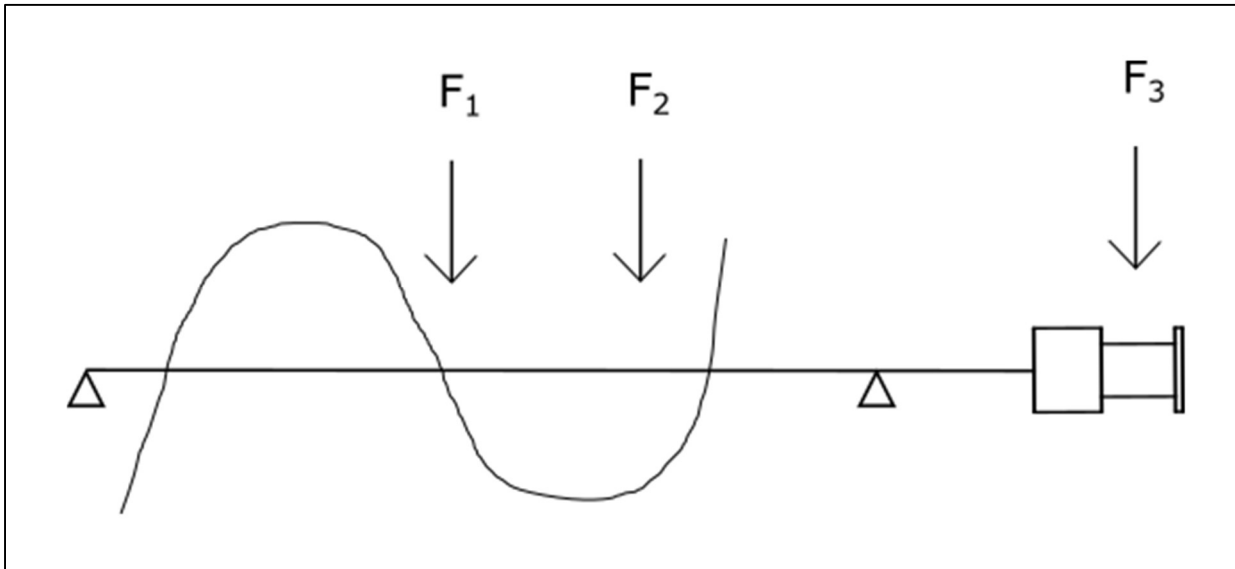
Figure 4.16: Eccentric loads and end load, applied to overhanging beam approximation

This force was applied at the center of mass of whichever body was assumed to provide this eccentric loading (as shown in Figure 4.16). Three such bodies were identified: the rotor (F_1), the shaft (F_2), and the friction drum (F_3). The following equation was used to apply a load at an arbitrary point a:

$$d_{max} = \frac{Fab(a+2b)\sqrt{3a(a+2b)}}{27EIL}$$

(4.4)

where a was the x-position of the eccentric load as measured from the first support, b was the x-position of the eccentric load as measured from the second (hanging end) support.

$$d_{x_1} = \frac{Fabx_1(L+a)}{6EIL}$$

(4.5)

By combining equation (4.3) with equations (4.4) and (4.5), the following equations were obtained,

98

$$d_{max} = \frac{m_e r_e \omega^2 ab(a + 2b)\sqrt{3a(a + 2b)}}{27EIL} \tag{4.6}$$

$$d_{x_1} = \frac{m_e r_e \omega^2 abx_1(L + a)}{6EIL} \tag{4.7}$$

By applying these loads at the appropriate points and treating the bearings as fixed points, the following estimates were calculated.

Table 4.3: Assumed variables used to calculate expected deflection in shaft

E	r_e	r_s	L	x_1	a	b	ω	F	m_s	m_e
GPa	in	in	cm	cm	cm	cm	rad/s	kg	g	g
205	0.375	0.25	60	60	30	30	100	10	1196	239.3
Pa	m	m	m	m	m	m	rad/s	N	kg	kg
2.05E+11	9.525E-3	6.35E-3	0.60	0.60	0.30	0.30	100	98.1	1.196	0.2393

Table 4.4: Expected deflection in shaft

	Eccentric load	End load	Total	Observation
	m	m	cm	--
d_{max}	2.07E-08	2.86E-06	2.88E-04	<<0.12cm
d_{x_1}	6.22E-08	2.75E-07	3.37E-05	<<0.12cm

An exaggerated projection was created, using a point load at the end instead of the smaller eccentric load.

Table 4.5: Exaggerated variables, used to calculate safe tolerance of deflection in shaft

E	r_e	r_s	L	$x_1 + L$	x_1	ω	F	m_s	m_e/m_s
GPa	in	in	cm	ft	--	rad/s	kg	g	--
97	3	0.25	60	6	--	200	100	1000	--
Pa	m	m	m	m	m	rad/s	N	kg	--
9.7E+10	7.62E-2	6.35E-3	0.60	1.8288	1.2288	200	981	1	1

Table 4.6: Legend of exaggerated variables

Variable	Exaggeration
E	Modulus of Copper, low-grade steel bar stock is 205 Gpa
r_e	Maximum eccentricity of blade
r	Minimum radius (ie. no epoxy or blade shaft)
$x_1 + L$	Uncut bar stock (ie. full 6')
L	No exaggeration
x_1	Uncut bar, minus non-exaggerated L
ω	Double expected rotational speed
F	Maximum load on scale
m_s	Reduced mass of shaft
m_e/m_s	Eccentric mass is equal to mass of 6' bar stock

Table 4.7: Exaggerated deflection in shaft

	Eccentric load	End load	Total	Observation
	m	m	cm	--
d_{max}	7.85E-04	4.62E-04	1.25E-01	~0.12cm
d_{x_1}	2.21E-05	1.42E-05	3.63E-03	<<0.12cm

Since the deflection was well within the proposed clearance, and only barely more with greatly exaggerated conditions, it was not expected that the blade would touch the inner wall of the pipe. After construction was completed and troubleshooting was performed upon the system, the final values (see section 4.2.5) could be updated to estimate reasonable limits for force and rotational speed.

Table 4.8: Measured variables, used to calculate realistic expected deflection in shaft

E	r_e	r_s	L	x_1	a_b	b_b	a_s, b_s	ω	F	m_s	m_e
GPa	in	in	cm	cm	cm	cm	cm	rad/s	kg	g	g
205	0.375	0.25	60	13.2	36.6	23.4	30	2000	100	729	146
Pa	m	m	m	m	m	m	m	rad/s	N	kg	kg
2.05E+11	9.525E-3	6.35E-3	0.60	0.132	0.366	0.234	0.30	209	981	0.729	0.146

Table 4.9: Realistic expected deflection in shaft

	Eccentric bar	Eccentric rotor	End load	Total	Observation
	m	m	m	cm	--
d_{max}	8.53E-08	9.10E-08	1.38E-06	1.56E-04	<<0.12cm
d_{x_1}	6.13E-08	6.00E-08	9.91E-07	1.11E-04	<<0.12cm

Thus, it was assumed that there should be little danger of hitting the sides of the pipe while working within the limits of the planned tests. Barring any alignment issues, or degradation of the steel shaft from overuse, it was believed that the current setup should be workable for the purposes of preliminary testing.

4.4 Justification of design aspects and procedures

4.4.1 Selection of bearings and pipe

The blade was scaled to fit the diameter of the outlet of the blower. Therefore, a PVC pipe with matching diameter was provided to be used as the duct for the turbine. The pipe was cut to cover the full length of the blade at the specified scale, rounded up to the nearest 10cm to allow for bearings to be mounted within the pipe. Based on these considerations, a 6" diameter schedule 40 PVC pipe was cut to a length of 60 cm to be used as the duct of the experimental turbine.

The SKF 6201 Explorer bearings were chosen based on the diameter of the shaft and validated based on the maximum rotating speed of the system. At the desired size (½" diameter shaft), the maximum speed tolerance of 10,000 rpm (SKF Group, 2018) was considerably higher than the simulated setpoints, which ranged to roughly 1000 rpm (100 rad/s). Based on this consideration, the bearing was deemed appropriate for experimental use.

Note also that the bearings have a basic static load rating of 3.1 kN, and a fatigue load limit of 0.132 kN. From Simscale, the largest thrust force applied to the blade surfaces (under the 15m/s flow) was 0.18 N. The similarity laws could be used to give an estimate of the thrust under high flows for the physical experiment. This would correspond with an expected force on the order of 20 N. Since this estimate was well below not only the static load rating, but also the fatigue load limit, thrust was deemed to be of little relevance.

4.4.2 Manufacture and assembly of helical blade

Using the existing CAD model from the simulations, a model was scaled up to the size of the blower (see section 4.3). Due to size limitations associated with the available 3D printer, the model was printed in two parts (as shown in Figure 4.9). Aside from cutting the model in half, a cylindrical cut was made through the shaft, to mate with a steel shaft (bar stock).

The two bearings were positioned based on the length of the pipe, with one at the extreme end of the shaft, and the other placed at 60 cm from the first (the length of the duct).

Figure 4.17: Blade, bearings and friction drum assembled on shaft
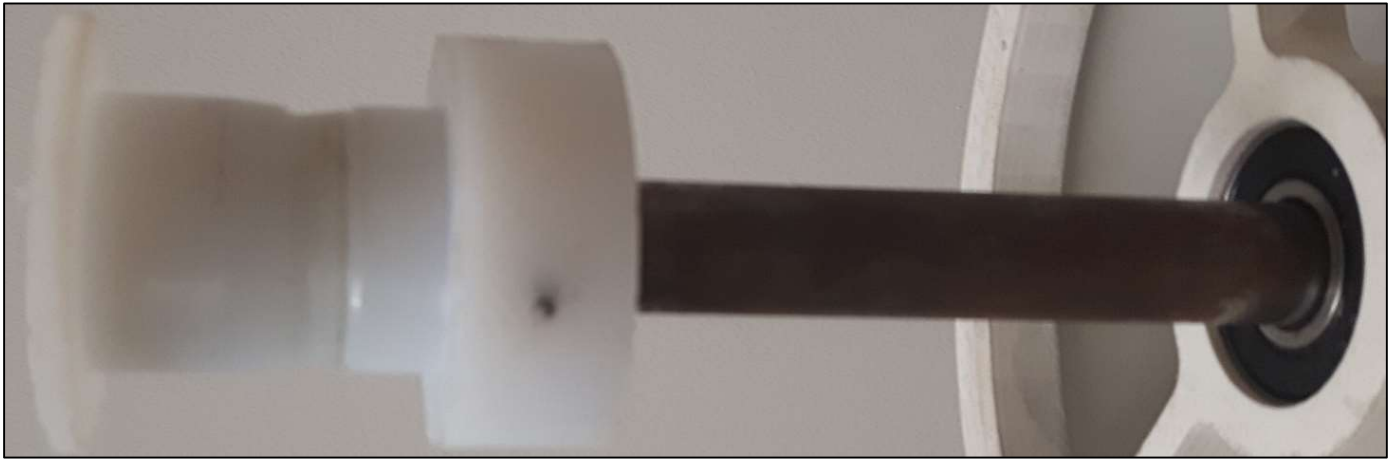
Figure 4.18: Pinned friction drum for dynamometer

The friction drum was affixed to the opposite end of the shaft to that where the initial bearing was mounted. To avoid slip, the drum was pinned in place (as shown in Figure 4.18). All other parts were friction fit.

Finally, any cracks or voids in the blade (from hammering or printing, respectively) were coated with epoxy (as shown in Figure 4.19). The same was done for the discontinuity where the two blade halves met. This was meant to provide a more continuous surface for testing of the blade.

Figure 4.19: Two half blades sealed together with epoxy

4.4.3   Manufacture of pipe mounts

A mount (as shown in Figure 4.10) was designed to fit the pipe to the bearings. The outer diameter was fit to the 6" pipe and the inner diameter was fit to the bearing OD.

The outer edges of the mount were chamfered slightly (as shown in Figure 4.20), with the outside end being slightly larger than the expected dimensions of the pipe. This allowed a friction fit, which centered the mount in the pipe.
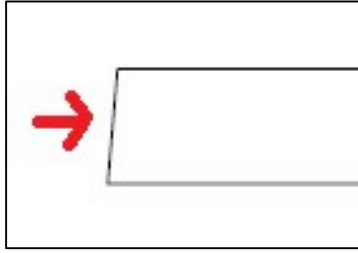
Figure 4.20: Enlarged view of chamfer on bearing mount

The Inner edge included a slight lip at the outside end, meant to resist the force of the wind and prevent slip between the bearing and the mount.
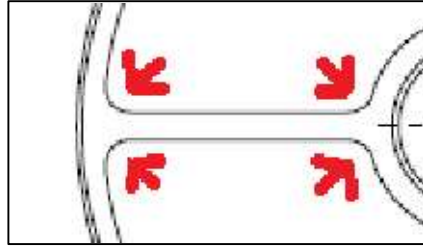
Figure 4.21: Enlarged view of filleted corners on bearing mount

Finally, the struts were spaced at 120 degrees from each other to create symmetrical triangular supports. One support was placed such that it resisted the normal force applied to the drum by the strap. Following the advice of G. Lakanen (Lakanen, personal correspondence, 2021), the corners were filleted (as shown in Figure 4.21) where the struts met the inner and outer rings.

4.5 Determination of the pressure drop across the turbine

4.5.1 Overall scheme

In the following, the symbol ΔP is reserved to denote a pressure *drop* associated with a component present within the experimental apparatus. The symbol P_G is reserved to denote a gauge pressure observation taken with a manometer with the negative port attached to the orifice plate downstream corner tapping, and the positive port of the manometer open to atmosphere (as denoted in Figure 4.23).

The set of observations {1} of the gauge pressure, $P_{G,1}$, at the orifice plate downstream tapping while the turbine under test was operating can be represented:

$$P_{G,1} = \Delta P_{blower} + \Delta P_{mounts} + \Delta P_{bearings} + \Delta P_{duct} + \Delta P_{rotor} \tag{4.8}$$

{1} includes the air flow rates measured corresponding to the $P_{G,1}$ measurements, undertaken over a range of rig Reynolds numbers. The set of observations {2} of the gauge pressure, $P_{G,2}$, at the orifice plate downstream corner tapping without the turbine under test attached at all is given:

$$P_{G,2} = \Delta P_{blower} \tag{4.9}$$

{2} includes the air flow rates measured corresponding to the $P_{G,2}$ measurements, undertaken over a range of rig Reynolds numbers.

$P_{G,2}$ characterizes the behaviour of the calibration rig itself fairly completely, accommodating all the interchanges between static and dynamic pressure that may be expected to occur due to changes in the cross-sectional area of the rig, all the major and minor losses associated with conditioning components, as well as exit loss.

The set of observations, {3}, of the gauge pressure, $P_{G,3}$, at the orifice plate downstream tapping with the turbine duct, containing the bearing mounts installed, but not the bearings themselves, is given:

$$P_{G,3} = \Delta P_{blower} + \Delta P_{mounts} + \Delta P_{duct} \tag{4.10}$$

and, again, {3} includes the corresponding flow rates.

In section 4.2.5, the absolute roughness of the PVC pipe comprising the turbine duct is 0.0015 mm, so that its relative roughness is of order 10^{-5}, and according to the Moody Chart in Figure 2.11, it may be considered smooth over the range of Reynolds numbers that the turbine was tested. This does not mean that the friction factor, f_D, for the duct is zero. The Moody chart for a smooth pipe returns values of f_D between 0.025 and 0.015 for the lower end of the test Reynolds numbers and the high end of the test Reynolds numbers, respectively. Since the simulated roughness is set to exactly 0, its friction factor can be modeled by the smooth pipe equation. By this reasoning, the resistance of the ducts (both simulated and physical) can be assumed to be equivalent. Consequently, for either length of duct:

$$\Delta P_{duct} = f_D \cdot \frac{L}{D} \cdot \rho \frac{v^2}{2} \tag{4.11}$$

The presence, or rather the absence, of the bearings themselves in observations {3} is expanded on in section 4.5.4, and is given:

$$\Delta P_{bearings} = 2.05 \cdot \frac{A_{bearing}}{A_{duct}} \cdot \rho \frac{v_{phys}^2}{2} \tag{4.12}$$

Using (4.10), the pressure drop due to the mounts can be found by using observations {3} and {2} with equation (4.11):

$$\Delta P_{mounts} = P_{G,3} - P_{G,2} - \Delta P_{duct} \tag{4.13}$$

This is done for observations {2} and {3} involving the 6.25" orifice in the rig only, as a set of observations {2} was not taken with the 4" orifice in place. With such observations, (4.13) can be correlated with flowrates Q with an equation of quadratic form with a co-efficient of correlation of 0.999954 and thereafter ΔP_{mounts} can be accurately estimated for the cases when the 4" orifice was installed, direct from the flow rate values. Note however, that the range of flowrates used to characterize the mounts is valid for all intended experimental setpoints except for the 5 m/s setpoint. As a result, this additional step would only be necessary when characterizing a pressure loss for that specific setpoint.

The CFD simulations, with which the experimental results are to be compared, apply virtual instruments for the measurement of the pressure drop just before the rotor and just after the rotor meaning that the virtual

instruments should sense the pressure drops due to the rotor and the duct only; the CFD simulations did not feature the bearing mounts or the bearings themselves. For the experimental results, these pressure drops due to rotor and duct (which correspond to the SL transformed CFD results, ΔP_β) are thus referred to as the pressure drop across the turbine, ΔP_{turb}, $where$:

$$\Delta P_{turb} = \Delta P_{rotor} + \Delta P_{duct} \tag{4.14}$$

Substituting (4.14) into (4.8), the pressure drop across the turbine can then be isolated with observations {1} and {2} and equations (4.12) and (4.13) as follows:

$$P_{G,1} = P_{G,2} + \Delta P_{mounts} + \Delta P_{bearings} + \Delta P_{turb}$$

or, re-arranging:

$$\Delta P_{turb} = P_{G,1} - P_{G,2} - \Delta P_{mounts} - \Delta P_{bearings} \tag{4.15}$$

4.5.2   Estimating pressure drop from blower

Owing to the practical necessity of the bearing mounts and their placement in the duct, pressure tappings were not created to directly measure the pressure drop across the duct. This is another reason why the existing corner pressure tappings at the orifice were used for all pressure measurements.

However, the CFD simulations with which the experimental results would be compared, only accounted for the length of the duct in an unobstructed stream, so pressure losses arising due to the presence of other fixtures and fittings of the calibration rig itself needed to be accounted for. Furthermore, since the duct of the turbine and the outlet of the blower both had the same inner diameter, the reduction method also accounted for the minor losses of the system (which are a function of dynamic pressure), so that the reduced value, ΔP_{phys}, would represent the pressure drop over the enclosed section of the turbine rotor only. This would include the surface roughness of the physical pipe, the bearing mounts, the shaft, and the blade.

At this stage in the reduction, note that:

$$\Delta P_{phys} = P_{G,1} - P_{G,2} \tag{4.16}$$
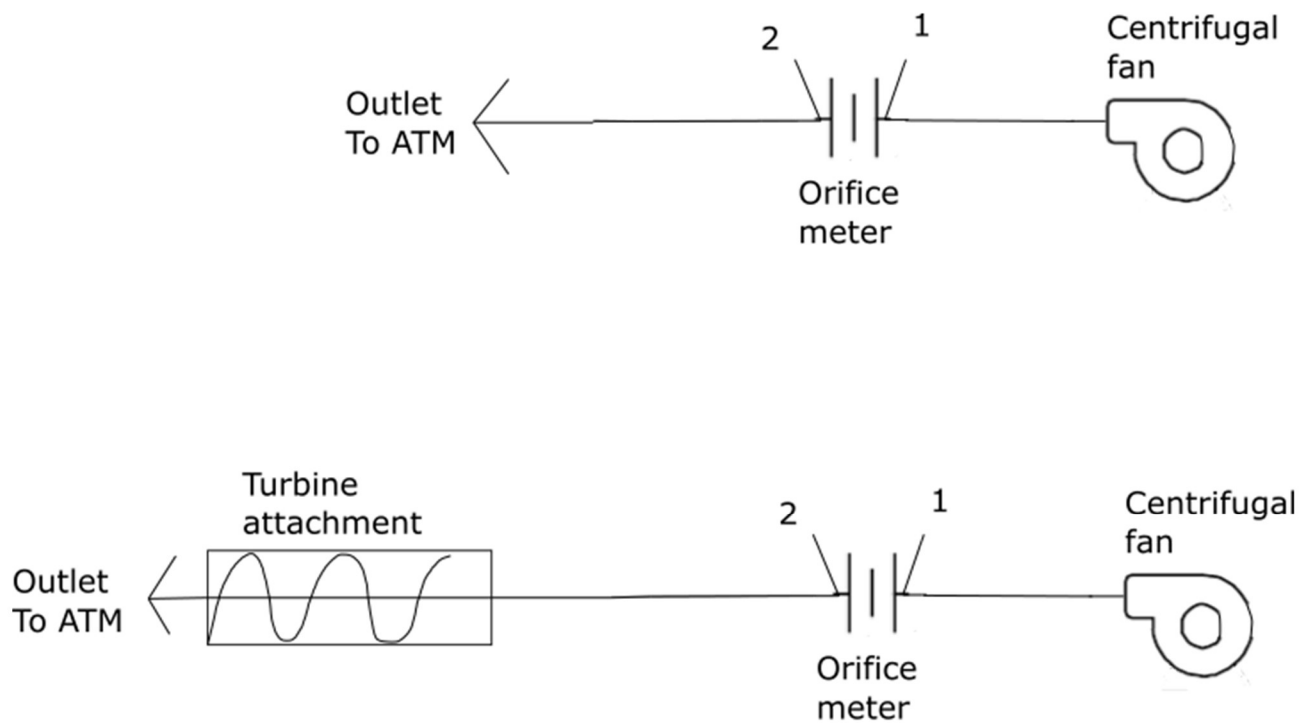
Figure 4.22: System diagram of physical test setup, with and without turbine attachment

The downstream corner tapping (point 2 in Figure 4.22) was used for all gauge pressure readings, with and without the turbine attachment. It was reasoned that, regardless of the nature of any major and minor losses, adoption of a consistent position for the pressure reading would lead to consistent observations, for the same flowrate through the system. In Figure 4.23, the pressure behaviour of the system is depicted with and without the turbine attachment; it being a requirement that the flow rate through the system is identical in each case. As noted in section 2.3, components of a duct system are associated with consistent losses; for the same flow rates through them, their associated pressure drops will be the same with and without the turbine assembly mounted.

In Figure 4.22 and Figure 4.23 the flow conditioner and associated components in the rig have been omitted from the diagram for clarity but are deemed present. The orifice meter is approximated from known orifice pressure behaviour (see Figure 4.24). The turbine assembly pressure behaviour is also approximated, knowing that the gauge static pressure will fall from a characteristic value at inlet to zero gauge (atmospheric) at the turbine assembly exit.
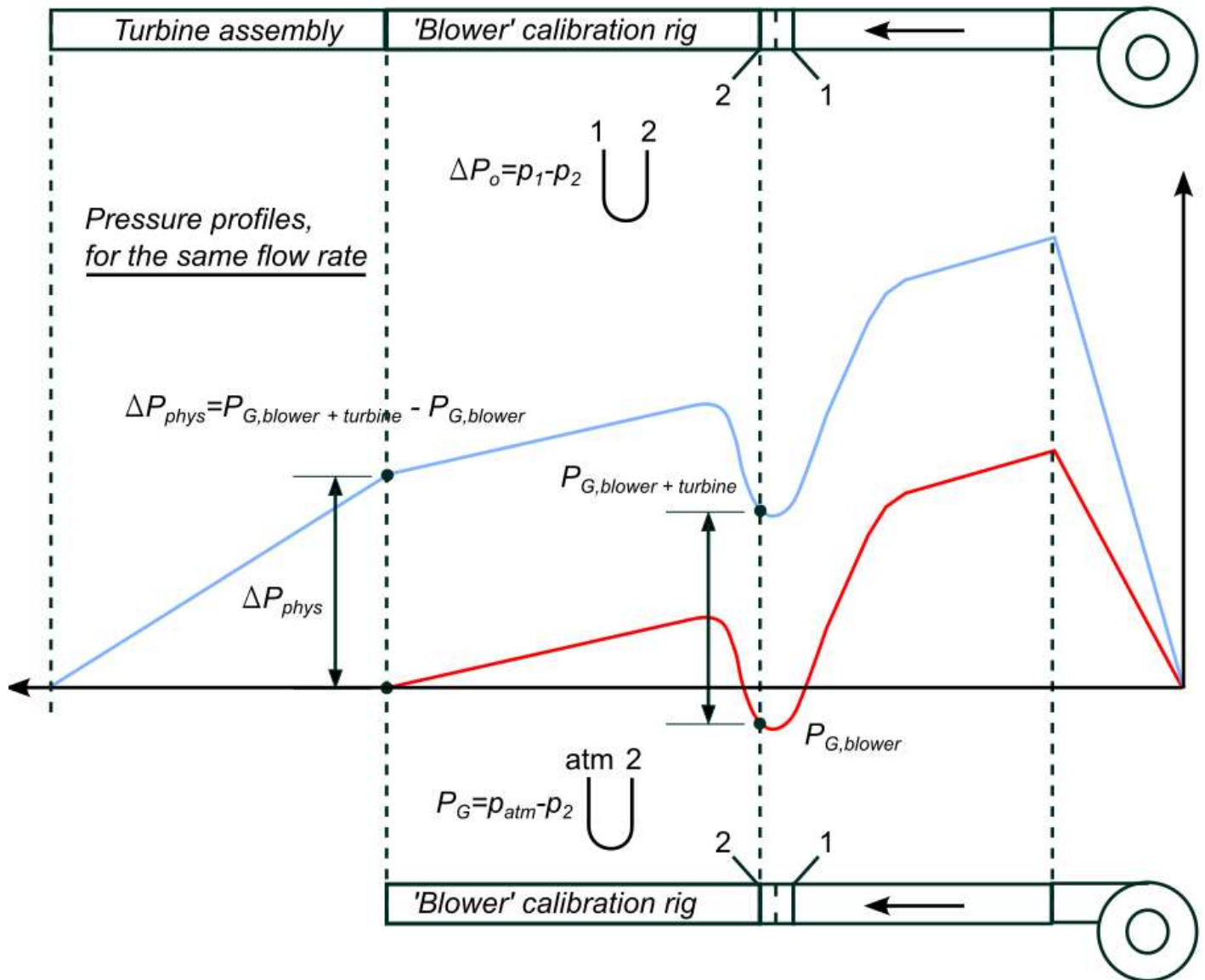
Figure 4.23: Diagram of pressure profile for the blower system (ala Figure 2.9); with and without turbine attachment

The pressure profiles in Figure 4.23 represent the situation at some arbitrary flowrate, the value of which is shared between the cases of i) the turbine mounted and operating and ii) the turbine removed from the apparatus. Were real curves produced using point data measured throughout the duct system, the curves would be expected to change based on different flowrates. However, for a given, specified, flowrate throughout the system, it will remain true that the pressure differences between the two curves would remain constant, despite the fact that the profiles are established at different times. That difference would represent the pressure drop across the turbine when that specified flow rate was passing through the system.

To model this pressure loss behaviour as a function of flowrate, the same orifice meter method (see section 2.7) was used to accurately determine flow rate values, and static pressure observations at the downstream orifice tapping, over an arbitrarily large range of flowrates – without the turbine assembly mounted. To account for the

randomness associated with the turbulent flow at high flowrates, many data points were recorded. With enough points, a curve of best fit could be generated to characterize the behaviour.
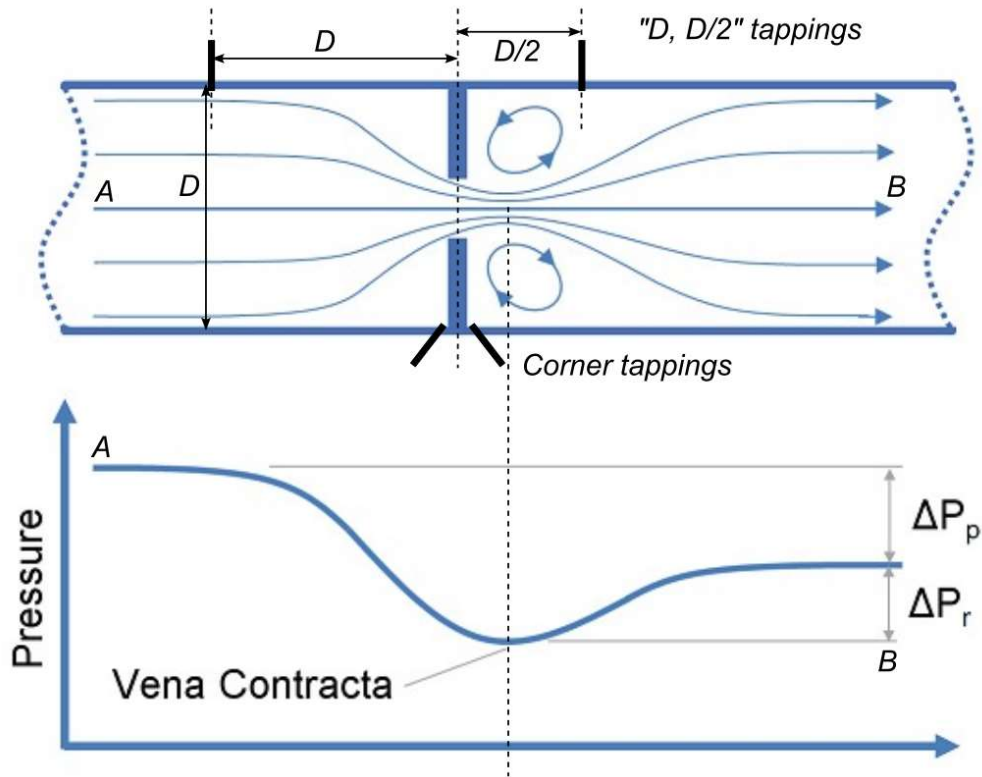
Figure 4.24: Expected pressure behaviour of an orifice plate along centreline of duct, as modified from Neutrium (2020)

Table 4.10: Calibration readings for pressure loss behaviour; 6.45" orifice plate

$P_{G,2}$	Diameter of orifice	Pressure drop across orifice	Flowrate
Pa	m	Pa	m³/s
-0.2	0.16383	51.2	0.157
-4.8	0.16383	111.9	0.231
-10.6	0.16383	186.4	0.297
-14.4	0.16383	234.3	0.332
-18.5	0.16383	280.3	0.363
-21.8	0.16383	329.0	0.393
-25.9	0.16383	383.2	0.423
-28.9	0.16383	442.8	0.455
-33.8	0.16383	507.0	0.486
-35.0	0.16383	573.9	0.517
-38.2	0.16383	649.2	0.549
-38.3	0.16383	727.7	0.581
-40.5	0.16383	811.7	0.613
-40.2	0.16383	895.5	0.643
-44.4	0.16383	977.1	0.671
-42.1	0.16383	1062.3	0.700

16 points were taken to create a curve of best fit. This was intended to model the expected pressure drop over the section of duct between the downstream orifice corner tapping and the rig outlet, as the rig flowrate varied. This modeled behaviour could then be used as a correction to the observed data when the turbine assembly was mounted and under test, to reduce the static pressure observation at the downstream orifice corner tapping to the pressure drop across the turbine assembly under test.

Note that, since the downstream corner tapping was used, the gauge pressures shown in Table 4.10 and depicted in Figure 4.25 were actually negative values.
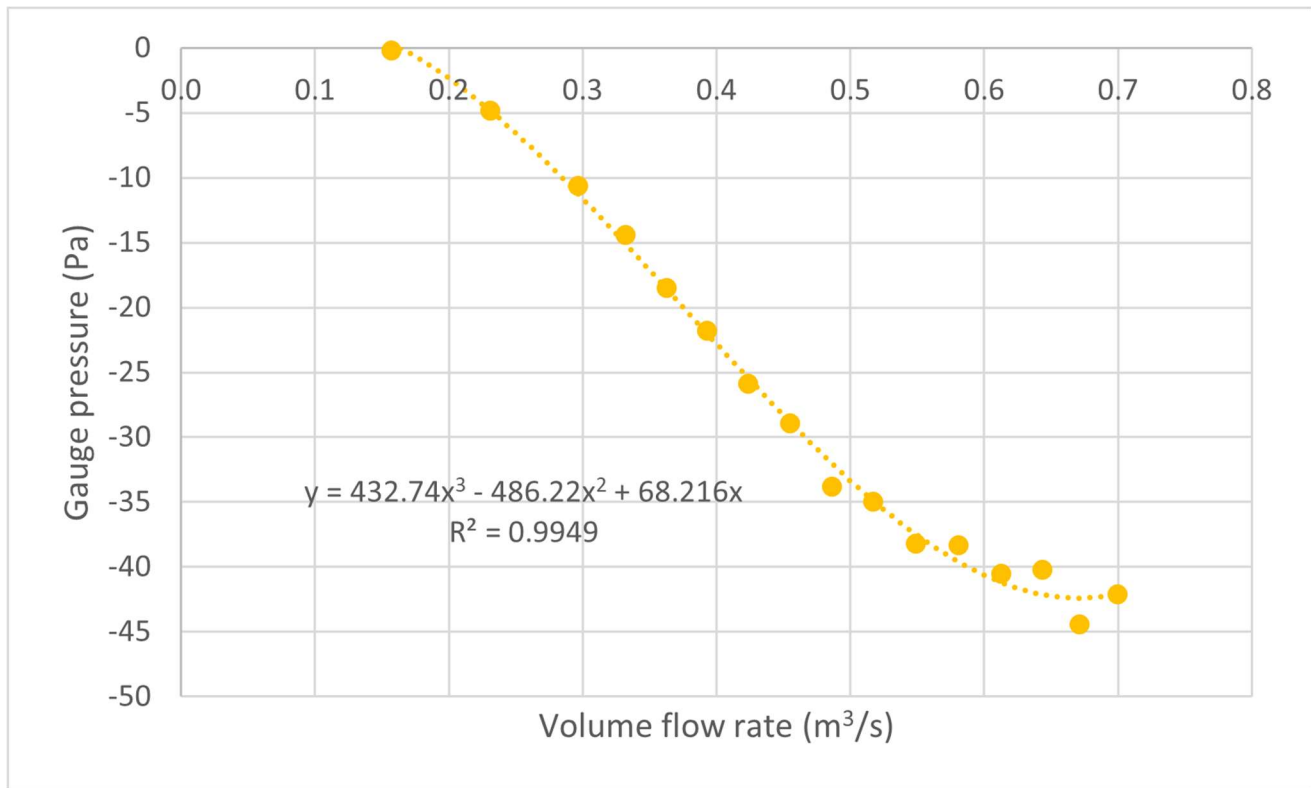
Figure 4.25: Curve of best fit characterizing pressure loss behaviour in duct section (6.45" orifice plate)

The x-intercept of the rig pressure loss behaviour curve (see Figure 4.25) represents the flowrate below which the orifice meter cannot produce reliable measurements with the default orifice diameter of 6.25". For low flow rate settings of the variable speed drive, the differential pressure reading across the orifice corner tappings became too small, relative to the resolution of the pressure sensor.

The calibration rig is equipped with a range of standard orifices to mount in the orifice meter location, to ensure that the magnitude of pressure difference observable across the orifice is compatible with the sensitivity, range and resolution of the pressure sensor. Table 4.11 and Figure 4.26 report the flow meter performance with a 4" orifice.

Table 4.11: Calibration readings for pressure loss behaviour; 4" orifice plate

$P_{G,2}$	Diameter of orifice	Pressure drop across orifice	Flowrate
Pa	m	Pa	m^3/s
-65.6	0.1016	311.0	0.118
-150.3	0.1016	694.8	0.176
-265.1	0.1016	1226.4	0.233
-415.6	0.1016	1904.4	0.290
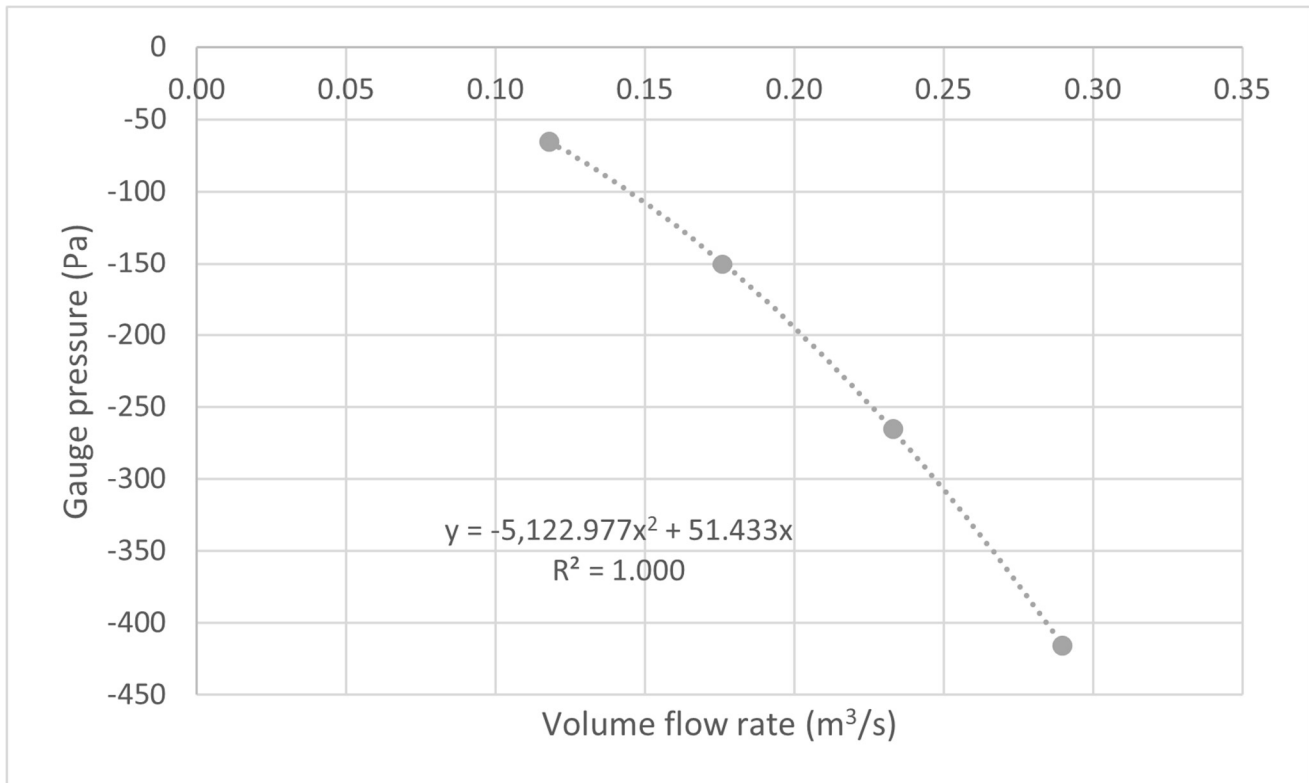
Figure 4.26: Curve of best fit characterizing pressure loss behaviour (4" orifice plate)

Note that lower flowrates (velocities) generally produce less turbulence. Thus, only 4 points were needed to produce a curve of best fit with an equal or greater R^2 value. The fitted curve can be used to estimate the pressure loss associated with the blower when the 4" orifice is installed, so that this can be subtracted from the static pressure reading when the turbine assembly is installed and operating (while the 4" orifice remains).

This characterization of pressure loss would be used to reduce experimental data to usable experimental results. The process can be graphically summarized as follows:

Raw physical data

Flow direction

Outlet

Corner tappings

To ATM

P_o - measured from corner tapping 1 to 2
P_G - measured from corner tapping 2 to ATM
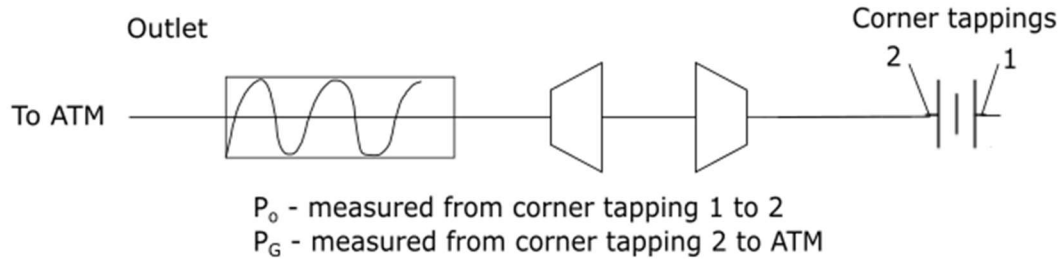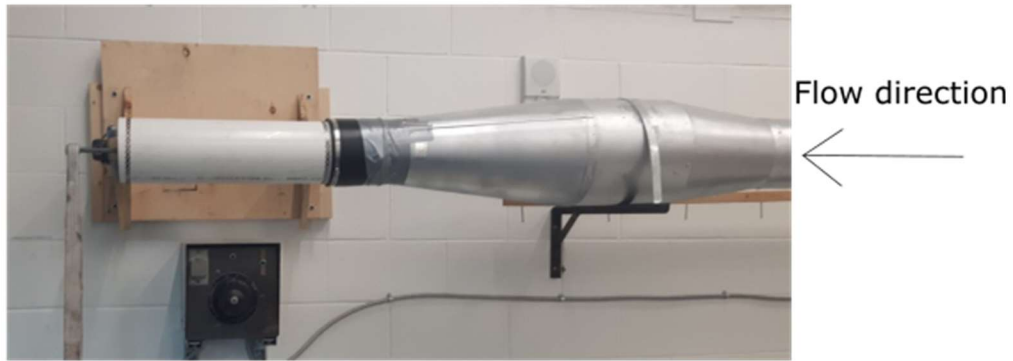
1. Plotting P_G as a function of flowrate, treat the flow conditioner and associated ducting as a Black Box, including dynamic exit losses and any flow effects at the orifice

P_{ATM} $P_{G,2}$

Dynamic loss (6" outlet) ___
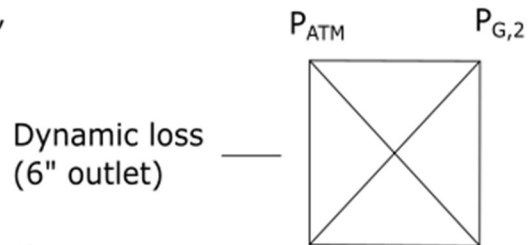
2. Given the same flowrate, exit diameter, and measurement location for P_G, any experimental data that is observed with the turbine assembly in place must include the same Black Box pressure loss

P_{ATM} $P_{G,1}$

Dynamic loss (6" outlet) ___
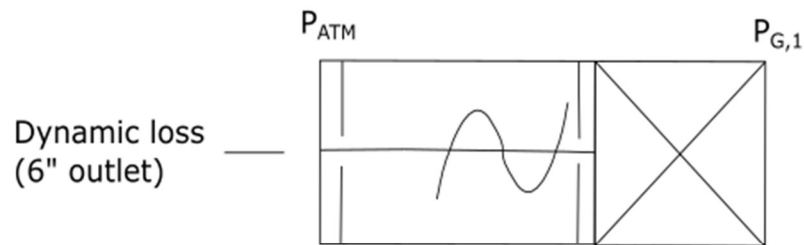
3. The pressure drop across physical rotor may be isolated by subtracting the calculated Black Box pressure loss

ΔP_{phys}
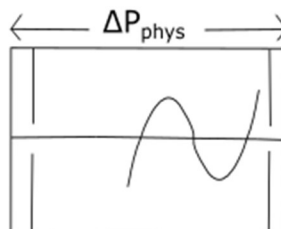
Figure 4.27: Diagrammatic explanation of physical data reductions

Referring to Figure 4.27, a gauge pressure reading, P_G, is taken at the downstream corner tapping of the orifice meter, with and without the turbine assembly present. $P_{G,1}$ represents the raw experimental gauge pressure data with the turbine assembly. $P_{G,2}$ represents the gauge pressure data which characterizes the blower. While the turbine assembly is removed, the pressure drop across the turbine assembly for the physical experiment, P_{phys}, is the difference between these two values – at the same flow rate.

Note that since the pressure is always measured at the same point and the outlet diameter is constant, the orifice behaviour and dynamic pressure exit loss are both included in the pressure reduction.

4.5.3   Estimating pressure drop from mounts

Recall from section 3.2.1, that the simulated geometry includes a diffuser, but no bearing mounts. The diffuser is accounted for by the placement of the virtual instruments, however a reduction must be applied to the experimental results, to account for the additional resistance from the bearing mounts in the physical experiment.

A similar method to that used in section 4.5.2 was used to characterize the losses incurred by the bearing mounts. With the duct and mounts in place, but with the rotor removed, the static pressure downstream of the orifice of the flowmeter was measured for 16 separate values of duct flowrate, reported in Table 4.12.

Table 4.12: Calibration readings for pressure loss behaviour; pipe and mounts with 6.45" orifice plate

$P_{G,3}$	Diameter of orifice	Pressure drop across orifice	Flowrate
Pa	m	Pa	m^3/s
7.9	0.16383	4.5	0.048
18.4	0.16383	13.2	0.081
31.3	0.16383	24.5	0.109
55.7	0.16383	46.4	0.150
85.8	0.16383	72.6	0.187
112.2	0.16383	96.5	0.215
140.3	0.16383	121.3	0.240
173.3	0.16383	147.4	0.264
209.1	0.16383	178.5	0.291
246.5	0.16383	211.8	0.316
291.1	0.16383	248.2	0.342
335.9	0.16383	286.9	0.367
382.5	0.16383	324.6	0.390
490.6	0.16383	414.3	0.440
617.0	0.16383	510.9	0.488
745.8	0.16383	614.7	0.534

Since it was impossible to test the mounts without the pipe (duct) and blower present, this model could only characterize the pressure drop, $P_{G,3}$, caused by the mounts, pipe, and blower together. The CFD simulated absolute roughness of the pipe wall was 0, smooth (see section 3.2.2). As such, the pressure reduction could justifiably include the measured pressure behaviour of the pipe wall. As demonstrated in the previous section, the pressure behaviour of the orifice and associated ducting (referred to as the blower for simplicity) could be subtracted from the observed pressure data to isolate the pressure behaviour of the mounts and pipe.

4.5.4   Estimating pressure drop from the bearings

Since the rotor was removed from the duct for this characterization, the bearings (which were already mounted on the shaft) were absent when the characterization data was recorded. Pressure behaviour related to an obstruction in a pipe may be approximated using the following equations:

$$\Delta P_{bear} = k_{loss} \frac{\rho v_{phys}^{2}}{2} \tag{4.17}$$

$$k_{loss} = C_D \frac{A_{bear}}{A_{duct}} \tag{4.18}$$

where

ΔP_{bear} - pressure loss associated with an obstruction having the size and cross-section of the bearings used in the physical experiment

k_{loss} - loss coefficient for free-standing obstructions in a flowing fluid

v_{phys} - flow velocity in the physical experiment

C_D - drag coefficient

A_{bear} - area of the bearing which is perpendicular to the flow (annular area does not include 3D printed rotor shaft)

A_{duct} - cross-sectional area of the physical duct (annular area does not include 3D printed rotor shaft)
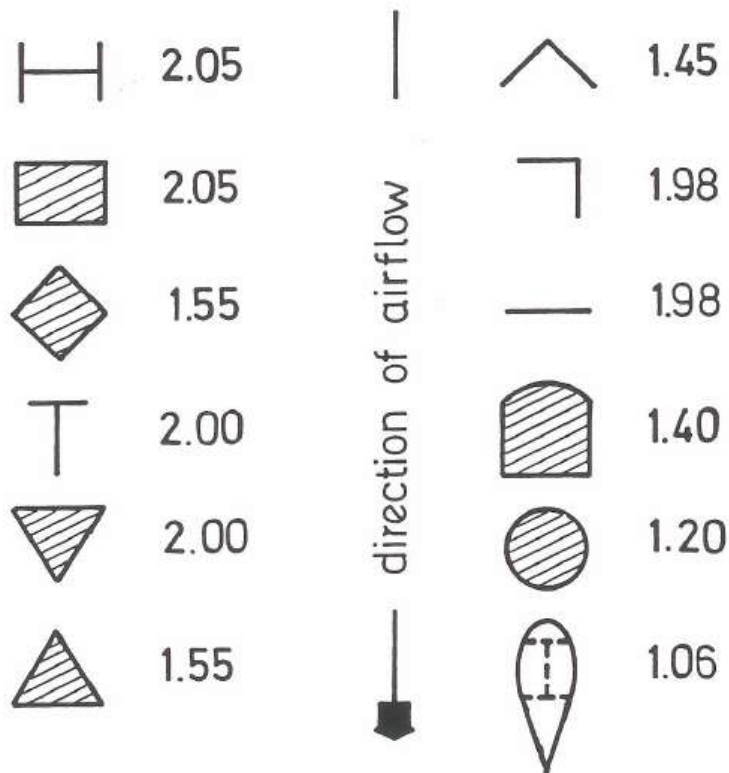
Figure 4.28: Drag coefficients associated with various cross-sectional profiles, as presented in McPherson (1993)

The drag coefficient, C_D, is selected based on the profile of the obstruction, with respect to the oncoming flow. For a rectangular cross-section (as seen in Figure 4.28), the drag coefficient is 2.05.

So, equations (4.17) and (4.18)resolve to:

$$\Delta P_{bear} = 2.05 \frac{\rho A_{bear} v_{phys}^2}{2 A_{duct}}$$

(4.19)

Thus, equation (4.18) produced reduction factors for the intended velocity setpoints, to be used later during data analysis. For interpolated values, the data from Table 4.13 was used to produce a curve of best fit (see Figure 4.29). With a sufficient R^2 value, the polynomial could be used to interpolate an aggregate of the reduction factors in Table 4.13 for any given velocity within the range of setpoints. This is a similar pressure reduction method as the one outlined in section 4.5.2.

Note that the blower characterization, $P_{G,2}$, is approximated as 0Pa in Table 4.13 for the 5m/s setpoint. As mentioned previously in section 4.5.1, the mount characterization, $P_{G,3}$, was obtained using the 6.45" orifice plate only. Thus, the 6.45" orifice reduction (which is only valid with flowrates greater than that of the 5m/s setpoint) was applied to the mount characterization.

As will become evident in the following chapter, this does not present any issue in the application of the pressure reduction, since the flowrates of the experimental data that were used in the final analysis all exceed this point. For this reason, the use of the following interpolation curve was deemed to be justified.

v	q	$P_{G,2}$	$P_{G,3}$	ΔP_{duct}	$\Delta P_{bearings}$	ΔP_{corr}
m/s	m³/s	Pa	Pa	Pa	Pa	Pa
20	0.365	-18.8	333	14.0	10.8	348
15	0.274	-8.88	184	8.49	6.1	191
10	0.182	-1.11	82.2	4.18	2.71	81.9
5	0.0912	0*	22.3	1.24	0.68	21.7

*-   this setpoint falls below the minimum flowrate for the 6.45" orifice, per section 4.5.2
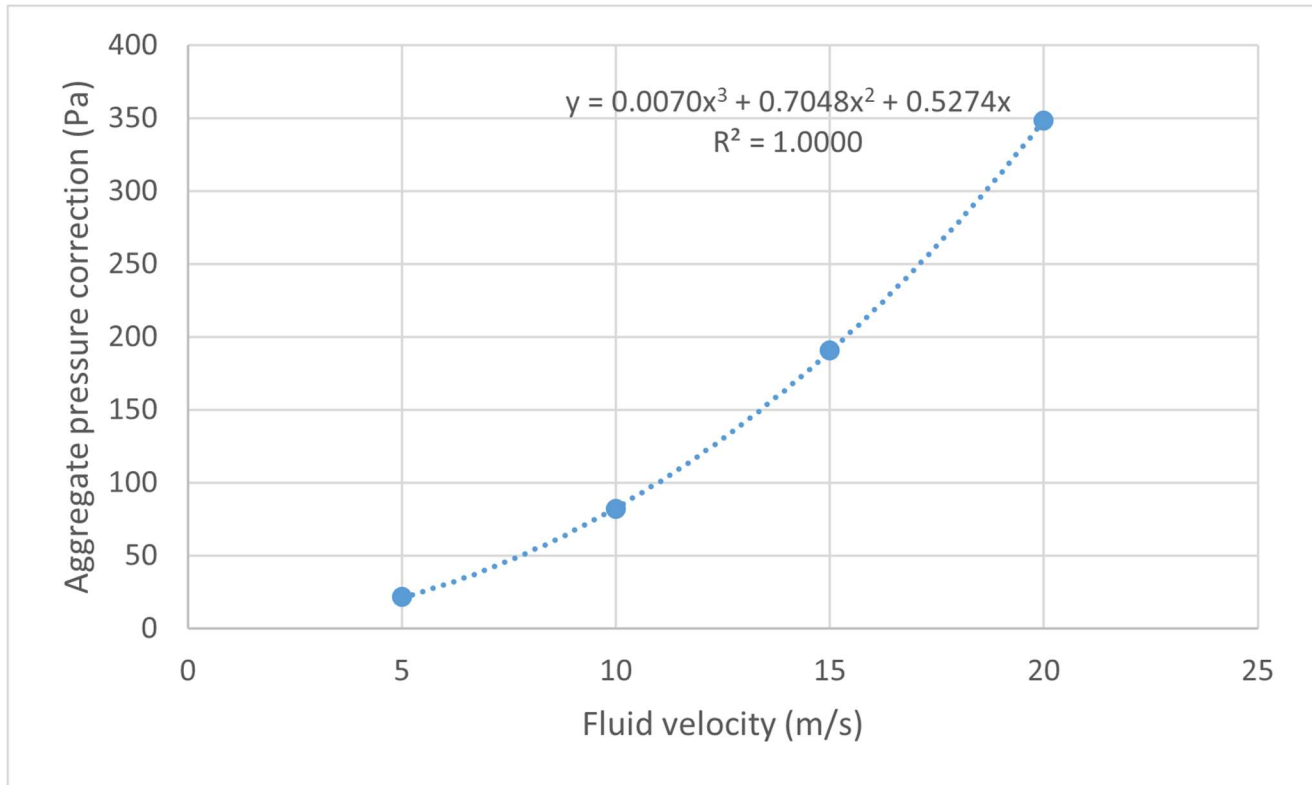
Figure 4.29: Curve of best fit, for interpolating aggregate pressure reduction

This would represent the final step of reductions that would be applied to the physical experimental data. The process can be summarized as follows:

Raw CFD data

Flow direction

1. Placement of the virtual instruments removes any pressure effects associated with the diffuser and extrusions

P_{ATM} P_2 P_1 P_0

ΔP_α
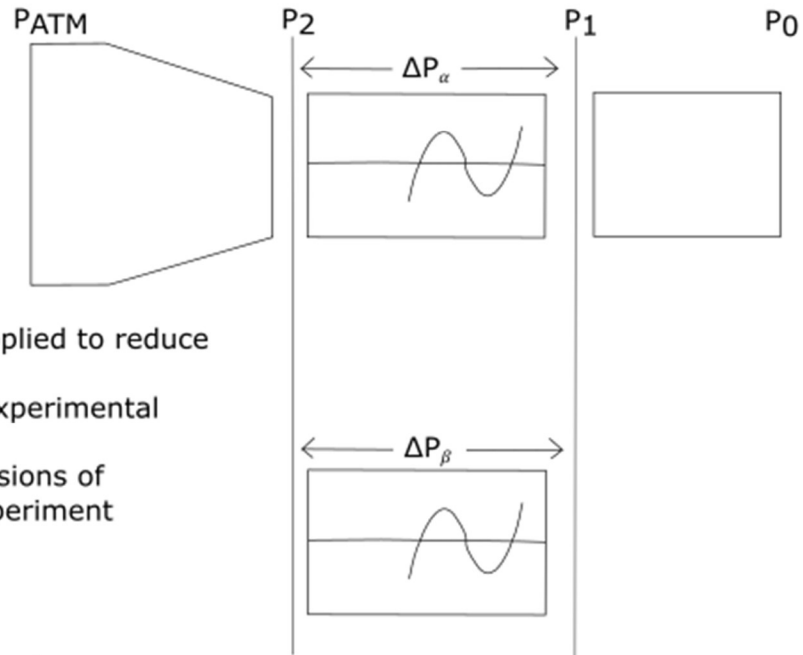
2. Similarity laws are applied to reduce the simulated data:
   a) to physical experimental setpoints, and
   b) to the dimensions of the physical experiment

ΔP_β

3. The observed pressure drop across the physical rotor are adjusted to approximate the conditions of the simulated CFD geometry by subtracting the aggregate pressure correction for the bearing mounts (Mounts are present in the physical setup and not in the simulation)

ΔP_{phys}
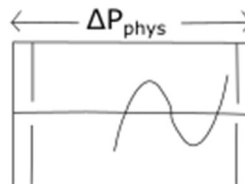
4. Finally, the conditions in the two duct systems are equivalent (in terms of geometry and features in the system) and present a direct comparison

ΔP_{turb}
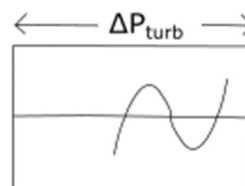
Figure 4.30: Diagrammatic explanation of CFD data reductions

116

Referring to Figure 4.30, ΔP_α would be taken as the difference between P_1 and P_2 (section 3.3.1). Note that, since P_2 was placed before the diffuser, the pressure drop was measured across the blade section only. This measured pressure drop would then be converted to an equivalent ΔP_β at a larger diameter, using the similarity laws (section 3.6). To directly compare the performance data from the physical experiment with the performance data from the CFD simulations, a pressure reduction, ΔP_{corr}, would then be applied to the physical experimental pressure (ΔP_{phys}, obtained in Figure 4.27). ΔP_{corr} would account for the bearing mounts, which were not explicitly represented in the CFD model. At this point, ΔP_{turb} (the reduced physical experimental pressure drop) approximates the conditions of ΔP_β (the SL transformed, simulated pressure drop) as closely as possible and the two can be compared directly.

4.6   Estimating torque loss from bearing friction

Since two identical digital scales have been used to measure a friction force as a difference between their two readings, and since both scales are tared before every use, no offset error should exist. However, internal friction applied to the rotor (such as internal friction in the ball bearings at high speeds) may not be measured by the scales. This would result in an offset error in the friction force measurement.

To ensure that the friction losses due to the bearings were negligible, a method was devised for estimating the torque loss. This method was developed with input from A. Hutchison (Hutchison, personal correspondence, 2021).

Conditions were recorded for a no-load setpoint at low airflow. This represented a system whose only losses were the bearing friction. At a greatly increased airflow (one corresponding to 20 m/s, the maximum velocity for which experimental data would be taken), a friction was applied using the tension arm to reduce rotating speed to match the no-load rotating speed. This applied friction could then be assumed to greatly outweigh the bearing friction. Therefore, friction for this second point was assumed to be wholly due to the applied friction.

By assuming that both points operated at efficiencies that were of the same approximate order of magnitude, the following relation was used to calculate an approximate bearing friction:

$$T_2 \propto T_1 * \frac{N_1 P_2 Q_2}{N_2 P_1 Q_1} \tag{4.20}$$

Referring to Table 3.16, it was observed that efficiency increased as flowrate decreased (assuming rotational speed remained constant). Efficiency also increased with a decreased rotational speed (assuming flowrate remained constant). Since rotational speed would have an inverse relationship to the applied load, the efficiency should increase with an increased load (once again, assuming a constant flowrate). This suggested that the efficiency of the no-load condition should have been lower than the high flow condition. Therefore, the relationship described by equation (4.20) should be viewed as an inequality, where the true bearing friction should be less than the calculated estimate.

Table 4.14: Calibration data and calculated estimate of bearing torque loss

	N	$P_{G,1}$	ΔP_o	ΔP_{phys}	Q	ΔF_T
	rpm	Pa	Pa	Pa	m^3/s	kg
Loaded	265	725.5	285.8	744	0.365	2.36
No load	265	-0.4	183.5*	36.9	0.0905	*0.0290*

*-   4" orifice plate used

The estimate of $0.0290\ kg$ was only slightly more than the minimum resolution of the digital scales ($0.02\ kg$). As demonstrated, for example, in Meyer (1975), the additive uncertainty associated with the difference of two identical scales can be calculated using the following equation:

$$\delta(\Delta F_T) = \sqrt{2\delta(F_T)^2} \qquad (4.21)$$

where $\delta(\Delta F_T)$ is the uncertainty associated with the difference of the two scales and $\delta(F_T)$ is the uncertainty associated with one scale.

This resulted in a combined error of ±0.0141kg for the friction reading. When viewed in the context of an inequality, where the true bearing friction would be strictly less than the estimated value, this meant that the maximum possible torque error (due to bearing friction loss) would be only slightly greater than the uncertainty of the reading.

As a result, the bearing losses will be unlikely to account for a large variance in torque between the expected results and observed physical results. While some level of uncertainty will remain, measuring the bearing friction would require greater precision than the experimental apparatus can provide. In the absence of a more precise measurement of the bearing losses, it was deemed sufficient to demonstrate that the magnitude of the error was of the same order as the combined uncertainty of the scales, or less.

5 Experimental testing of rotor performance

This section details the methodology used in the physical experimentation that was carried out on the prototype device. Included is a factual reporting of the observed data in that experimentation, and a brief analysis thereof.

5.1 Physical Testing

Based on the calibration tests which have been documented in chapter 4.5.2, the following experimental method was developed. Systemic issues that were identified, but could not be mitigated through procedure, are included subsequently. These practical limitations of the experiment would dictate conditions that would invalidate a test.

5.1.1 Experimental method

If necessary, refer to section 4.2 for a detailed description of the terminology and physical setup of the apparatus.

1. Place the tension strap on the friction drum.
2. Increase power supply to the centrifugal fan until desired orifice pressure is displayed on the manometer. (Pressures which correspond to intended setpoint velocities have been determined in advance, using calibration data.)
3. Tighten the main bolt on the tension arm using a wrench until intended rotational setpoint is displayed on the tachometer.
4. Confirm orifice pressure and adjust power to the centrifugal fan to correct for added system resistance, as needed.
5. Confirm rotational speed and adjust tension to correct for added airflow, as needed.
6. Repeat steps 5 and 6 until orifice pressure and rotational speed are within the desired margin of error for their intended setpoints.
7. Record orifice pressure, gauge pressure, and rotational speed. Record any observations such as scraping sounds coming from the pipe, scales losing contact with the hook, or melting/catching of the drum/strap. (See following section.)
8. Turn on both digital scales and confirm that they read 0.00 kg.
9. Pull down on the strap to create a negative reading on both scales.
10. Loosen the main bolt on the tension arm until the tension strap can be removed from the friction drum.
NOTE: Ensure that the readings remain negative throughout Step 10. If either scale reads positive, triggering its Hold function, the test will be invalidated.
11. Allow scales to settle and record digital readout on scales.
12. Repeat steps 1-11 for all intended setpoints listed in Table 5.1, and label the data line with the proper designation code.

Recall, from section 3.5, that the physical experiment was tested at a range of setpoints combining flow velocity and rotational speed. The flow velocity setpoints were 5, 10, 15, and 20 m/s. The rotational setpoints were 100, 150, 200,

250, 500, 750, and 1000 RPM. Every combination thereof represented a unique experimental setpoint, which was represented using the following setpoint codes:

Table 5.1: Designation codes for intended physical experimental setpoints (repeat of Table 3.15)

Rotational speed (rpm)	Airflow velocity (m/s)			
	5	10	15	20
100	A5	A10	A15	A20
150	B5	B10	B15	B20
200	C5	C10	C15	C20
250	D5	D10	D15	D20
500	E5	E10	E15	E20
750	F5	F10	F15	F20
1000	G5	G10	G15	G20

5.1.2   Practical limitations of experimentation

Three conditions were observed which, due to physical limitations of the test, may skew or invalidate certain data, or end a test outright if they were noted. These conditions constituted physical indications of the quirks inherent to the selected instrumentation, and a more detailed exploration thereof can be found in Appendix D.

The first such observation was a scraping sound coming from the pipe. This observation indicated that the normal force applied to the drum was too high and the blade had begun to scrape against the inner surface of the duct. While the test could still be completed, the observation must be noted, as this behaviour would reduce the recorded torque reading, skewing the data.

The second observation was slipping or catching of the strap against the drum. If the tachometer reading began to vary to a higher degree than the desired margin of error, this was taken as an indication of melting of the drum due to friction heat. If this was not caught in time, the drum would eventually catch on the strap as the melted plastic solidified, causing the rotor to stop. Extended periods of high speed and/or friction increased the likelihood of friction-heat-induced melting. If this observation was noted, the test would end immediately. At this point, the strap would be detached and cleaned of any hardened plastic. Then, the drum and strap would be allowed to cool before starting the next test.

Finally, unhooking of the low-tension (slack-side) digital scale would also invalidate a test. Extreme variations in measured rotational speed were taken as an indication that friction was too low, and that the scale had lost contact with the tension arm. The observation could be confirmed by checking the contact at the tension arm. If the scale or hook was rotating freely (as shown in Figure 5.1), then it meant that the scale had come unhooked. The test would end immediately, and the technician would move on to the next setpoint.

Figure 5.1: Unhooked scale (right), rotating freely

5.2 Reduced experimental results

This section reduces the full set of experimental data to only what is relevant to the paper's conclusion. For a factual statement of all data, see Appendix C.

5.2.1 Experimental data

Table 5.2: Table of observations, internal duct diameter = 152.42mm

Intended Setpoint			Experimental conditions					Raw observations			
Code	v^*	N^*	$T(°C)_{atm}$	P_{atm}	Orifice	D_o	D_d	N_{phys}	ΔP_o	$P_{G,1}$	ΔF_T
#	m/s	rpm	°C	kPa	in	cm	mm	rpm	Pa	Pa	kg
A15	15	100	19.7	98.774	6.45	16.383	23.76	100	157.5	404.5	1.40
B15	15	150	19.7	98.774	6.45	16.383	23.76	150	157.9	402.8	1.36
C15	15	200	19.7	98.774	6.45	16.383	23.76	195	157.9	398.2	1.30
D15	15	250	19.7	98.774	6.45	16.383	23.76	250	157.1	390.5	1.16
E15	15	500	19.7	98.774	6.45	16.383	23.76	495	157.2	371.0	0.96
F15	15	750	19.7	98.774	6.45	16.383	23.76	755	159.0	353.1	0.76
F15	15	750	19.7	98.774	6.45	16.383	23.76	755	159.0	353.2	0.74
G15	15	1000	19.7	98.774	6.45	16.383	23.76	1005	159.0	329.2	0.42
A20	20	100	21.5	98.686	6.45	16.383	22.67*	100	285.5	733.4	2.70
B20	20	150	21.5	98.686	6.45	16.383	22.67	150	284.4	723.1	2.64
C20	20	200	21.5	98.686	6.45	16.383	22.67	205	284.2	721.1	2.54
D20	20	250	21.5	98.686	6.45	16.383	22.67	250	284.2	714.8	2.44
E20	20	500	21.5	98.686	6.45	16.383	22.67	500	285.2	696.3	2.12
E20	20	500	21.5	98.686	6.45	16.383	22.67	500	285.0	695.1	2.14
A10	10	100	21.7	97.502	4.00	10.160	22.67	105	750.8	16.7	0.64
B10	10	150	21.7	97.502	4.00	10.160	22.67	150	750.9	16.3	0.58
C10	10	200	21.7	97.502	4.00	10.160	22.67	200	750.6	14.1	0.56
D10	10	250	21.7	97.502	4.00	10.160	22.67	250	748.3	9.6	0.42
E10	10	500	21.7	97.502	4.00	10.160	22.67	490	753.2	-4.1	0.32

*-   Drum diameter reduces due to friction heat from high-speed or high-tension testing over extended periods (see Appendix D)

Intended Setpoint			Reduced results					Data Setpoint	
Code	v^*	N^*	T_{phys}	ω_{phys}	ΔP_{turb}	Q_{phys}	η_{phys}	v_{phys}	N_{phys}
#	m/s	rpm	N-m	rad/s	Pa	m³/s	%	m/s	rpm
A10	10	100	0.0712	11.0	96.0	0.183	4.45	10.05	105
B10	10	150	0.0645	15.7	95.6	0.183	5.78	10.05	150
C10	10	200	0.0623	20.9	93.3	0.183	7.62	10.05	200
D10	10	250	0.0467	26.2	88.6	0.183	7.54	10.03	250
E10	10	500	0.0356	51.3	75.4	0.184	13.2	10.07	490
A15	15	100	0.163	10.5	226	0.271	2.78	14.87	100
B15	15	150	0.158	15.7	224	0.272	4.09	14.89	150
C15	15	200	0.152	20.4	220	0.272	5.18	14.89	195
D15	15	250	0.135	26.2	213	0.271	6.14	14.85	250
E15	15	500	0.112	51.8	193	0.271	11.1	14.86	495
F15	15	750	0.0886	79.1	173	0.273	14.8	14.94	755
F15	15	750	0.0862	79.1	173	0.273	14.4	14.94	755
G15	15	1000	0.0489	105	149	0.273	12.6	14.94	1005
A20	20	100	0.300	10.5	403	0.365	2.13	20.01	100
B20	20	150	0.294	15.7	394	0.364	3.21	19.98	150
C20	20	200	0.282	21.5	393	0.364	4.24	19.97	205
D20	20	250	0.271	26.2	386	0.364	5.05	19.97	250
E20	20	500	0.236	52.4	367	0.365	9.23	20.00	500
E20	20	500	0.238	52.4	366	0.365	9.34	20.00	500

The data from the physical experiment has been used to characterize the performance of the turbine design, in the form of a set of performance curves. Note that the following performance curves have been transformed to a constant rotational setpoint, while maintaining the dimensions of the physical geometry. Only the reduced results (from the data selected in Table 5.3) were included.
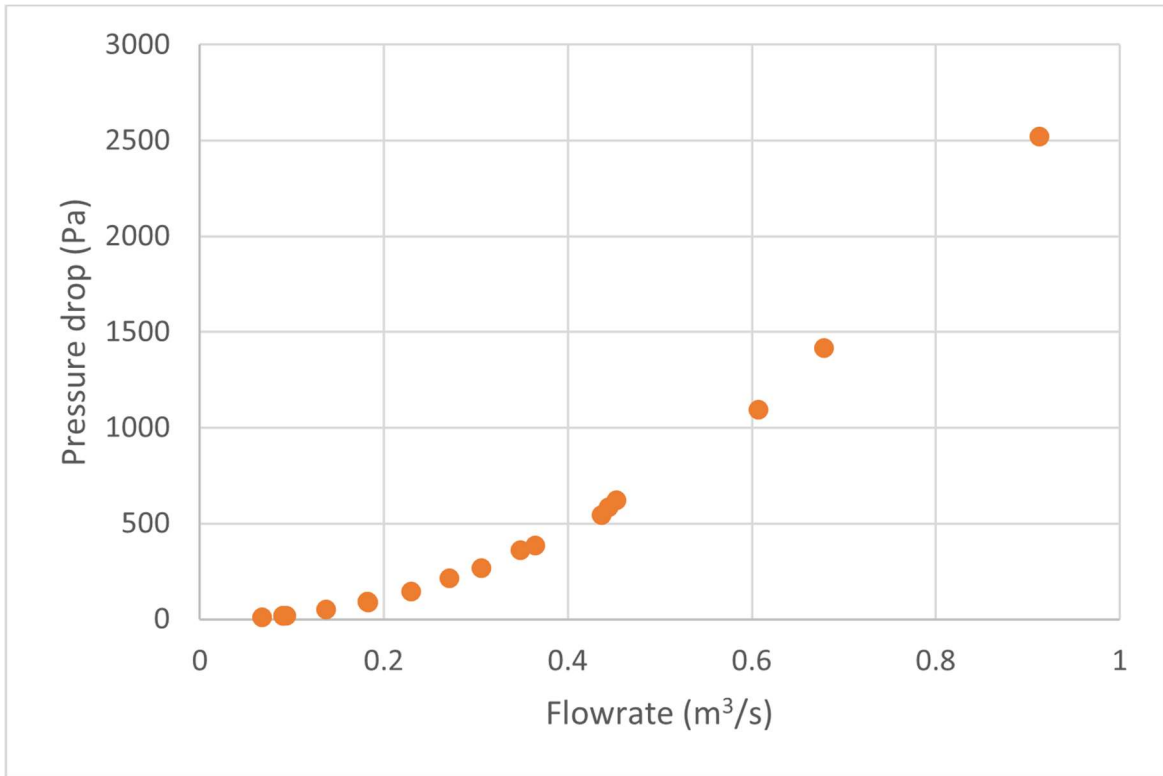
Figure 5.2: Performance curve from reduced physical results (pressure vs flowrate), 0.15242m diameter, transformed to 250 rpm setpoint
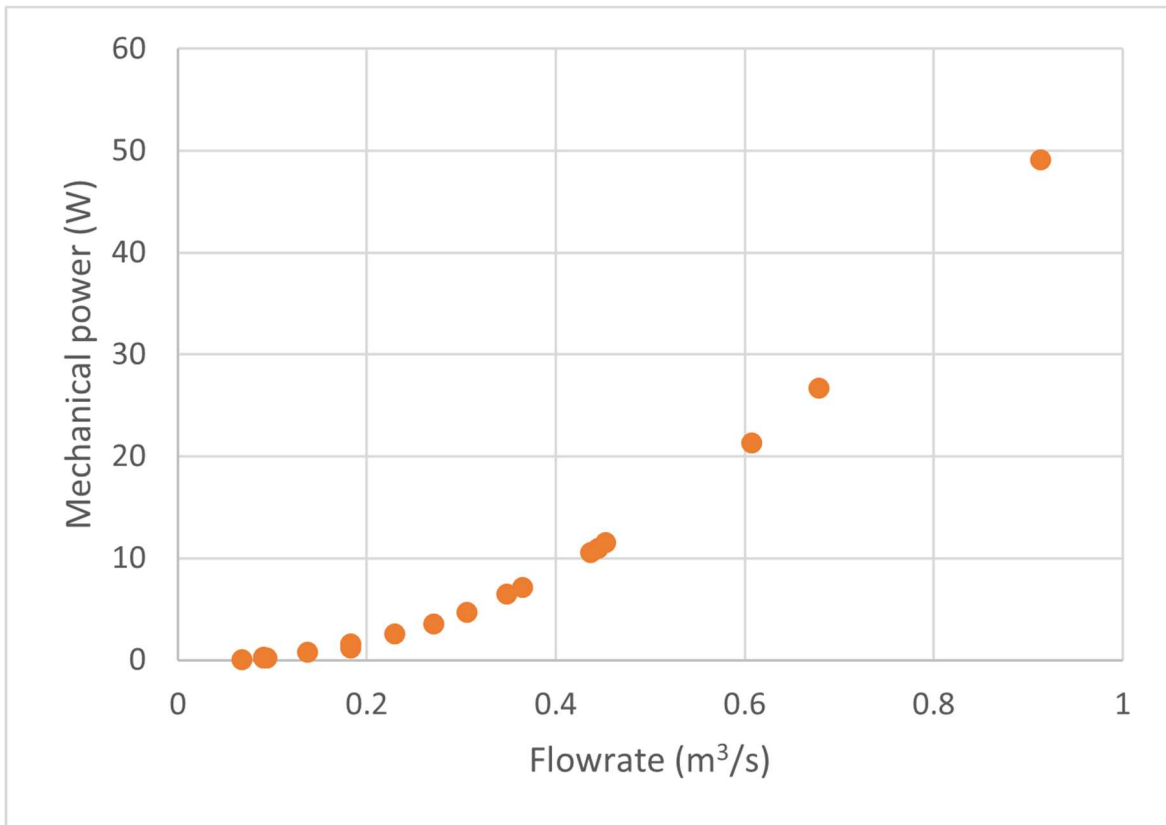
Figure 5.3: Performance curve from reduced physical results (mechanical power vs flowrate), 0.15242m diameter, transformed to 250 rpm

setpoint

124
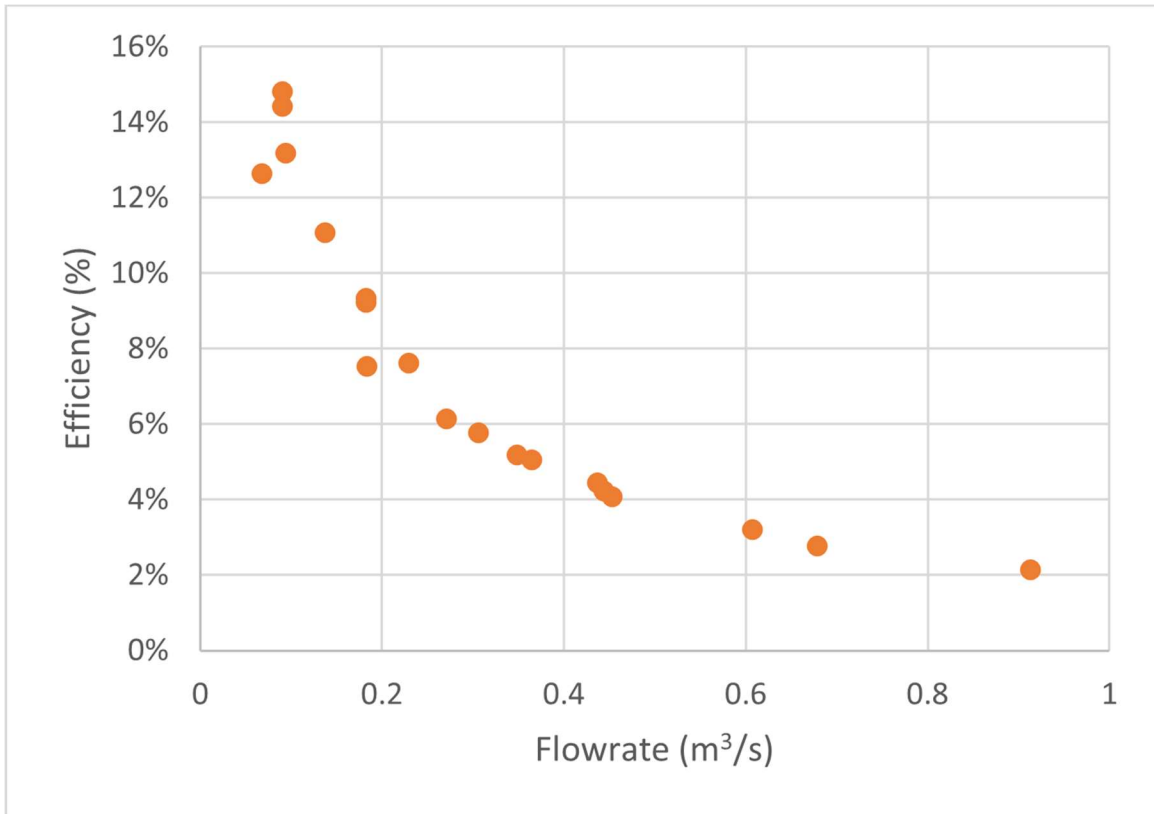
Figure 5.4: Performance curve from reduced physical results (efficiency vs flowrate), 0.15242m diameter, transformed to 250 rpm setpoint

5.2.2   Notes on data sets

The collection of all observed data and reduced results is included in Appendix C. Any data that were collected expressly for calibration were deemed to be irrelevant.

The final data set was taken using a revised experimental method, based on observations detailed in Appendix D. Since this revised torque measurement method was determined to be more accurate, the previous method was deemed invalid, and all data obtained using said method have also been disregarded for the final analysis.

6 A discussion of the extensions of analysis for comparison of results

Here, the reduced data sets (both simulated and experimental) are compared to identify possible sources of error or flaws in the experimental model.

6.1 Comparison of CFD and Experimental results

As seen in Table 5.3, the observed data setpoints do not match the intended setpoints for the physical experiment. To accommodate this difference, a more precise set of expected data may be generated (using the procedure demonstrated in section 3.6). By generating SL transformed curves of pressure and torque behaviour for the observed values of N_{phy} , the influence of any rotational error could be eliminated. By interpolating expected torque and pressure values for the observed values of v_{phys}, the influence of any flow error could be eliminated. In the following table, the expected results (generated using the observed data setpoints) are compared to the observed results of the physical experiment.

Table 6.1: Comparison of projected CFD results (expected) to observed experimental results

Intended Setpoint			Data Setpoint		Expected*		Observed		Error	
Code	v^*	N^*	v_{phys}	N_{phys}	T_{exp}	ΔP_β	T_{phys}	ΔP_{turb}	T_{err}	P_{err}
#	m/s	rpm	m/s	rpm	N-m	Pa	N-m	Pa	%	%
A10	10	100	10.05	105	0.0977	97.0	0.0712	96.0	-27.2	-1.04
B10	10	150	10.05	150	0.0945	94.0	0.0645	95.6	-31.7	1.73
C10	10	200	10.05	200	0.0908	90.5	0.0623	93.3	-31.4	3.09
D10	10	250	10.03	250	0.0868	86.9	0.0467	88.6	-46.2	1.97
E10	10	500	10.07	490	0.0699	71.3	0.0356	75.4	-49.1	5.81
A15	15	100	14.87	100	0.220	218	0.163	226	-25.8	3.90
B15	15	150	14.89	150	0.215	213	0.158	224	-26.3	5.05
C15	15	200	14.89	195	0.210	209	0.152	220	-27.9	5.11
D15	15	250	14.85	250	0.203	202	0.135	213	-33.5	5.17
E15	15	500	14.86	495	0.177	178	0.112	193	-36.8	8.50
F15	15	750	14.94	755	0.151	154	0.0886	173	-41.4	12.3
F15	15	750	14.94	755	0.151	154	0.0862	173	-42.9	12.4
G15	15	1000	14.94	1005	0.124	129	0.0489	149	-60.5	15.6
A20	20	100	20.01	100	0.403	399	0.300	403	-25.6	1.05
B20	20	150	19.98	150	0.394	391	0.294	394	-25.6	0.89
C20	20	200	19.97	205	0.386	383	0.282	393	-26.9	2.44
D20	20	250	19.97	250	0.380	377	0.271	386	-28.6	2.41
E20	20	500	20.00	500	0.345	345	0.236	367	-31.6	6.25
E20	20	500	20.00	500	0.345	345	0.238	366	-30.9	6.05

*   -CFD simulated, then SL transformed, and interpolated to match velocity setpoint

Note that each rotational speed will correspond to a specific performance, as noted in section 2.6. To compare the data directly, the similarity laws may be used to transform all data to the same rotational speed.
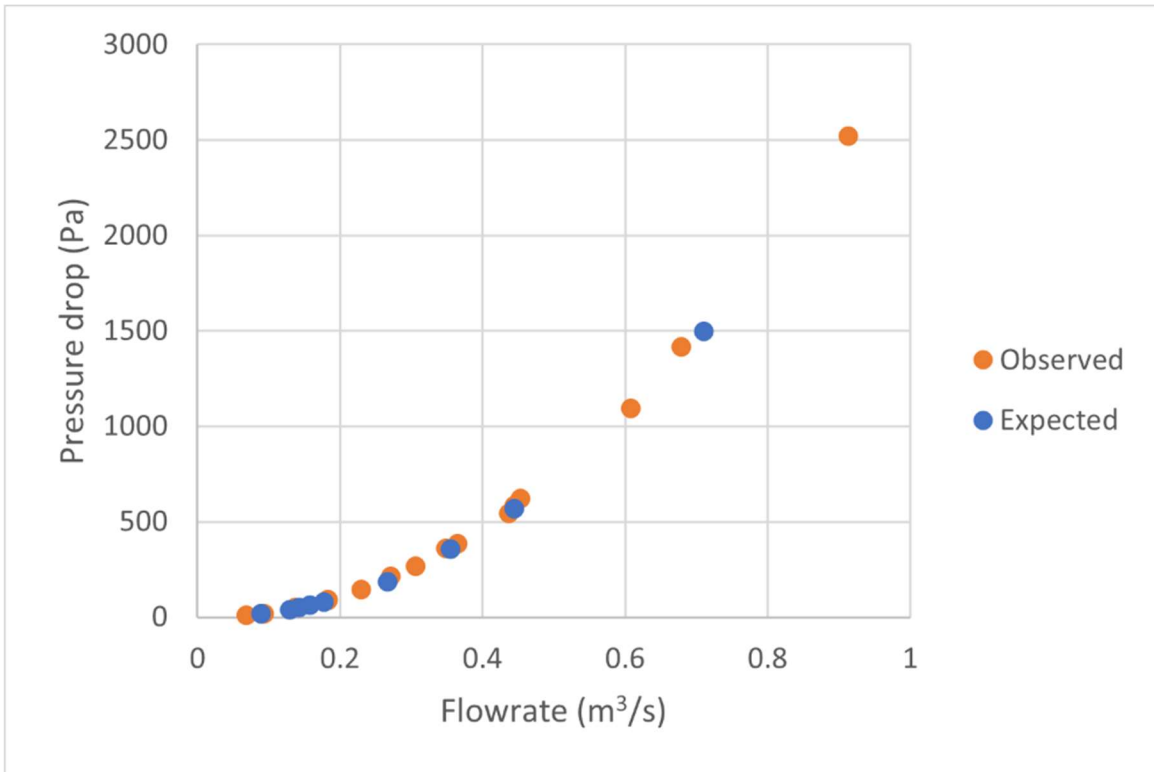
Figure 6.1: Comparison of pressure trends in physical and simulated results, transformed to 250 rpm and 0.15242m diameter
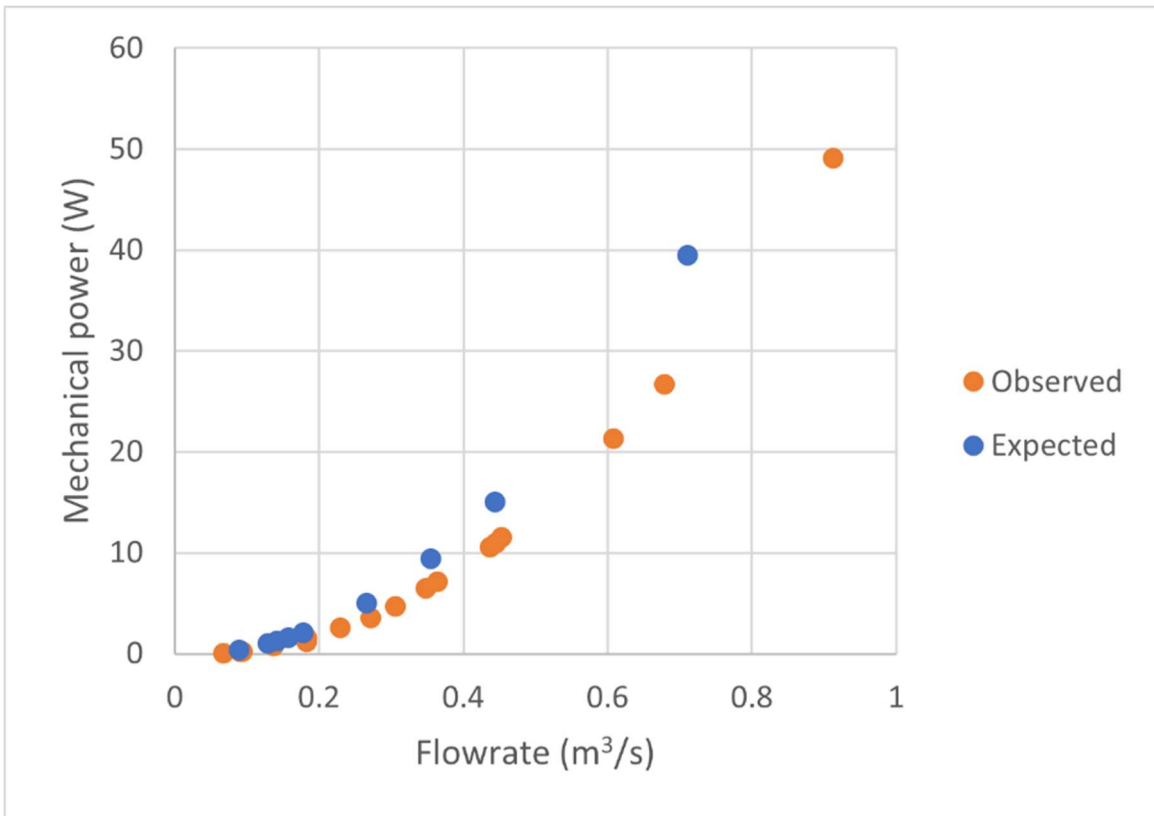
Figure 6.2: Comparison of mechanical power trends in physical and simulated results, transformed to 250 rpm and 0.15242m diameter

Despite the relative error between the two sets of pressure results (noted as P_{err} in Table 6.1), Figure 6.1 demonstrates that the agreement between the respective data sets is very good.

The relative error between the two sets of pressure results (noted as T_{err} in Table 6.1) is quite high. However, Figure 6.2 demonstrates that the agreement between the is still reasonable. While this indicates that the experimental results are consistent with each other, it is desirable to identify some specific source of error which might explain this discrepancy.

6.2   Discussion of errors

Two types of error have been identified in the previous section, pressure and torque. This section will propose possible explanations for these errors and, by characterizing these errors mathematically, the most plausible explanations will be identified.

6.2.1   Characterization of error behaviour

Using equations (2.17), (2.18), and (2.19), the reduced physical experimental results and CFD results can be plotted in non-dimensional terms. This also allows for a direct comparison, without the use of the similarity laws. Recall that the aggregate pressure reduction from section 4.5.3 must be subtracted from the physical results to ensure that the duct systems are equivalent for the comparison.
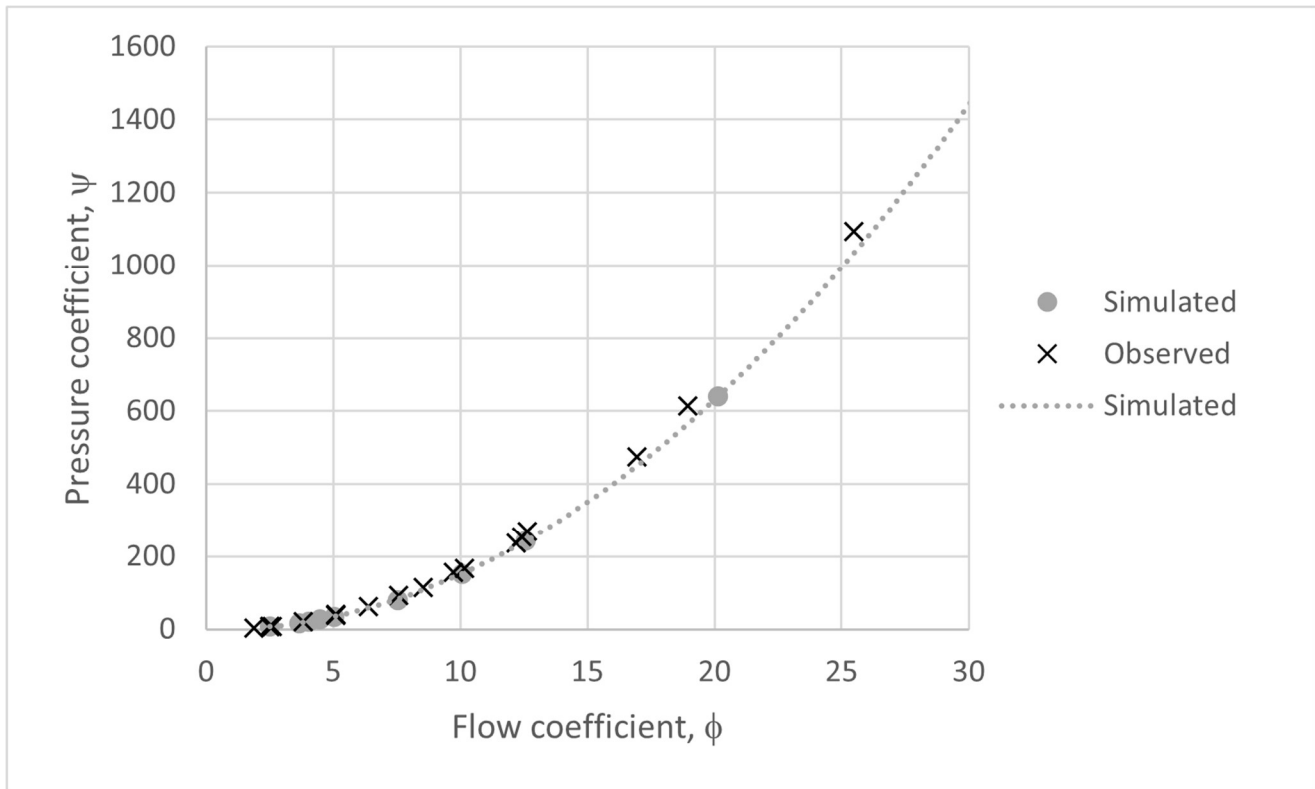
Figure 6.3: Comparison of performance curves using nondimensionalized coefficients (pressure vs flowrate)
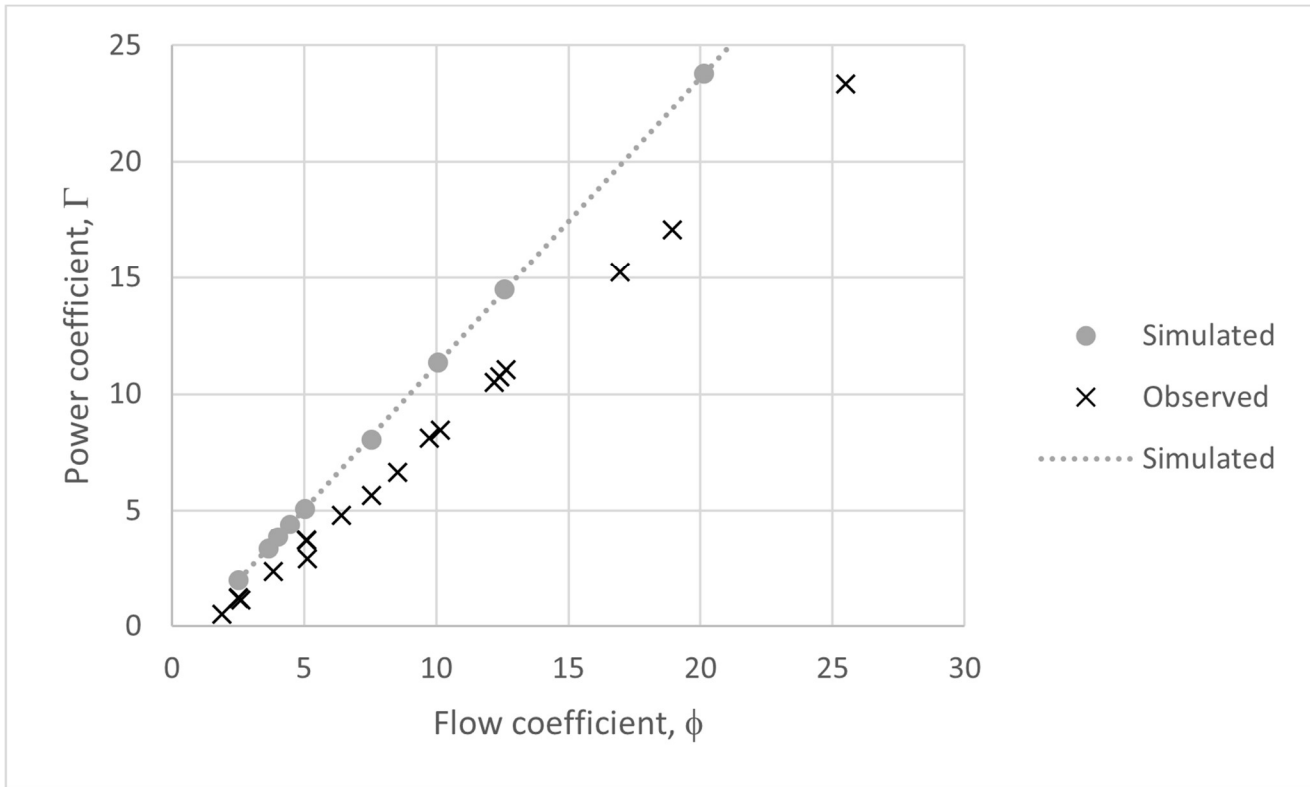
Figure 6.4: Comparison of performance curves using nondimensionalized coefficients (mechanical power vs flowrate)

Figure 6.3 shows very good agreement between the pressure trend in simulation and the pressure trend in the physical experiment. Within the range of the physical experimental data, the discrepancy is minor. It can be noted that the magnitude of the discrepancy increases at higher flowrates, which is typical of a pressure resistance.

Figure 6.4 demonstrates that there is some discrepancy in torque between the simulation and the physical experiment. It is worth noting that the magnitude of the discrepancy increases at higher flowrates. Thus, the largest source of torque error must be a function of flowrate. This is not typical of a mechanical torque loss. In fact, recalling equation (2.17), the flow coefficient, φ, is inversely proportional to rotational speed, which reveals that mechanical losses must not be a large source of error. This discounts the possibility of mechanical torque resistances as major sources of error- such as bearing friction, which would be expected to increase at higher rotational speeds.

Incidentally, Figure 6.3 and Figure 6.4 represent nondimensionalized versions of the same performance curves which have been used to characterize the performance of the device in sections 3.7 and 5.2.1. The final performance curve (efficiency) is included here for completeness.
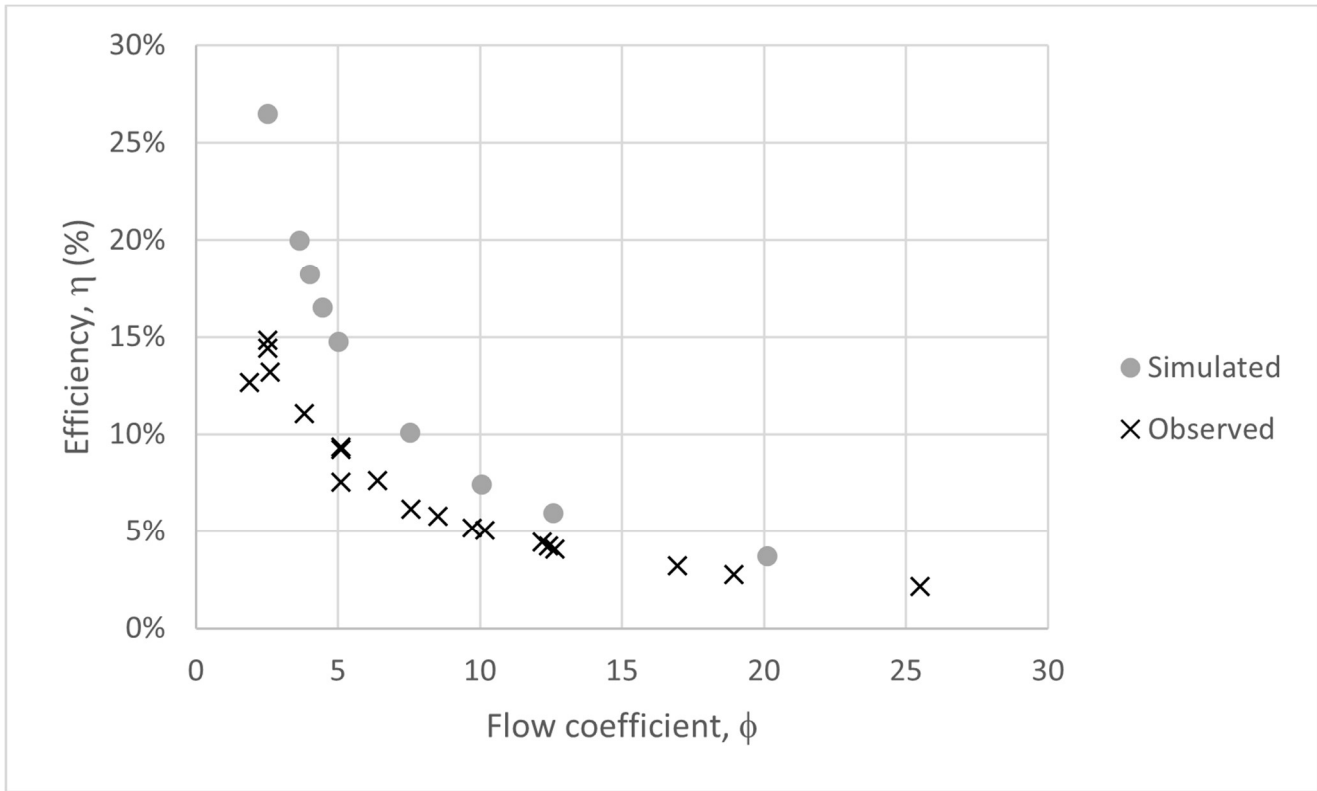
Figure 6.5: Comparison of performance curves using nondimensionalized coefficients (efficiency vs flowrate)

6.2.2   Discussion of discrepancies in expected pressure

As evidenced by Figure 6.3, agreement between the two models is very precise. Comparing the observed experimental results to the expected results from CFD (see Table 6.1), the pressure values produced by the two experiments differ by no greater than 15.6% of the expected value. It should be noted that the small magnitude of the pressure values means that even very small errors can result in a relative error that seems very high. While this error is not negligible, it can be accounted for by the imprecise nature of the reduction factors.

The methodology described in sections 4.5.2 and 4.5.3 is used as a way of estimating a pressure reduction for a duct system. However, it relies on the ability to take accurate readings for the various configurations of that system. Note that the measurements used to characterize the pressure behaviour associated with the mounts did not include the flat face of each bearing as they would appear in the assembled system. Since the bearings were attached to the rotor shaft when the measurements were taken, the bearing mounts were placed in the duct while empty. While a mathematical reduction has since been estimated, it has been based on assumptions that could not be verified experimentally.

Referring to Table 4.13, it is evident that the bearing mounts are the largest source of resistance in the pressure reduction. This means that inaccuracy here would be the most likely source of error in the overall reduction factor. To eliminate this as a potential source of error in future experiments, a "dummy rotor" might be manufactured with the same dimensions as the bearings and shaft, but with no blades. This would fill the space that would be taken up by the rotor, allowing for a more precise calibration.

130

6.2.3 Discussion of discrepancies in expected torque

Comparing the observed experimental results to the projected CFD results (see Table 6.1), the torque values produced by the two experiments differ by up to 60.5% of the expected value. This degree of error implies some larger flaw in either (or both) of the experimental methods. Possible sources of error may include unidentified torque losses in the physical experiment, or a flawed implementation of the similarity laws.

In terms of the physical experiment, measuring a friction applied to the rotor's shaft is a common method for calculating a resistance torque. However, resistance from any other source in the system cannot be measured in this way. Therefore, bearing friction, other mechanical friction, and any other unidentified loss of torque in the system cannot be measured.

It is worth noting that the relative torque error is consistently negative. This is to say the observed torque from the physical experiments is always less than the expected values based on simulated data. This is consistent with the idea that the error is caused by an unidentified torque loss in the physical experiment.

Aside from bearing friction and other sources of mechanical friction, a torque loss may be explained by an increased shear friction on the helical blade surface, as compared to the CFD simulation. This would be consistent with an improper application of the similarity laws. As has been previously mentioned in section 2.5, the similarity laws include specific conditions which must be met to ensure that the transformation will be applied appropriately. It has already been noted that one of these conditions (the Fan Reynolds threshold) has not been met. This suggests that the transformed CFD results have not accounted for a change in the nature of the viscous effects between the simulated and physical tests.

Finally, some methodological issue with the torque measurement might result in an apparent loss in torque (such as the issue of the "Hold function" which is described in Appendix D). The dynamometer may be analyzed to confirm that further issues do not exist which must be addressed.

In section 6.2.1, it was determined that the largest source of torque error must be some function of flowrate. Among the possible sources of error that have been discussed thus far, only two are consistent with this analysis of the data. Firstly, some methodological issue with the dynamometer, related to the magnitude of airflow, could account for a loss in torque. Failing that, the only remaining solution which comports with data trends is an increased shear friction on the helical blade surface, explained by an improper application of the similarity laws.

The consistency of the pressure results suggests that any methodological error in the CFD setup is not a major source of error in the model. Based on this assumption, the dynamometer must be assessed in order to identify some plausible source of error which would explain the discrepancy in measured torque.

6.2.4 Torque measurement discrepancy related to a sail force applied to the cloth tension strap

One possibility was investigated which may explain a torque error which correlates to air flowrate. Air flow leaving the calibration rig, equipped with the turbine rotor and duct under test, then impinged on the cloth belt coupling the friction drum to the scales, and caused the belt to 'flap open' (like the sail on a boat) and to vibrate. It became

131

evident that these occurrences could convert to the application of an unexpected 'sail force' to the dynamometer friction belt that altered the dynamometer scale readings.

While it cannot be definitively stated how great an effect these sail forces had on the measured torque, it is a plausible explanation for the error behaviour which has been observed, in that the magnitudes of the unexpected forces would increase with flow rate. A mathematical exploration of this phenomenon has been undertaken, producing results which support the plausibility of the hypothesis. However, since the magnitude of the error cannot be simply measured and the occurrence of such behaviour constituted a flaw in the dynamometer design (use of a folded cloth belt), the explanation is considered somewhat speculative and so, the mathematical details have also been deferred to an appendix, Appendix E.

6.2.5 Fan Reynolds discrepancy and other surface shear effects

As previously discussed in section 2.5, there are certain conditions which must be met to ensure a proper application of the similarity laws. Namely, when the Fan Reynolds number associated with either turbine is less than 3000000, there may be a noticeable difference between the efficiency of the model and the efficiency of the scaled-up system.

Recall that conventional fans and turbomachines can often ignore this requirement, due to the fact that they typically operate well above this threshold. However, this prototype turbine device operates best in low flow, low rotation speed conditions. As such, it is particularly relevant to confirm that the "size effect" associated with this Fan Reynolds threshold does not greatly affect the accuracy via some error in the transformation.

Table 6.2: Tables of Fan Reynolds values for simulated and experimental setpoints

	D_b	ω^*	Re_F	$Re_F > 3000000$
	m	rad/s	--	Y/N
Simulated	0.03975	137.5	7178	N
	0.03975	125	6525	N
	0.03975	112.5	5873	N
	0.03975	100	5220	N
	0.03975	50	2610	N
	0.03975	40	2088	N
	0.03975	25	1305	N
	0.03975	7.54	394	N
Experimental	0.15	10.5	7785	N
	0.15	15.7	11677	N
	0.15	20.9	15569	N
	0.15	26.2	19461	N
	0.15	52.4	38923	N
	0.15	78.5	58384	N
	0.15	104.7	77846	N

Both the simulated and physical models used in this comparative study were below the threshold for all setpoints. While the magnitude of the difference in efficiency is not known, it cannot be treated as negligible as it would be in the fully turbulent case. Therefore, this size effect must be explored in order to determine whether it is a plausible explanation for the torque error which has been observed.

As it is explained in Pelz and Stonjek (2013), the boundary layer of a fan's rotor is altered by the change in size and speed of the fan (see Figure 6.6). To wit, the greater speed of the rotor will result in an imbalance in the thickness of boundary layers due to the ratio of flow to rotation. In a fan system, this imbalance would be corrected by increasing the flow until the boundary layers on the pressure and suction sides of the blades are made even again. As a result, the flow angle, β, is optimized (made equal to the attack angle of the rotor) at a greater flowrate (depicted as flow coefficient, φ). Thus, for fans, size effect can be understood in practical terms by the increase in pressure which is required to correct the flow.
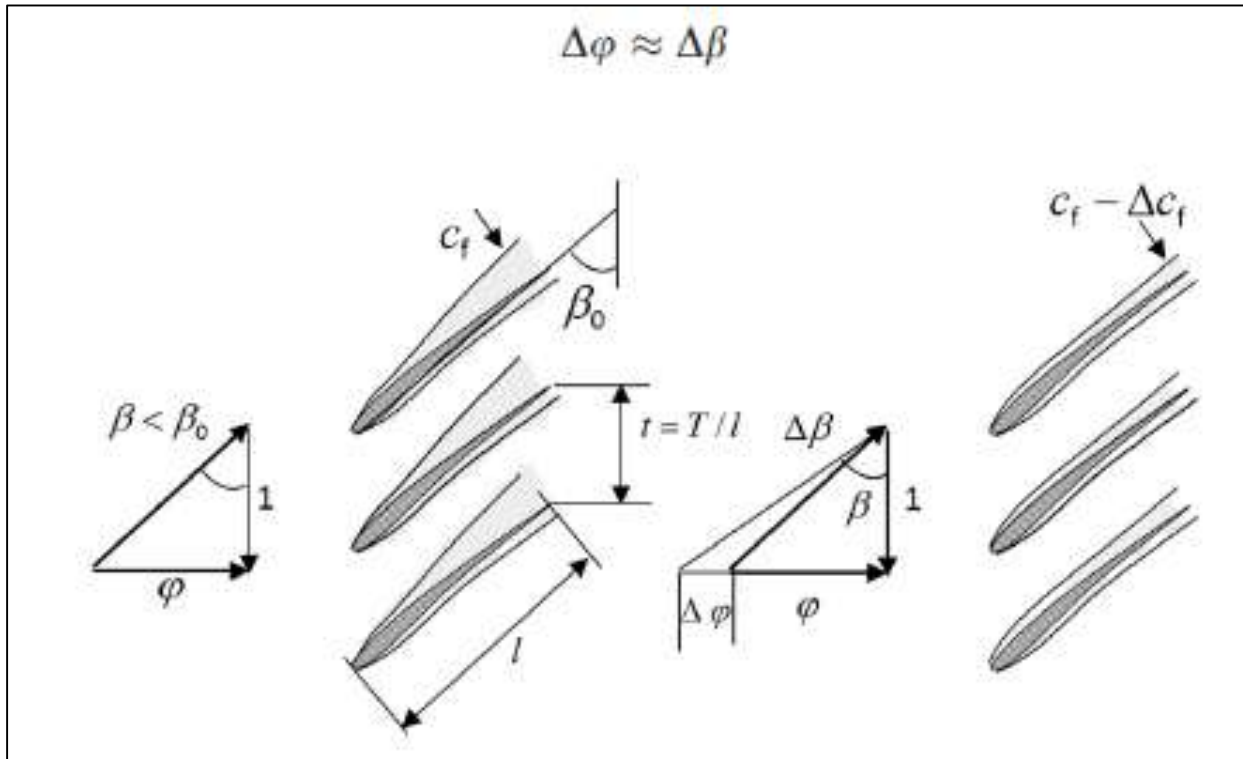
Figure 6.6: Correcting for size effect in a fan system, visualized with boundary layers (Pelz & Stonjek, 2013)

However, size effect may also be understood as a difference in the viscous torque applied to the rotor. The scale of the contours and the difference in surface roughness (relative to a larger size) will result in a different shear friction behaviour on different sized rotors. A difference in shear friction would be observed as a difference in the torque due to the viscous resistance on the surfaces of the rotor. This is of greater concern in turbines since power is supplied to the turbine by the fluid (instead of to the fluid by a fan). As a result, power may be lost before it can be extracted by the turbine's rotor. In contrast, a fan would simply supply more power to the rotor, thus increasing the air power supplied to the flow.

Note that, in the testing of this prototype turbine, the flowrate can not be changed to accommodate changes in boundary layer. Data setpoints are based on a constant flow and rotation. Practically speaking, this means that some resistance torque must be applied to the rotor at a given flowrate to achieve the desired rotation, whether or not the entirety of that torque can be measured by the dynamometer. This means that the portion of that overall resistance torque which may be measured will decrease, equal to any increase in viscous torque. The other practical consequence of maintaining a constant flowrate is that any change in pressure could only be the result of a change in the system resistance associated with the rotor. If a change in the boundary layer of the rotor results in a greater system resistance, then the air power delivered to the system must be increased to maintain the flowrate.

The disparity between the expected results and the observed results cannot be conclusively attributed to an increased shear friction in the physical experiment. However, the pressure and torque behaviour are consistent with

this theory. At the least, it must be acknowledged that the change in shear friction will have a non-negligible effect on the system since the Fan Reynolds threshold has not been met (as demonstrated in Table 6.2).

At first blush, it might seem that the use of non-dimensional coefficients would bypass the possibility of this error, since it is ostensibly a prediction error caused by improper use of the similarity laws. However, it must be stressed that the discrepancy is not inherent to the similarity laws but is in fact the reason why such an application is improper. Referring to the works of Pelz and Hess (2010) and Pelz and Stonjek (2013), the discrepancy between fans/pumps at different Reynolds numbers is depicted using these same non-dimensional coefficients. (Recall that Figure 2.12 plots efficiency against a non-dimensional flow coefficient). It is known that some discrepancy exists. It is also known that the discrepancy will become more significant in low-Reynolds flows. What remains unknown is the magnitude of the discrepancy. In Patil and Morrison (2019), the maximum error observed in terms of head is approximately 8% of the measured value. While this should not be applied directly as an estimate of maximum torque error here, it does offer an idea of the possible magnitude of such an error.

With that said, the maximum observed error in Table 6.1 is 60.5%, and it does not seem plausible that shear friction could be responsible for such a large error in torque. Still, if no other source of error can be identified which correlates to flowrate (section 6.2.1) and which would result in a sufficient magnitude of error, then size effect must be treated as a plausible source of error.

6.2.6   A check on results with Euler's turbomachine equation

While it is possible that there has been some mistake in the implementation of the CFD, the consistency of the pressure results (see Figure 6.3) suggests that this would not be a major source of error in the model. However, this assumption may be verified to some degree by attempting an independent check using Euler's turbomachine equation. Another independent calculation was undertaken using the steady flow energy equation. Although the calculation was consistent, the observable it predicted was a temperature difference across the turbine which was not physically observed on the experimental rig so its value is moot and the material is deferred to Appendix F.

In section 2.1.1, Euler's turbomachine equation was given:

$$T = \dot{m}(r_2 v_{2,t} - r_1 v_{1,t}) \tag{6.1}$$

This relates the torque developed by an ideal turbine rotor to the difference in tangential velocities between inlet at station 2 and outlet at station 1 (for a turbine). Euler's turbomachine equation will estimate torque developed by the turbine completely independently of the CFD methodology or the prototype experimental methodology reported hitherto. Consequently, applying the Euler turbomachine equation to the case of the helical air turbine rotor discussed herein, as is done in this section, serves as a 'reality check' that all with well with the CFD, and hence the overall experimental analyses. As the Euler turbomachine equation considers ideal impeller/rotor behaviour, it will be applied to the CFD simulation results, as these also represent an idealized version of the experiment.

With reference to case 2AI-9 (where the impinging axial velocity was 15 m/s and the angular velocity was 100 rad/s) as well as the rotor geometry, the velocity diagram in Figure 6.7 can be constructed, following the constructions set out in Figure 2.2 and Figure 2.3. For the CFD prototype, the rotor outer radius is r_o = 0.020 m and the inner radius at the shaft is r_i = 0.003 m.
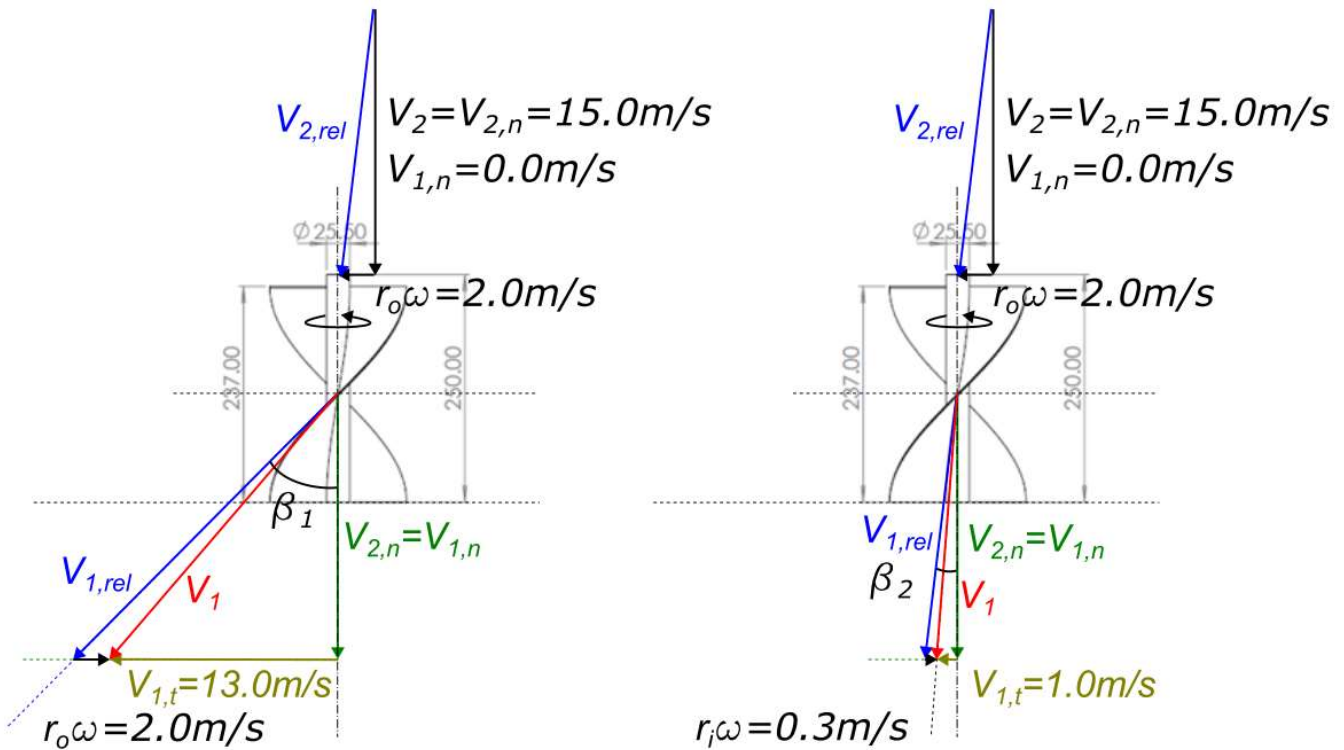
Figure 6.7: Velocity diagrams for the blade profile at the blade tip and the blade profile at the shaft

At the inlet, the velocity of the air relative to the blade is $V_{2,rel}$, the absolute velocity of the air is V_2, and there is no component of the absolute velocity of the air in the tangential direction. At the trailing, outlet, edge of the helical blades, the air is assumed to flow off them in at angle b, parallel to the blade surface. Mass conservation along the duct containing the rotor requires that $V_{2,n}$ = $V_{1,n}$, so that the intersection of the perpendicular to $V_{1,n}$ and the blade tangent defines the velocity of the air relative to the blade at outlet, $V_{1,rel,}$. The blade edge velocity varies radially along the blade from the rotor shaft (hub), $v_{b,i}=r_i w$ to the blade tip, $v_{b,o}=r_o w$ so that distinct velocity triangles need to be prepared for these two locations, to determine the absolute velocity of the air at outlet, V_1 at these locations. The tangential component of the absolute velocity at outlet, $V_{1,t}$ is also then determined. For the inlet conditions and rotor speed, these are 13.0 m/s and 1.0 m/s at tip and shaft, respectively, and the variation is assumed linear between these locations. Given this, the average value of $V_{1,t}$ is 7.0 m/s. For duct diameter, 0.0401 m and a uniform rotor radius between inlet and outlet, $r_2 = r_1$, with air density 1.2 kg/m³, (2.3) yields:

$$T = 1.2 \times 15.0 \times \pi \times \left(\tfrac{0.02005}{2}\right)^2 (0.02005 \times 0 - 0.02005 \times 7) = 0.0032 \text{ Nm} \tag{6.2}$$

which compares well with the CFD computed value of 0.0035 Nm for case 2AI-9 and suggests that overall, simulation and experimental methodologies are sound.

6.3   Recommendations for methodological improvements

As discussed in section 6.2.1, there is a discrepancy in the torque results. While the exact sources of this discrepancy have not been definitively identified, it will be possible to eliminate some of the identified sources of error and mitigate others.

First and foremost, the sail force error described in section 6.2.4 (and further explored in Appendix E) should be eliminated as a possible source of error. This can be accomplished by using a better quality of dynamometer.

The size effect associated with the Fan Reynolds threshold (section 6.2.4) may also be eliminated as a source of error. Any subsequent experiments should observe the Fan Reynolds threshold wherever the similarity laws will be applied.

In any case where this is not possible, additional simulations may be produced which would conclusively validate the implementation of the various data reductions performed in this thesis. First, the CFD simulation may be validated by running a simulation with the transformed dimensions. By comparing such a simulation to the second order curves in section 3.6, that were used to interpolate the expected results, the magnitude of the size effect can be examined. Next, the physical experiment may be validated by adding the bearing mounts into the CFD simulated geometry. By comparing to the reduced physical results tabulated in section 5.2.1, the pressure change associated with the bearing mounts then may be eliminated from consideration.

Bearing friction was deemed not to be a major source of error (see Appendix D 4.6), yet its effects may be increased under higher flow conditions and at higher rotational velocities. This effect can be mitigated by using higher quality bearings. Regardless of the quality of the bearings used, a more precise method for characterizing the bearing loss can help to eliminate the friction error from the results.

Other mechanical losses may also be worsened at higher rotational velocities and higher flowrates. As discussed in section 4.5.3, a greater flow will require a greater resistance torque to reach the same rotational setpoint. This in turn will require a greater normal force on the friction drum, which poses a greater risk of bending the shaft. To allow for the tip speeds that would be required to exceed the Fan Reynolds threshold, a stiffer shaft must be selected to mitigate bending effects.

As discussed in section 6.2.2, possible sources of pressure error that have been identified in the physical experiment include the bearing mount pressure reduction, and the pseudo-nozzle effect of the swirling flow in the straight pipe.

To account for the bearing mount pressure loss, the most direct solution would be to add the bearing mounts to the CFD model. Alternatively, a more accurate predictive model might be generated by repeating the same method described in section 4.5.3, but with the center holes entirely obstructed (previously suggested in section 6.2.2).

Regardless of the selected course of action, it is recommended to redesign the arms and edges of the bearing mounts to minimize added resistance. One possible design change that would have such an effect would be to change the cross-section of the supports to a "tear drop" profile.

To account for the pseudo-nozzle effect observed in section 3.3.5, which may be present in the physical experiment, subsequent turbines might incorporate pre-swirlers in their design, or flow straighteners at the trailing edge of the rotor.

Additionally, these behaviours may be more readily isolated if there is a greater distance (greater than one duct diameter) between the leading edge of the rotor and the duct inlet, and between the trailing edge of the rotor and the duct exit. If the dimensions of the duct allow for it, it is also recommended that pressure tappings be added to the duct directly. With the correct spacing, this would isolate the rotor from the pressure effects of the bearing mounts altogether, as well as any pressure effects at the duct exit.

Finally, tip leakage may influence the pressure behaviour associated with the rotor. The obvious solution is to reduce the leak area. The more precisely the diameter of the rotor can be matched to the diameter of the duct, the less the flow will be able to escape past the edges of the rotor. Once again, a stiffer shaft will be necessary to reduce deflection.

7   Conclusions

This chapter will summarize the outcomes of the work and proposes further work that might be undertaken to build upon it.

7.1   Review of thesis aims

This section will seek to establish whether the aims of this thesis (see section 1.3) have been achieved.

7.1.1   Characterization of performance using CFD simulation

The simulated data has been used to characterize the performance of the turbine design, in the form of a set of performance curves. Note that the following performance curves have been transformed to a constant rotational setpoint, while maintaining the dimensions of the simulated geometry. Aside from the SL transformation (section 2.4), no other reductions (from section 3.6) have been applied to the data.

As discussed in section 6.2.4, the application of the Similarity Laws is imperfect since the simulated conditions are below the Fan Reynolds threshold. Nevertheless, these performance curves represent an important first step in characterizing the overall performance of the device.
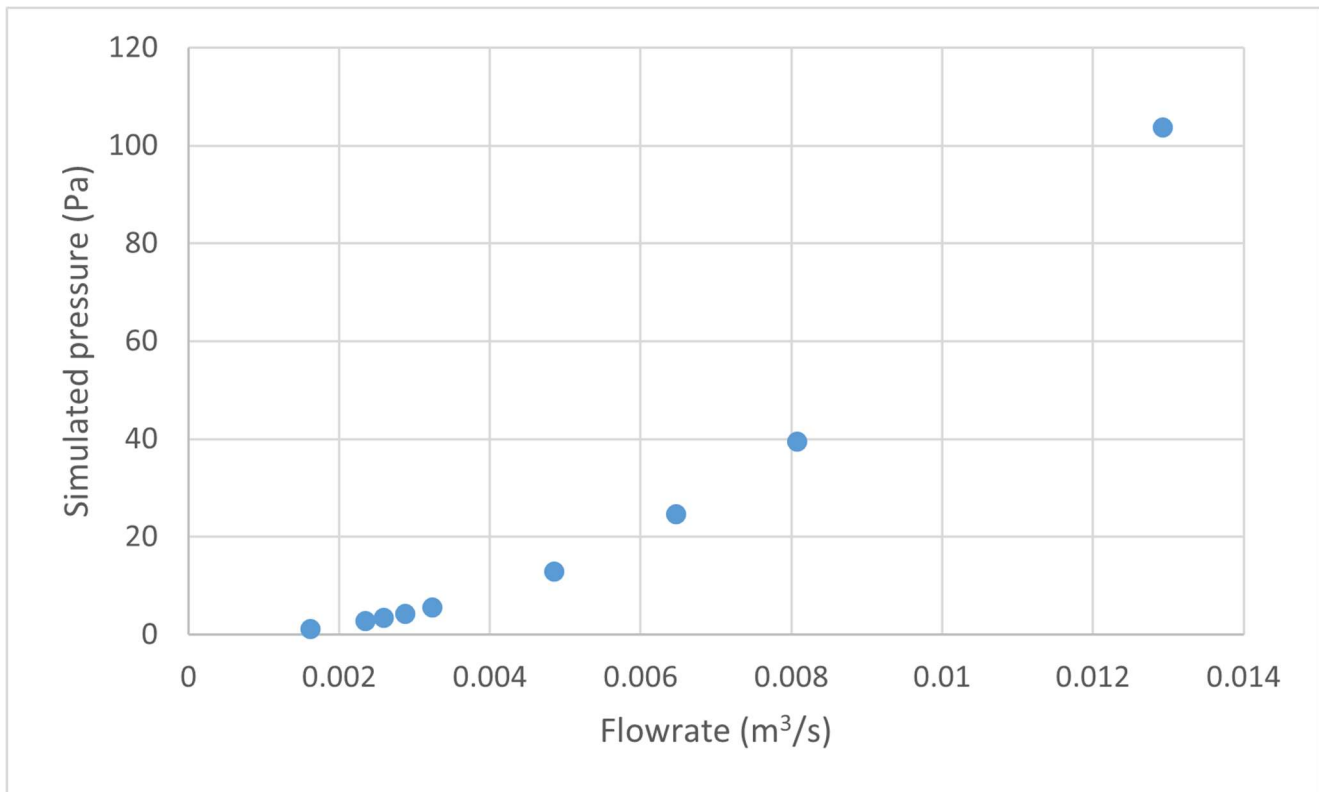
Figure 7.1: Performance curve (pressure vs flowrate), simulated 0.0401m diameter, transformed to 250 rpm setpoint
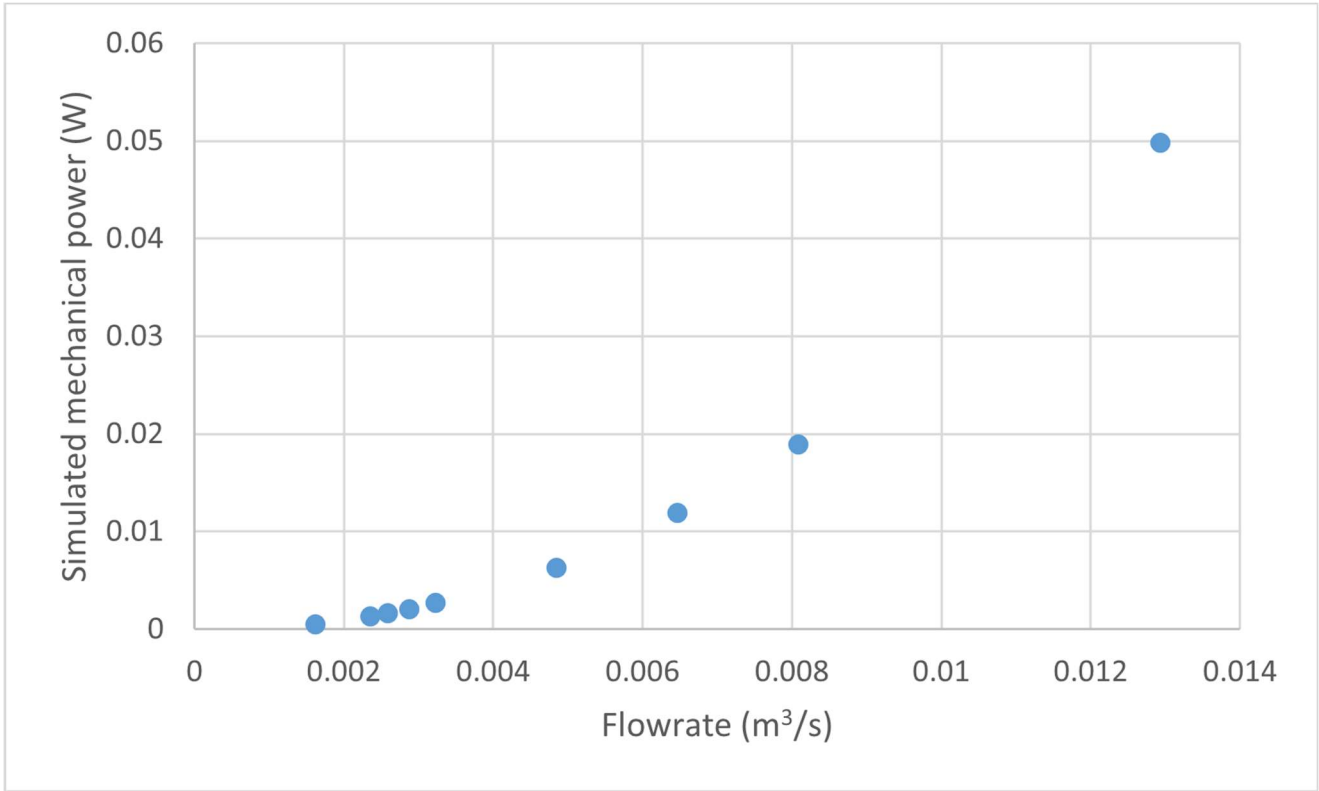
Figure 7.2: Performance curve (mechanical power vs flowrate), simulated 0.0401m diameter, transformed to 250 rpm setpoint
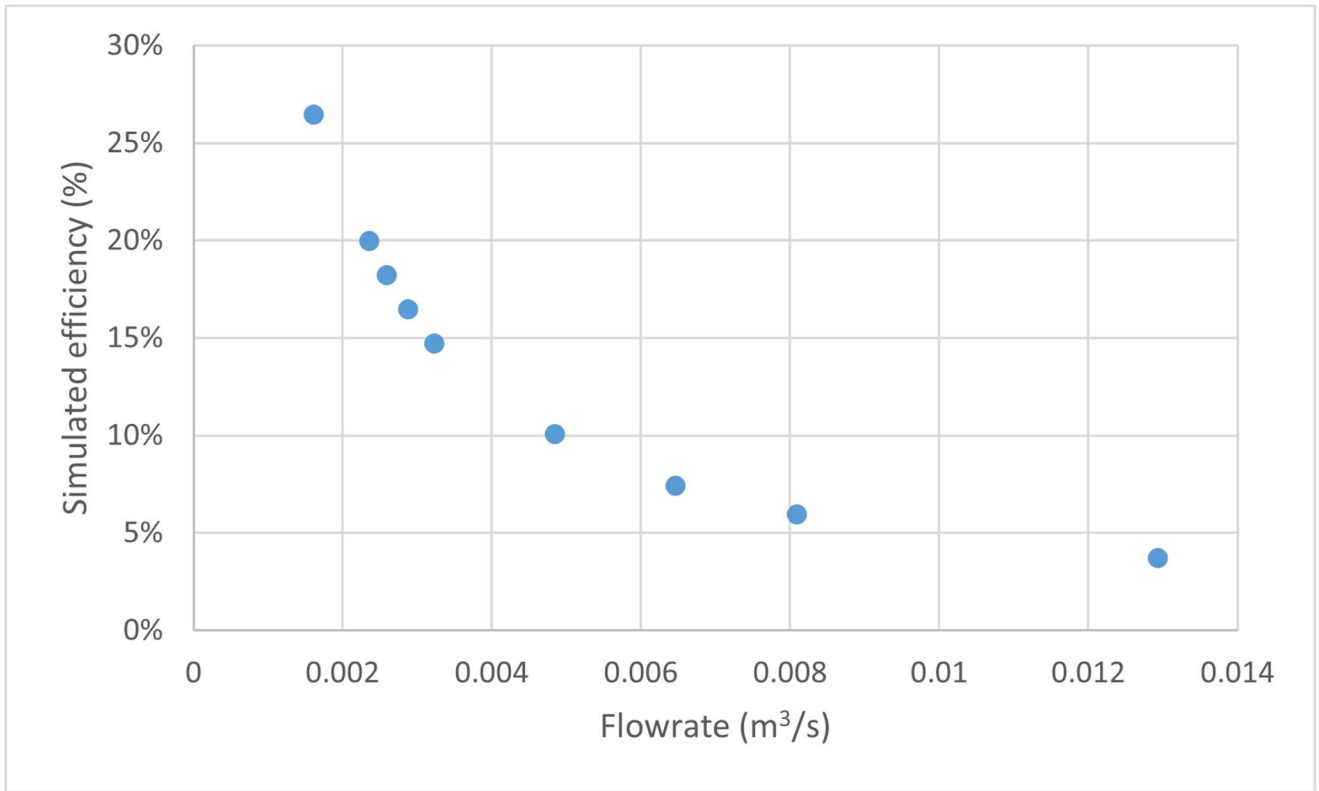
Figure 7.3: Performance curve (efficiency vs flowrate), simulated 0.0401m diameter, transformed to 250 rpm setpoint

140

7.1.2 Characterization of performance using physical testing

The data from the physical experiment has been used to characterize the performance of the turbine design, in the form of a set of performance curves. Note that the following performance curves have been transformed to a constant rotational setpoint, while maintaining the dimensions of the physical geometry. Only the reduced results (from the data selected in section 5.2) were included.

As discussed in section 6.2.4, the application of the Similarity Laws is imperfect since the simulated conditions are below the Fan Reynolds threshold. Nevertheless, these performance curves represent an important first step in characterizing the overall performance of the device.
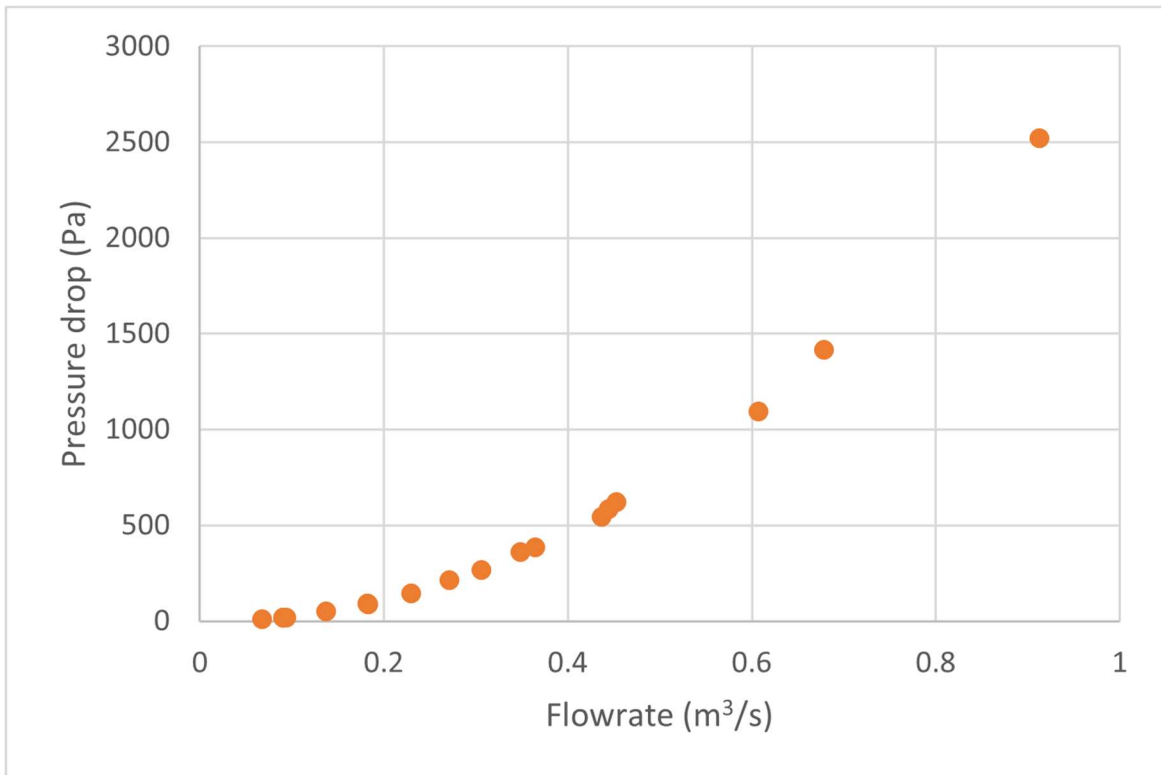
Figure 7.4: Performance curve from reduced physical results (pressure vs flowrate), 0.15242m diameter, transformed to 250 rpm setpoint
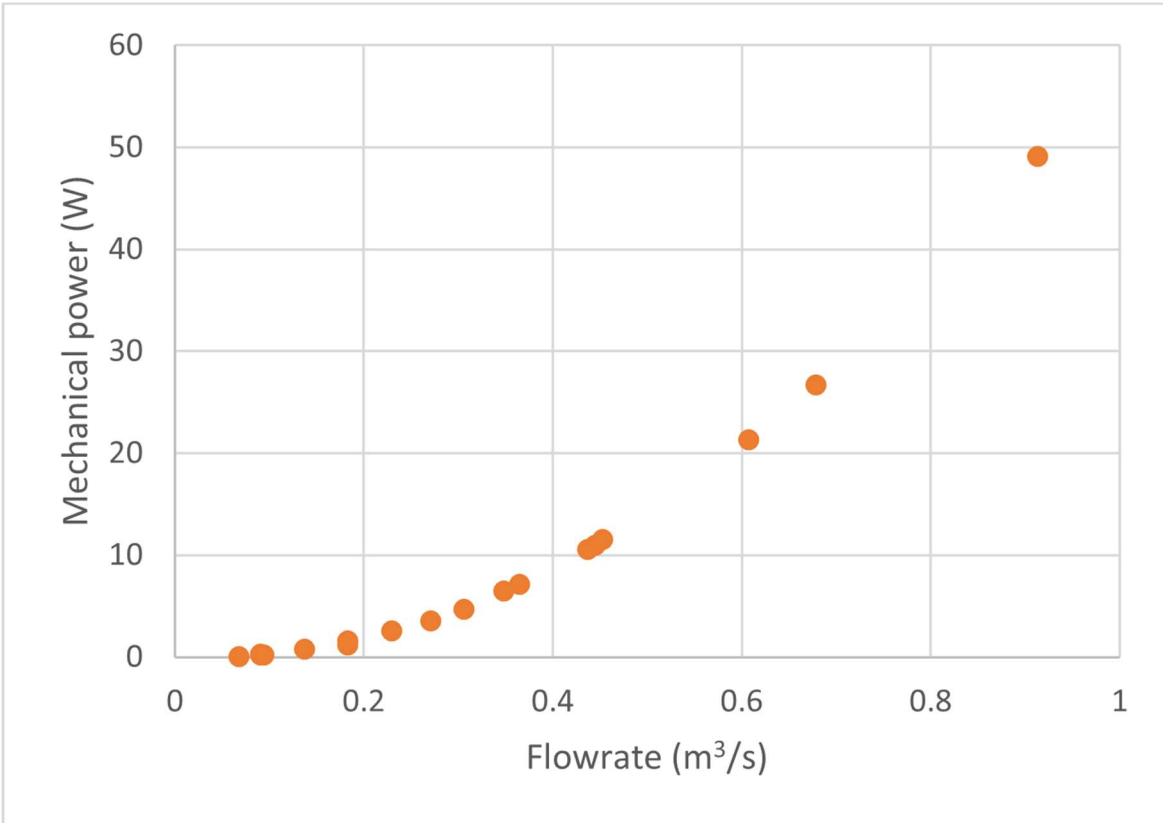
Figure 7.5: Performance curve from reduced physical results (mechanical power vs flowrate), 0.15242m diameter, transformed to 250 rpm setpoint
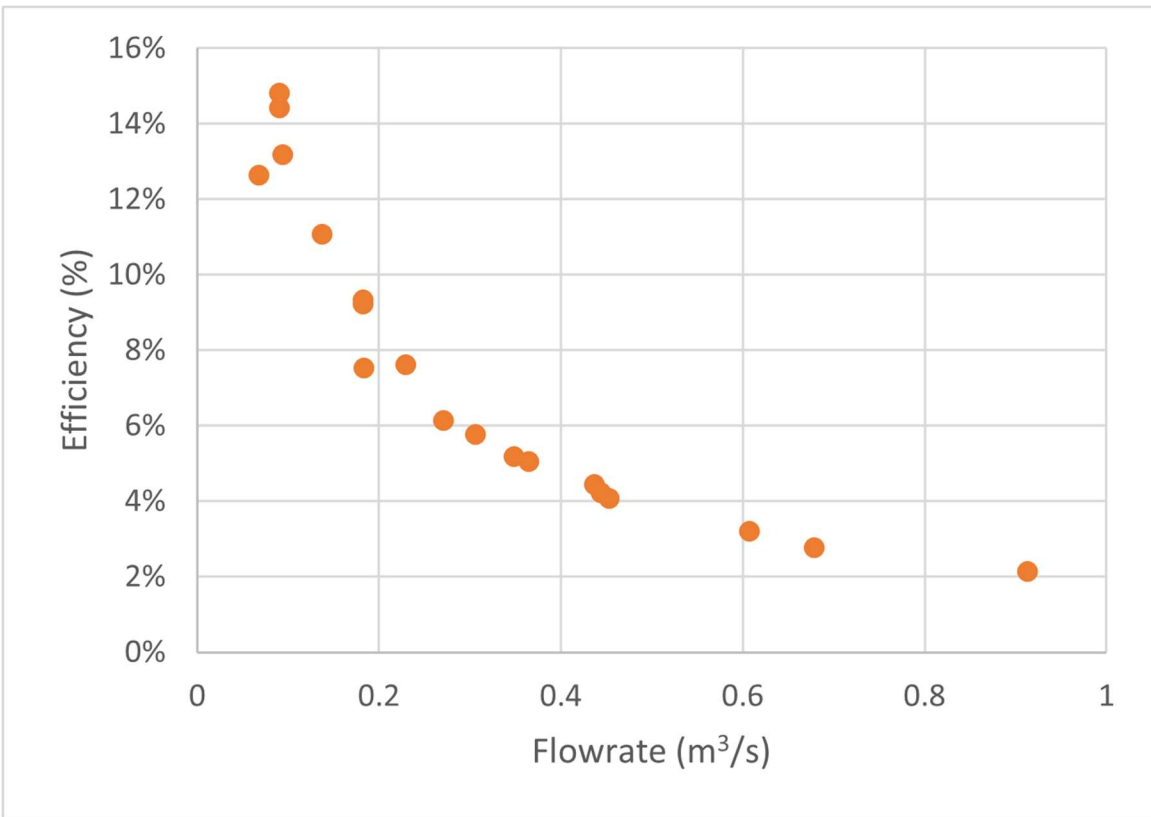
Figure 7.6: Performance curve from reduced physical results (efficiency vs flowrate), 0.15242m diameter, transformed to 250 rpm setpoint

142

7.1.3   Agreement between simulated and experimental results

As shown in section 6.1, there is consistent agreement between the two data sets. As previously discussed in section 2.6, it is difficult to directly compare performance data that has been collected over a variety of operating points. For this reason, nondimensionalized coefficients for flow, φ, pressure, ψ, and power, Γ, may be used, along with efficiency, η, to compare the data in a standardized way.

These nondimensionalized performance curves represent a good agreement between the CFD based model and the physical test but suggest an issue with the quality of the dynamometer that was created for experimentation, particularly in terms of the torque readings. This is encouraging when considering CFD as a tool for use in future performance analysis of the prototype device.

Companion plots have been presented in Appendix E, along with a lengthy explanation of a proposed torque reduction. They demonstrate a much better agreement between the two sets of torque data and support the "sail force" hypothesis introduced in section 6.2.4.
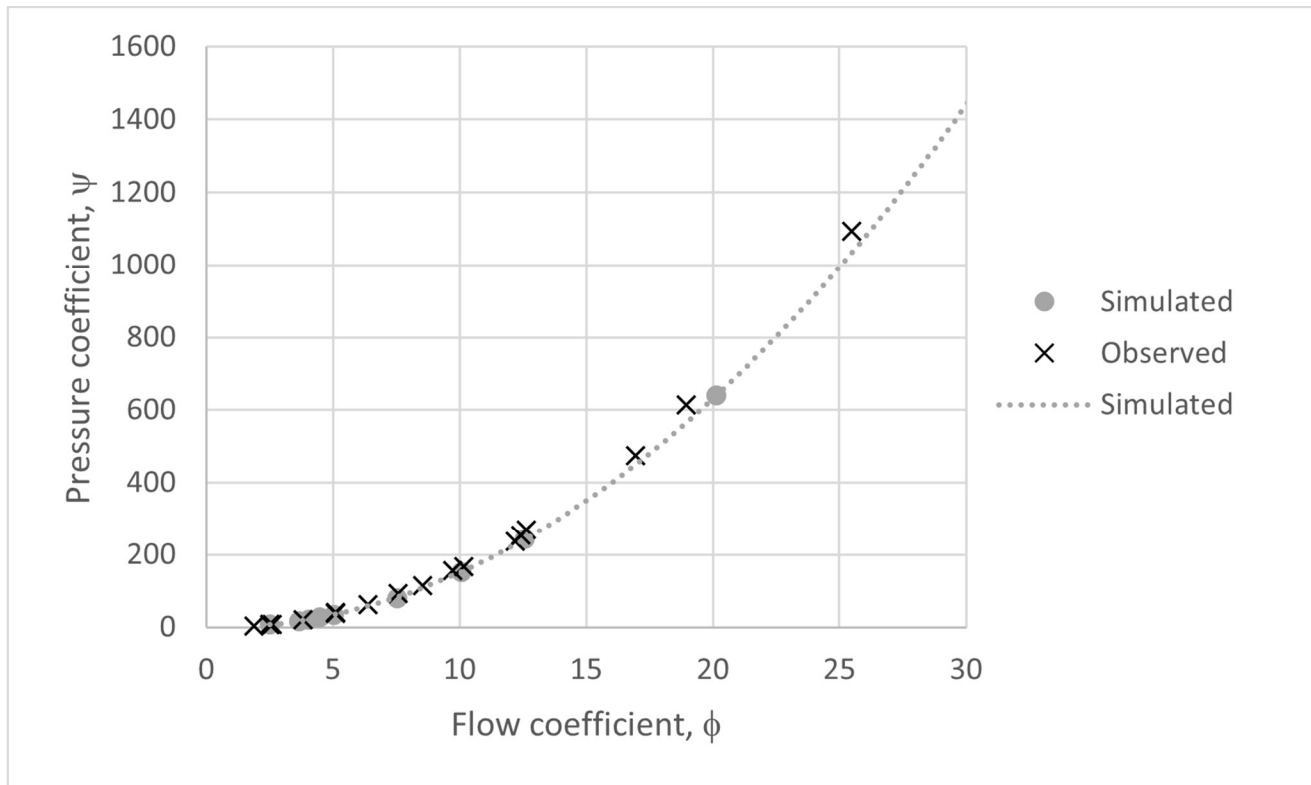
Figure 7.7: Comparison of performance curves using nondimensionalized coefficients (pressure vs flowrate)
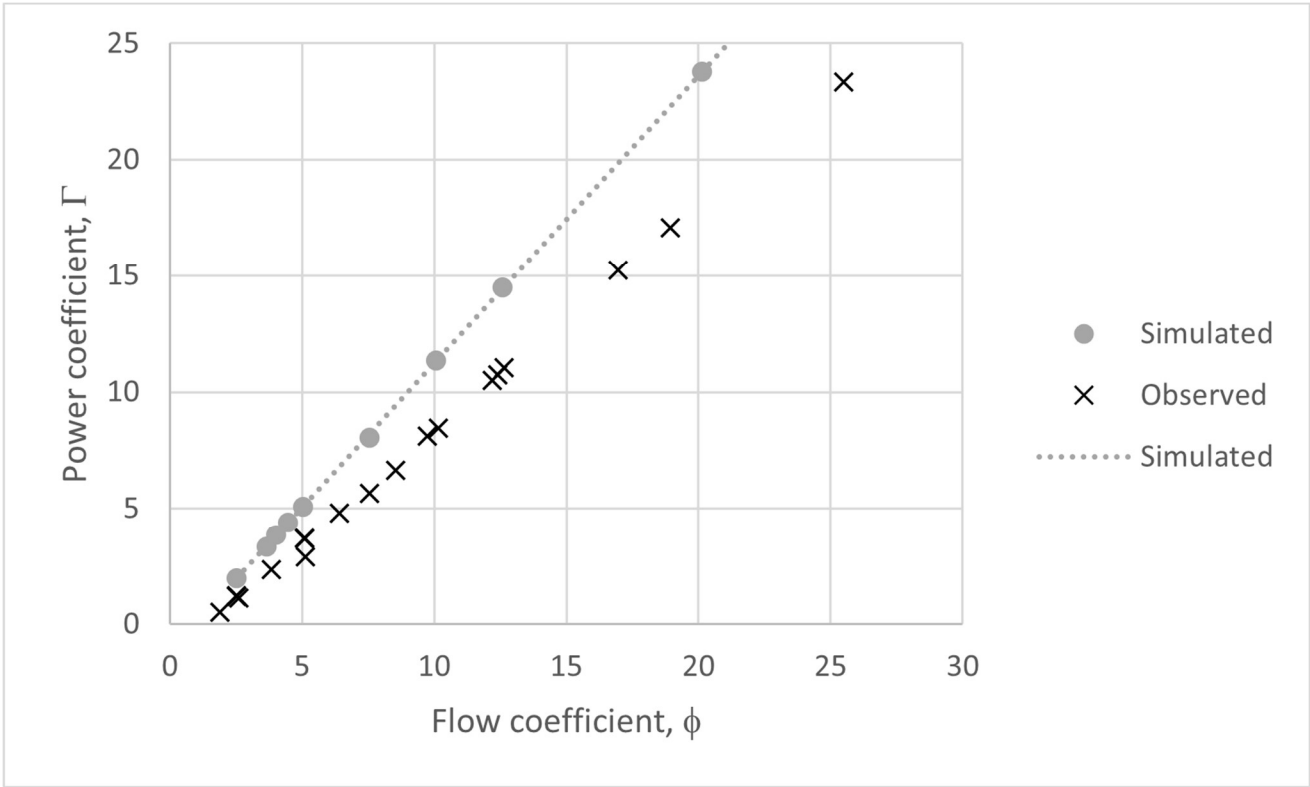
Figure 7.8: Comparison of performance curves using nondimensionalized coefficients (mechanical power vs flowrate)
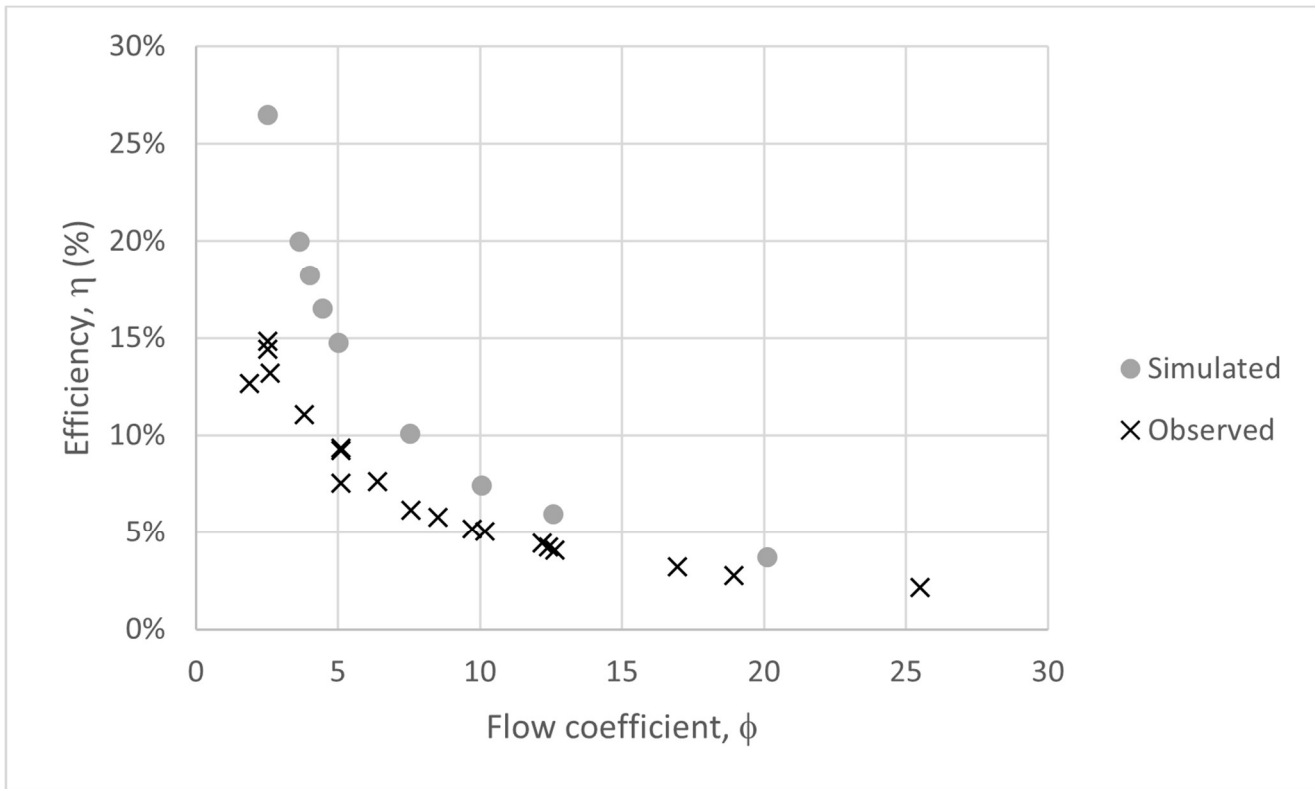
Figure 7.9: Comparison of performance curves using nondimensionalized coefficients (efficiency vs flowrate)

7.2 Answers to key research questions

Table 7.1: Sample of mechanical power and efficiency results, by desired setpoint

v^*	N^*	$\dot{W}_M$	η
m/s	rpm	W	%
10	500	1.83	13.2
15	500	5.80	11.1
15	750	7.00	14.8
15	750	6.82	14.4
20	200	6.06	4.24
20	250	7.10	5.05
20	500	12.3	9.23
20	500	12.5	9.34

As seen in Table 7.1, power can be generated at highway speeds. In terms of the thesis' overall objective of producing a device that can generate power for auxiliary vehicle systems, the detailed experimental and computational investigations have shown that the concept remains feasible. With further exploration and optimization of the device, the ideal conditions for operation can be determined. That information will help to determine whether a cost-effective implementation of the device exists.

7.2.1 What is the expected performance of a helical turbine?

The characteristic performance curves for the device (see section 7.1) do not seem to reach the maximum efficiency of the ducted rotor configuration. As such, it is unclear whether there can be any definite benefit from this type of helical turbine. While the CFD analysis (see section 2.2) suggests that there is a limited benefit to the helical shape under these operating conditions, further research is required to determine the optimum performance of the device. A more rigorous performance analysis could offer a conclusive determination as to the advantages and disadvantages of a ducted helical rotor over a ducted rotor with a conventional blade.

7.2.2 What design methodology should be adopted for helical turbines?

Only one configuration of the device was used in physical experimentation. As such, it will require further research to determine an optimal configuration for a given application of the turbine. CFD analysis has proven to be a powerful and reliable tool for such an endeavour. Over the course of this work, the experimental results have been verified by error checking. A supervisor performed an independent check of the trends in the experimental results of both the physical and CFD experiments. It was noted that, even with the same data and methodology, specific policy choices could result in a difference in the results (such as the use of blade tip radius as opposed to the duct radius, or approximating error reductions with quadratic as opposed to cubic functions). While the trends remained consistent, there was a magnitude difference in the pressure coefficient, ψ, of up to 6%. This observation highlights the importance of a consistent methodology when comparing performance data between different turbines (or other turbomachinery). While the comparative trends of like data sets (taken with consistent methodology) seemed

consistent with each other, comparing sets that were reduced with different methodologies would have produced wildly different trends.

In terms of specific conclusions that can be drawn from the experiment, some interesting observations can be made concerning the use of diffusers in the prototype design. As seen in section 3.3.5, varying the diffuser angle under uniform operating conditions can greatly increase the efficiency of the device.
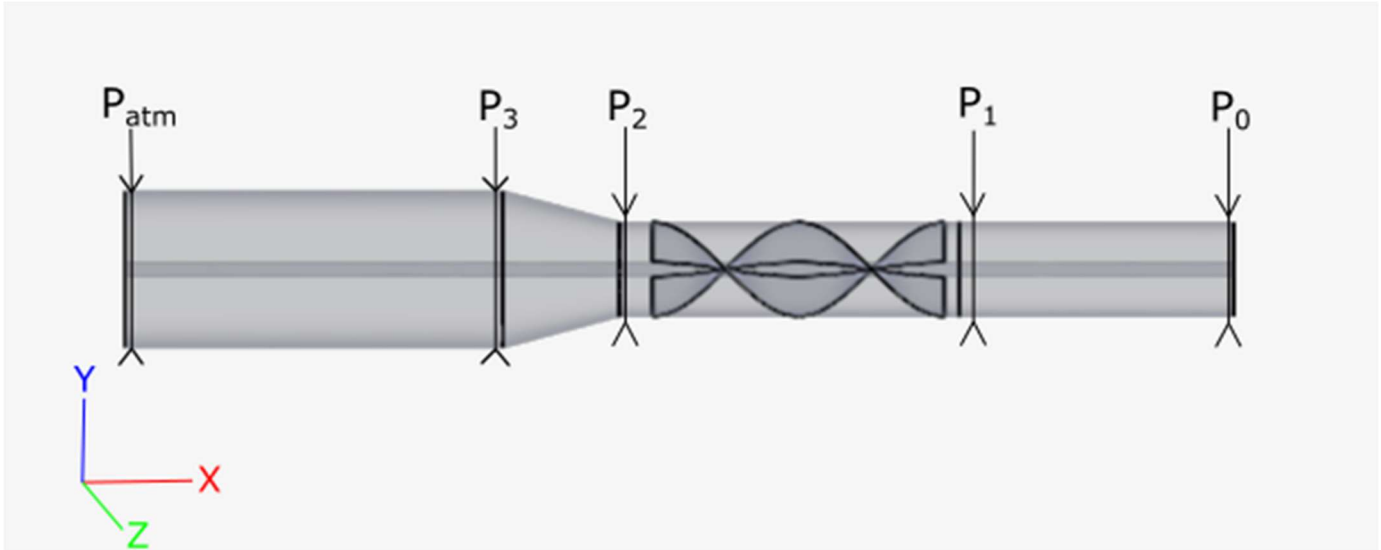
Figure 7.10: Positions of virtual instruments, placed for diffuser pressure analysis (geometry 4 used for illustration)

Table 7.2: Pressure behaviour over the entire duct system, for each diffuser geometry

Half angle of diffuser	v_{in}	P_1	P_3	$P_1 - P_3$	T_α	$\eta_{sim}{}'$
degrees	m/s	Pa	Pa	Pa	Nm	%
4.7	5	7.513	-0.8076	8.321	0.000299	57.2
15	5	9.456	-3.557	13.01	0.000295	36.1
45	5	9.015	-6.145	15.16	0.000289	30.3

Note that, since v_{in} and ω_α remain constant, efficiency over the entire duct system is most affected by changes in the pressure drop over the duct.

While this is not the conventional way to calculate the efficiency of a turbine, it is a useful depiction when considering which design will simultaneously maximize power generation and minimize added pressure resistance. For a practical implementation of the vehicle-mounted device, this would be crucial.

7.3   Further work

Aside from the suggested improvements outlined in section 6.3, there are many opportunities for further study of the device. Some suggested topics include:

- The influence of shear friction under low Fan Reynolds conditions may be investigated in future simulations by specifying a surface behaviour for the rotor.

- The influence of tip leakage may be investigated in future simulations by generating a new, finer mesh; especially, with more elements between the blade edge and the duct wall.
    - As mentioned in section 3.3.3, the mesh that was generated near the blade edge boundary was constrained so that at least two elements would always exist between the rotor and the duct wall.
- Further experimentation may reveal the optimal configuration of the device (nozzle, diffuser, etc.) for practical use under different applications (see section 7.4).
    - Experimentation with different atmospheric conditions, greater flowrates (including supersonic flows), and with different working fluids may produce different optimal configurations for different applications.
- Implementation of a shutter admission should be considered, linked to the acceleration of the vehicle, so as to minimize any added energy consumption associated with the device.
    - Optimal implementation of the shutter admission can be investigated, by comparing performance under different behaviours.
- Any practical application of the device must overcome the resistance it adds to the vehicle upon which it is mounted.
    - In section 1.1, it is suggested that this loss may be mitigated by taking advantage of existing areas of a vehicle's form which already add resistance to the overall vehicle. However, some resistance will always be added and in future it will be necessary to quantify this loss of power and conclusively determine whether an optimal implementation may overcome such a loss.
- A vehicle in motion would result in a negative pressure at the outlet of the device in some cases; the effects of this behaviour may be investigated in future experiments.
- As previously mentioned in section 3.3.9, it may be fruitful to explore the start-up performance of the device using a transient model in subsequent CFD experiments.

7.4   Practical applications of the prototype device

The CAD model that was used for CFD analysis, and to create the physical test piece, represents a general case implementation of the device. Should the device be deemed viable for practical usage, many variants may be considered based on specific applications. This section outlines a list of proposed applications of the device, to be explored in future experimentation.

7.4.1   Automobiles

The basic application of the device is to be mounted on automobiles. This is the simplest form of the device, in practice, because it involves the fewest variables.

The scale of the vehicle limits the maximum size of the device, and the relatively low speeds (highway) of motor vehicles means the fluid can be treated as incompressible. Additionally, operating on the ground means that atmospheric conditions should remain within a standard range.

A distinction between acceleration and deceleration of the vehicle provides an important clue toward device functionality. Whereas resistance should be minimized during acceleration, it becomes irrelevant while braking, since the brakes are already intentionally resisting the motion of the automobile. This provides an opportunity to derive power without greatly affecting overall vehicle efficiency.

7.4.2 Aircraft

The next proposed application is an extension of the first. Mounting the device on aircraft expands upon the variables that must be considered.

A much wider range of vehicle sizes and speeds will necessitate different scales and configurations of the device. Aircraft travel at speeds which range from transonic to supersonic, therefore requiring consideration of compressibility behaviour. Varying altitudes would also cause greater fluctuations in atmospheric temperature and pressure.

A distinction between takeoff and cruising would be analogous to the delineation between acceleration and deceleration in automobiles. There are greater opportunities for power generation in situations where the vehicle is expending less energy to remain in motion.

7.4.3 Watercraft

The final vehicle application introduces another variable to the design. By mounting the device on watercraft, the fluid medium is changed to water.

With a range of sizes and speeds comparable to aircraft, different scales of the device are necessary once again. The density and properties of water provide new challenges to the design. Acceleration and resistance in the denser medium present an obvious departure from the first two applications.

However, it must be noted that a similar turbine (Archimedean Screw, see section 2.2.1) accounts for this difference in density by allowing only the bottom half of the helical rotor to be acted upon by the denser fluid. This suggests that the device should be installed at water level. A fully submerged configuration might result in an entirely different configuration.

7.4.4 Stationary ducted helical turbine in areas of known flow direction

One limitation of stationary, ducted turbines is that they require a consistent, known direction of fluid flow. Short of conditioning the flow at intake (as with the Invelox ducted turbine discussed in Hosseini & Ganji, 2020), this can be achieved with a stationary turbine by mounting it in a high flow area created by pre-existing artificial environments.

To wit, infrastructure in large cities can create such "wind tunnel" effects in highway underpasses or on a main thoroughfare between skyscrapers. The operating conditions would be similar to the automobile application but would lack the negative pressure at outlet associated with a moving vehicle.

8 References

AMCA. (2012). *Fan and Air System Applications Handbook.* Air Movement and Control Association International, Inc.

AMCA. (2007). *Fans and Systems, AMCA Publication 201* (Vol. 02)*.* Air Movement and Control Association International, Inc.

Ariff, M., Salim, S. M., & Cheah, S. C. (2009, September 11). *Wall y+ Approach for Dealing with Turbulent Flows over a Surface Mounted Cube: Part 2 - High Reynolds Number* [Paper]. Seventh International Conference on CFD in the Minerals and Process Industries, Melbourne, Australia.
https://www.researchgate.net/publication/209105898_Wall_y_Approach_for_Dealing_with_Turbulent_Flows_over_a_Surface_Mounted_Cube_Part_2_-_High_Reynolds_Number

Bardina, J. E., Huang, P. G., Coakley, T. J. (1997). *Turbulence Modeling Validation, Testing, and Development.* NASA Technical Memorandum 110446

Barnard, R. H. (2001). *Road Vehicle Aerodynamic Design: An Introduction* (2r.e. ed.). Gardners Books.

Bedford, A., & Fowler, W. (2007). *Engineering Mechanics: Statics & Dynamics* (5th ed.). Pearson.

Blue Tidal Energy. (2022). *Blue Tidal Energy*. http://bluetidalenergy.com/

Boyle, G. (2012). *Renewable Energy: Power for a Sustainable Future* (Third). Oxford University Press.

Burton, T., Sharpe, D., Jenkins, N., & Bossanyi, E. (2001). *Wind Energy Handbook* (1st ed.). Wiley.

Castellani, F., Astolfi, D., Peppoloni, M., Natili, F., Buttà, D., & Hirschl, A. (2019). Experimental Vibration Analysis of a Small Scale Vertical Wind Energy System for Residential Use. *Machines*, *7*(2), 35.
https://doi.org/10.3390/machines7020035

Cebeci, T., Shao, J.P., Kafyeke, F., Laurendeau, E (2005). *Computational Fluid Dynamics for Engineers.* Horizon Publishing Inc. ISBN: 0-9766545-0-4.

Cengel, Y., & Cimbala, J. (2013). *Fluid Mechanics Fundamentals and Applications* (3rd ed.). McGraw-Hill Education.

CFD Online. (2014, January 15). *Turbulence free-stream boundary conditions -- CFD-Wiki, the free CFD reference*.
https://www.cfd-online.com/Wiki/Turbulence_free-stream_boundary_conditions

Chaplin, R. A. (2009). *Thermal Power Plants* (Vol. 3). EOLSS Publishers Co. Ltd.

Cheng, A. H. D., & Cheng, D. T. (2005). Heritage and early history of the boundary element method. *Engineering Analysis with Boundary Elements*, *29*(3), 268–302. https://doi.org/10.1016/j.enganabound.2004.12.001

Crisalli, K. (2006). *AFRL Propulsion Directorate-Edwards Research Site*. AFRL Propulsion Directorate.
https://web.archive.org/web/20080626160619/http://www.pr.afrl.af.mil/aeolipile.html

Darling, D. (2016). *Pelton turbine*. David Darling.
https://www.daviddarling.info/encyclopedia/P/AE_Pelton_turbine.html

David, Š., Pavel, Z., Martin, H., & Pavel, R. (2015). Numerical and experimental investigation of swirling flow in a conical diffuser. *Epj Web of Conferences*. https://doi.org/10.1051/epjconf/20159202085

Eastop, T. D., & McConkey, A. (1993). *Applied Thermodynamics for Engineering Technologists* (5th ed.). Pearson Education.

Engineer's Edge. (2022). *Band Brake Design Equations.*
https://www.engineersedge.com/mechanics_machines/band_brake_design_13699.htm

Engineer's Edge. (2020). *Viscous Torque and Power on Rotating Shafts Equations and Calculator.*
https://www.engineersedge.com/calculators/viscous_torque_and_power_on_rotating_shafts_15252.htm

Florida Institute for Instructional Technology. (2012, February 15). *Hero's Simple Steam Turbine*. ClipArt ETC.
https://etc.usf.edu/clipart/77800/77844/77844_herostm_trbn.htm

Fluke & Cole Parmer. (2020, June 22). *How to Make a Duct Traversal Airflow Measurement.* Cole Parmer.
https://www.coleparmer.ca/tech-article/how-to-make-a-duct-traversal-airflow-measurement

Geurts, B. J. (2022). *Direct and Large-Eddy Simulation*. Walter de Gruyter GmbH & Co KG.

Gorlov, A. M. (1995). *Unidirectional helical reaction turbine operable under reversible fluid flow for power systems* (U.S. Patent No. 55451137). U.S. Patent and Trademark Office.

Greenshields, C. (2019, November 22). *Computational Fluid Dynamics | OpenFOAM*. CFD Direct.
https://cfd.direct/openfoam/computational-fluid-dynamics/

Greenshields, C. (2021, July 20). *OpenFOAM User Guide: CFD Direct, Architects of OpenFOAM.* CFD Direct.
https://cfd.direct/openfoam/user-guide/

Gulliver, J. S., & Arndt, R. E. A. (1990). *Hydropower Engineering Handbook*. McGraw-Hill.

Hau, E., & Renouard, H. V. (2006). *Wind Turbines: Fundamentals, Technologies, Application, Economics* (2nd ed.). Springer.

Hosseini, S. R., & Ganji, D. D. (2020). *A novel design of nozzle-diffuser to enhance performance of INVELOX wind turbine.* Energy, 198, 117082. https://doi.org/10.1016/j.energy.2020.117082

Idel'chik, I. E. (1984). *Handbook of Hydraulic Resistance.* Israel Program for Scientific Translations.

McPherson, M. J. (1993). *Subsurface Ventilation Systems*. Springer Publishing.

Menter, F. R. (1992). *Improved two-equation k-omega turbulence models for aerodynamic flows.* NASA Technical Memorandum 103975

Meyer, S. L. (1975). *Data Analysis for Scientists and Engineers* (First Edition). John Wiley & Sons.

Murad, J. (2020, November 6). *What is y+ (yplus)?* SimScale CAE Forum. https://www.simscale.com/forum/t/what-is-y-yplus/82394

Neutrium. (2020). *Cavitation in Restriction Orifices and Valves*. https://neutrium.net/fluid-flow/cavitation-in-restriction-orifices-and-valves/

Nuclear Power. (2021, October 25). *Moody Diagram - Friction Loss | Application | nuclear-power.com*.
https://www.nuclear-power.com/nuclear-engineering/fluid-dynamics/major-head-loss-friction-loss/moody-diagram/

Patil, A., & Morrison, G. L. (2019). Affinity Law Modified to Predict the Pump Head Performance for Different Viscosities Using the Morrison Number. *Journal of Fluids Engineering-Transactions of the Asme*, *141*(2). https://doi.org/10.1115/1.4041066

Pelz, P. F., & Hess, M. (2010). *Scaling Friction and Inertia Losses for the Performance Prediction of Turbomachines*. 13th International Symposium on Transport Phenomena and Dynamics of Rotating Machinery, Honolulu, Hawaii, USA. https://doi.org/10.26083/tuprints-00020950

Pelz, P. F., & Stonjek, S. S. (2013). The Influence of Reynolds Number and Roughness on the Efficiency of Axial and Centrifugal Fans—A Physically Based Scaling Method. *Journal of Engineering for Gas Turbines and Power*, *135*(5). https://doi.org/10.1115/1.4022991

Phelan, J. J., Russell, S. H., & Zeluff, W. C. (1979). A Study of the Influence of Reynolds Number on the Performance of Centrifugal Fans. *Journal of Engineering for Power*, *101*(4), 670–676. https://doi.org/10.1115/1.3446639

Reynolds, O. (1883). XXIX. An experimental investigation of the circumstances which determine whether the motion of water shall be direct or sinuous, and of the law of resistance in parallel channels. *Philosophical Transactions of the Royal Society of London*, *174*, 935–982. https://doi.org/10.1098/rstl.1883.0029

Rogers, G., & Mayhew, Y. (1992). *Engineering Thermodynamics Work and Heat Transfer* (4th ed.). Pearson Education.

SimScale. (2022a, March 15). *Aerodynamic Flow Behavior Around a Vehicle Tutorial*. alhttps://www.simscale.com/docs/tutorials/aerodynamic-simulation-vehicle/

SimScale. (2022b, January 24). *CFD Numerics | Simulation Setup | SimScale Documentation.* https://www.simscale.com/docs/simulation-setup/numerics/

SimScale. (2021a, May 25). *Hex-Dominant Meshing | Simulation Setup.* https://www.simscale.com/docs/simulation-setup/meshing/hex-dominant/

SimScale. (2021b, October 18). *Initial Conditions | Simulation Setup.* https://www.simscale.com/docs/simulation-setup/initial-conditions/

SimScale. (2021c, December 9). *Relaxation Factors | CFD Numerics Setup.* https://www.simscale.com/docs/simulation-setup/numerics/relaxation-factors/

SimScale. (2021d, September 9). *Rotating Zones | Advanced Concepts.* https://www.simscale.com/docs/simulation-setup/advanced-concepts/rotating-zones/#multi-reference-frame-mrf

SimScale. (2021e, September 3). *Standard Mesher | Meshing for CAE | Documentation.* https://www.simscale.com/docs/simulation-setup/meshing/standard/

SimScale. (2022c, January 27). *Tutorials and User Guides | Cloud-Based CAE.* https://www.simscale.com/docs/tutorials/

SimScale. (2023, February 13). *What Are Navier-Stokes Equations? Documentation | SimScale*. https://www.simscale.com/docs/simwiki/numerics-background/what-are-the-navier-stokes-equations/

SimScale. (2021f, September 2). *What is Computational Fluid Dynamics (CFD)? |.*
https://www.simscale.com/docs/simwiki/cfd-computational-fluid-dynamics/what-is-cfd-computational-fluid-dynamics/

SKF Group. (2018). *Deep groove ball bearings | SKF.* SKF. https://www.skf.com/ca/en/products/rolling-bearings/ball-bearings/deep-groove-ball-bearings

Stokes, G. (1850). *On the Effect of the Internal Friction of Fluids on the Motion of Pendulums.* Transactions of the Cambridge Philosophical Society, 9, 8-106.

Streeter, V. L., Wylie, B. E., & Bedford, K. W. (1997). *Fluid Mechanics* (9th ed.). McGraw-Hill College.

StructX. (2014). *Overhanging Beam - Point Load on Beam End*. https://structx.com/Beam_Formulas_026.html

Sutton, M. (1967). Paper 10: Pump Scale Laws as Affected by Individual Component Losses. *Proceedings of the Institution of Mechanical Engineers, Conference Proceedings*, *182*(13), 76–107.
https://doi.org/10.1243/pime_conf_1967_182_393_02

The Engineering Toolbox. (2001). *Friction - Friction Coefficients and Calculator*.
https://www.engineeringtoolbox.com/friction-coefficients-d_778.html

Thompson, J. F., Soni, B. K., & Weatherill, N. P. (1998). *Handbook of Grid Generation*. CRC Press.

Vipond, P. C. W. (2019). *VEHICLE-MOUNTED, FLOW-CAPTURE HELICAL TURBINE (HAWT)* (Application No. 3060653). Canadian Intellectual Property Office.

Wilcox, David C (1998). *Turbulence Modeling for CFD*. Second edition. Anaheim: DCW Industries, 1998.

Yahya, S. M. (2000). *Turbomachines: For Under Graduate and Post Graduate Courses*. Satya Prakashan.

YoosefDoost, A., & Lubitz, W. D. (2020). Archimedes Screw Turbines: A Sustainable Development Solution for Green and Renewable Energy Generation—A Review of Potential and Design Procedures. *Sustainability*, *12*(18), 7352.
https://doi.org/10.3390/su12187352

9 Bibliography

Akwa, J. V., Vielmo, H. A., & Petry, A. P. (2012). A review on the performance of Savonius wind turbines. *Renewable and Sustainable Energy Reviews, 16*(5), 3054–3064. https://doi.org/10.1016/j.rser.2012.02.056

American Meteorological Society. (2012, April 25). *Isotropic turbulence - Glossary of Meteorology*. https://glossary.ametsoc.org/wiki/Isotropic_turbulence#:~:text=Atmospheric%20turbulence%20is%20generally%20nonisotropic,theoretical%20analysis%20of%20turbulent%20flow

Atesmen, K. M. Ideal Gas Flow in Nozzles and Diffusers. (2019). In Case Studies in Fluid Mechanics with Sensitivities to Governing Variables (pp. 97–102). John Wiley & Sons, Ltd. https://doi.org/10.1002/9781119524861.ch15

Betz, A. (2013). The Maximum of the Theoretically Possible Exploitation of Wind by Means of a Wind Motor. *Wind Engineering, 37*(4), 441–446. https://doi.org/10.1260/0309-524x.37.4.441

Damak, A., Driss, Z., & Abid, M. (2013). Experimental investigation of helical Savonius rotor with a twist of 180°. *Renewable Energy*, *52*, 136–142. https://doi.org/10.1016/j.renene.2012.10.043

Damak, A., Driss, Z., & Abid, M. (2018). Optimization of the helical Savonius rotor through wind tunnel experiments. *Journal of Wind Engineering and Industrial Aerodynamics*, *174*, 80–93. https://doi.org/10.1016/j.jweia.2017.12.022

Le, T. Q., Lee, K., Park, J., & Ko, J. H. (2014). Flow-driven rotor simulation of vertical axis tidal turbines: A comparison of helical and straight blades. *International Journal of Naval Architecture and Ocean Engineering*, *6*(2), 257–268. https://doi.org/10.2478/ijnaoe-2013-0177

Li, D., He, Z., Sun, S., Wang, C., Chen, W., & Xing, Z. (2021). Development and analysis of novel six-lobe helical rotors for hydrogen fuel cell vehicle roots blowers. *International Journal of Hydrogen Energy*, *46*(59), 30479–30493. https://doi.org/10.1016/j.ijhydene.2021.06.199

Lucidchart. (2023). *P&ID Symbols and Notation.* https://www.lucidchart.com/pages/p-id-symbols-legend

Rahman, M., Salyers, T. E., Ahmed, M., El-Shahat, A., Soloiu, V., & Maroha, E. (2016). Investigation of Aerodynamic Performance of Helical Shape Vertical-Axis Wind Turbine Models With Various Number of Blades Using Wind Tunnel Testing and Computational Fluid Dynamics. *Volume 7: Fluids Engineering*. https://doi.org/10.1115/imece2016-68081

SimScale. (2021x, July 30). *Turbulent Flow Through Pipe | Validation Case.* https://www.simscale.com/docs/validation-cases/turbulent-pipe-flow/

Zhang, Z., Ramakrishna, S., Guan, C., Ding, Y., & Yan, H. (2013). Numerical study on thermo-hydraulic characteristics of turbulent flow in a circular tube fitted with helical blade rotors. *International Journal of Heat and Mass Transfer*, *60*, 603–611. https://doi.org/10.1016/j.ijheatmasstransfer.2013.01.050

Appendix A   Simulated pressure gradient plots
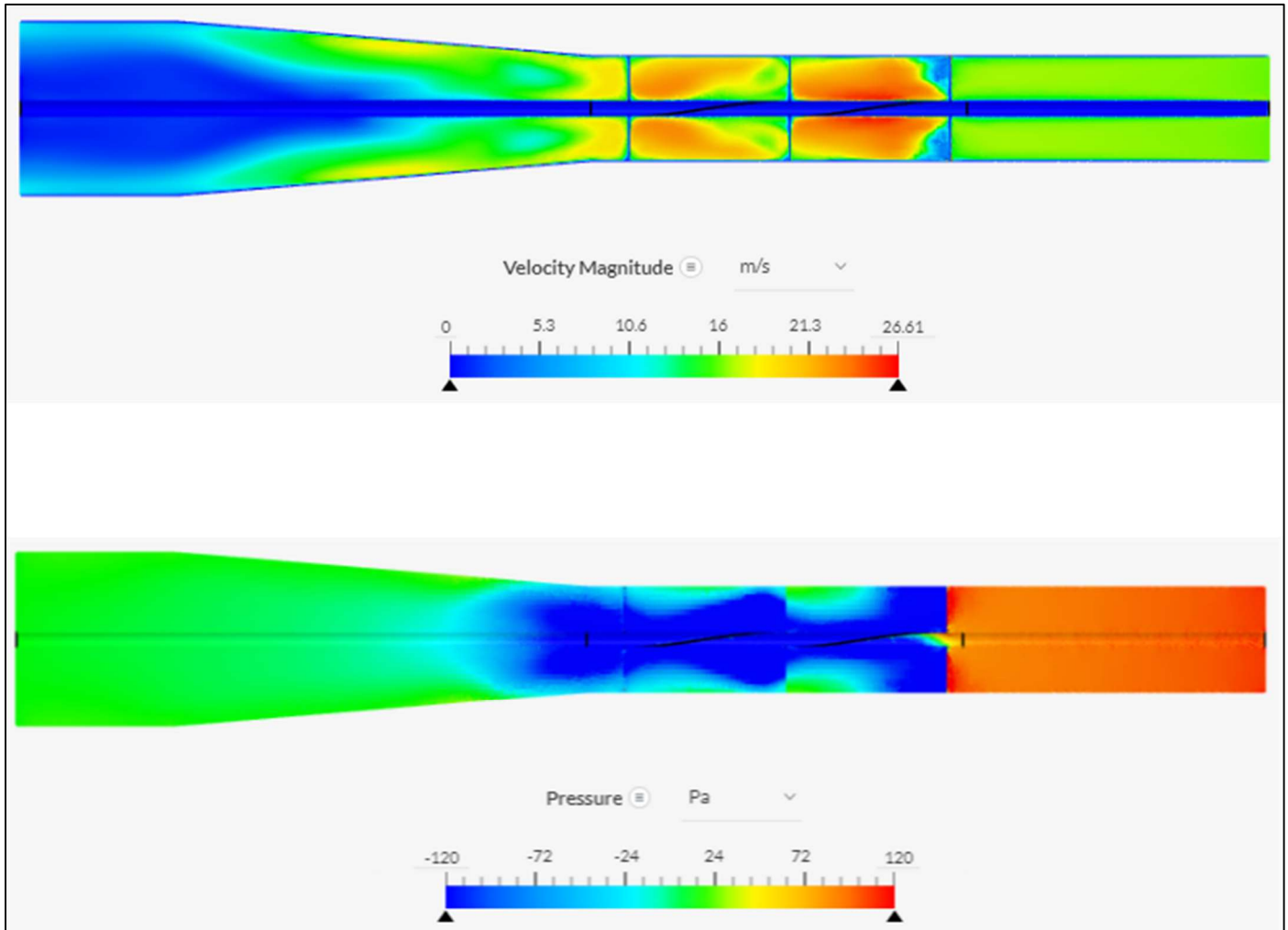
Figure A-1: 15 m/s, 5 degree half angle

Velocity Magnitude ☰   m/s   ⌄

0   3.4   6.8   10.2   13.6   17.02

Pressure ☰   Pa   ⌄

-70   -42   -14   14   42   70
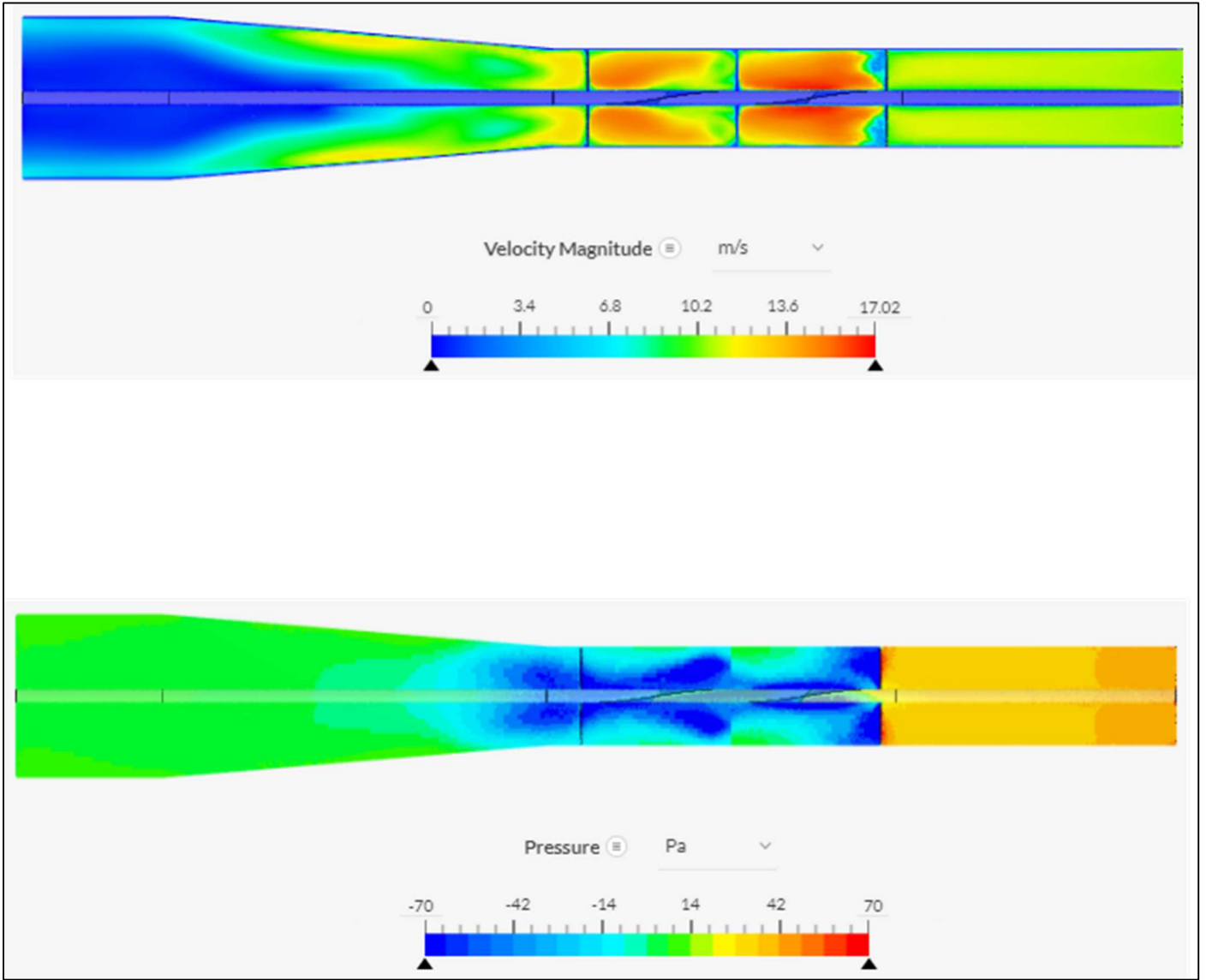
Figure A-2: 10 m/s, 5 degree half angle
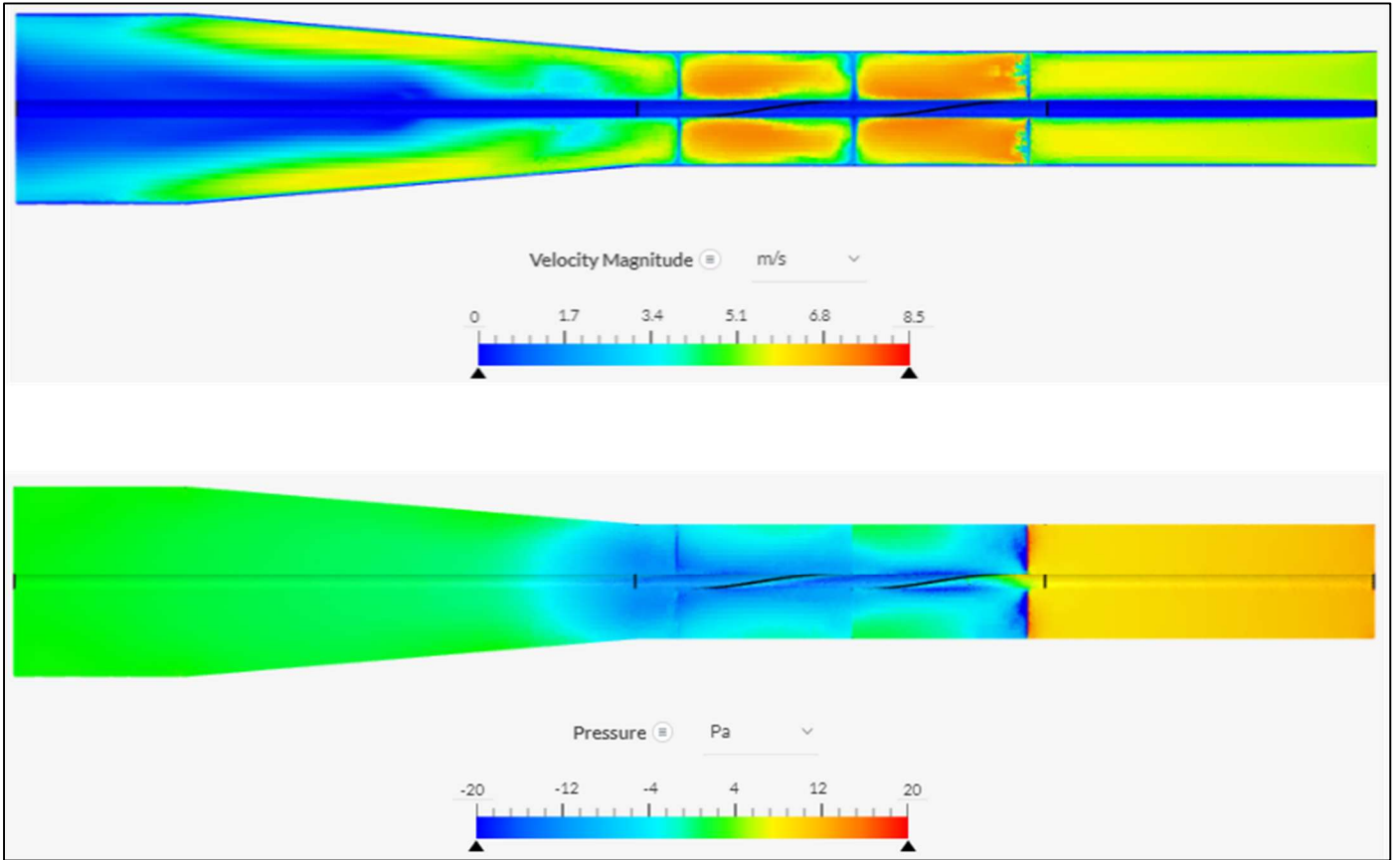
Figure A-3: 5 m/s, 5 degree half angle

Velocity Magnitude ≡ m/s ⌄

0   1.6   3.2   4.9   6.5   8.11

Pressure ≡ Pa ⌄

-20   -12   -4   4   12   20
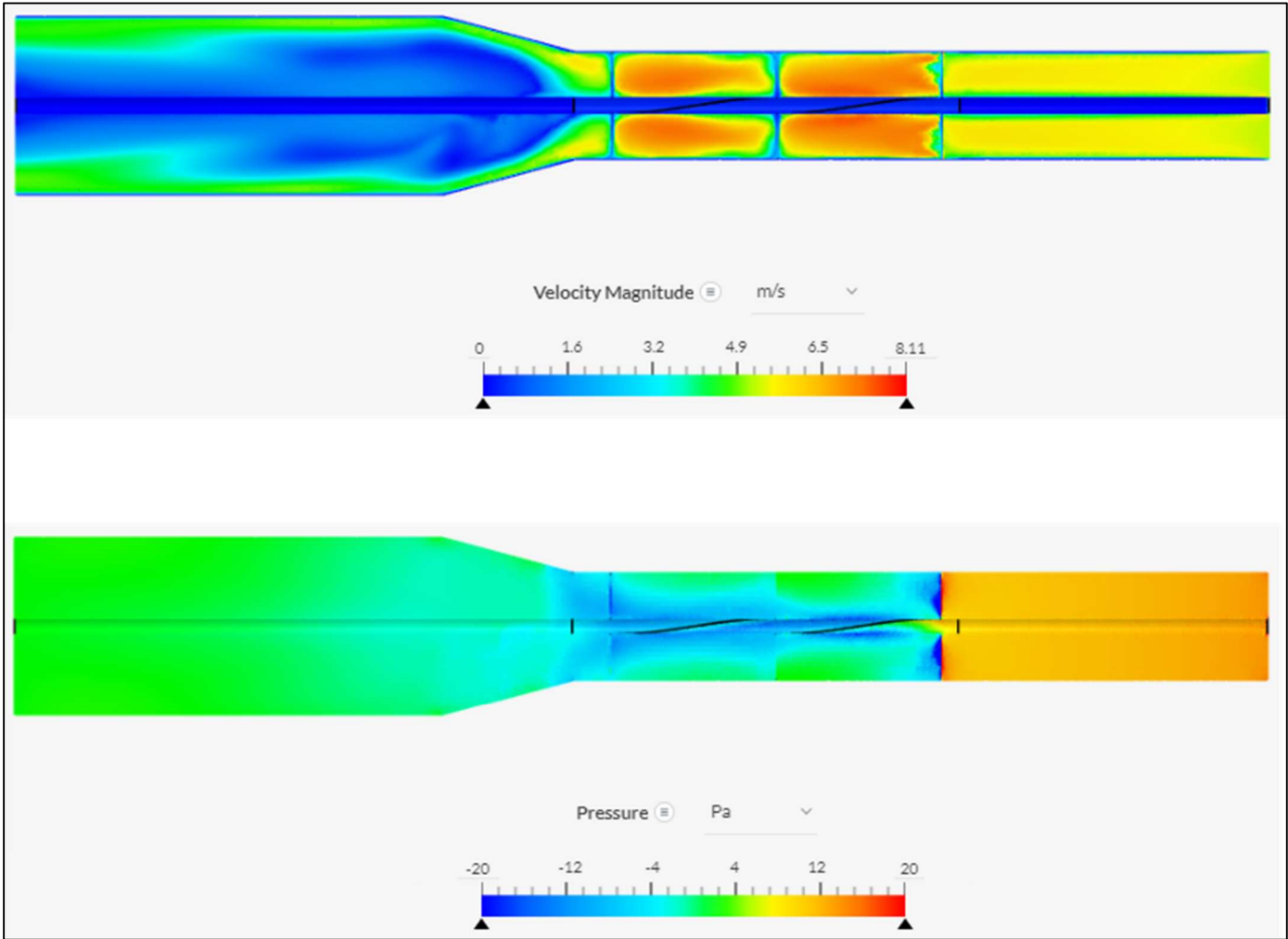
Figure A-4: 5 m/s, 15 degree half angle
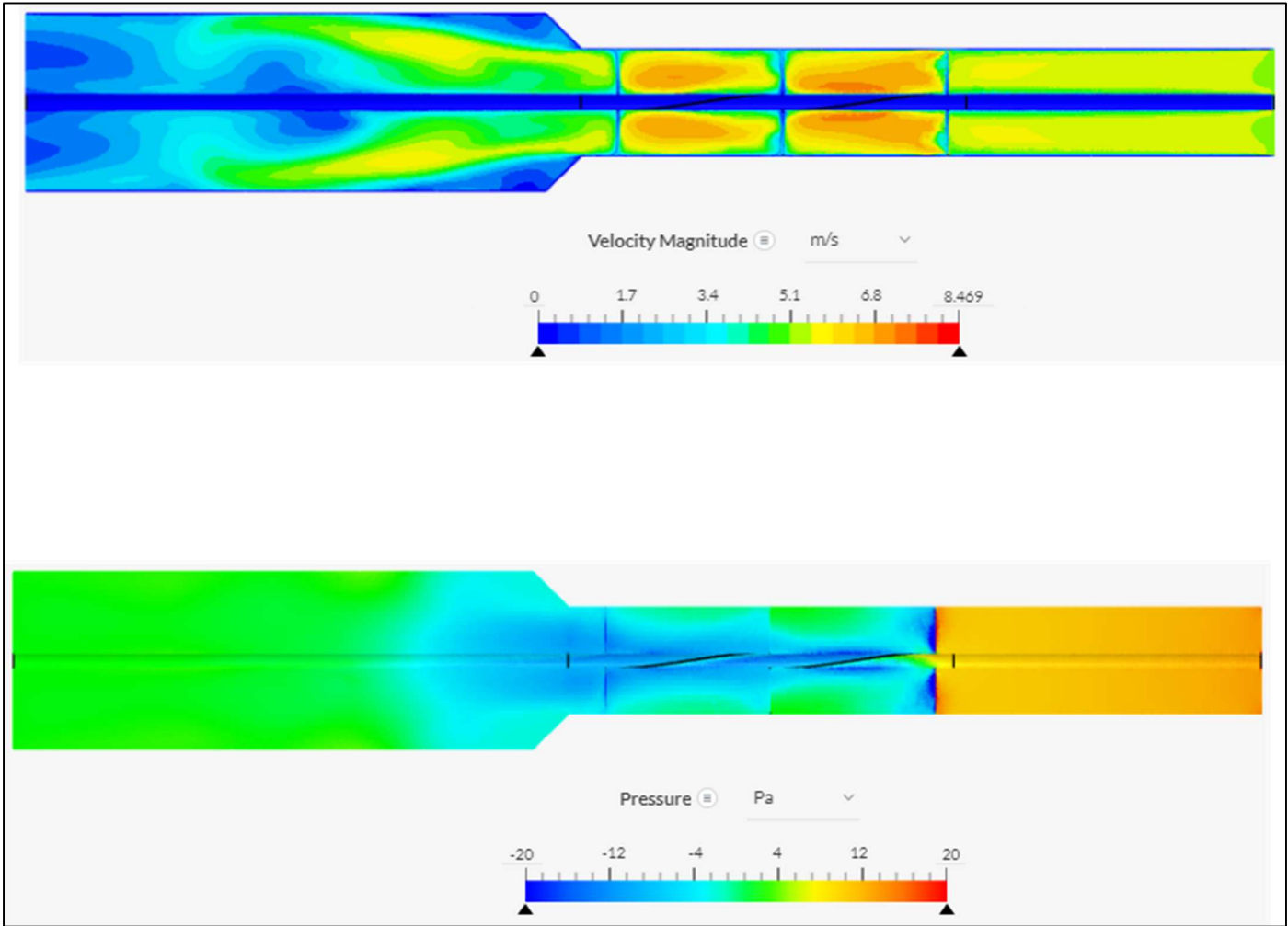
Figure A-5: 5 m/s, 45 degree half angle
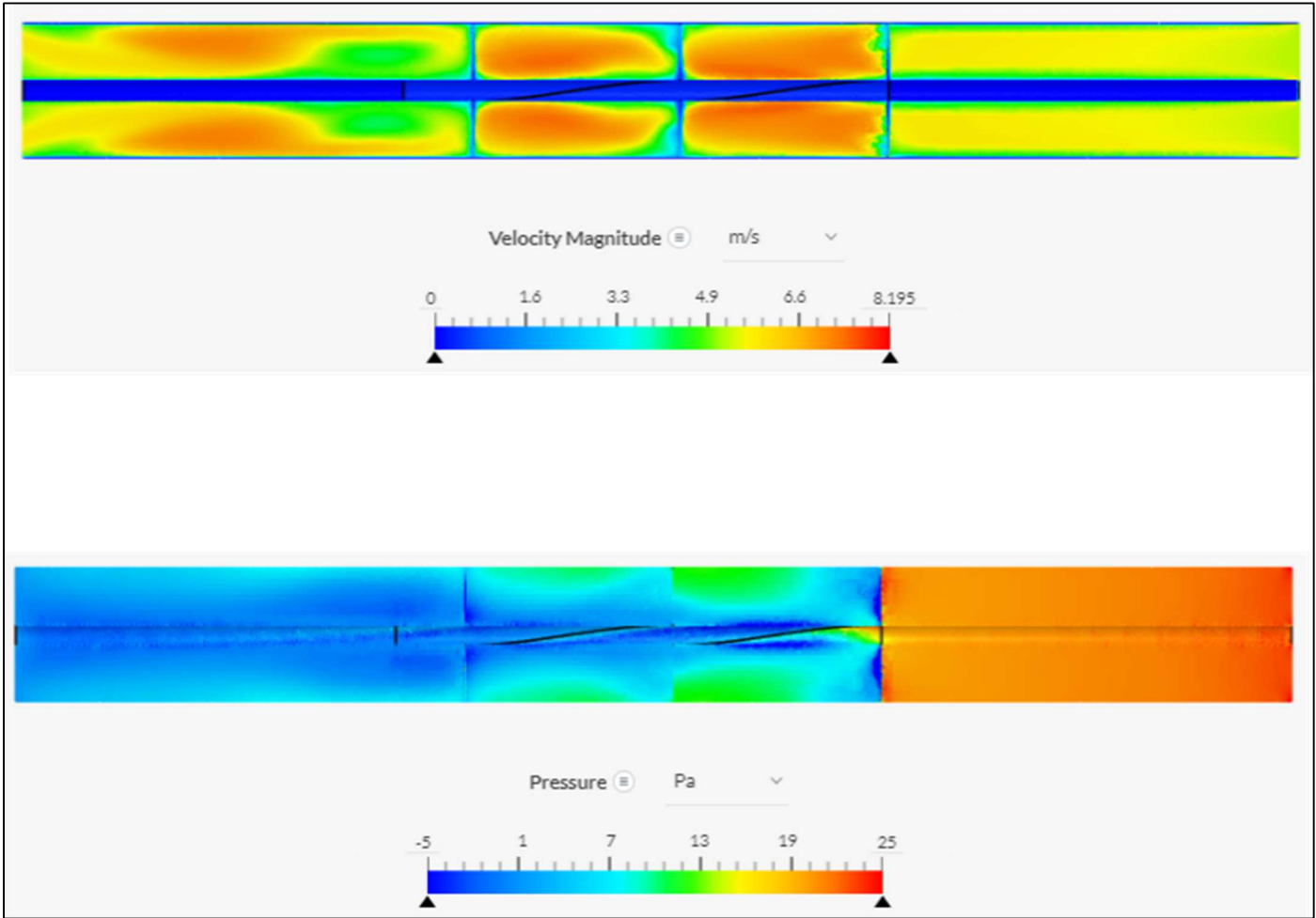
Figure A-6: 5 m/s, no diffuser
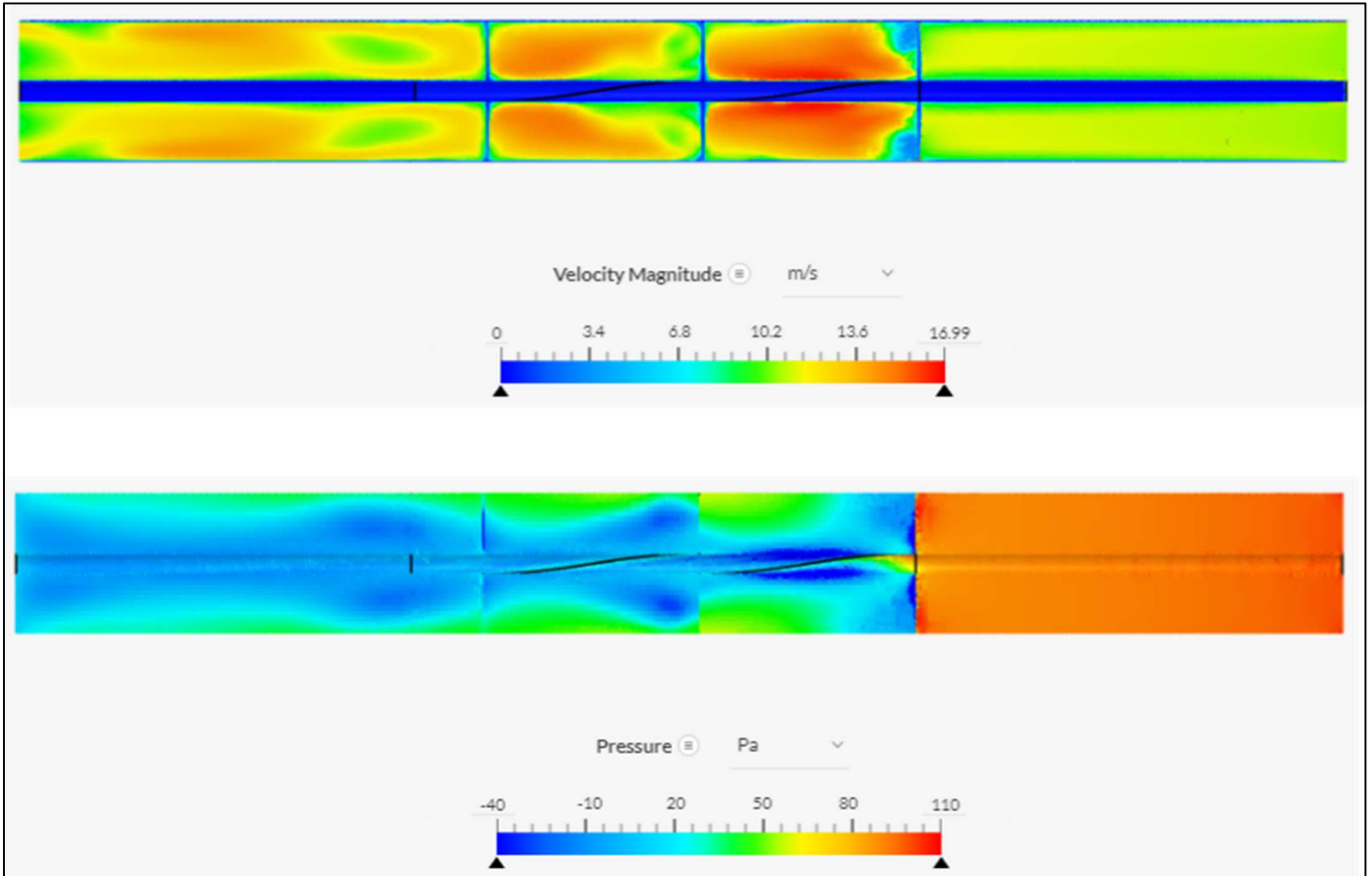
Figure A-7: 10 m/s, no diffuser
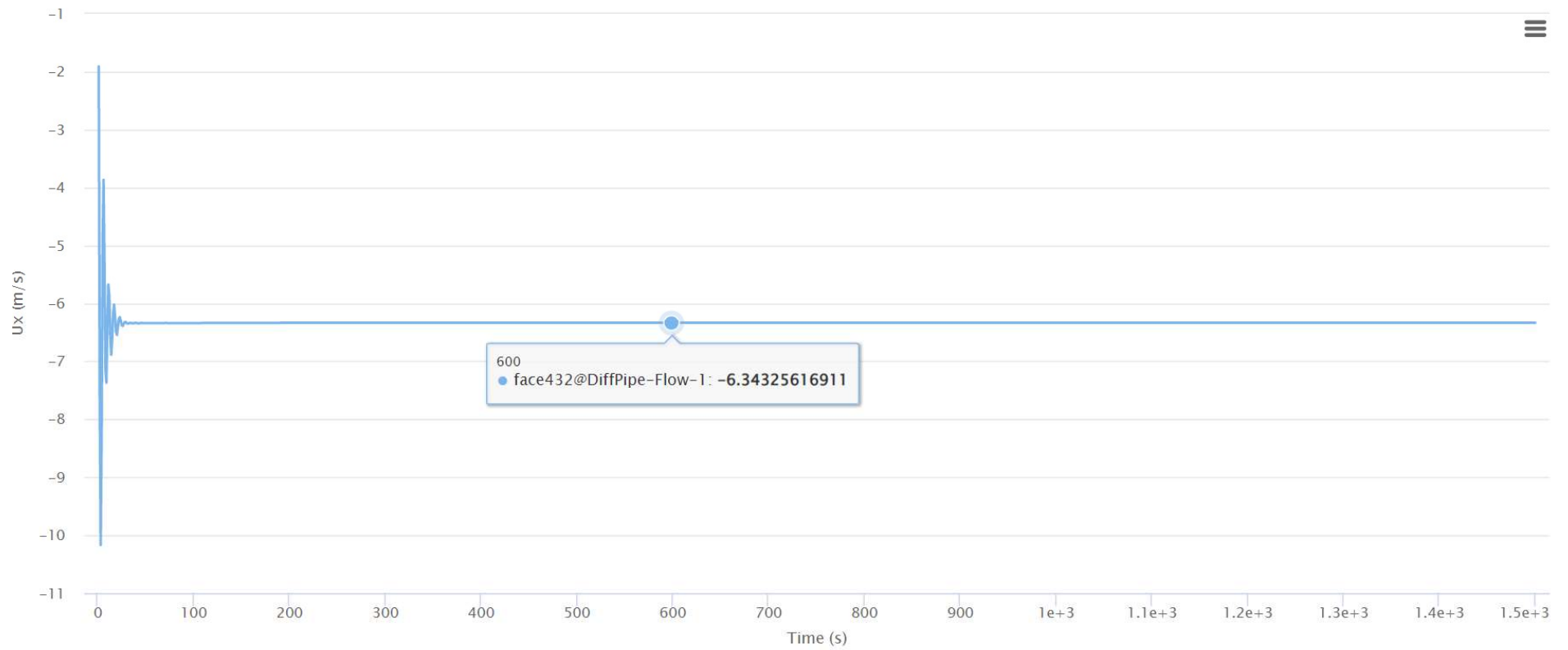
Figure B-1: CFD velocity output, for Geometry 1 test case (diffuser outlet velocity)

Appendix C   Factual statement of all experimental data

Table C-1 a: Observed data from physical experiment (Experimental conditions)

Test	Notes	v^*	N^*	$T(°C)_{atm}$	P_{atm}	Orifice	D_o	D_d
#	--	m/s	rpm	C	kPa	"	cm	mm
1	Test	n/a	n/a	23.5	98.299	6.45	16.383	24.66‡
2	Test	n/a	n/a	23.6	98.294	6.45	16.383	24.66
3	Test	n/a	n/a	23	97.721	6.45	16.383	24.66
4	Test	n/a	n/a	23.1	98.540	6.45	16.383	24.66
5	D10	10	250	23.1	98.540	6.45	16.383	24.66
6	D15	15	250	23.1	98.540	6.45	16.383	24.66
7	D15	15	250*	23.1	98.540	6.45	16.383	24.66
8	D15	15	250	23.1	98.540	6.45	16.383	24.66
9	A5	5	100	23.1	98.540	6.45	16.383	24.66
10	NL	5	n/a	23.1	98.540	6.45	16.383	24.66
11	NL	5	n/a	22	97.745	6.45	16.383	24.66
12	NL	10	n/a	22	97.745	6.45	16.383	24.66
13	NL	15	n/a	22	97.745	6.45	16.383	24.66
14	Stop	15	0	22	97.745	6.45	16.383	24.66
15	Stop	20	0	21.8	97.709	6.45	16.383	24.66
16	NL	20	n/a	21.8	97.709	6.45	16.383	24.66
17	A15	15	100	22.1	97.673	6.45	16.383	24.66
18	B15	15	150	22.1	97.673	6.45	16.383	24.66
19	C15	15	200	22.1	97.673	6.45	16.383	24.66
20	D15	15	250	22	97.745	6.45	16.383	24.66
21	E15	15	500	21.8	97.673	6.45	16.383	24.66
22	F15	15	750	21.8	97.673	6.45	16.383	24.66
23	G15	15	1000	21.8	97.673	6.45	16.383	24.66
24	NL	5	n/a	22.1	98.423	6.45	16.383	24.66
25	NL	10	n/a	22.1	98.423	6.45	16.383	24.66
26	NL	15	n/a	22.1	98.423	6.45	16.383	24.66
27	NL	20	n/a	22.1	98.423	6.45	16.383	24.66
28	NL	25	n/a	22.1	98.423	6.45	16.383	24.66
29	B15	15	150	22.1	98.347	6.45	16.383	24.66
30	C15	15	200	22.1	98.347	6.45	16.383	24.66
31	D15	15	250	22.1	98.347	6.45	16.383	24.66
32	E15	15	500	22.1	98.347	6.45	16.383	24.66
33	B20	20	150	22	98.610	6.45	16.383	24.66
34	D20	20	250	22	98.610	6.45	16.383	24.66
35	E20	20	500	22	98.610	6.45	16.383	24.66
36	F20	20	750	22	98.610	6.45	16.383	24.66
37	NL	10	n/a	22.2	98.561	4.00	10.160	24.66
38	A10	10	100	22.2	98.561	4.00	10.160	24.66
39	B10	10	150	22.2	98.561	4.00	10.160	24.66
40	C10	10	200	22.2	98.561	4.00	10.160	24.66
41	D10	10	250	22.2	98.561	4.00	10.160	24.66

*-   same test as previous, but data is taken at the end of the testing period

‡-   diameter of first, unpinned friction drum

Test	Notes	v^*	N^*	$T(°C)_{atm}$	P_{atm}	Orifice	D_o	D_d
#	--	m/s	rpm	C	kPa	"	cm	mm
42	NL	5	n/a	22.2	98.561	4.00	10.160	23.76*
43	NL	5	n/a	20	98.319	4.00	10.160	23.76
44	N_NL	20	n/a	20	98.319	6.45	16.383	23.76
45	NL	10	n/a	20	98.319	4.00	10.160	23.76
46	NL	15	n/a	20	98.319	6.45	16.383	23.76
47	NL	20	n/a	20	98.319	6.45	16.383	23.76
48	NL	25	n/a	20	98.319	6.45	16.383	23.76
49	A15	15	100	19.7	98.774	6.45	16.383	23.76
50	B15	15	150	19.7	98.774	6.45	16.383	23.76
51	C15	15	200	19.7	98.774	6.45	16.383	23.76
52	D15	15	250	19.7	98.774	6.45	16.383	23.76
53	E15	15	500	19.7	98.774	6.45	16.383	23.76
54	F15	15	750	19.7	98.774	6.45	16.383	23.76
55	F15	15	750	19.7	98.774	6.45	16.383	23.76
56	G15	15	1000	19.7	98.774	6.45	16.383	23.76
57	A20	20	100	21.5	98.686	6.45	16.383	22.67‡
58	B20	20	150	21.5	98.686	6.45	16.383	22.67
59	C20	20	200	21.5	98.686	6.45	16.383	22.67
60	D20	20	250	21.5	98.686	6.45	16.383	22.67
61	E20	20	500	21.5	98.686	6.45	16.383	22.67
62	E20	20	500	21.5	98.686	6.45	16.383	22.67
63	A10	10	100	21.7	97.502	4.00	10.160	22.67
64	B10	10	150	21.7	97.502	4.00	10.160	22.67
65	C10	10	200	21.7	97.502	4.00	10.160	22.67
66	D10	10	250	21.7	97.502	4.00	10.160	22.67
67	E10	10	500	21.7	97.502	4.00	10.160	22.67

*-   diameter of final, pinned friction drum, measured at time of installation

‡-   diameter of final, pinned friction drum, remeasured for melt at end of 20 m/s setpoint

Setpoint notes

Test-   Preliminary calibration test, with arbitrary flow settings

Stop-   Stopped torque (minimum torque for 0 rpm)

NL-   No load

N_NL-   Rotational speed matching no load setpoint (see Appendix D)

Test #	N	ΔP_o	$P_{G,1}$	ΔF_T	T_{phys}	ω_{phys}	ΔP_{phys}	Q_{phys}	η_{phys}
	rpm	Pa	Pa	kg	N-m	rad/s	Pa	m³/s	W/W
1	230	123.0	304.0	1.00	0.121	24.1	309.9	0.242	0.0388
2	275	125.0	305.5	0.88	0.106	28.8	311.6	0.244	0.0403
3	205	118.6	292.3	0.94	0.114	21.5	297.8	0.239	0.0343
4	355	99.7	240.7	0.36	0.044	37.2	244.5	0.218	0.0303
5	250	70.3	171.6	0.32	0.039	26.2	172.8	0.184	0.0319
6	245	156.2	383.3	0.82	0.099	25.7	392.0	0.272	0.0238
7	300	156.2	383.3	0.76	0.092	31.4	392.0	0.272	0.0271
8	255	158.5	389.5	0.82	0.099	26.7	398.4	0.274	0.0242
9	100	17.0	40.0	0.02	0.002	10.5	40.0	0.092	0.0069
10	400	17.0	44.0	0.00	0.000	41.9	44.0	0.092	0.0000
11	320	16.8	33.0	0.00	0.000	33.5	33.0	0.091	0.0000
12	1000	69.3	123.3	0.00	0.000	104.7	124.4	0.183	0.0000
13	1685	157.7	268.0	0.00	0.000	176.5	276.9	0.274	0.0000
14	0	156.5	405.3	0.96	0.116	0.0	414.1	0.273	0.0000
15	0	285.3	744.1	2.06	0.249	0.0	763.2	0.367	0.0000
16	2400	283.2	469.6	0.00	0.000	251.3	488.5	0.366	0.0000
17	100	158.3	396.8	0.94	0.114	10.5	405.8	0.275	0.0107
18	150	156.8	390.7	0.94	0.114	15.7	399.6	0.273	0.0163
19	200	157.1	388.7	0.86	0.104	20.9	397.6	0.274	0.0200
20	250	158.2	388.7	0.94	0.114	26.2	397.7	0.275	0.0273
21	500	157.7	390.3	0.70	0.085	52.4	399.2	0.274	0.0405
22	750	158.2	367.9	0.56	0.068	78.5	376.9	0.275	0.0514
23	1000	157.8	326.4	0.38	0.046	104.7	335.3	0.274	0.0524
24	355	17.4	34.4	0.00	0.000	37.2	34.4	0.093	0.0000
25	1020	69.1	121.5	0.00	0.000	106.8	122.6	0.182	0.0000
26	1745	158.3	266.7	0.00	0.000	182.7	275.6	0.274	0.0000
27	2400	284.6	474.0	0.00	0.000	251.3	492.9	0.365	0.0000
28	3050	443.5	745.6	0.00	0.000	319.4	774.4	0.455	0.0000
29	150	157.8	395.7	1.26	0.152	15.7	404.5	0.273	0.0217
30	200	157.7	393.4	1.16	0.140	20.9	402.2	0.273	0.0267
31	245	157.0	386.3	1.14	0.138	25.7	395.1	0.273	0.0328
32	480	158.5	372.0	0.88	0.106	50.3	380.9	0.274	0.0513
33	155	284.0	730.9	2.58	0.312	16.2	749.7	0.365	0.0185
34	250	284.1	722.3	2.48	0.300	26.2	741.1	0.365	0.0291
35	495	284.2	701.3	1.88	0.227	51.8	720.1	0.365	0.0449
36	750	284.0	648.0	1.50	0.181	78.5	666.8	0.365	0.0586
37	975	749.9	28.2	0.00	0.000	102.1	189.4	0.182	0.0000
38	100	750.9	19.5	0.50	0.060	10.5	180.9	0.183	0.0192
39	150	751.0	16.5	0.46	0.056	15.7	177.9	0.183	0.0270
40	200	751.2	15.0	0.44	0.053	20.9	176.4	0.183	0.0347
41	250	751.3	13.1	0.38	0.046	26.2	174.6	0.183	0.0378

Test #	N rpm	ΔP_o Pa	$P_{G,1}$ Pa	ΔF_T kg	T_{phys} N-m	ω_{phys} rad/s	ΔP_{phys} Pa	Q_{phys} m³/s	η_{phys} W/W
42	310	185.3	-1.1	0.00	0.000	32.5	36.8	0.091	0.0000
43	265	183.5	-0.4	0.00	0.000	27.8	36.9	0.091	0.0000
44	265	285.8	725.5	2.36	0.275	27.8	744.3	0.365	0.0281
45	910	750.7	-28.5	0.00	0.000	95.3	132.0	0.182	0.0000
46	1635	157.7	276.8	0.00	0.000	171.2	285.5	0.272	0.0000
47	2345	285.2	486.1	0.00	0.000	245.6	504.9	0.365	0.0000
48	3025	445.4	760.1	0.00	0.000	316.8	788.9	0.454	0.0000
49	100	157.5	404.5	1.40	0.163	10.5	413.1	0.271	0.0152
50	150	157.9	402.8	1.36	0.158	15.7	411.5	0.272	0.0223
51	195	157.9	398.2	1.30	0.152	20.4	406.9	0.272	0.0280
52	250	157.1	390.5	1.16	0.135	26.2	399.1	0.271	0.0327
53	495	157.2	371.0	0.96	0.112	51.8	379.6	0.271	0.0564
54	755	159.0	353.1	0.76	0.089	79.1	361.9	0.273	0.0710
55	755	159.0	353.2	0.74	0.086	79.1	362.0	0.273	0.0691
56	1005	159.0	329.2	0.42	0.049	105.2	338.0	0.273	0.0559
57	100	285.5	733.4	2.70	0.300	10.5	752.3	0.365	0.0114
58	150	284.4	723.1	2.64	0.294	15.7	741.9	0.364	0.0171
59	205	284.2	721.1	2.54	0.282	21.5	739.9	0.364	0.0225
60	250	284.2	714.8	2.44	0.271	26.2	733.6	0.364	0.0266
61	500	285.2	696.3	2.12	0.236	52.4	715.1	0.365	0.0473
62	500	285.0	695.1	2.14	0.238	52.4	713.9	0.365	0.0478
63	105	750.8	16.7	0.64	0.071	11.0	179.6	0.183	0.0238
64	150	750.9	16.3	0.58	0.064	15.7	179.2	0.183	0.0309
65	200	750.6	14.1	0.56	0.062	20.9	176.9	0.183	0.0403
66	250	748.3	9.6	0.42	0.047	26.2	171.9	0.183	0.0389
67	490	753.2	-4.1	0.32	0.036	51.3	159.3	0.184	0.0625

Note that pressure results in this appendix are reported as ΔP_{phys}, which signifies that the aggregate pressure reduction, ΔP_{corr} (see section 4.5.3) has not been applied. This is because the majority of the data was not used in the final comparative analysis.

Appendix D Developing best practices for selected instrumentation

Upon constructing and beginning to run the test dynamometer, certain inconsistencies were observed in the readings. As a result, a series of tests was devised to identify sources of error and develop best practices for the final testing procedure. Those tests and their results represent a justification of the final methodology, which has been outlined in chapter 4.6. These justifications are especially relevant to the so-called "stop conditions" outlined in section 5.1.2, which would result in an invalid test if they were observed.

Dynamometer belt and loading design revisions

The initial calibration tests of the blower resulted in some inconsistent behaviour. It was theorized that this was due to the complexity of the system, and a test was undertaken to determine some time constant or minimum running time to reach equilibrium.

Periodic readings were taken at a set tension and airflow. The intention was to stop when the readings remained constant, signifying a minimum time to equilibrium.

Table D- 1: Output data over time; used to attempt determination of system settling time

Time	N	ΔP_O	P_G
min	rpm	Pa	Pa
0	130	119.6	302.5
10	210	120.6	301.9
15	215	120.3	300.3
20	220	121.3	302.9
25	225	121.4	304.0
30	230	123.1	304.2
35	230	122.9	303.8
40	235	122.7	306.2
45	235	124.0	306.3
50	245	124.2	306.3
55	255	125.2	308.8
60	250	124.5	307.8
70	260	124.4	308.5
80	270	126.6	311.6
90	270	125.5	310.6
100	290	127.2	308.2
105	280	125.5	306.4
110	270	124.5	304.6

From the observed data, it was determined that the rubber bungee used as a strap was undergoing stretching due to the friction heat. To account for this, a new strap was selected which would not stretch.

While the new strap did make the system much more responsive, similarly inconsistent behaviour was observed at higher tensions. To ensure that the drum was not slipping, a line was drawn across the shaft and drum before starting another test. The drum was observed to slip, confirming another source of tachometer error.

A new drum was manufactured and pinned in place on the shaft to prevent slip. This was the final drum used to produce experimental data, as described in section 4.4.1. One final test was carried out to diagnose any other inconsistencies in the tachometer readings. At a constant airflow, tension was adjusted in increments to allow for a plot of rotational speed against tension.

In the absence of a live friction reading, some analogous reading must be used. As previously discussed in section 4.1.2, Torque, T, could be taken as a function of the radius of the dynamometer drum, r_d, times the Friction Force, F_f,

$$T = r_d F_f \tag{D.1}$$

Friction Force is a function of the kinetic friction coefficient, μ_k, times the normal force, F_N,

$$F_f = \mu_k F_N \tag{D.2}$$

In the dynamometer, the normal force would be proportional to the spring force, F_S, applied by the two scales,

$$F_N \propto 2F_S \tag{D.3}$$

Furthermore, the Spring Force would be inversely proportional to the height of the tension arm, $h - x_0$ (shown in Figure D-1), as it related to spring coefficient, k_S, and the distance from the unstretched position of the spring, x_0,

$$F_S = k_S x_0 \tag{D.4}$$

such that

$$F_S \propto \frac{k_S}{h - x_0} \tag{D.5}$$

Therefore, height was assumed to have an approximately linear, negative relation to applied torque, and by extension, an approximately linear positive relation to rotational speed.

$$T \propto r_d \mu_k \frac{2k_S}{h - x_0} \tag{D.6}$$
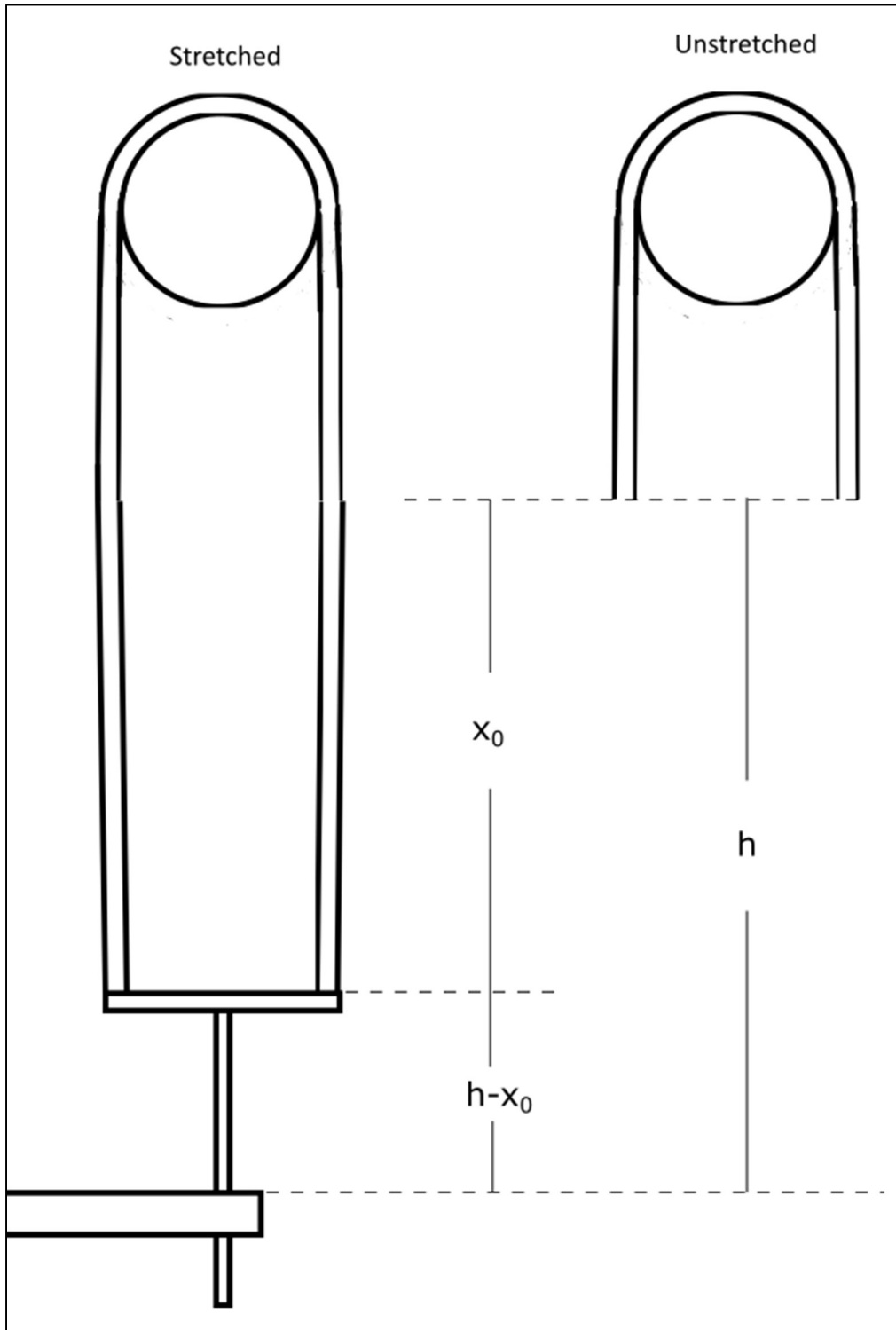
Figure D-1: Diagram of dynamometer (as seen in Figure 4.2 and Figure 4.3); threaded rod height as a function of distances x_0 and h
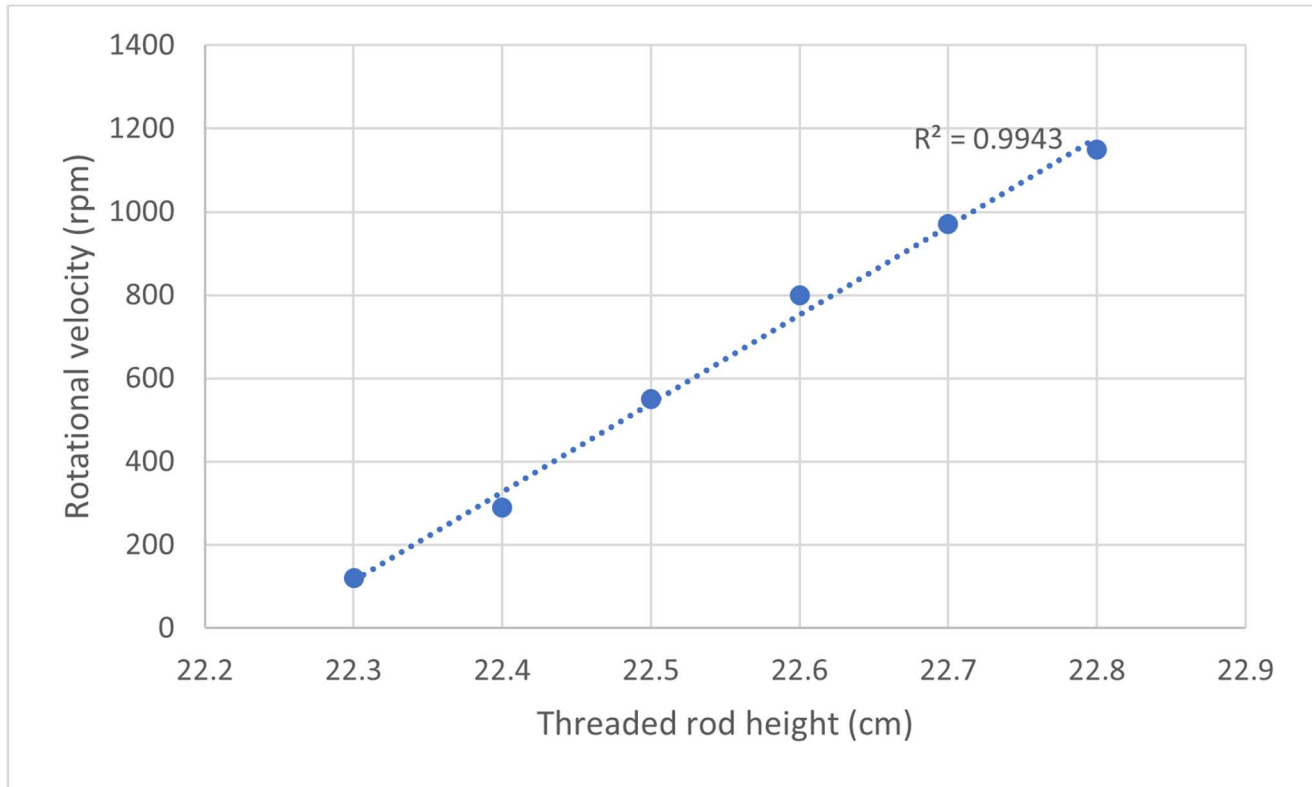
Figure D-2: Plot of rotational speed as a function of a height measurement (analogous with torque)

The observations from the test were plotted, confirming a roughly linear relationship between the torque analog and rotational speed. This consistent behaviour matched the expected tachometer readings.

While the behaviour was consistent during ideal running conditions, two practical limitations were observed which, by altering the applied friction on the shaft, could change the behaviour of the tachometer readings. These limitations were identified as insufficient friction and excessive normal force applied to the drum.

Qualitative analysis to control for an insufficient friction force

An insufficient friction force on the drum caused the low-tension scale to reach a negative tension and unhook from the tension arm. This immediately changed the applied friction on the drum, causing the tachometer reading to vary wildly. It also had the additional effect of removing part of the tension reading when trying to measure torque.

To avoid this, a relation was determined algebraically with the aim of finding control variables to limit instances of this error. For the following equations,

F_N - combined normal force applied to the drum,

F_S - combined spring force contributed by the scales,

m_{str} - mass of the strap,

g - gravitational constant,

F_f - friction force applied to the drum by the strap,

F'_{Si} - spring force at system equilibrium for scale i,

F_{Ni} - portion of overall normal force on drum provided by side i,

170

μ_k - coefficient of kinetic friction between drum and strap,

$$F_N = F_S + m_{str}g \tag{D.7}$$

$$F_f = F'_{S1} - F'_{S2} \tag{D.8}$$

$$\frac{F_N}{2} = F_{Si} + \frac{m_{str}g}{2} \tag{D.9}$$

$$F_{Ni} = F'_{Si} + \frac{m_{str}g}{2} - \frac{F_f}{2} \tag{D.10}$$

$$F_{N2} = \left(F_{S2} - \frac{F_f}{2}\right) + \frac{m_{str}g}{2} + \frac{F_f}{2} \tag{D.11}$$

For $F'_{S2} < 0$, $F_{S2} < \frac{F_f}{2}$. Find $F'_{S2} = 0$.

$$F_{N2} = \frac{F_N}{2} = (0) + \frac{m_{str}g}{2} + \frac{F_f}{2}$$

$$F_N = m_{str}g + F_f = \frac{F_f}{\mu_k}$$

$$m_{str}g = \frac{F_f}{\mu_k} - F_f = \left(\frac{1}{\mu_k} - 1\right)F_f$$

$$m_{str}g = \frac{1 - \mu_k}{\mu_k}F_f \tag{D.12}$$

From equations (D.11) and (D.12), limits were determined to be

$$F_{S2} > \frac{F_f}{2}, F_f > \frac{\mu_k}{1 - \mu_k}m_{str}g$$

Based on these relations, independent variables were identified which could be limited to keep the test conditions within an acceptable range. To increase F_{S2}, possible solutions included decreasing m_{str}, increasing F_N, or decreasing F_f. To increase F_f, possible solutions included decreasing m_{str}, increasing F_N, or increasing μ_k. The best solution for both cases was to decrease m_{str}. However, this investigation also identified an inevitable problem in the testing, which was that low-speed tests with low torque would require a very low F_N, increasing the likelihood of this error.

Qualitative analysis to control for an excessive normal force

An excessive normal force on the drum caused the shaft to deflect beyond the projected clearance between the blade and the pipe. This resulted in an added friction force which caused the tachometer readings to vary wildly. Since the friction force was applied by the pipe instead of the strap, it was unmeasurable using the dynamometer as it was.

To avoid this, a relation was determined algebraically with the aim of finding control variables to limit instances of this error. For the following equations,

$F_{N,0}$ - the normal force required to bend the shaft such that the blade reaches the pipe wall,

N - rotating speed of shaft and blade,

Δr - clearance between the blade edge and the pipe wall,

Δd_e - maximum deflection in the shaft caused by a rotating eccentric mass,

F_{f2} - friction force applied to the blade by the pipe wall,

k - unknown coefficient to convert drum normal force into a resultant force exerted by the blade,

μ_{k2} - coefficient of kinetic friction between the blade edge and the pipe wall,

ΔF_T - equivalent torque force, as measured from the radius of the dynamometer drum,

T - torque applied to the shaft,

r_d - radius of the dynamometer drum,

r_2 - radial distance between the shaft and the point where the blade meets the pipe wall,

$$F_{N,0}(N) = F_{N,0}\big(\Delta r - \Delta d_e(N)\big) \tag{D.13}$$

$$F_{f2} = \big(kF_N - kF_{N,0}\big)\mu_{k2}; \; F_N \geq F_{N,0} \tag{D.14}$$

For $F_N > m_{str}g + F_S$,

$$\Delta F_T = F_f = \mu_k(m_{str}g + F_S) \tag{D.15}$$

For $F_N \leq m_{str}g + F_S$,

$$T = r_d F_f + r_2 F_{f2} \tag{D.16}$$

$$\Delta F_T = \frac{T}{r_d} = F_f + F_{f2}\left(\frac{r_2}{r_d}\right)$$

$$F_f = \Delta F_T - \left(k\left((m_{str}g + F_S) - F_{N,0}\right)\mu_{k2}\right)\left(\frac{r_2}{r_d}\right) \tag{D.17}$$

Based on these relations, independent variables were identified which could be limited to keep the test conditions within an acceptable range. To increase F_N, possible solutions included decreasing m_{str}, increasing F_N directly, or decreasing F_S. To increase $F_{N,0}$, possible solutions included decreasing $\Delta d_e(N)$, increasing Δr, or increasing k. The best solution was to decrease m_{str}. However, this investigation also identified two inevitable problems in the testing, which were that high-speed tests would result in a very high $\Delta d_e(N)$, and high torque tests would require a very high F_S. Both would increase the likelihood of this error.

Accounting for digital balance Hold function

The cheap digital scales used for the rudimentary dynamometer were programmed to shut off after 1 min without any user input on the buttons on their faces. To overcome this, readings were taken such that the zero point is the equilibrium for a given setpoint.

After achieving the desired airflow and rotational speed, the blower was turned off so that the scales read a negative value of the force applied by the friction on the drum.

However, another flaw associated with the selected scales was identified and needed to be overcome. The scales were also programmed with a Hold function which would lock the display on a consistent positive value. As the blower was turned off, the scales would slowly return to the rest position of their internal springs. This meant that one scale would trigger the Hold function whenever this process was too gradual.

To overcome this function, a new method was devised. For the revised method, the strap was given a negative tension, which was then maintained so that the tension arm could be released. By holding this negative tension and releasing the strap from the drum, the Hold function could not be triggered because both scales always read a negative value.

The new method was tested to compare torque readings. It was expected that readings would be equal to or greater than the old method.

Table D-2: Comparison of data gathered using old and new torque measurement methods

Old method				New method			
N	ΔP_o	P_G	ΔF_T	N	ΔP_o	P_G	ΔF_T
rpm	Pa	Pa	kg	rpm	Pa	Pa	kg
100	158.3	396.8	0.94	100	157.5	404.5	1.40
150	156.8	390.7	0.94	150	157.9	402.8	1.36
200	157.1	388.7	0.86	195	157.9	398.2	1.30
250	158.2	388.7	0.94	250	157.1	390.5	1.16
500	157.7	390.3	0.70	495	157.2	371.0	0.96
750	158.2	367.9	0.56	755	159.0	353.1	0.76
1000	157.8	326.4	0.38	755	159.0	353.2	0.74
150	157.8	395.7	1.26	1005	159.0	329.2	0.42
200	157.7	393.4	1.16	100	285.5	733.4	2.70
245	157.0	386.3	1.14	150	284.4	723.1	2.64
480	158.5	372.0	0.88	205	284.2	721.1	2.54
155	284.0	730.9	2.58	250	284.2	714.8	2.44
250	284.1	722.3	2.48	500	285.2	696.3	2.12
495	284.2	701.3	1.88	500	285.0	695.1	2.14
750	284.0	648.0	1.50	105	750.8	16.7	0.64
100	750.9	19.5	0.50	150	750.9	16.3	0.58
150	751.0	16.5	0.46	200	750.6	14.1	0.56
200	751.2	15.0	0.44	250	748.3	9.6	0.42
250	751.3	13.1	0.38	490	753.2	-4.1	0.32

As seen in Table D-2, the comparative test showed an increased torque reading for equivalent setpoints, suggesting an improvement in the method.

Appendix E   Maximum plausible correction due to "sail error"

One possible source of torque error has been hypothesized, which is the force applied to the tension strap of the dynamometer by the airflow which exits the duct. Figure E-1 and Figure E-2, depicting the assembled dynamometer, were previously included in section 4.1.2.

Figure E-1: Friction drum with tension strap (older tension strap used in calibration, photo is illustrative only)

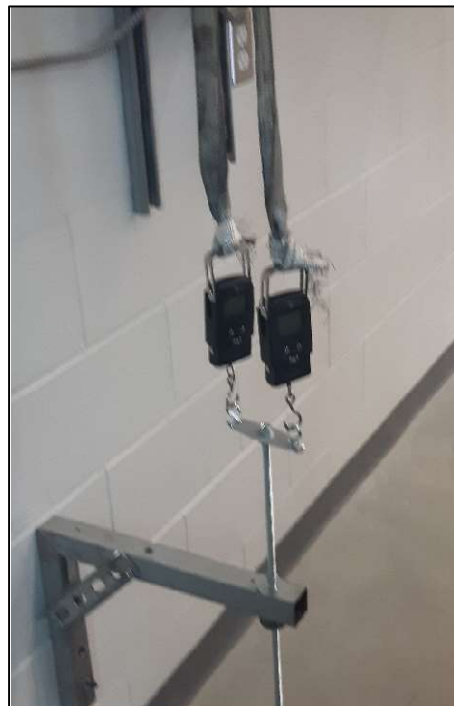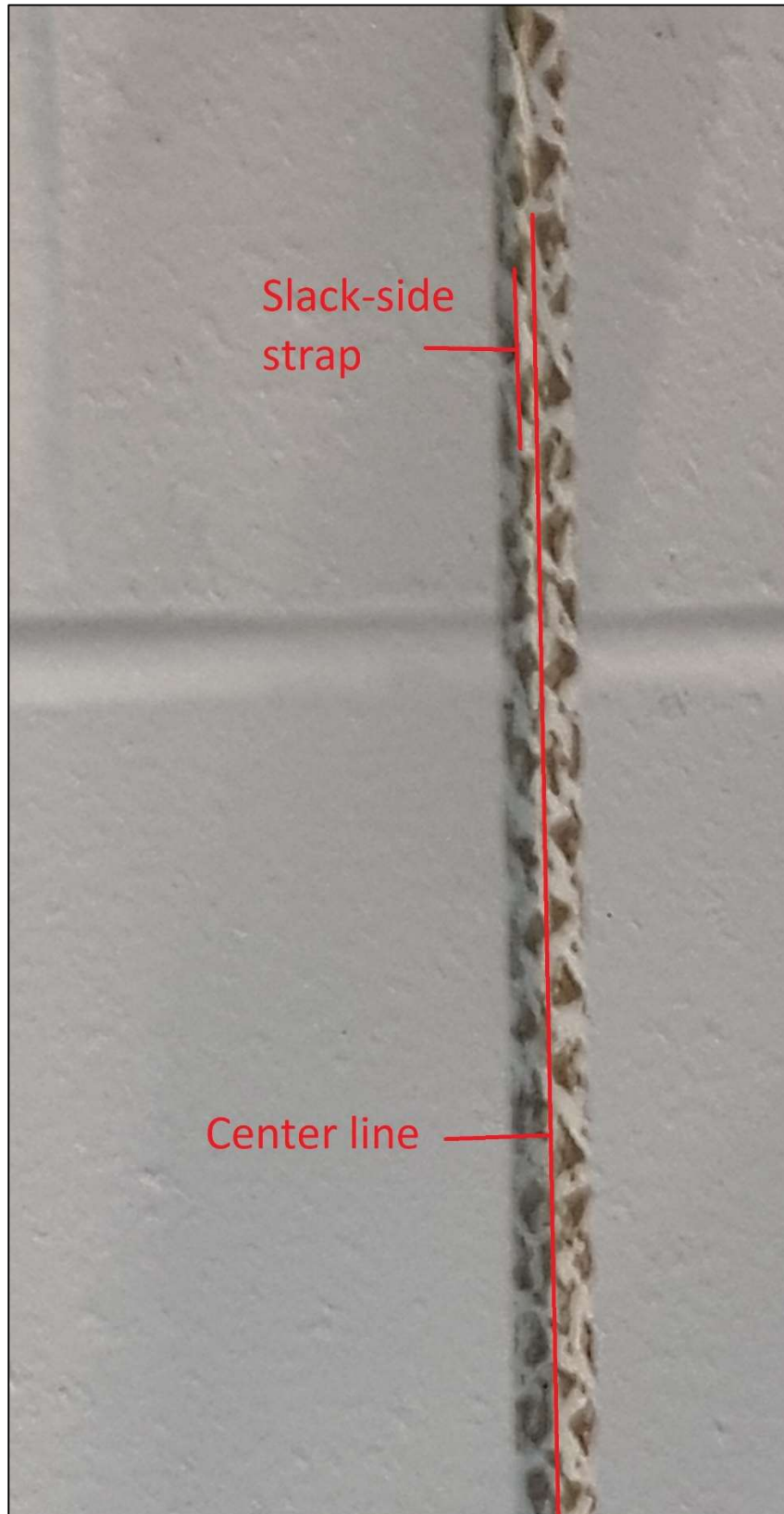*Figure E-2: Tension strap and tension arm, connected by threaded rod*

Figure E-3: Photo of deflection in vibrating slack-side strap (final tension strap used in physical experimentation)

During experimentation, it was observed that the slack-side strap would vibrate during tests with higher flowrates. The strap would also flatten out to be perpendicular to the airflow exiting the duct (see Figure E-3). Hence, the flow

acts upon the strap like a sail and this sail force must be analyzed to determine whether it is plausible as a major source of error.

In Figure E-4, the taut-side strap is held flat against the rotating drum because it is subject to greater tension. Meanwhile, the slack-side strap is free to twist and flatten out. Recall, from section 4.2.6, that the cotton strap is folded in half to ensure a consistent friction surface from the material, which has a rough side and a smooth side. When subject to high velocity winds from the duct, this cloth is unfolded, increasing the surface area that can be acted upon.

Furthermore, note that the orientation of the straps with respect to the airflow will dictate the nature of the force applied to the strap. The force applied to the slack-side strap will be applied as a force would be applied to a sail. The force applied to the taut-side strap will be applied as shear friction along the sides of the cloth. It is therefore assumed that the force applied to the taut-side strap will be negligible for the purpose of these calculations.
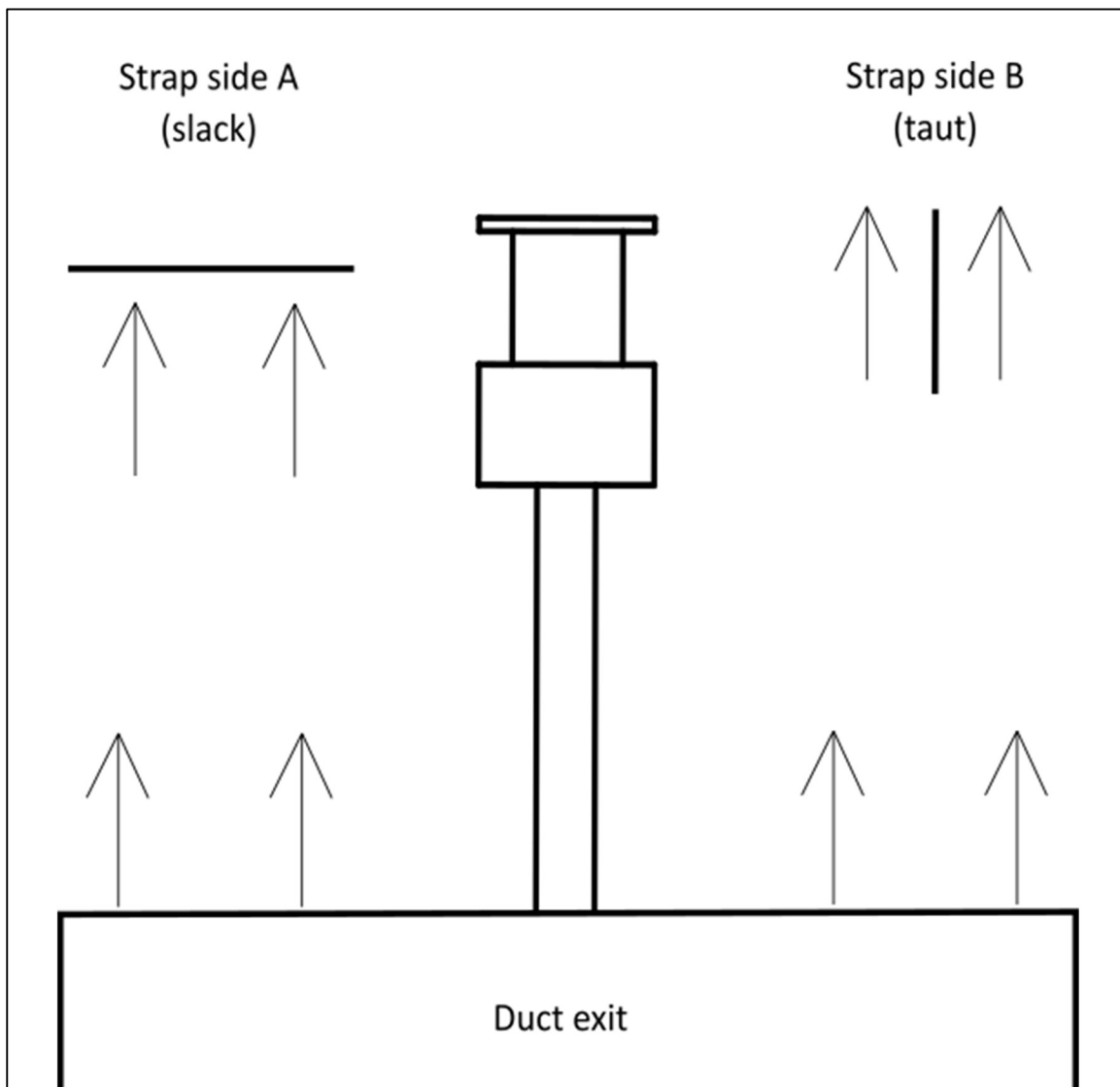
Figure E-4: Sail behaviour of slack-side and taut-side of tension strap
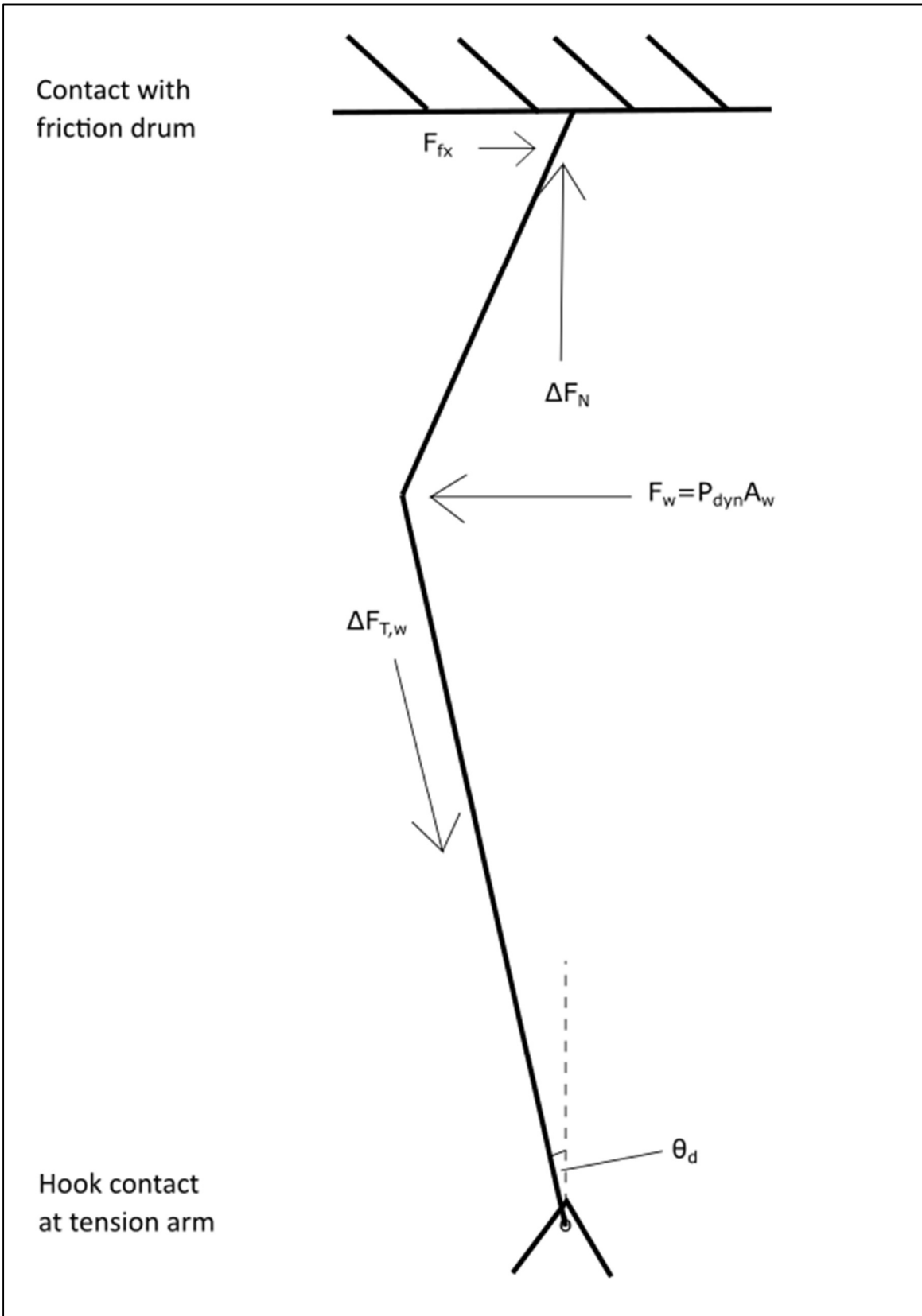
Figure E-5: Free body diagram of sail force applied to slack tension strap (greatly exaggerated deflection angle)

In Figure E-5, the sail force (applied to the slack-side strap by the airflow, as in Figure E-4) is depicted as a point force. Note that the digital scale is connected to the tension arm by a hook. As such, it is free to rotate and will therefore

resist the increased tension directly, with the spring of the digital balance. However, at the point of contact with the friction drum, there is no physical attachment. As such, the increased tension in the strap must be resisted by an increased normal force on the friction drum, ΔF_N, and an axial friction, F_{fx}. Though the axial friction should have no effect on the dynamometer's function, the increased normal force will increase the torque which is applied to the rotor via friction. This may be disregarded however, since the final observations for any given experiment will not be recorded until a constant flowrate and rotational speed have been reached (see section 5.1.1). Furthermore, for a distance of approximately 36" between the friction drum and tension arm (see section 4.2.7), the point force would be applied no more than 3" (the radius of the duct) from the point of contact with the friction drum. This observation allows for the forces to be balanced by approximating the strap as a rigid body when pulled taut by the airflow from the duct. The following equation is used for balancing moments about a point in a rigid body (as shown, for example, in Bedford & Fowler, 2007):

$$\Sigma M_0 = 0 = \Sigma(L_i F_i) \tag{E.1}$$

Here, ΣM_0 is the sum of all moments about the point where the force is acting upon the strap as point 0). Thus, L_1 is the distance from point 0 to the contact with the friction drum (measured perpendicular to the force, F_1, applied at the point of contact), and L_2 is the distance from point 0 to the hook attached to the tension arm (measured perpendicular to the force, F_2, applied at the point of contact). Based on the standard length of 36" for the tension strap and the estimated maximum value of L_1 (3"), the tension arm must resist at least 11/12 of the total sail force.

Since this sail force is applied by the airflow (which exits at some velocity, v_{exit}), it can be calculated as a function of the dynamic pressure:

$$P_{dyn} = \frac{\rho v_{exit}^2}{2} \tag{E.2}$$

The sail force, F_w, can be calculated with the following equation:

$$F_w = P_{dyn} A_w \tag{E.3}$$

The affected area, A_w, is depicted in Figure E-6, which corresponds to Figure E-1.

For calculation, this area has been approximated as the unfolded width of the cloth strap (approx. 0.025m), times the radius of the duct that is not impeded by the bearing mount (approx. 0.05m). This represents the maximum possible overlap between the duct exit and the unfolded cloth strap, assuming the flow exiting the duct maintains its direction.
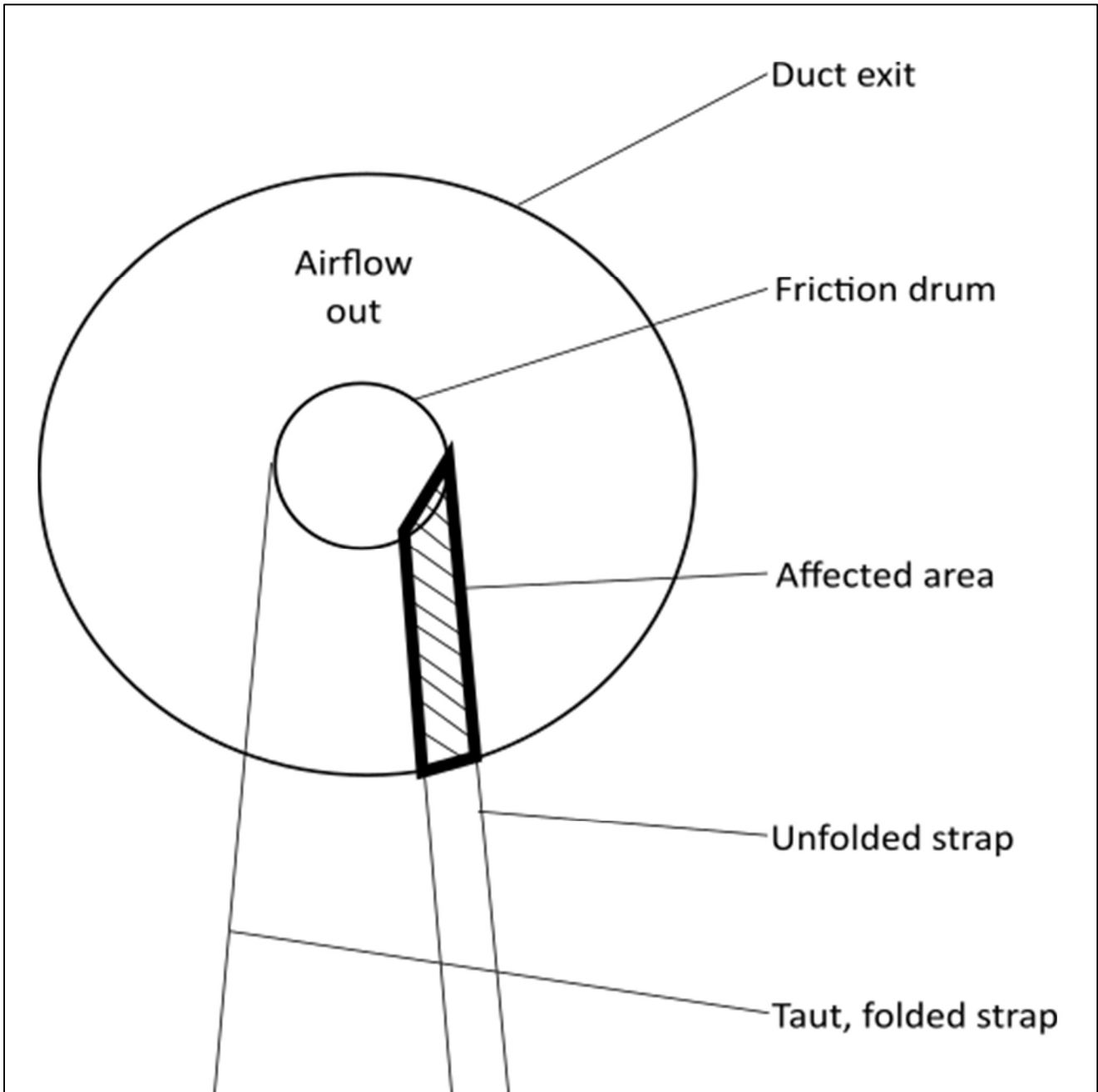
Figure E-6: Diagram depicting approximate strap area affected by sail force from duct outflow (hash marked)

Since the surface area is estimated as a maximum, and since the dynamic pressure will begin to dissipate as soon as the flow exits the duct, the force acting upon the strap should be multiplied by some coefficient k_w, which is less than 1. Thus, by combining equations (E.2) and (E.3) and multiplying by k_w, the estimated sail force applied to the strap is calculated as

$$F_w = k_w \left(\frac{\rho v_{exit}^2}{2} \right) A_w \qquad \text{(E.4)}$$

The magnitude of the force which is transmitted to the digital scale would be determined by the deflection angle of the strap, θ_d. As shown in Figure E-5, $\Delta F_{T,w}$ is the hypotenuse of the triangle which depicts the tension in the strap. Therefore,

$$\Delta F_{T,w} = \frac{F_w}{\sin(\theta_d)} \tag{E.5}$$

Note that, $\Delta F_{T,w}$ is inversely proportional to $\sin(\theta_d)$. As such, a smaller deflection angle will produce an exponentially larger tension. During experimentation, the deflection of the strap was nearly imperceptible (see Figure E-3). To estimate this deflection, a maximum can be calculated based on the folded width of the taut-side strap (½"). The centroid of the slack-side strap would be expected to pass through the vertical plane which is parallel to the duct exit, and which passes through the centroid of the taut-side strap. Thus, the deflection is measured from the center of the taut-side strap. Since the slack-side strap has not passed the rear edge of the taut-side strap in Figure E-3, the deflection can be safely estimated as less than half of the folded width of the strap (¼", or 6.25mm).

Based on the length of 36", an angle of 0.5° would result in a deflection of approximately 8mm, which is greater than the estimated maximum deflection. This observation is evidence that a sail force on the tension strap is plausible as a major source of error.

For calculation, the angle of deflection is estimated to be 0.5°. This angle corresponds with a maximum deflection of 8mm.

To convert the tension force calculated in equation (E.5) into a useful correction factor, it must be depicted as a torque.

$$\Delta T_w = r_d \Delta F_{T,w} \tag{E.6}$$

Recall from section 4.2.5 that the plastic friction drum was melted by friction heat over the course of many experiments. Since a range of drum diameters exists, r_d will be calculated from the average drum diameter (of 23.00mm).

The final correction can be obtained by combining equations (E.4) through (E.6).

$$T_{corr,w} = \Delta T_w = k_w \frac{r_d \rho v_{exit}^2 A_w}{2 \sin(\theta_d)} \tag{E.7}$$

Thus far, the identified sources of error effectively apply additional resistance to the rotor, such that they can not be measured by the digital scales. From this observation, it may be assumed that the magnitude of the correction may not exceed the magnitude of the torque error.

While it would be exceedingly difficult to precisely model the torque correction, there is sufficient information to calculate the maximum plausible correction by maximizing the value of k_w, while minimizing the magnitude of torque error. By observing the inequality,

$$T_{err} - T_{corr,w} > 0 \tag{E.8}$$

the data in Table E-1 is processed using a solver which minimizes the differences of the squared errors.

Table E-1: Difference of squares analysis of torque correction model

Code	T_{err}	$T_{err} - T_{corr,w}$	$\left(T_{err} - T_{corr,w}\right)^2$
#	Nm	Nm	$(Nm)^2$
A10	0.0266	0.0010	0.0000
B10	0.0300	0.0044	0.0000
C10	0.0285	0.0030	0.0000
D10	0.0401	0.0147	0.0002
E10	0.0344	0.0087	0.0001
A15	0.0568	0.0009	0.0000
B15	0.0566	0.0005	0.0000
C15	0.0588	0.0027	0.0000
D15	0.0681	0.0122	0.0001
E15	0.0651	0.0092	0.0001
F15	0.0625	0.0060	0.0000
F15	0.0649	0.0084	0.0001
G15	0.0751	0.0186	0.0003
A20	0.1031	0.0017	0.0000
B20	0.1009	0.0000	0.0000
C20	0.1038	0.0029	0.0000
D20	0.1084	0.0075	0.0001
E20	0.1091	0.0079	0.0001
E20	0.1066	0.0055	0.0000

The value of k_w which minimizes the sum of the squares is 0.644. The correction can be added to the observed torque values, as though the digital scales were reading the full tension (without the sail force being applied). In Table E-2, these corrected values are compared to the observed torque values (uncorrected) and the expected torque values.

Table E-2: Reduced torque results, with proposed corrections

| Code	T_{phys}	T_{exp}	$T_{phys} + T_{corr,w}$
#	Nm	Nm	Nm
A10	0.0712	0.0977	0.0967
B10	0.0645	0.0942	0.0901
C10	0.0623	0.0903	0.0878
D10	0.0467	0.0861	0.0722
E10	0.0356	0.0680	0.0612
A15	0.163	0.220	0.219
B15	0.159	0.215	0.215
C15	0.152	0.210	0.208
D15	0.135	0.203	0.191
E15	0.112	0.174	0.168
F15	0.089	0.147	0.145
F15	0.086	0.147	0.143
G15	0.049	0.118	0.105
A20	0.300	0.404	0.402
B20	0.294	0.395	0.394
C20	0.282	0.386	0.383
D20	0.271	0.379	0.372
E20	0.236	0.342	0.337
E20	0.238	0.342	0.339
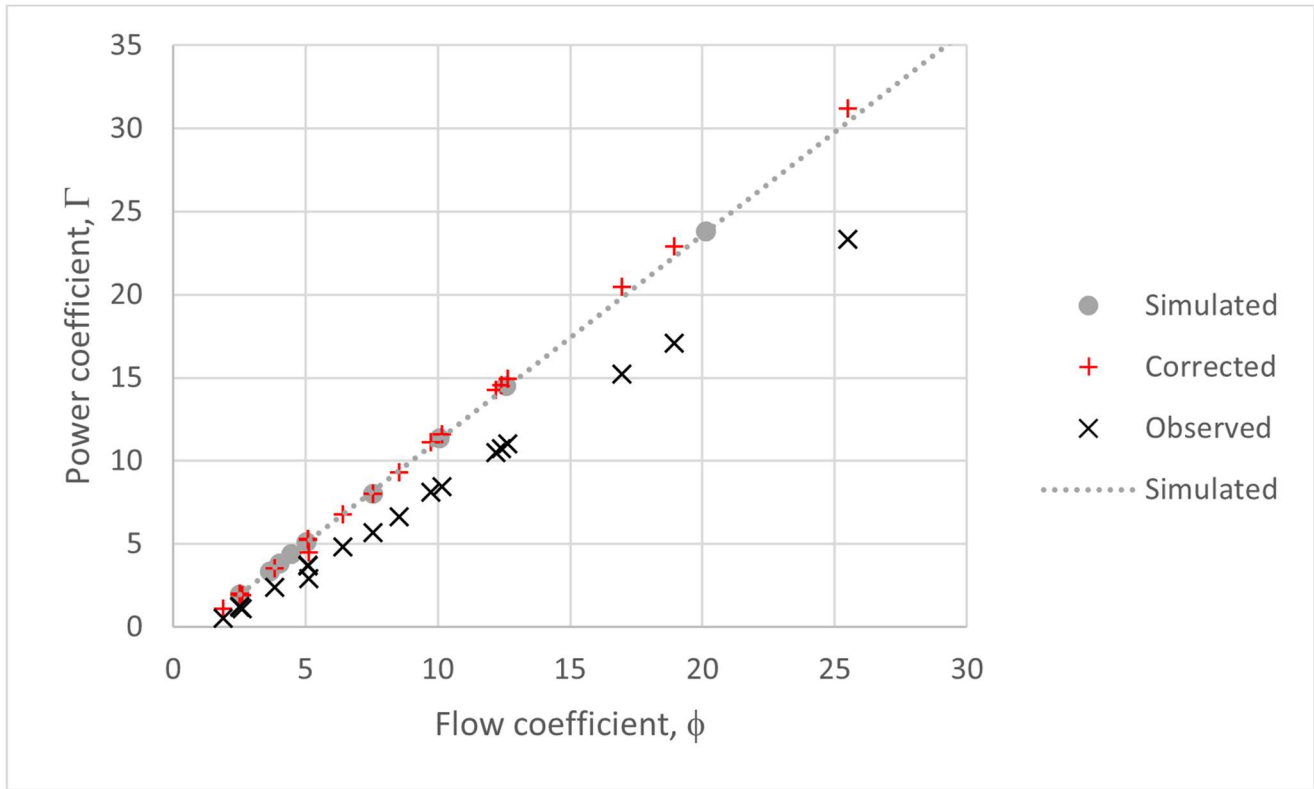
Figure E-7: Comparison of performance curves using nondimensionalized coefficients (mechanical power vs flowrate), before and after the proposed data correction

While it cannot be definitively stated how big an effect the sail error has on the overall torque error, Figure E-7 is a graphical representation of the maximum possible correction for such an error. The correlation between the expected torque and the observed torque is visibly better with the correction. The true values of the observed torque without the sail effect should cause the data to fall somewhere between the black x's and red +'s. The remainder of the error can be explained by some combination of bearing error, viscous error (size effect), and any methodological errors related to the torque measurement (such those described as in Appendix D).
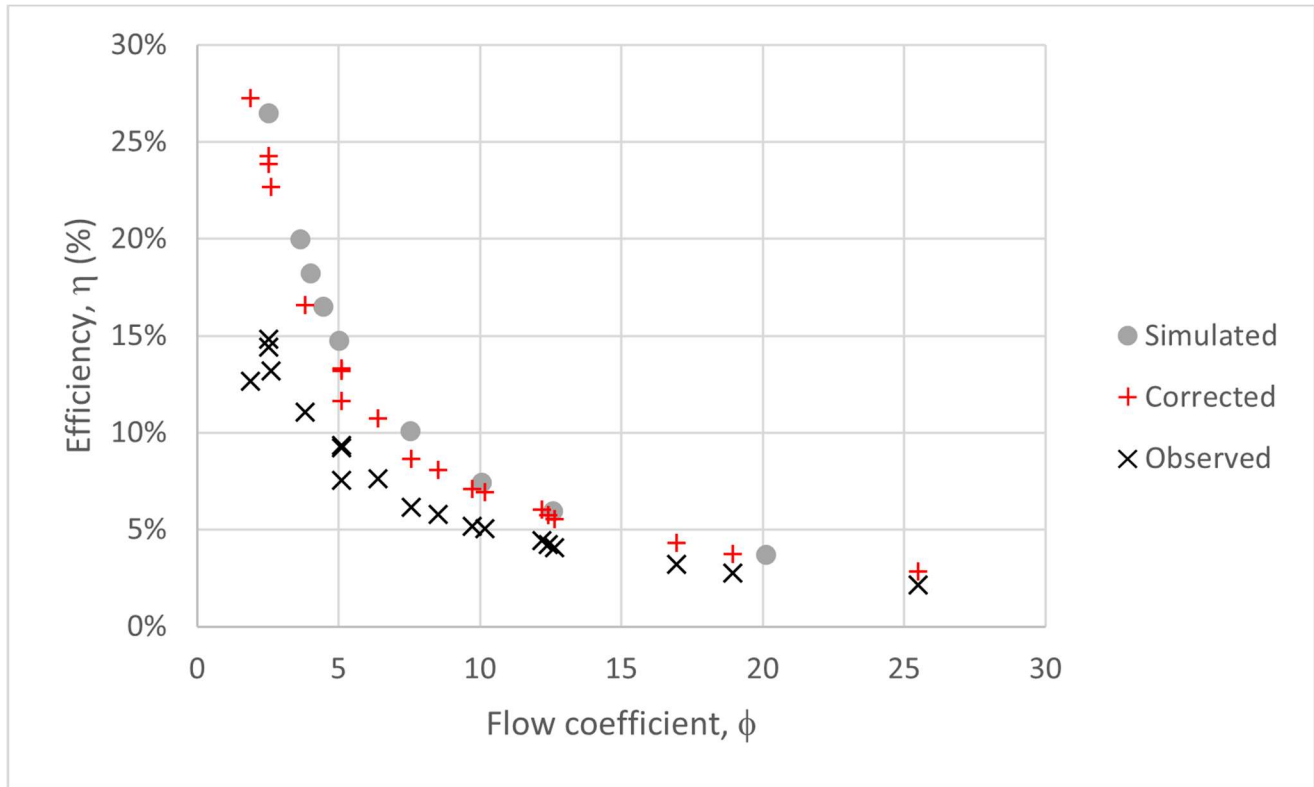
Figure E-8: Comparison of performance curves using nondimensionalized coefficients (efficiency vs flowrate), before and after the proposed data correction

Figure E-8 demonstrates that the same effect is present with a plot of efficiencies, suggesting that torque presented the largest source of error among the independent variables which were recorded. By applying the sail force correction, the plot is now in near perfect agreement with the raw simulated data. The remaining discrepancies may be explained by physical torque losses or some imprecision in the aggregate pressure correction from section 4.5.3.

Appendix F   Calculation of expected temperature change in the duct system

To eliminate the possibility that a major blunder has occurred in either the simulated or physical experiments, the ducted turbine system may be considered in terms of the steady-flow energy equation (as seen, for example in McPherson, 1993). For pressure, P, volume, V, internal energy, U, the specific gas constant of air, R_{air}, and temperature, $T(°C)$, the enthalpy, H, of a volume of air may be calculated using the following equation:

$$H = PV + U = R_{air}T(°C) + U \tag{F.1}$$

$$\frac{1}{2}(v_1{}^2 - v_2{}^2) + g(z_1 - z_2) + w_{12} = \int VdP + f_{12} = C_P(T(°C)_2 - T(°C)_1) - q_{12} \tag{F.2}$$

Here, v is the bulk flow velocity, z is the vertical displacement between two points, w_{12} is the work energy added over the length of duct, f_{12} is the energy loss due to friction in the system, C_P is the heat capacity of the gas at a constant pressure, and q_{12} is the heat energy lost from the system. Note that the formulation of the steady-flow energy equation shown in (F.2) has units of J/kg, or m^2/s^2.

Mass continuity dictates that, for a duct of constant cross-section,

$$v_1 = v_2$$

Since the enclosed duct section is oriented horizontally,

$$z_1 = z_2$$

Assuming no heat is added to the enclosed duct section

$$q_{12} = 0$$

And so, equation (F.2) becomes

$$w_{12} = \frac{P_2 - P_1}{\rho} + f_{12} = C_P(T(°C)_2 - T(°C)_1) \tag{F.3}$$

Note that f_{12} has effectively been determined by the experiment, as the difference between the air power and the mechanical power. Therefore, the only new information that can be determined is the expected temperature difference that occurs in the duct system. As a final check to confirm that the experimentally obtained data (both simulated and physical) are within a plausible range, this temperature difference must be sufficiently low. Since the temperature sensor used in experimentation has a resolution of 0.1°C (see section 4.2.1), the expected temperature difference must fall below this threshold.

Code	ΔH	$\Delta T\,(°C)$
#	J/kg	°C
2AI-1	11.85	0.012
2AI-2	12.53	0.012
2AI-3	10.98	0.011
2AI-4	10.06	0.010
2AI-5	5.607	0.006
2AI-6	4.579	0.005
2AI-7	2.939	0.003
2AI-8	0.9145	0.001
2AI-9	15.87	0.016
2AI-10	3.895	0.004

Table F-2: Expected temperature differences for physical experimental setpoints (calculated)

Code	ΔH	$\Delta T\,(°C)$
#	J/kg	°C
A10	3.568	0.003
B10	4.618	0.005
C10	5.947	0.006
D10	5.584	0.006
E10	8.311	0.008
A15	5.264	0.005
B15	7.661	0.008
C15	9.520	0.009
D15	10.92	0.011
E15	17.88	0.018
F15	21.48	0.021
F15	20.91	0.021
G15	15.80	0.016
A20	7.199	0.007
B20	10.58	0.011
C20	13.91	0.014
D20	16.30	0.016
E20	28.28	0.028
E20	28.55	0.028

All the expected temperature differences fall below the threshold of 0.1°C. Thus, the temperature difference should not be measurable using the temperature sensor from the experiment. Therefore, if a major blunder has occurred, it cannot be positively identified with a simple hand calculation.